# 博 士 論 文

Improvement of $\theta_{13}$ Measurement in
the Double Chooz Experiment and
the First Effective $\Delta m^2_{31}$ Measurement from Reactor
Neutrino Oscillation at Different Baselines

$$\left( \begin{array}{c} \text{ダブルショー実験での}\theta_{13}\text{測定の改良及び} \\ \text{異なるベースラインでの原子炉ニュートリノ} \\ \text{振動による有効}\Delta m^2_{31}\text{の初めての測定} \end{array} \right)$$

Thiago Junqueira de Castro Bezerra

**東北大学**

平 成 ２ ５ 年

# Improvement of $\theta_{13}$ Measurement in the Double Chooz Experiment and the First Effective $\Delta m^2_{31}$ Measurement from Reactor Neutrino Oscillation at Different Baselines

Thiago Junqueira de Castro Bezerra

A dissertation submitted to the Graduate School of Science of Tohoku University in partial fulfilment of the requirements for the degree of Doctor of Philosophy in Physics

Recommended for Acceptance by the Department of Physics
**Adviser:** Professor Dr. Fumihiko Suekane

**Examination Committee**
Professor Dr. Kazushige Maeda
Professor Dr. Ken-ichi Hikasa
Professor Dr. Kunio Inoue
Professor Dr. Tomoyuki Sanuki

August 2013

# Abstract

Recently, three reactor neutrino experiments, Daya Bay, Double Chooz and RENO have directly measured the last unknown neutrino mixing angle $\theta_{13}$, also being independently measured by MINOS and T2K accelerator based experiments. This dissertation presents results from a search for reactor $\bar{\nu}_e$ flavour oscillation using the Double Chooz far detector and in combination with the other experiments results. Using the neutron capture on Gadolinium (Hydrogen) selection method, a number of 8249 (36284) candidate electron antineutrino events were observed in a data taking period of 251.27 days with 33.71 (113.1) GW-ton-year (reactor power $\times$ detector mass $\times$ run time) exposure using a 10.3 (32.6) $m^3$ fiducial volume detector located 1050 m far from the two reactor cores of the Chooz nuclear power plant in France. The expectation in case of $\theta_{13} = 0$ is 8937 (36680) events, and the deficit is interpreted as evidence of electron antineutrino disappearance. A combined rate and energy dependent fit, using both neutron capture on Gadolinium and Hydrogen, finds $\sin^2 2\theta_{13} = 0.100 \pm 0.034$. In addition, the other important oscillation parameter, effective $\Delta m_{31}^2$ ($= \Delta \tilde{m}_{31}^2$) is measured for the first time, using baseline dependence of the reactor neutrino disappearance. A global fit is applied to the available data and $\Delta \tilde{m}_{31}^2 = 2.95_{-0.61}^{+0.42} \times 10^{-3}$ $eV^2$, $\sin^2 2\theta_{13} = 0.099_{-0.012}^{+0.016}$ are obtained by setting both parameters free. This result is complementary to $\Delta \tilde{m}_{31}^2$ to be measured by spectrum shape analysis. The measured $\Delta \tilde{m}_{31}^2$ is consistent with $\Delta \tilde{m}_{32}^2$ measured by $\nu_\mu$ disappearance in MINOS, T2K and atmospheric neutrino experiments within errors. Finally, the measured $\sin^2 2\theta_{13}$ is independent of $\Delta \tilde{m}_{32}^2$, and consistent with the reactor and accelerator results.

**Cosmic Gall**

*by John Updike*
The New Yorker, December 1960

Neutrinos, they are very small.
They have no charge and have no mass
And do not interact at all.
The earth is just a silly ball
To them, through which they simply pass,
Like dustmaids down a drafty hall
Or photons through a sheet of glass.
They snub the most exquisite gas,
Ignore the most substantial wall,
Cold shoulder steel and sounding brass,
Insult the stallion in his stall,
And scorning barriers of class,
Infiltrate you and me! Like tall
and painless guillotines, they fall
Down through our heads into the grass.
At night, they enter at Nepal
and pierce the lover and his lass
From underneath the bed-you call
It wonderful; I call it crass.

# Acknowledgements

This work would not be concluded without the help of many amazing people, that I would like to thank.

# Contents

# List of Figures

# List of Tables

# Chapter 1

# Introduction

The neutrino is one of the several elementary particles believed to form all existing matter, and the most enigmatic. This particle history is bonded with the discovery of radioactivity in the beginning of $20^{\text{th}}$ century, when the atom structure, which were believed to be indivisible and imperishable, started to be understood as a composition of more elementary elements.

In radioactive decays, an atomic nucleus or particle, spontaneous emits another particle. It is the case for an alpha ($\alpha$), beta ($\beta$) and gamma ($\gamma$) decays, where a Helium nucleus, an electron and a photon are emitted, respectively. Choosing the reference frame in which the the initial particle or nucleus is at rest, a well defined energy is expected for the the two bodies after the decay, by conservation of total energy and momentum. Although this was true for the $\alpha$ and $\gamma$ decays, measurements of the $\beta$ decay energy spectrum showed a continuum distribution, instead of a peak.

The hypothesis of the neutrino existence was presented in late 1930 in an attempt to explain the $\beta$ decay, in the famous letter written by Wolfgang Pauli.[1] Proposing a neutral (zero charge) and with a tinny mass (or completely massless) particle, the three particle $\beta$ decay would be explained by part of the energy being carried out by this new particle, initially called neutron. However, in 1932, James Chadwick discovered a second constituent of the atomic nucleus, which he named neutron, since it does not have electric charge. Two years latter, Enrico Fermi develops a theory for the $\beta$ decay, which considered a third particle. He called this particle neutrino, since in Italian the suffix "-ino" means tiny.

Being a particle that hardly interacts with ordinary matter, the neutrino discover only happened almost 30 years latter. In the 1950's Clyde Cowan and Frederick Reines worked in ways to detect the neutrino using intense sources, in order to suppress the small interaction cross section. In the beginning a nuclear blast was considered, but with the advent of nuclear reactors, they could make the measurement of electron antineutrino interaction. In 1956 they publish their discovery and Reines received the Nobel Prize in Physics in 1995. Cowan died in 1974.

---

[1] *"Dear radioactive ladies and gentlemen,..."* addressed to the Physical Institute of the Federal Institute of Technology, Zürich.

Since then, our understanding on the physics of elementary particles and subsequently the neutrino physics has been developed much. According to the Standard Model, which is the most accepted theory that describes elementary particles and their interactions, the $\beta$ decay is described as a decay of a $W^-$ boson, the weak force mediator particles, in an electron and its respective antineutrino. The other two neutrinos type, the muon- and tau-neutrino were discovered only in 1962 and 2000 respectively. Moreover the ALEPH collaboration publish in 2006 their results on a precision electroweak measurements on the Z boson (another weak force mediator) resonance, where they conclude that only three (not two or four) neutrinos flavours, or types, exist interacting through the weak force.

Nowadays, the neutrino research field is very varied due to the different ways of creating them. Neutrinos are generated in the Sun, arise from the decay of cosmic radiation products, result of collapsing stars (supernovas), referring to the history of the universe (cosmological neutrinos) and from human made sources, such as nuclear reactors and particle accelerators.

This dissertation proposes to improve our understanding in a very interesting property of neutrinos, the neutrino oscillation, which is not expected by the Standard Model. In the past 20 years rapid progress has been made on neutrino oscillation parameters measurements, remaining only few questions to be answered. The Double Chooz experiment proposes to measure one of those parameters, $\theta_{13}$, also being possible to test the three neutrino oscillation scheme by combining its data with the other reactor neutrino experiments. The contents of this work is divided as follows: next chapter of this dissertation contains a review of neutrino oscillation and the most important experiments and results concerting the measurement of oscillation parameters is given as well. Chapter 3 is dedicated to the Double Chooz experiment, giving the details of the detector and its principles. On chapter 4, the Double Chooz detector simulation, efficiency calculation, neutrino selection and background estimation are presented. The fifth chapter describes the methods to extract the oscillation parameters from the experiments data and presents a discussion about the results. Finally, on chapter 6 the conclusions of this work are presented.

# Chapter 2

# Neutrino Oscillation

This chapter is dedicated to review and explore both theoretical and experimental point of view of neutrino physics, particularly to neutrino oscillations. The current state of the art regarding the measurement of the oscillation parameters is given with a description of the most important experiments in the field. The problem related to the nature of the neutrino mass is also briefly described. Finally, the open questions and the future efforts to be addressed by the neutrino community are also discussed.

## 2.1 Neutrinos and the Standard Model of Particle Physics

The Standard Model ($\mathcal{SM}$) of particle physics is the theory describing how the fundamental constituents of our universe interact. From the technical point of view the $\mathcal{SM}$ is a re-normalisable gauge field theory, based on the symmetry group $SU(3)_C \bigotimes SU(2)_L \bigotimes U(1)_Y$ which describes the strong, weak and electromagnetic interaction, via the exchange of spin-1 gauge field: eight massless gluons for the strong interaction, one massless photon for the electromagnetic interaction and three massive bosons, $W^\pm$ and $Z^0$ for the weak interaction.

The known elementary particles and antiparticles are fermions with spin-$\frac{1}{2}$ and are organised in two families according on how they interact: quarks and leptons. Quarks interacts with all the three forces, while leptons interact only through the electromagnetic and/or the weak force. Quarks and leptons exist in three generations or flavours, with different masses and flavour quantum numbers, but with identical interactions, which make the $\mathcal{SM}$ symmetric with respect to the flavour. A summary of $\mathcal{SM}$ fermions and bosons is shown figure 2.1.

The fermions are a representation of the symmetry group and can be written as:

$$\left( \begin{array}{c} \nu_l \\ l^- \end{array} \right)_L, \left( \begin{array}{c} q_u \\ q_d \end{array} \right)_L, l_R^-, q_{uR}, q_{dR}, \tag{2.1}$$

where the left-handed fields are $SU(2)_L$ doublet, while the right handed fields are $SU(2)_L$ singlets. Neutrinos interact only via the weak force and they are experimentally observed with left-handed helicity, thus a right-handed neutrino is not included in the $\mathcal{SM}$.

Due to the gauge symmetry of the theory, particles are so far massless. While such assumption appears as a good approximation at high energies ($E \gg M_Z, M_W$), where the weak and electromagnetic interactions have similar strengths and are described by

Figure 2.1: Fermions and Bosons described by the Standard Model of elementary particles. For each fermion (three generations of matter) there is an antiparticle, which are not shown for brevity.The gauge bosons are in the fourth column and the Higgs boson in the fifth.

the unique electroweak force, at low energies the mass of the W$^\pm$ and Z bosons make the weak interaction weaker than the electromagnetic interaction.

The weak gauge bosons masses are acquired by introducing a new scalar field and breaking the gauge symmetry by choosing an expectation value for its vacuum state. This mechanism, known as spontaneous symmetry breaking, generates the masses for the weak bosons and give rise to the appearance of the spin-0 Higgs boson. The photon and the gluons remain, by construction, massless particles in agreement with experimental observations.

Once the gauge symmetry is broken, also fermions are allowed to acquire a mass term through the so called Higgs mechanism which couples the right-handed singlets with the left-handed doublets via the Yukawa coupling constant, providing masses of the form of

$$\mathcal{L}_Y = m_l \bar{l}_L l_R + m_q \bar{q}_L q_R + h.c., \tag{2.2}$$

where the mass term for the fermions (for example) is given by $m_l$:

$$m_l = \frac{v}{\sqrt{2}} \Gamma_l, \tag{2.3}$$

where $v$ is the vacuum expectation value of the Higgs field and $\Gamma_l$ is the Yukawa coupling constant, that assumes different values for the different fermions. To explain the observed masses, $\Gamma_l$ varies from $\sim 1$ for the heaviest fermion, the top quark, to $\sim 10^{-5}$ for the lighter charger fermion, the electron.

Since the observed neutrinos are only left-handed, they are not allowed to acquire mass though the Higgs mechanism, remaining massless in the $\mathcal{SM}$. The $\mathcal{SM}$ provides a beautiful theoretical model which is able to accommodate most of the present knowledge on electroweak and strong interactions. It is able to explain many experimental facts and, in some cases, it has successfully passed very precise tests. Even the long search for the Higgs boson has recently provided conclusive evidence for the discovery of a new particle, consistent with the $\mathcal{SM}$ Higgs boson hypothesis [1].

In spite of the impressive phenomenological success, the $\mathcal{SM}$ leaves many unanswered questions to be considered as a complete description of the fundamental forces. There is no understanding regarding the existence of three (and only three) fermions families as well as their origins. There is no answer to the observed mass spectrum and mixing pattern. These, and others questions remain open and require new physics beyond the $\mathcal{SM}$. As will be stressed in the rest of this chapter, the first hint from such new physics has emerged with evidence of neutrino oscillations.

## 2.2 Neutrino Oscillation Theory

Neutrino oscillation were postulated in 1957 by Pontecorvo [2]. In analogy with $K^0 \leftrightarrow \bar{K}^0$ oscillations, Pontecorvo suggested the possibility of neutrino-antineutrino oscillation ($\nu \leftrightarrow \bar{\nu}$). When the second neutrino family where discovered, Maki, Nakagawa and Sakata proposed in 1962 the possibility of oscillation among the neutrino families introducing the concept of lepton flavour mixing [3]. The neutrino oscillation mechanism is based on the fact that if neutrino have a non-zero mass, flavour states $|\nu_\alpha\rangle$ (interaction states) and mass states $|\nu_i\rangle$ (propagation states) could not coincide, in analogy to the mixing in the quark sector, i.e.,

$$|\nu_\alpha\rangle = \sum_i U^*_{\alpha,i} |\nu_i\rangle, \tag{2.4}$$

where $\alpha$ represent the flavour families $(e, \mu, \tau)$, $|\nu_i\rangle$ the mass states of mass $m_i$ (with i = 1, 2, 3) and $U$ is the so called PMNS (Pontecorvo-Maki-Nakagawa-Sakata) unitary mixing

matrix. Neutrinos are produced via weak interaction in a defined flavour eigenstate $|\nu_\alpha\rangle$ together with the corresponding lepton $\alpha$. For a neutrino produced at time $t = 0$, $|\nu\rangle (t = 0) = |\nu_\alpha\rangle$, and propagating it as a free particle following the Schrödinger equation, after a time $t$ and travelled distance $L$, it will be described by

$$|\nu_\alpha(t, L)\rangle = \sum_i U^*_{\alpha,i} e^{-i(E_i t - pL)} |\nu_i\rangle, \tag{2.5}$$

where $E$ and $p$ is the neutrino energy and momentum, respectively. Assuming the three mass eigenstates propagate with the same momentum with relativistic energies ($p \simeq E \gg m_i$):

$$E_i = \sqrt{p^2 + m_i^2} \simeq p + \frac{m_i^2}{2p} \simeq E + \frac{m_i^2}{2E}. \tag{2.6}$$

Thus, equation 2.5 can be re-written, using natural units ($c = \hbar = 1$), as

$$|\nu_\alpha(t, L)\rangle = \sum_i U^*_{\alpha,i} e^{-i\frac{m_i^2}{2E}L} |\nu_i\rangle. \tag{2.7}$$

In other words, the initial mass state components evolve independently acquiring phases depending from their masses. Equivalently, equation 2.7 can be reverted to express the mass eigenstate $|\nu_i\rangle$ as a function of the flavour eigenstate $|\nu_\beta\rangle$,

$$|\nu_\alpha(L)\rangle = \sum_{\beta=e,\mu,\tau} \left( \sum_i U^*_{\alpha,i} e^{-i\frac{m_i^2}{2E}L} U_{\beta,i} \right) |\nu_\alpha\rangle. \tag{2.8}$$

A neutrino created at $t = L = 0$, with $\alpha$ flavour state, evolves as a linear superposition of the existing lepton states. Like the production, the detection of neutrinos occurs via the weak interaction. The probability to observe a neutrino created with flavour $\alpha$, at $L = 0$, with a different flavour $\beta$, after a distance $L$, is defined as

$$
\begin{aligned}
P\left(\nu_\alpha \rightarrow \nu_\beta\right) &= |\langle \nu_\beta | \nu_\alpha(L)\rangle|^2 = \left| \sum_i U^*_{\alpha,i} U_{\beta,i} e^{-i\frac{m_i^2}{2E}L} \right|^2 \\
&= \sum_i \left| U_{\alpha,i} U^*_{\beta,i} \right|^2 + 2Re \left( \sum_{i>j} U_{\alpha,i} U^*_{\beta,i} U^*_{\alpha,j} U_{\beta,j} e^{-i\frac{\Delta m_{ij}^2}{2E}L} \right).
\end{aligned} \tag{2.9}
$$

In the equation above an oscillation term appears as a function of the distance between the neutrino creation point (source) and the detection point (detector), and the neutrino energy. The oscillation frequency is proportional to the squared difference between the mass states, $\Delta m_{ij}^2 = m_j^2 - m_i^2$, while the oscillation amplitude is proportional to the PMNS matrix elements, $U_{\alpha,i}$.

The PMNS matrix is defined as

$$U = \begin{pmatrix} c_{12}c_{13} & s_{12}c_{13} & s_{13}e^{-i\delta} \\ -s_{12}c_{23} - c_{12}s_{23}s_{13}e^{i\delta} & c_{12}c_{23} - s_{12}s_{23}s_{13}e^{i\delta} & s_{23}c_{13} \\ s_{12}s_{23} - c_{12}c_{23}s_{13}e^{i\delta} & -c_{12}s_{23} - s_{12}c_{23}s_{13}e^{i\delta} & c_{23}c_{13} \end{pmatrix}, \tag{2.10}$$

where $c_{ij} = \cos\theta_{ij}$ and $s_{ij} = \sin\theta_{ij}$. The angles $\theta_{12}$, $\theta_{13}$ and $\theta_{23}$ represent the mixing angles and $\delta$ is a CP violation phase. Two additional phases have to be taken into account if neutrinos are Majorana particles, but such phase do not impact the neutrino oscillation.

As shown in equation 2.9, neutrino oscillations depend also on the mass squared differences between the mass states, namely $\Delta m_{21}^2$, $\Delta m_{32}^2$ and $\Delta m_{31}^2$, which only two of them are independent, since there is the relation

$$\Delta m_{31}^2 = \Delta m_{32}^2 + \Delta m_{21}^2. \tag{2.11}$$

Consequently, neutrino oscillation depends on six free parameters: three mixing angle, two mass squared differences and one complex CP violation phase. For practical reasons, the mixing matrix is usually factorized in terms of three matrices $M_{2,3} \times M_{1,3} \times M_{1,2}$ as

$$U = \begin{pmatrix} 1 & 0 & 0 \\ 0 & c_{23} & s_{23} \\ 0 & -s_{23} & c_{23} \end{pmatrix} \begin{pmatrix} c_{13} & 0 & s_{13}e^{-i\delta} \\ 0 & 1 & 0 \\ -s_{13}e^{i\delta} & 0 & c_{13} \end{pmatrix} \begin{pmatrix} c_{12} & s_{12} & 0 \\ -s_{12} & c_{12} & 0 \\ 0 & 0 & 1 \end{pmatrix}. \tag{2.12}$$

As one can see, each matrix is related to a different mixing angle. $M_{2,3}$ is parametrized in terms of $\theta_{23}$ which is the mixing angle dominating the $\nu_\mu \to \nu_\tau$, related to the oscillation of atmospheric and accelerator neutrino. $M_{1,2}$ is parametrized in terms of $\theta_{12}$ dominating the transition $\nu_e \to \nu_{\mu,\tau}$, related to the oscillation of neutrino coming from the sun and long baseline reactors. Finally, $M_{1,3}$ depends on $\theta_{13}$ which is the mixing matrix dominating the oscillation $\nu_\mu \to \nu_e$, and short baseline reactor $\bar{\nu}_e \to \bar{\nu}_e$. The CP phase always appears multiplied by the terms $\sin\theta_{12} \sin\theta_{23} \sin\theta_{13}$, so it would be measurable only if $\theta_{13}$ is different than zero[1].

Finally, the observation of the neutrino oscillations has two main consequences: neutrinos have a non-zero mass and the lepton flavour is not conserved.

## 2.3   Matter Effects

When discussing oscillation searches where the neutrino beam passes through a portion of the Earth, one must consider the influence of matter on neutrino propagation. During propagation, electron neutrinos and antineutrinos may forward-scatter via charged current interactions with electrons in the surrounding matter medium. This phenomena was first considered by Mikheyev and Smirnov [4], and Wolfenstein [5], and is now known as the MSW effect. While most neutrinos observed in experiments pass through part of the Earth at some point, it has been been shown by [6] that matter effects only impact experiments with a baseline in the order of 1000 km. Thus, while this effect has little impact on experiments where $L \sim 1$ km, as in reactor neutrino experiments, it does need to be considered in accelerator based neutrino experiments searching for neutrino appearance at long baselines.

Any area of electron density $N_\alpha$ can be considered to contribute an effective potential term to the flavor basis Hamiltonian $V_\alpha = \sqrt{2}G_F N_\alpha$, where $G_F$ is the Fermi constant. Since the Earth presents a density of only electrons, $V = (\sqrt{2}G_F N_e, 0, 0)$. Neutral current scattering contributes a term which is equal for all flavour eigenstates, and thus a negligible multiple of the identity matrix. The MSW effect will modify the oscillation probability, defined in equation 2.9, as proposed in [7].

Depending on the experimental parameters, matter effects can mimic a CP-violating signal. This effect also depends on the ordering of the neutrino masses, or the mass hierarchy. Since the absolute hierarchy has not yet been established, this variable can affect an experiment's sensitivity to measuring $\delta_{CP}$.

The Sun is a pure source of $\nu_e$, as described in section 2.5.1.1. In analogy to neutrinos travelling through the Earth, solar neutrinos oscillations have to account for the matter effects. However, in the Sun, the electron density $N_\alpha$ changes as a function of the radius.

---

[1]Some experiments showed non zero value for the other two angles, as it is showed in next sections

If the evolution of the propagation Hamiltonian is adiabatic, then $\nu_e$ produced in the Sun's interior will evolve into $\nu_2$, which is defined such that $\nu_2 > \nu_1$. Evidence suggests that $> 90\%$ of $^8$B's $\nu_e$ produced in the Sun's core evolve into $\nu_2$ due to matter effects [8]. Therefore, to a first approximation, the $\nu_e$ flavour content of $^8$B solar neutrinos reach the Earth is expected to be $|U_{e2}| \sim \sin^2 \theta_{12}$.

## 2.4 Mass Hierarchy

In the full three flavour model of neutrino mixing, a hybrid approach to labelling the neutrino mass eigenstates is taken. The mass squared splittings are known to be hierarchical, therefore it is possible to define $\nu_3$ as the neutrino mass eigenstate whose mass is very different from the masses of the other two mass eigenstates (either much larger or much smaller), i.e. $|\Delta m_{21}^2| \ll |\Delta m_{32}^2| \sim |\Delta m_{31}^2|$. However, this definition does not specify the mass hierarchy, i.e. whether $m_3 > m_{1,2}$ or $m_3 < m_{1,2}$. Therefore, the sign of $\Delta m_{31}^2$ and $\Delta m_{21}^2$ can be either positive or negative. If $\Delta m_{31}^2 > 0$, this is called the "normal" mass hierarchy. If however, $\Delta m_{31}^2 < 0$, this is called the "inverted" mass hierarchy, as shown in figure 2.2. Matter effects from accelerator neutrino beams passing through the earth can be used to determine the mass hierarchy. The $m_2^2 > m_1^2$ hierarchy, was solved by the solar neutrino experiments, described in section 2.5.1.1.
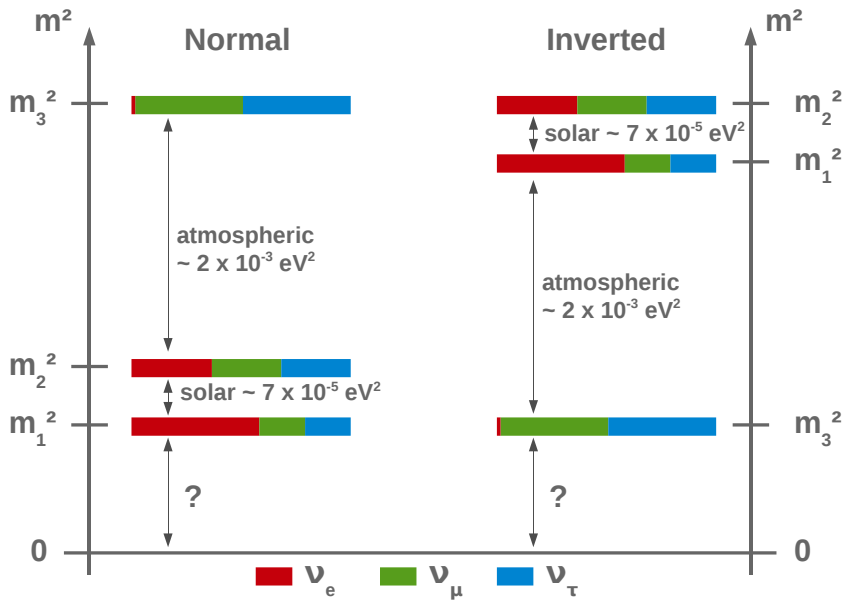


Figure 2.2: Neutrino mass eigenstates spectra for both cases of normal or inverted hierarchy, and composition in terms of $\nu_e$, $\nu_\mu$, and $\nu_\tau$. Neither the absolute scale, nor the masses values, nor the 3-2 hierarchy arrangement are known so far.

## 2.5 Measuring Neutrino Oscillation Parameters

To easily understand neutrino oscillation experimental results, the simplified case for two active neutrino is considered. The mixing between two neutrino families is described by a real and orthogonal $2 \times 2$ matrix with one mixing parameter, the rotation angle $\theta$ between the flavour and the mass eigenstates:

$$\begin{pmatrix} \nu_\alpha \\ \nu_\beta \end{pmatrix} = \begin{pmatrix} \cos\theta & \sin\theta \\ -\sin\theta & \cos\theta \end{pmatrix} \begin{pmatrix} \nu_1 \\ \nu_2 \end{pmatrix}, \tag{2.13}$$

and the oscillation probability takes the form

$$P(\nu_\alpha \to \nu_\beta) = \sin^2 2\theta \sin^2 \left( \frac{\Delta m^2 L}{4E} \right). \tag{2.14}$$

The oscillation amplitude, $\sin^2 2\theta$, is determined by the mixing angle $\theta$ and does not allow to distinguish between $\theta$ and $\pi/2 - \theta$, which are not physically equivalent.

Restoring to physics units, the oscillation phase, $\phi$, becomes

$$\phi = 1.27 \left( \frac{\Delta m^2 [\text{eV}^2] L[\text{km}]}{E[\text{GeV}]} \right). \tag{2.15}$$

In the limit where $\phi \ll 1$, $P(\nu_\alpha \to \nu_\beta) \simeq \sin^2 2\theta (\Delta m^2 L/4E)^2$, so the measurement of the oscillation probability would determine information only on the product $\sin^2 2\theta \times \Delta m^2$. The oscillation would not have enough time to develop and the number of neutrino oscillation events measured in the detector is approximately independent from the distance $L$, since the oscillation goes with $(L/E)^2$ and the neutrino flux diminish with $1/L^2$.

In the opposite where $\phi \gg 1$, the oscillation are so fast that get averaged out, $P(\nu_\alpha \to \nu_\beta) \simeq 1/2 \sin^2 2\theta$. In this limit the oscillation probability does not depend from the oscillation phase and the number of events decrease with $1/L^2$.

In order to measure both oscillation parameters, the measurement of the averaged probability is not enough, and the $L$ (or $E$) dependence must also be measured to characterise the oscillation pattern. Thus, a good possible experimental condition to characterise oscillation parameters is then to have an oscillation phase of $\simeq 1$.

Even if three neutrino families exist, the mixing parameters are such that the dominant oscillation pattern is driven by the two flavour mixing, while the third flavour contribute at the second or higher order. For this reason the results of oscillation experiments are often shown in a two neutrino scenario and determine a single mixing angle and squared mass difference.

### 2.5.1  Measurement of $\Delta m_{21}^2$ and $\theta_{12}$

Measurement of $\Delta m_{21}^2$ and $\theta_{12}$ oscillation parameters has been performed by the experiments detecting $\nu_e$ produced by the Sun's thermonuclear reactions and non-natural terrestrial $\bar{\nu}_e$ source, such as nuclear reactors.

#### 2.5.1.1  By Solar Neutrinos

Solar neutrinos are $\nu_e$ produced by the reactions responsible for solar energy production, such as $4p + 2e^- \to {}^4\text{He} + 2\nu_e + 26.7$ MeV. This process takes place through different nuclear reactions and consequently solar neutrinos are characterised by different energy spectra as shown in figure 2.3. The typical neutrino flux reaching the Earth is of about $10^{12}$ $\nu/\text{s}/\text{cm}^2$. Several experiments measured the solar neutrino flux, starting in 1970 with the pioneering Chlorine experiment in the Homestake mine, proposed by Raymond Davis Jr. [10]. The $\nu_e$ flux were measured in a tank of 380 m$^3$ filled with C$_2$Cl$_4$, placed 1478 m underground, counting the number of radioactive ${}^{37}$Ar nuclei produced by the inverse beta decay reaction ${}^{37}\text{Cl} + \nu_e \to {}^{37}\text{Ar} + e^-$, which has a threshold energy of 814 keV. Only one third of the neutrino flux predicted by the Standard Solar Model (SSM) were measured. Although this could be the first indication of neutrino oscillation ($\nu_e$ disappearance), at that time an error on the experimental measurements or in the SSM was assumed as possible explanation of the observed deficit.

Another type of radiochemical experiments (Gallex [11], GNO [12] and SAGE [13]), used ${}^{71}$Ga which interacts through the reaction ${}^{71}\text{Ga} + \nu_e \to {}^{71}\text{Ge} + e^-$ that has a
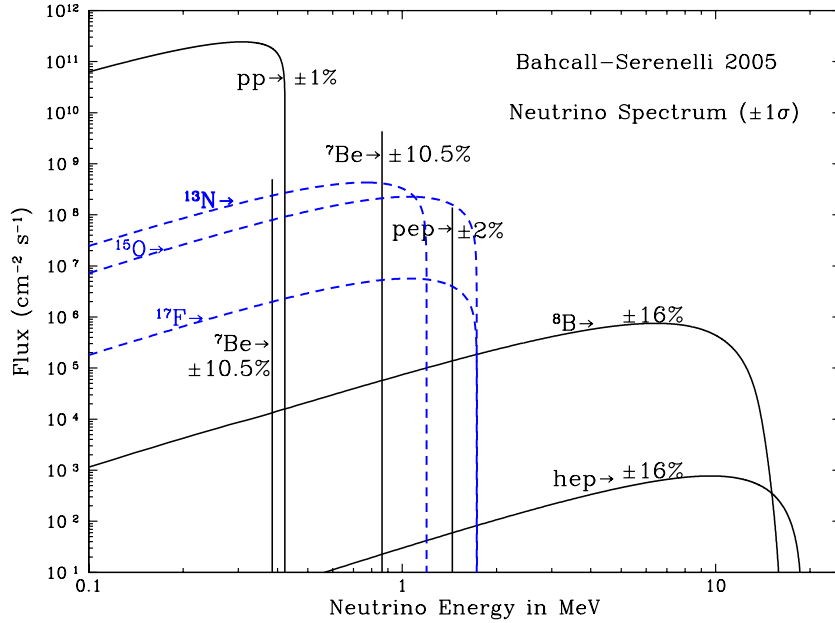
Figure 2.3: The solar neutrino energy spectrum of each SSM production process [9].

threshold energy of 233 keV. Thus, the neutrinos from the pp-chain can be detected, and the solar neutrino flux can be known model independent. These experiments also found a deficit when comparing with the SSM prediction flux. The Super-Kamioka Neutrino Detection Experiment (Super-Kamiokande or simply SK) [14] measured the energy spectrum of solar $^8$B neutrinos. The observed spectrum was compared with the SSM prediction without oscillation, resulting in a poor agreement at 4.6% confidence level. While all these experiments, performed with different techniques, confirmed the deficit in the solar neutrino flux, the theoretical model uncertainty were excluded by a better understanding of the Sun, and this deficit became the so called Solar Neutrino Anomaly.

The solar neutrino anomaly was only solved later by the Sudbury Neutrino Observatory (SNO) experiment [15] using a heavy water ($D_2O$) Čerenkov detector, sensible to neutrino interactions through three different interaction processes:

- Elastic scattering (ES): $\nu_x + e^- \to \nu_x + e^-$ with $x = e, \mu, \tau$, involving all neutrino types but with a different cross-section for $\nu_\mu$ and $\nu_\tau$;

- Charged current (CC): $D + \nu_e \to 2p + e^-$, involving only electron neutrinos;

- Neutral current (NC): $D + \nu_x \to p + n + \nu_x$, involving all neutrino flavour with the same cross-section.

Naming $\Phi_x$ the neutrino flux for the flavour $x$, ES allows to determine the flux $\Phi_{ES} = \Phi_e + 0.155(\Phi_\mu + \Phi_\tau)$, CC determines $\Phi_{CC} = \Phi_{\nu_e}$ and NC determines the total flux $\Phi_{Tot.} = \Phi_e + (\Phi_\mu + \Phi_\tau)$. Thus, the ratio of CC/NC can be interpreted as a ratio of $\nu_e$ flux to the total flux of the three flavours. The measured fluxes are

$$\begin{aligned}
\Phi_{ES} &= 2.35 \pm 0.22(\text{stat.}) \pm 0.15(\text{sys.}) \times 10^6 \ \text{cm}^{-2}\text{s}^{-1} \\
\Phi_{CC} &= 1.68 \pm 0.06(\text{stat.})^{+0.08}_{-0.09}(\text{sys.}) \times 10^6 \ \text{cm}^{-2}\text{s}^{-1} \\
\Phi_{NC} &= 4.94 \pm 0.21(\text{stat.})^{+0.38}_{-0.34}(\text{sys.}) \times 10^6 \ \text{cm}^{-2}\text{s}^{-1}
\end{aligned}$$

These three different reactions measured three independent linear combination of electron, muon and tau neutrino fluxes, as shown in figure 2.4. Such measurement
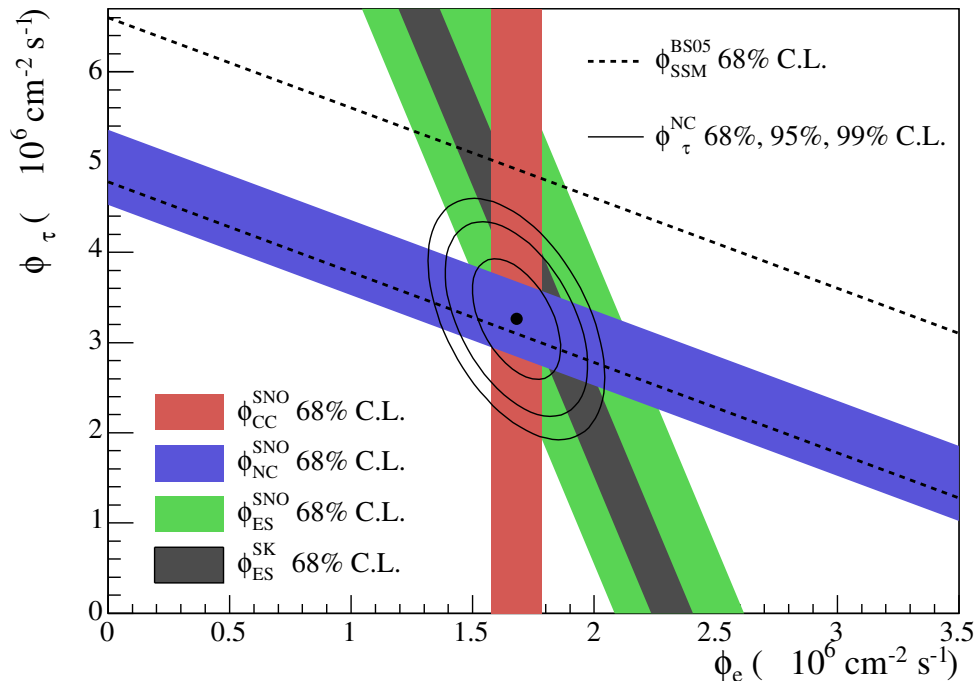
Figure 2.4: $\nu_\mu + \nu_\tau$ versus $\nu_e$ flux determined (1 $\sigma$ allowed region) by SNO through ES, NC and CC interactions. The $^8$B expected flux from the SSM and the SK result are also shown, and they are in agreement with the measured total flux.

allowed to obtain clear evidence of solar neutrino transmutation in terms of $\nu_e \to \nu_{e,\mu,\tau}$, of which $\nu_e$ is only one third of the total. Moreover, the total initial $\nu_e$ flux has been determined independently from theoretical model. Finally, since $\nu_\mu$ or $\nu_\tau$ can not be generated in the SSM, the result of non-zero $\nu_\mu + \nu_\tau$ fluxes is a strong evidence of the neutrino oscillation.

### 2.5.1.2   By Long Baseline Reactor Neutrinos

The Kamioka Liquid Scintillator Antineutrino Detector (KamLAND) experiment also played an important role in the determination of the solar oscillation parameters [16]. The KamLAND experiment, a 1 kton liquid scintillator detector located a the Kamioka mine under 2700 m.w.e (meters water equivalent), detected $\bar{\nu}_e$ emitted by several nuclear power plants in Japan. The neutrino energy is of the order of few MeV and the average distance between detector and reactors is of about 180 km (flux weighted baseline). Given the mass squared difference measured by solar experiments of $\sim 7.5 \times 10^{-5}$ eV$^2$, the oscillation phase, equation 2.15, is of the order of 1, which provides a good condition for a precise measurement of the oscillation parameters. The $\bar{\nu}_e$ detection is performed by the Inverse Beta Decay (IBD) process, described in details in section 3.2, where the neutron is captured by the scintilaltor's Hydrogen nucleus.

Results of the KamLAND experiment show a significant spectral distortion in the final state positron energy spectrum, shown in the left plot of figure 2.5. The spectrum expected in non oscillation scenario is rejected with a significance better than 5 $\sigma$. The ratio of background subtracted $\bar{\nu}_e$ events to the non oscillation expectation is shown in the right plot of figure 2.5. In addition, due to the Great East Japan Earthquake of 2011, all the Japanese nuclear power plants were turned off for inspection, and
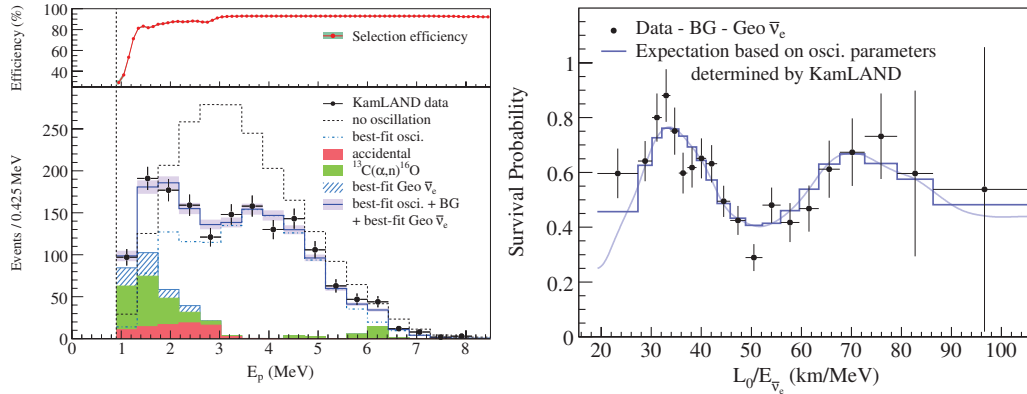
Figure 2.5: Energy spectrum and survival probability of $\bar{\nu}_e$ from the KamLAND experiment [16]. On the left is the prompt event energy spectrum of $\bar{\nu}_e$ candidates corresponding to reactor spectra and expected backgrounds incorporating the energy dependent selection efficiency (top panel). On the right is the ratio of the background subtracted $\bar{\nu}_e$ spectrum to the expectation for non oscillation as a function of $L_0/E$, where $L_0$ is the effective baseline taken as a flux-weighted average ($L_0 \sim 180$ km).

the KamLAND collaboration could improve its result by a longer and more precise background measurement. This lead to a precise determination of the solar oscillation parameters of

$$\Delta m_{21}^2 = 7.54_{-0.18}^{+0.19} \times 10^{-5} \text{ eV}^2 \qquad (2.16)$$

$$\tan^2 \theta_{12} = 0.481_{-0.080}^{+0.092} \qquad (2.17)$$

Results from a global three neutrino flavour oscillation analysis, combining both solar and KamLAND results without any constrain to $\theta_{13}$, are shown in figure 2.6 [17], which gives the following best fit values,

$$\Delta m_{21}^2 = 7.53_{-0.18}^{+0.19} \times 10^{-5} \text{ eV}^2 \text{ and } \tan^2 \theta_{12} = 0.437_{-0.026}^{+0.029}, \qquad (2.18)$$

and also $\sin^2 \theta_{13} = 0.023 \pm 0.015$. This is the solar neutrino oscillation parameters measurement with the best precision so far.

### 2.5.2   Measurement of $\Delta m_{32}^2$ and $\theta_{23}$

The first measurement of $\Delta m_{32}^2$ and $\theta_{23}$ has been performed by SK using atmospheric neutrinos. Further measurements have been performed to confirm SK results by K2K, MINOS and Opera long baseline experiments, using $\nu_\mu$ produced by particle accelerators.

#### 2.5.2.1   By Atmospheric Neutrinos

Atmospheric neutrinos are produced by cosmic rays interacting in the high atmosphere producing mainly pions ($\pi^\pm$) and kaons (**K**). The majority of charged pions decay through the weak charged current $\pi^\pm \rightarrow \mu^\pm \nu_\mu(\bar{\nu}_\mu)$. The muons subsequently decay as $\mu^\pm \rightarrow e^\pm \nu_e(\bar{\nu}_e) + \bar{\nu}_\mu(\nu_\mu)$ giving, as a first approximation, two muon neutrinos for each electron neutrino. Their energy spans from a few MeV up to several GeV.

Atmospheric neutrinos observed at different zenith angles have various flight path lengths which vary from 10 to 30 km, for downward neutrinos, or up to $10^4$ km, for upward neutrinos, running through the Earth. Since neutrinos can be generated at any

Figure 2.6: Allowed region for neutrino oscillation parameters from KamLAND and solar neutrino experiments. The side panels show the $\chi^2$ distribution for KamLAND (dashed light blue line) and solar experiments (dotted black line), as well as the combination of both (solid red line).

point of the atmosphere, neutrinos of the same energy can travel very different distances before reaching the detector, giving different oscillation probabilities. Thus a detector able to distinguish muon neutrinos from electron neutrinos and also able to recognise their incoming direction is necessary, and thus being sensitive for a wide range of $\Delta m^2$.

SK is a large water Čerenkov detector located in the Japanese Kamioka mine, under 2700 m.w.e. depth to shield the detector from cosmic rays. It contains about 50 ktons of water and it is surrounded by about 13000 PMTs. Neutrinos undergo charged current interaction producing charged leptons. The lepton is generally produced with relativistic energy and it is detected through the cone of Čerenkov light produced as it travels through the detector. The flavour of the lepton is identified by the sharpness of the Čerenkov ring. The position of the ring allows to determine the lepton directions, which is correlated to the neutrino direction for energies larger than $\sim 1$ GeV. The lepton energy could also be obtained from the amount of light collected by the PMTs if the lepton stops into the detector. Even if the lepton energy is not strongly correlated to the neutrino energy it allows to handle the energy dependence of the oscillation probability. SK provided in 1998 the first firm evidence of neutrino flavour transition comparing the expected number of events with the observed ones, as a function of the zenith angle. SK observed that there are twice as many downward going $\nu_\mu$ than upward going $\nu_\mu$, as shown in the left plot of figure 2.7 [18]. The right plot shows the ratio between data and
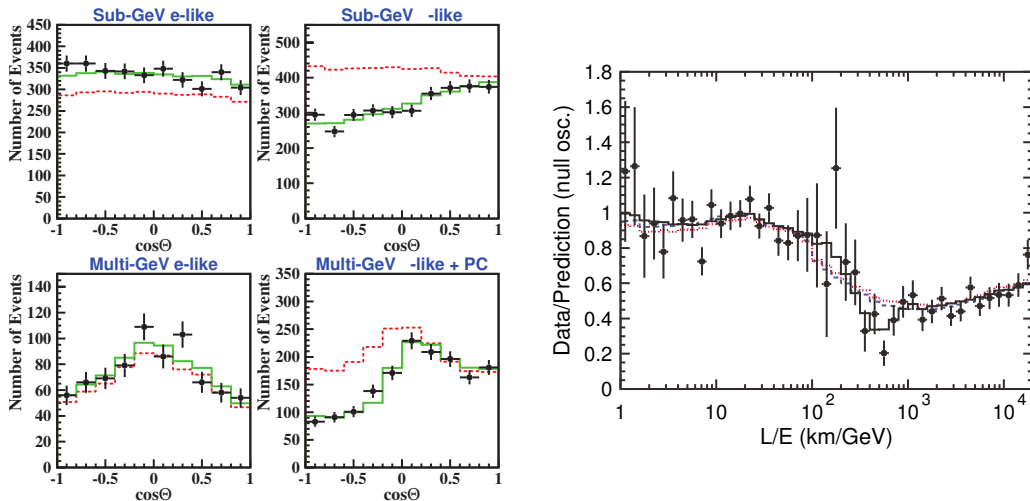


Figure 2.7: Results from SK phase I atmospheric neutrino data [19]. The left plot shows the zenith angle distributions for fully contained 1-ring $e$-like and $\mu$-like events for sub-GeV and multi-GeV energies. Non oscillated MC events are represented by the doted lines and the solid lines represent the best fit expectation for $\nu_\mu \to \nu_\tau$ oscillations. The right plot shows the ratio between data and MC prediction without oscillation, as a function of the reconstructed $L/E$. The solid line represents the best fit in the two flavour oscillation scheme.

prediction at large $L/E$. The hypothesis that $\nu_\mu$ have interacted crossing the earth is not reliable because the earth is nearly transparent for neutrinos with energy of about few GeV and a similar behaviour should have also been found for $\nu_e$. Moreover, since no excess of the electron neutrino flux has been found, the observed oscillation is attributed to the transition $\nu_\mu \to \nu_\tau$. As a result from the oscillation fit [9], a 90% confidence level region allows the following oscillation parameters

$$(1.9 < \Delta m^2_{32} < 3.0) \times 10^{-3} \text{ eV}^2 \text{ and } \sin^2 2\theta_{23} > 0.90. \tag{2.19}$$

### 2.5.2.2 By Accelerator Neutrinos

Long Baseline Neutrino Experiments use a muon neutrino beam from accelerators at energies of a few hundred MeV to a few GeV, produced by pion decay, where the pions are generated from protons hitting on targets. These experiments have been performed to be an independent measurement of neutrino oscillation seen in atmospheric neutrino experiments. The oscillation parameters are measured through $\nu_\mu$ disappearance, $P(\nu_\mu \to \nu_\mu) = 1 - P(\nu_\mu \to \nu_x)$, in a detector hundreds of km far from the neutrino source.

The KEK to Kamioka (K2K) experiment in Japan used $\nu_\mu$ produced from a pulsed beam at The High Energy Accelerator Research Organization (KEK) and the 250 km far away SK detector. The average neutrino energy is slightly above 1 GeV. Given the mass squared difference of about $2.5 \times 10^{-3} \text{eV}^2$ measured with atmospheric neutrino by SK, the oscillation phase is of the order of 1, which represent the best condition to measure oscillation. K2K compared the $\nu_\mu$ flux observed at SK with the non-oscillated flux measured by a 1 kton water Čerenkov detector placed at about 300 m from the neutrino source. K2K excluded the non oscillation with a confidence of 4.3 $\sigma$ and, in a two flavour oscillation scenario, the allowed $\Delta m^2$ region at $\sin^2 2\theta = 1$, with 90% C.L., is

$$(1.9 < \Delta m_{32}^2 < 3.5) \times 10^{-3} \text{ eV}^2, \qquad (2.20)$$

where the best fit value is $\Delta m_{32}^2 = 2.8 \times 10^{-3} \text{ eV}^2$ [20]

Another important experiment is the Main Injector Neutrino Oscillation Search (MINOS), placed in the Sudan mine, 735 km far from a neutrino pulsed beam produced at Fermilab. The neutrino energy, 1 to 5 GeV, is higher than K2K to obtain an oscillation phase of the order of 1. Like K2K, the initial flux is measured by a near detector, $L \sim 1$ km, and compared with the flux at the far detector to observe $\nu_\mu$ disappearance. Both detectors are based on magnetised steel and plastic scintillator (alternating planes) tracking calorimeters, of 1 kton targe mass (27 ton fiducial) for the near detector and 5.4 kton (4.0 kton fiducial) for the far detector. The beam capability to switch between $\nu_\mu$ to $\bar\nu_\mu$ allows to measure oscillation parameters in case of $\bar\nu_\mu$ disappearance [21], and MINOS can also detect $\nu_e$ interaction through compact electromagnetic showers and attempts measurement of $\nu_\mu \to \nu_e$ oscillation, thus $\theta_{13}$ [22]. With an exposure of $7.25 \times 10^{20}$ protons on target, the ratio between the observed energy spectrum with the prediction without oscillation is shown in the bottom left plot of figure 2.8, where a clear sharp dip in the oscillation probability around 1 GeV, as expected by the SK results, is present. A fit to the data results in

$$|\Delta m_{32}^2| = 2.32^{+0.12}_{-0.08} \times 10^{-3} \text{ eV}^2 \text{ and } \sin^2 2\theta_{23} > 0.90 \text{ at } 90\% \text{ C.L.} \qquad (2.21)$$

From the result in equation 2.18 together with the $\Delta m_{32}^2$ value of equation 2.21, it is noticed that $\Delta m_{21}^2$ is significantly smaller than $\Delta m_{32}^2$ and it is possible to make the approximation $\Delta m_{32}^2 \approx \Delta m_{31}^2$, since there is the relation of equation 2.11.

Another attempt to explore neutrino oscillation using particle accelerators is the Oscillation Project with Emulsion-tRacking Apparatus (OPERA), installed at Italy's Laboratori Nazionali del Gran Sasso (LNGS). Instead of measuring oscillation parameters via $\nu_\mu$ disappearance, OPERA is designed to explicit detect $\nu_\tau$ appearance. Direct observation of $\nu_\tau$ would confirm the interpretation of SK results in terms of $\nu_\mu \to \nu_\tau$ oscillation. The $\nu_\mu$ beam, with a mean energy of about 17 GeV, is produced from a pulsed proton beam at CERN's Super Proton Synchrotron (SPS), about 730 km from Gran Sasso. The $\tau$ lepton produced by $\nu_\tau$ charged current interaction is detected through the topology of its decay in nuclear emulsion films. The expected signal statistics is not very high, and only two $\nu_\tau$ have been observed (2.1 events expected and 0.2 expected background) since data taking started in 2008 [24].
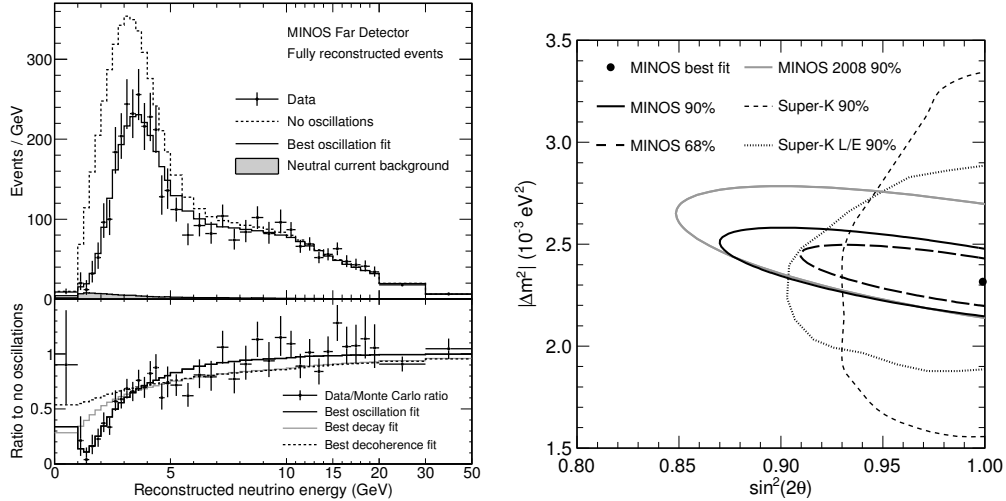
Figure 2.8: Results of $\nu_\mu$ disappearance in the MINOS experiment [23]. The left plot shows the energy spectrum of fully reconstructed events in the far detector classified as CC interactions. The dashed line represents the spectrum predicted from the near detector assuming no socillations, while the solid histogram reflects the best fit of the oscillation. The right plot shows the confidence level contours of 1 $\sigma$ and 90%, around the oscillation parameters best fit values.

### 2.5.3    Measurement of $\theta_{13}$

The mixing angle $\theta_{13}$ is the smallest angle of the PMNS matrix. For this reason the related oscillations have been the most difficult to observe. While several experiments precisely measured the other two mixing angle, $\theta_{12}$ and $\theta_{23}$, only an upper limit of $\theta_{13}$ was given by the Chooz experiment [25], as $\sin^2 2\theta_{13} < 0.15$, not excluding a non oscillation scenario. The value of $\theta_{13}$ become accessible just recently, in mid-2011, thanks to the new generation of reactor and accelerator experiments, which provide sensitivities to small mixing angle of about one order of magnitude better than previous limits. Moreover reactor $\bar{\nu}_e$ experiments are complementary to long baseline accelerator experiments in determining $\theta_{13}$, since they are insensitive to the violation phase $\delta_{\mathrm{CP}}$, and the dependence from the solar mass split is weak. Furthermore, over short baselines of about 1 km the reactor $\bar{\nu}_e$ does not suffer from matter effects.

#### 2.5.3.1    By Accelerator Neutrinos

Long baseline accelerator experiments are designed to detect the appearance of $\nu_e$ from a $\nu_\mu$ beam with energy from few hundred MeV to few GeV, using far detectors at a few hundred km far from the neutrino source. This type of experiment has also sensitivity to the CP violation phase and the neutrino mass hierarchy. However, there are potentially parameter degeneracies leading to the following ambiguities:

- $\delta_{\mathrm{CP}} - \theta_{13}$ ambiguity;

- sign of $\Delta m^2_{32}$ ambiguity;

- $\theta_{23}$ ambiguity.

In addition, accelerator experiments have to take into account matter effects on the neutrino oscillation, shortly described in section 2.3, to determine the $\theta_{13}$ value.

As said in section 2.5.2.2, the MINOS experiments can also perform a $\nu_e$ appearance measurement. With an exposure of $8.2 \times 10^{20}$ protons on target, the expected number of $\nu_e$ CC interactions on the far detector, based on the near detector data, was calculated to be $49.6 \pm 7.0(\text{stat.}) \pm (\text{sys.})$, assuming no oscillation, while 62 events were observed. Assuming $\delta_{CP} = 0$, $\Delta m_{32}^2 = 2.32 \times 10^{-3}$ eV$^2$ and normal (inverted) hierarchy, the upper limit of $\theta_{13}$, at a 90% C.L., was set as $2 \sin^2 \theta_{23} \sin^2 2\theta_{13} < 0.12(0.20)$, while the $\theta_{13} = 0$ hypothesis is disfavoured by the data at the 89% C.L.

The Tokai to Kamioka experiment (T2K) uses a muon neutrino beam produced at the Japan Proton Accelerator Research Complex (J-PARC), a segmented near detector ($L = 280$ m) with a tracking system to precisely measure the non-oscillated flux and the well known SK detector in order to directly measure the appearance of $\nu_e$. The $\nu_\mu$ beam is directed 2.5 degree away from the SK baseline of about 295 km. This off-axis configuration lower the neutrino flux but provide a narrow energy spectrum peaked at about 600 MeV. In summer 2011 T2K reported the observation of six $\nu_e$ in the SK detector, with an expected background level of $1.5 \pm 0.5$ events, providing a signal significance of about 2.5 $\sigma$ [26]. The T2K results have been updated in the beginning of 2013 with about more statistics and improved systematics uncertainty. A total of 11 $\nu_e$ events have been observed in the SK detector, with $3.3 \pm 0.4$ expected background events, as shown in figure 2.9 [27]. The background only hypothesis is rejected with a
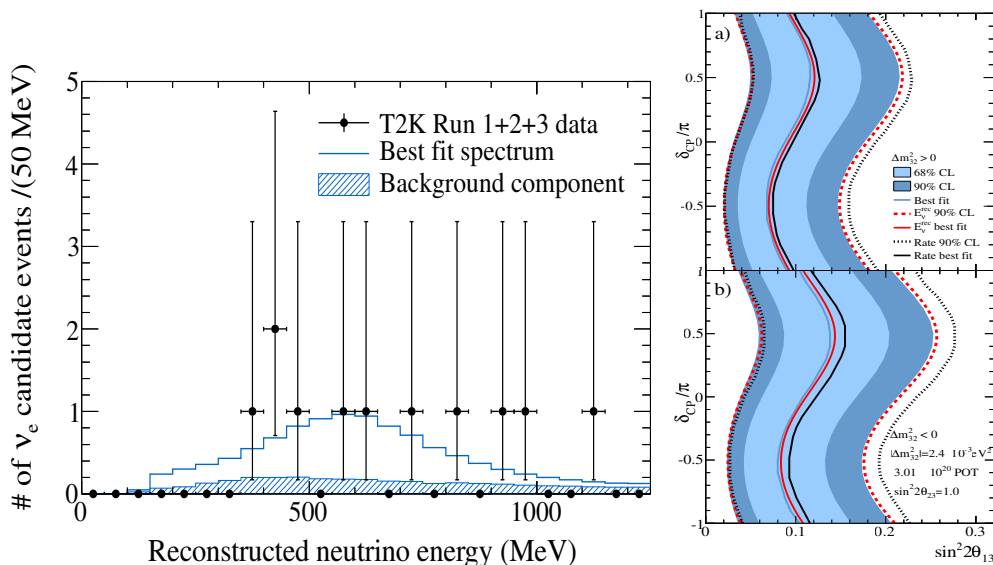


Figure 2.9: Results of the T2K experiment searching for $\nu_\mu \rightarrow \nu_e$ appearance. The left plot shows the data and prediction reconstructed energy distribution, and the background expectation. The solid line represent the best fit spectrum assuming $\delta_{CP} = 0$ and normal hierarchy. The right plot shows the 68% and 90% C.L. regions for $\sin^2 2\theta_{13}$ scanned over values of $\delta_{CP}$ assuming normal (a) or inverted (b) hierarchy. The best values of $\sin^2 2\theta_{13}$ for the energy spectrum and the rate analysis are also shown.

significance of 3.1 $\sigma$, and a fit, assuming $|\Delta m_{32}^2| = 2.4 \times 10^{-3}$eV$^2$, $\delta_{CP} = 0$, $\sin^2 2\theta_{23}$, and normal hierarchy, yields $\sin^2 2\theta_{13} = 0.088^{+0.049}_{-0.039}$.

### 2.5.3.2 By Short Baseline Reactor Neutrinos

The new generation reactor experiments, Double Chooz, Daya Bay and RENO aim to measure $\theta_{13}$ by looking for distortion in the measured energy spectrum due to $\bar{\nu}_e$

disappearance, in a similar way KamLAND did for solar oscillation. Since the phase for $\theta_{13}$ oscillation is proportional to $\Delta m_{31}^2 \simeq \Delta m_{32}^2$, about two order of magnitude bigger than the solar mass split, the baseline for $\theta_{13}$ measurements has to be of the order of 1 km, two order of magnitude smaller than KamLAND. The three reactor experiments are similar in concept and design, while differ mainly in the number of detectors and reactors and their relative positions. A near detector is used to compare its data with the far detector. In this way, the uncertainties related to the $\bar{\nu}_e$ flux and detection efficiencies can be largely suppressed. Details on the detector technology and $\bar{\nu}_e$ are exemplified in the next chapters, where the Double Chooz experiment is described in depth.

Daya Bay uses 6 detectors placed at different distances from 6 reactors, as shown in figure 2.10, and started the data taking in September of 2011. Each of its detectors
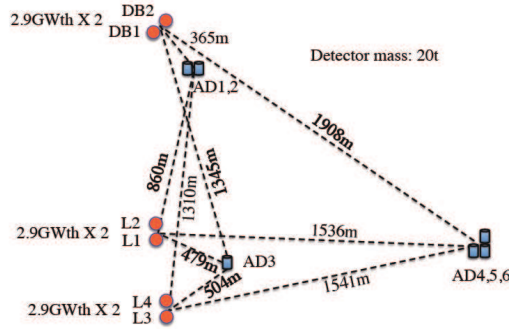


Figure 2.10: Relative locations of detectors and reactors of Daya Bay Experiment. Scale is approximate.

has 20 tons of Gd loaded liquid scintillator and the reactors generates 2.9 $W_{th}$ each. They released their first result in early 2012 [28] using 55 days of data. This result was updated later using 139 days of data, giving a measurement of $\theta_{13}$ as follows

$$\sin^2 2\theta_{13} = 0.089 \pm 0.010(\text{stat.}) \pm 0.005(\text{syst.}), \tag{2.22}$$

assuming a three neutrino framework and rejecting $\theta_{13} = 0$ with a significance of 5.2 $\sigma$. More two detectors are being installed in this year of 2013. Details of the Daya Bay analysis, which is based on the detectors' interaction rate, are given in section 5.2.2.1.

RENO experiment uses two detectors, one near and one far from an array of 6 reactors, as shown in figure 2.11, and started the data taking in August of 2011. The
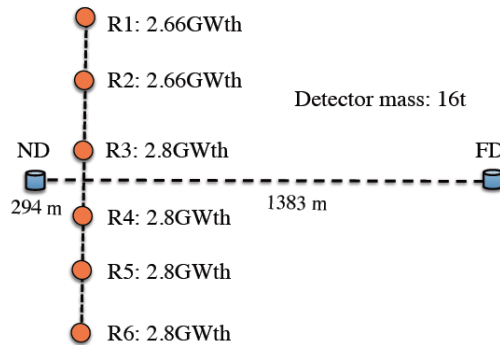


Figure 2.11: Relative locations of detectors and reactors of RENO. Scale is approximate.

detectors contains 16 ton of Gd loaded liquid scintillator, and with 229 days of data

taking the collaboration also released their result on $\theta_{13}$ in early 2012. Based on the observed rate on their two detectors, a fit to the data yields

$$\sin^2 2\theta_{13} = 0.113 \pm 0.013 (\text{stat.}) \pm 0.019 (\text{syst.}), \qquad (2.23)$$

assuming a three neutrino framework and rejecting $\theta_{13} = 0$ with a significance of 4.9 $\sigma$. An updated result with more statistics and improved analysis will be released by the RENO collaboration soon.

The Double Chooz experiment, has its detector concept and design described in full detail in chapter 3. The first result from reactor experiment was released by Double Chooz in November 2011 [29] and an updated analysis with major improvements with twice the statistics was released in July 2012 [30]. One objective of this dissertation is to use the Double Chooz data in order to improve the $\theta_{13}$ measurement of

$$\sin^2 2\theta_{13} = 0.109 \pm 0.030 (\text{stat.}) \pm 0.025 (\text{sys.}), \qquad (2.24)$$

using only a far detector, performing a new style spectrum distortion analysis.

Finally, these new measurements of $\theta_{13}$ could provide further constrains on the measurements of $\Delta m_{21}^2$ and $\tan^2 \theta_{12}$, by a three flavour oscillation analysis [17]. Although it does not change the central value and 1 $\sigma$ uncertainty of these parameters (equation 2.18), this constrain improves the significance of the result, making a narrower C.L. region, as it is possible to see in figure 2.12 when compared with figure 2.6.
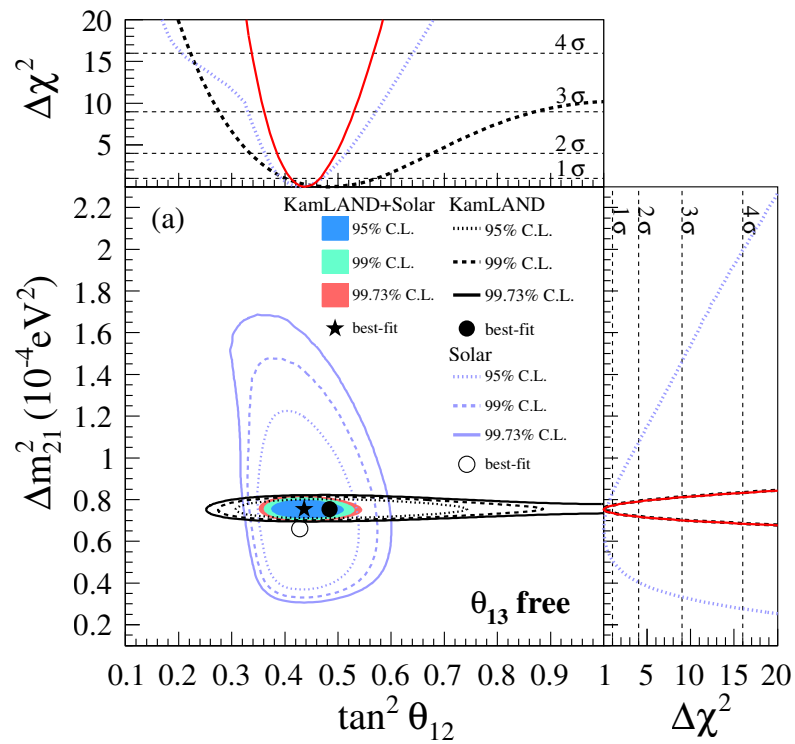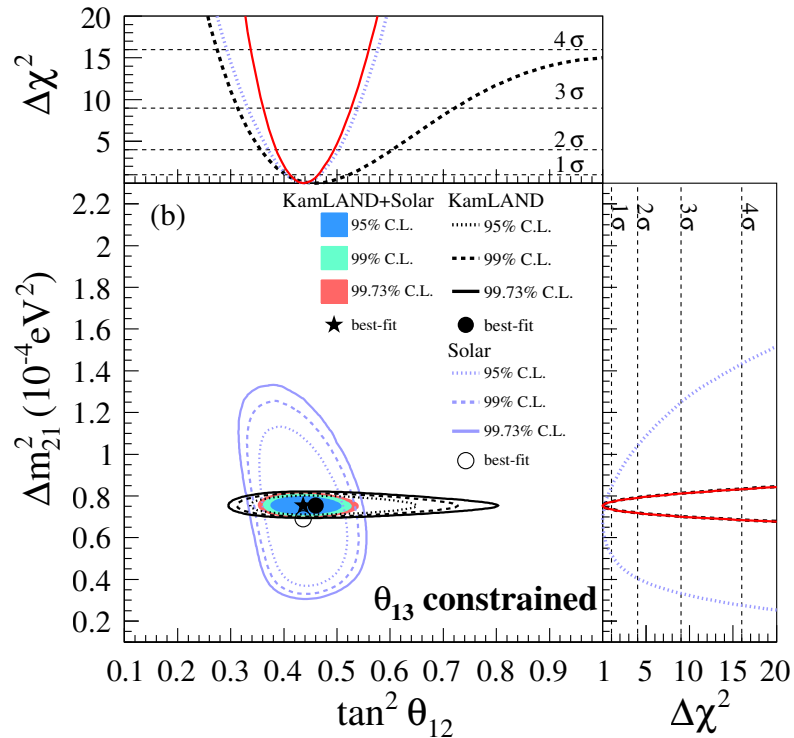


Figure 2.12: Allowed region for neutrino oscillation parameters from KamLAND and solar neutrino experiments when $\theta_{13}$ is constrained by reactor and accelerator experiments. Plot structure is the same as in figure 2.6.

The small, but non-zero, value of $\theta_{13}$ is a very good news for future neutrino programs for $\delta_{CP}$ measurement.

### 2.5.4   Measurement of $\Delta m_{31}^2$

The mass squared difference $\Delta m_{31}^2$ can be measured by energy spectrum distortion and baseline dependence of the reactor-$\theta_{13}$ experiments. The neutrino oscillation probability going to the same flavour, expressed by equation 2.9, can be re-written in terms of the oscillation angles and squared mass difference, for $\bar{\nu}_e$, as follows

$$P(\bar{\nu}_e \to \bar{\nu}_e) = 1 - \sin^2 2\theta_{13} \left( c_{12}^2 \sin^2 \frac{\Delta m_{31}^2 L}{4E} + s_{12}^2 \sin^2 \frac{\Delta m_{32}^2 L}{4E} \right) + O(10^{-3}). \quad (2.25)$$

On the other hand, the survival probability of high energy $\nu_\mu$ which is produced by accelerator is,

$$P(\nu_\mu \to \nu_\mu) = 1 - \sin^2 2\theta_{23} \times \left( \begin{array}{c} (s_{12}^2 + s_{13}t_{23}\sin 2\theta_{12}\cos\delta)\sin^2 \frac{\Delta m_{31}^2 L}{4E} \\ +(c_{12}^2 - s_{13}t_{23}\sin 2\theta_{12}\cos\delta)\sin^2 \frac{\Delta m_{32}^2 L}{4E} \end{array} \right) + O(10^{-2}).$$
$$(2.26)$$

Usually oscillation data are analysed by assuming two flavour oscillation formula,

$$P(\nu_\alpha \to \nu_\alpha) = 1 - \sin^2 2\theta \sin^2 \frac{\Delta \tilde{m}^2 L}{4E}, \quad (2.27)$$

and the measured mass square difference corresponds to a weighted mean of $\left| \Delta m_{32}^2 \right|$ and $\left| \Delta m_{31}^2 \right|$ [31],

$$\Delta \tilde{m}_{31}^2 = c_{12}^2 \left| \Delta m_{31}^2 \right| + s_{12}^2 \left| \Delta m_{32}^2 \right| \text{ and}$$
$$\Delta \tilde{m}_{32}^2 = (s_{12}^2 + s_{13}t_{23}\sin 2\theta_{12}\cos\delta) \left| \Delta m_{31}^2 \right| + (c_{12}^2 - s_{13}t_{23}\sin 2\theta_{12}\cos\delta) \left| \Delta m_{32}^2 \right|,$$
$$(2.28)$$

where $t_{ij} = \tan\theta_{ij}$. They are called effective $\Delta m^2$. Note that $\Delta \tilde{m}^2$ is not a difference of the mass square and is positive definite. Since there is a relation

$$\Delta m_{31}^2 = \Delta m_{32}^2 + \Delta m_{21}^2, \quad (2.29)$$

in the standard three-flavor scheme, the difference between $\Delta \tilde{m}_{31}^2$ and $\Delta \tilde{m}_{32}^2$ is expressed as follows

$$\frac{2(\Delta \tilde{m}_{31}^2 - \Delta \tilde{m}_{32}^2)}{\Delta \tilde{m}_{31}^2 + \Delta \tilde{m}_{32}^2} \sim \pm(1 - s_{13}t_{23}\tan 2\theta_{12}\cos\delta) \times \frac{2\cos 2\theta_{12}|\Delta m_{21}^2|}{|\Delta m_{31}^2| + |\Delta m_{32}^2|} \sim \pm 0.012 \times (1 \pm 0.3),$$
$$(2.30)$$

where the overall sign depends on mass hierarchy, and the $\pm 0.3$ term comes from the ambiguity of $\cos\delta$. If $\Delta \tilde{m}_{31}^2 > \Delta \tilde{m}_{32}^2$, it is normal hierarchy, and vise versa.

In order to distinguish the mass hierarchy cases, it is necessary to distinguish the separation of 1.7~3.1% depending on $\delta$. $\Delta \tilde{m}_{32}^2$ has been measured with precision of $\sim 3.5\%$ [32]. So far there has been no reported measurement of $\Delta \tilde{m}_{31}^2$ and this thesis proposes to measure it for the first time. If the difference between $\Delta \tilde{m}_{31}^2$ and $\Delta \tilde{m}_{32}^2$ is larger than 1.6%, it can not be explained by the standard three flavour oscillation scheme. If both $\Delta \tilde{m}_{31}^2$ and $\Delta \tilde{m}_{32}^2$ are measured with a 1% accuracy or better in the future, the mass hierarchy and $\cos\delta$ can be measured.

## 2.6   Neutrino Mass

As highlighted in section 2.1, $\mathcal{SM}$ neutrinos are not allowed to acquire masses through the Higgs mechanism because they exist only in the left-handed chiral state (right-handed for anti-neutrinos). However, experimental evidences of neutrino oscillations

imply the neutrino must be a massive particles. Further hints of a non-null neutrino mass can be investigated independently from neutrino oscillation. In particular, experiments looking for distortion induced by massive neutrinos on the beta decay end point of tritium, $^3\text{H} \rightarrow\, ^3\text{He}+e^-+\bar{\nu}_e$, set a limit $\bar{\nu}_e$ mass below 2 eV [18]. Similarly, the observation of the cosmic microwave background and the density fluctuations, and other cosmological measurements, put a combined upper limit on neutrino mass around 0.5 eV [33], which is six orders of magnitude smaller than the electron mass.

Given the evidences of neutrinos being massive particles, it is necessary to extend the $\mathcal{SM}$ to include neutrino masses. The most simple extension of the $\mathcal{SM}$ is to add a right-handed neutrino singlet. In this case, neutrino masses are acquired through the Higgs mechanism, like all other fermions:

$$\mathcal{L}_D \simeq -m_D\bar{\nu}_L\nu_R + h.c. \tag{2.31}$$

$m_D$ is the so called Dirac mass term and has the same form of the fermion masses in equation 2.3:

$$m_\nu = \frac{v}{\sqrt{2}}\Gamma_\nu. \tag{2.32}$$

With this model the Yukawa coupling constant $\Gamma_\nu \simeq m_\nu/v$ needs to be of the order of $10^{-12}$, which is far too small compared to the other fermions ($\Gamma_e \simeq 0.3 \times 10^{-5}$) and it is commonly considered as unnatural.

Since neutrinos do not have electromagnetic charge, they could be described in term of a Majorana particles:

$$\nu^c = C\bar{\nu}^T \equiv \nu, \tag{2.33}$$

where $\nu^c = C\bar{\nu}^T$ is the charge conjugate of the field $\nu^c$, and $C$ is the charge conjugation. Considering a left-handed Majorana particle, $\nu = \nu_L + \nu_L^c$, a Majorana mass term of the form:

$$\mathcal{L}_D \simeq -m_M\bar{\nu^c}_L\nu_L + h.c. \tag{2.34}$$

could be considered. It should be noted that the Majorana mass term involves left-handed neutrino only and is not gauge invariant, $m\bar{\nu^c}\nu \rightarrow m\bar{\nu^c}e^{i2\alpha}\nu$, violating lepton flavour number by two units.

The smallness of the neutrino mass term is no longer dependent on the unnatural Yukawa coupling constant, but nonetheless a mass term for a left-handed neutrino is not allowed by the $\mathcal{SM}$ because it implies an Higgs triplet with isospin one.

Once a right-handed neutrino is introduced to obtain a Dirac mass term, a Majorana mass term could also be obtained in case the right-handed neutrino is Majorana particle. The most general mass term can thus be written as mix of Dirac and Majorana term:

$$\begin{aligned}\mathcal{L}_{D+M} &= \mathcal{L}_D + \mathcal{L}_{M_R} + \mathcal{L}_{M_L} \\ &= -m_D\bar{\nu}_L\nu_R - m_{M_R}\bar{\nu^c}_R\nu_R - m_{M_L}\bar{\nu^c}_L\nu_L + h.c.\end{aligned} \tag{2.35}$$

which can be written as

$$\mathcal{L}_{D+M} = -\frac{1}{2}\begin{pmatrix} \bar{\nu^c}_L & \bar{\nu}_R \end{pmatrix}\begin{pmatrix} m_L & m_D \\ -m_D & m_R \end{pmatrix}\begin{pmatrix} \nu_L \\ \bar{\nu}_R \end{pmatrix} + h.c. \tag{2.36}$$

The term $m_L$ is the left-handed neutrino Majorana mass, $m_R$ is the right-handed neutrino Majorana mass and $m_D$ is the Dirac mass. The mass matrix can be diagonalised in term of the mass eigenstate:

$$\begin{aligned}\nu_L &= \cos\theta\nu_1 + \sin\theta\nu_2 \tag{2.37} \\ \nu_R^c &= -\sin\theta\nu_1 + \cos\theta\nu_2 \tag{2.38}\end{aligned}$$

with eigenstate $m_{1,2}$

$$m_{1,2} = \frac{1}{2}\left(m_L + m_R \pm \sqrt{(m_L - m_R)^2 + m_D^2}\right) \tag{2.39}$$

and

$$\tan 2\theta = \frac{2m_D}{m_R - m_L}. \tag{2.40}$$

Since the left handed Majorana mass term requires an Higgs triplet, in the minimal $\mathcal{SM}$ extension, $m_L$ is usually set to zero. The right-handed Majorana neutrino is an electroweak singlet acquiring a mass independently from the Yukawa coupling. In the limit where $m_L = 0$ and $m_R \gg m_D$:

$$\tan 2\theta \simeq \frac{2m_D}{m_R} \simeq 0,\ m_1 \simeq \frac{m_D^2}{m_R}\ \text{and}\ m_2 \simeq m_R, \tag{2.41}$$

with one light left-handed neutrino and one heavy right-handed neutrino:

$$\nu_1 \simeq (\nu_L - \nu_L^c), \tag{2.42}$$
$$\nu_2 \simeq (\nu_R + \nu_R^c). \tag{2.43}$$

This is the so called see-saw mechanism, which involves two Majorana particles: a very heavy right-handed neutrino and the observed light left-handed neutrino. The smallness of the observed neutrino mass could then be explained in terms of a Dirac mass of the order of the electroweak energy scale, without the unnatural Yukawa coupling constant, and a much bigger Majorana mass term. The term $m_R$ is generally related to the grand unification scale around the Planck scale at $10^{16}$ eV.

The Dirac or Majorana nature of the neutrino is not yet known. Experimentally it is possible to investigate this question through processes violating the lepton number like the neutrino-less double beta decay, which violated the lepton quantum number by two units. Many experiment are currently, or will soon, searching the neutrino-less double beta decay, CUORE [34], GERDA [35], EXO [36] and SUPER-NEMO [37], but not signal has been observed up to now.

## 2.7 Neutrino Anomalies

So far neutrino oscillation is well established in terms of a three flavour framework. However, there are some experiments whose results are not explained by this framework and might require the introduction of an extra sterile neutrino, i.e. a neutrino not participating in the $\mathcal{SM}$ interactions.

The first evidence of more than three neutrino flavours came from the Liquid Scintillator Neutrino Detector (LSND) experiment [38]. Using a $\bar{\nu}_\mu$ from pion decay detected in a liquid scintillator, LSND found $> 3\ \sigma$ evidence of $\bar{\nu}_\mu \rightarrow \bar{\nu}_e$ transition which would require a mass splitting of about 0.2 eV$^2$, larger than the atmospheric one. The LSND anomaly has been tested by the Fermilab's MiniBooNE (Mini Booster Neutrino Experiment) in both neutrino and antineutrino mode. The results obtained in the neutrino mode disfavour most of the parameter space defined by LSND but were not conclusive [39]. The results obtained in the antineutrino mode instead were consistent with LSND signal and consistent with a mass split of between 0.1 eV$^2$ and 1 eV$^2$ [40]. Further hints of the existence of sterile neutrinos came from measurements of neutrino fluxes from intense radioactive sources in the GALLEX [41] and SAGE [42] detectors. An unexpected reduction of the $\nu_e$ flux consistent with $\nu_e$ disappearance has been found

at 2.7 $\sigma$. The interpretation in terms of sterile neutrino oscillation indicates a value for the squared mass difference of about 0.35 eV$^2$.

Recent re-evaluation of the expected antineutrino flux from nuclear reactor indicate that the measured flux is about 6% below the prediction with 3 $\sigma$ significance, as shown in figure 2.13. Even if such a deficit could still be due to some unknown effects in
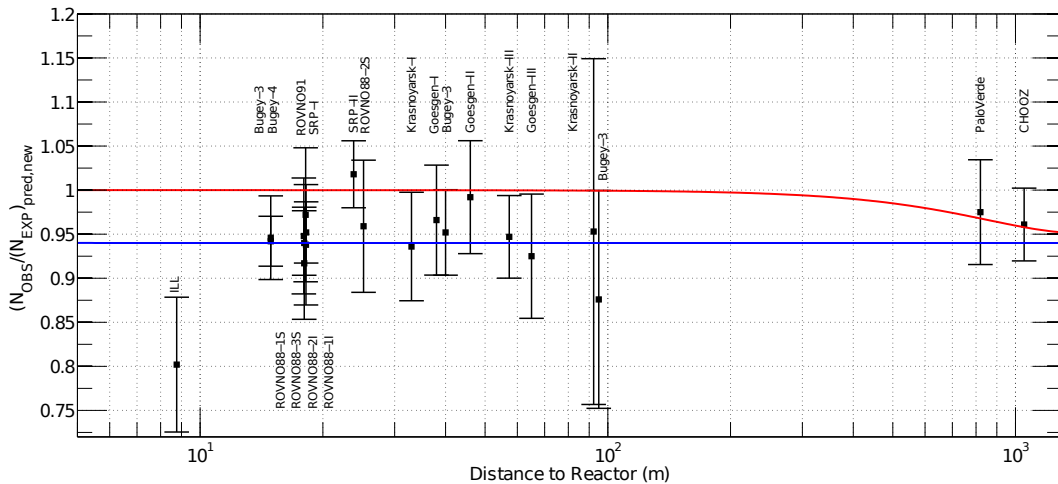


Figure 2.13: Illustration of the short baseline reactor antineutrino anomaly. The experimental results are compared to the prediction without oscillation, taking into account the new antineutrino spectra, the corrections of the neutron mean lifetime, and the off-equilibrium effects. The red line shows a possible 3 active neutrino mixing solution, with $\sin^2 2\theta_{13} = 0.06$. The blue line displays a solution including a new neutrino mass state, such as $|\Delta m^2_{\mathrm{new}}| \gg 1$ eV$^2$ and $\sin^2 2\theta_{\mathrm{new}} = 0.12$, for illustration purpose [43].

the reactor neutrino production or a non accurate knowledge of the fission product contribution to the antineutrino spectrum, it is consistent with $\bar{\nu}_e$ flux suppression due to sterile neutrino oscillation with mass split of about 2.4 eV$^2$.

In summary, there are hints compatible with the existence of sterile neutrinos from several experiments, using different sources and detection technique, but none of them could claim a discovery. Many experiments have been proposed for for sterile neutrino search and an exhaustive list can be found in [44].

## 2.8  Summary and Open Questions

Over the last twenty years many experimental efforts have provided clear confirmation that neutrinos are massive particle and that there is mixing between flavour and mass eigenstates. The solar neutrino anomaly has been solved by SNO and KamLAND experiments, and the missing solar neutrino flux is interpreted within the neutrino oscillation scenario, of three neutrino flavours. Atmospheric neutrino oscillations has been characterised by SK and K2K and MINOS long baseline accelerator experiments. The observed disappearance of atmospheric neutrinos also has been interpreted in terms of oscillations. The latest mixing angle, $\theta_{13}$ was finally measured by reactor and accelerator experiments, and it is currently under precision determination era.

With the current characterisation of the PMNS matrix, new measurements will be possible in order to improve the current knowledge and to complete neutrino oscillation picture concerning the still open questions:

- Which is the value of the CP-violating phase, $\delta_{CP}$? It can be measured in long

baseline experiments, studying the oscillation probability asymmetries between neutrino and antineutrinos.

- What is the neutrino mass hierarchy? The matter effect could be used in long baseline experiments to measure the sign of $\Delta m_{32}^2$ and establish the neutrino mass hierarchy. This also can be done by reactor experiments with a baseline of $\sim 50$ km.

- What is the sign of $\cos 2\theta_{23}$? By the combination of reactor $\bar{\nu}_e$ and both accelerator $\nu_\mu$ disappearance and $\nu_e$ appearance. The degeneracy on the measurement of $\theta_{23}$ at accelerator experiment will be broken by the reactor $\theta_{13}$ measurement which does not depend on the first. Therefore, a discrimination of the fraction of $\nu_\mu$ and $\nu_\tau$ contained by the mass state $\nu_3$ will be possible to be performed.

Beyond neutrino oscillations, neutrinos absolute mass scale determination, their Dirac or Majorana nature understanding, and the confirmation or not of the existence of a fourth sterile neutrino, are also current challenges for the neutrino physics community.

# Chapter 3

# The Double Chooz Experiment

"Pure logical thinking cannot yield us any knowledge of the empirical world; all knowledge of reality starts from experience and ends in it."

*Albert Einstein*

The Chooz experiment had taken data between April 1997 and July 1998 and became famous for measuring the so far best upper limit on $\sin^2 2\theta_{13}$. However, the sensitivity of Chooz was limited by various factors. The uncertainty of the reactor flux (2%) was the main limitation on the systematic side resulting in an overall systematic uncertainty of 2.7%. Moreover, it was limited by statistics as the optical properties of the scintillator absorption length continuously degraded. Since it also could not exclude a scenario without oscillation, some different approaches were proposed to measure this mixing angle.

The Double Chooz experiment was proposed to be an improvement of the Chooz experiment and give a better constrain on $\sin^2 2\theta_{13}$, or measure it if it is different from zero. The main improvements, as will be explained in details through this chapter, are: the use of two identical near and far detectors from the neutrino source; low radioactivity emitting materials; improved monitoring and shielding of the background events; a new detector design; an enlarged target volume that increases the event rate by a factor two; and an improved scintillator composition, that result in a stability of several years.

The experiment is an international-wise collaboration effort and it is located at the vicinity of the two Chooz B, N4 design, commercial nuclear reactors that lies in the French municipality of Chooz in the Ardennes department. These reactors have a nominal thermal power of 4.25 GW$_{\text{th}}$ each, that is converted to 1.49 GW of electrical power. Figure 3.1 shows a plane view of the Chooz nuclear complex and the inset shows the location in the map of France. Table 3.1 shows the distances between the detectors and reactors, and figure 3.2 displays the positions the detectors on the reactors surrounding. While the far detector is located at the same experimental hall previously

Table 3.1: Distances of each Double Chooz detector to each Chooz B reactor, and the overburden.

| Detector | Chooz B1 | Chooz B2 | Overburden [m.w.e.] |
|----------|----------|----------|---------------------|
| Far | 1114.6 m | 988.1 m | 300 |
| Near | 466 m | 351 m | 120 |

Figure 3.1: Plane view of the Chooz Nuclear Power Station, near the Meuse river. The inset shows a map of France where the star indicates the location of the power plant, on the border with Belgium.



Figure 3.2: Satellite photograph of the Double Chooz site in Ardennes, France. The two Chooz B reactors are marked with yellow pins while the Near and Far detectors are indicated with green pins. The blue lines are the baseline of each detector to each reactor.

occupied by the Chooz experiment, the near detector location was chosen where the ratio of the flux from each reactor is the same as for the far detector.

In this chapter, the use of nuclear reactors as a neutrino source and the neutrino detection principles are explained. In addition, a explanation of how a scheme of two detectors can help to improve our knowledge on neutrino oscillations is presented. Finally, all the details of the Double Chooz detector and its current status are described.

## 3.1 Nuclear Reactor as a Neutrino Source

Nuclear energy is defined as the energy contained in the atom nucleus. When we compare the mass of a nuclei with the sum of its constituents, the nucleons, there is a deficit for the first. This difference is defined as the biding energy of the nucleus and it is the energy stored by the interaction potential that keep the nucleons together. Such energy can be released through process such as radioactive decay or nuclear fission. Although the energy released by a fission of a single uranium atom is tiny if compared with macroscopic values, the fission of 1 kg of the same element releases the same amount of energy as burning 1500 ton of coal.

Nuclear power plants use this energy released by the nuclear fission to generate electricity. This kind of plant have a nuclear reactor where controlled fission occurs. The world most common type of commercial nuclear reactor is the Pressurised Water Reactor (PWR), which uses enriched uranium as fuel. While natural uranium is found in a ratio of the isotopes $^{235}$U and $^{238}$U of 0.72% and 99.27%, nuclear reactors uses a ratio of about 3% of $^{235}$U in order to keep a stable fission chain reaction. When one neutron is absorbed by $^{235}$U, the resulting nucleus is in an excited and unstable state, and fissioning in two other nucleus, is a possible way to reach a more stable state. The energy released is on the form of gamma radiation and kinetic energy of the daughter elements, which not necessary has the same mass. In addition, these lighter nucleus are neutron rich, and will suffer beta decay until they became stable. Consequently, a nuclear reactor works as a neutrino source, since that for each beta decay an electro antineutrino ($\overline{\nu}_e$) is emitted. Also, two or three neutrons is released during the fission and a suitable choice of materials make it possible to use one of this neutrons for fissioning another uranium atom. This process is the so called controlled chain reaction and it is represented by figure 3.3.
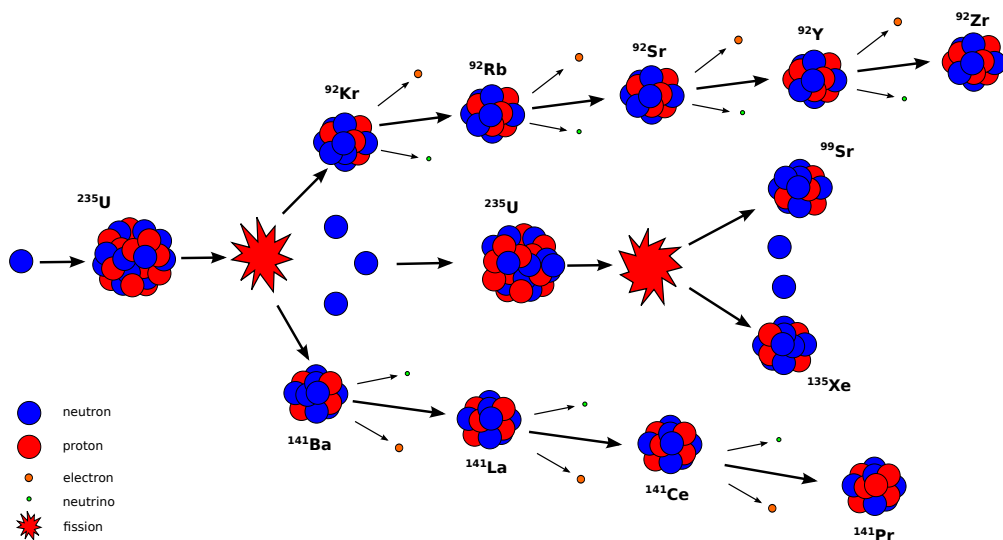


Figure 3.3: Nuclear fuel chain reaction and $\overline{\nu}_e$ production in a nuclear reactor

The artificial element plutonium is created inside the reactor when a neutron is absorbed by $^{238}$U, and instead of fissioning, it will decay as follows:

$$n + \ ^{238}\text{U} \ \rightarrow \ ^{239}\text{U} \ \rightarrow \ ^{239}\text{Np} \ \rightarrow \ ^{239}\text{Pu} \tag{3.1}$$
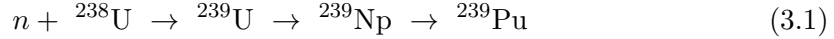
The first and second decays of equation 3.1 has a life-time of 23.5 minutes and 2.33 days, respectively. When a sufficiently amount of plutonium is created, it will also create a chain reaction as uranium does. The fissile isotopes that most contribute to the total thermal power, during a typical fuel cycle, of a PWR are: $^{235}$U, $^{239}$Pu, $^{238}$U and $^{241}$Pu. Their fission rate over the time is shown in figure 3.4. The next leading contributions come from the isotopes $^{240}$Pu and $^{242}$Pu at the order of 0.1% or less [45].
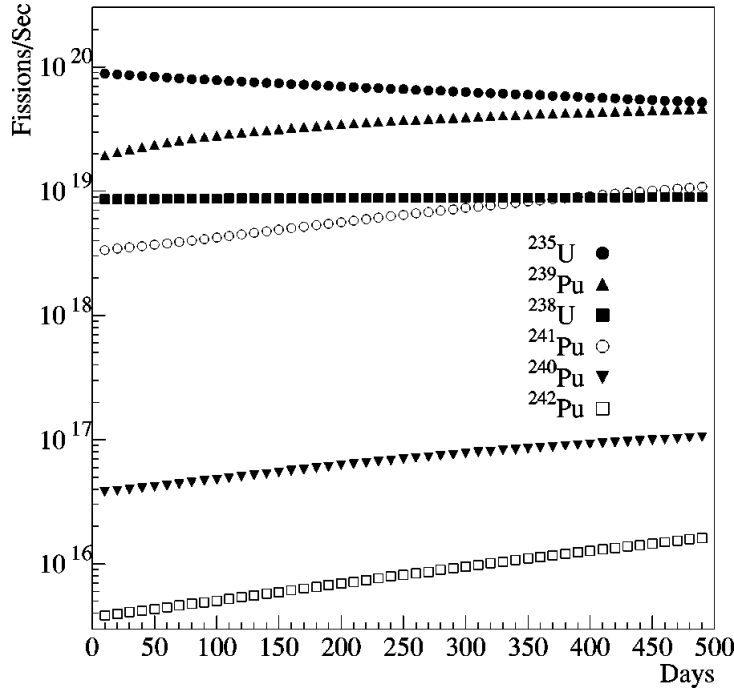


Figure 3.4: Time evolution of fission rates for each of the six most important isotopes in one of the Palo Verde reactor cores. The horizontal scale covers a full fuel cycle, at the end of which about 1/3 of the core is replaced with fresh fuel. Only the four most important isotopes are normally used to predict $\bar{\nu}_e$ yields [45].

The conversion of nuclear to electric energy is done as follows: the energy released by the chain reaction heats the water in a pressurized first loop, so it is kept in liquid state; heated water of first loop heats a second loop, vaporizing its water; hot steam powers up an electricity generator; and finally a third loop is used to condensate the steam of the second loop. This process is represented by figure 3.5.

Considering that an usual commercial reactor has a thermal power of 4 GW and that for each fission about 200 MeV and 6 $\bar{\nu}_e$ are released, a flux of $8.5 \times 10^{20}$ $\bar{\nu}_e$ per second is emitted, which makes nuclear reactor a copious neutrino source.

The emitted neutrinos' energy spectrum can be calculated if the distribution of the fission yields and the branching ratios of their decays are know, as done in [46, 47], and shown in figure 3.6. In addition, one could have a pure sample of one of the fissile isotopes and irradiate it with neutrons. With a precise spectrometer, the energy of the electrons can be measured and converted to neutrino energy. Such work was performed [48, 49], but a measurement of the neutrino spectrum regarding the fission of $^{238}$U have not been done by the time of this thesis.
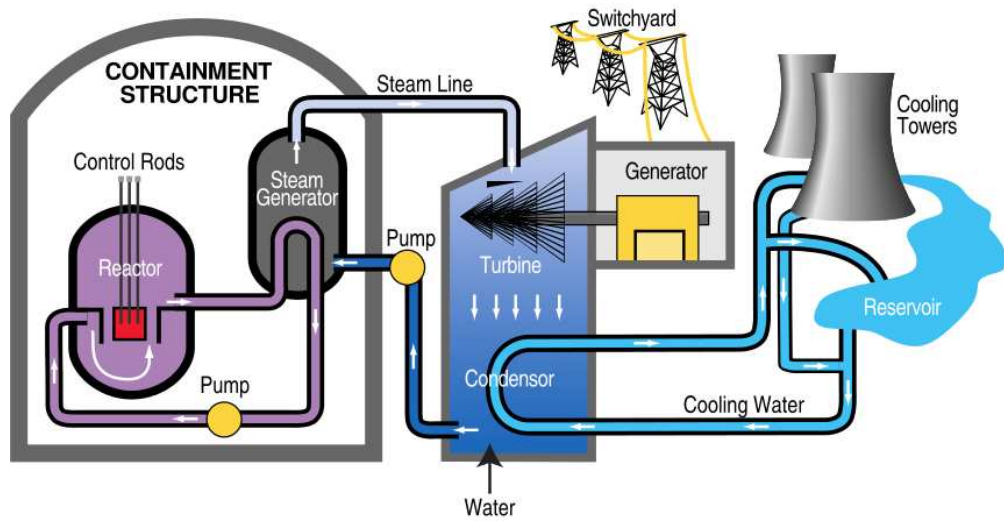
Figure 3.5: Scheme of a Pressurised Water Reactor nuclear power plant
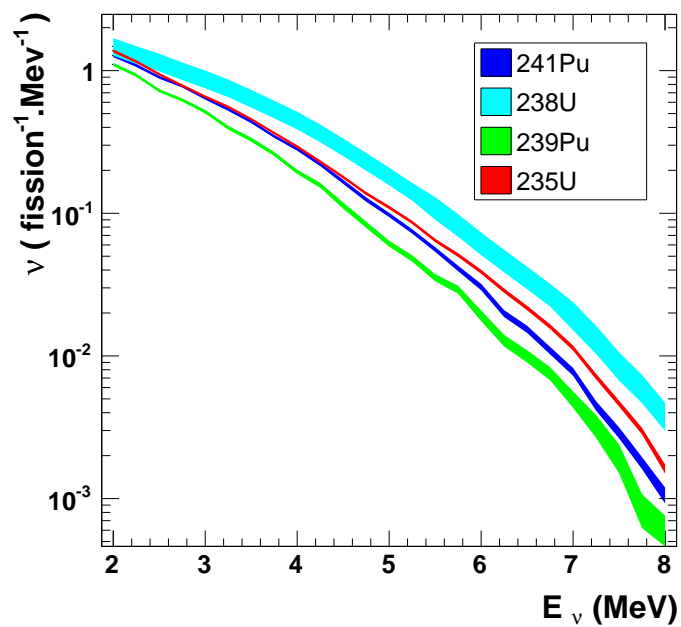


Figure 3.6: Neutrino emission spectrum flux for each of the main fissile components of the nuclear fuel. $^{235}$U, $^{239}$Pu and $^{241}$Pu spectra were taken from [47] while $^{238}$U spectrum was taken from [46].

## 3.2  Neutrino Detection

The basic neutrino detection idea of the Double Chooz is the same as in the legendary Cowan-Reines experiment in 1956. In a volume of liquid scintillator the neutrino undergoes inverse beta decay (IBD) with a proton, producing a positron-neutron pair, as represented in the following equation:

$$\bar{\nu}_e + p \rightarrow e^+ + n \tag{3.2}$$

The positron immediately loses its kinetic energy by scattering with the scintillator molecules and than either annihilates with an electron or forms a state of positronium, with a lifetime of 125 ps (25%) for the S = 0 state (para-positronium) or 140 ns (75%) for the S = 1 state (ortho-positronium). The positronium itself produces either 2 or 3 gamma rays totalling $2 \times m_e = 1.022$ MeV [50]. The scintillation light, of this so called prompt signal, is directly related to the energy of the incoming antineutrino plus $2 \times m_e$ and is detected by photomultiplier tubes observing the scintillator. The ejected neutron has only about a negligible 10 keV recoil energy, and it will thermalize before being captured on either a Hydrogen or Gadolinium nucleus, some tens to hundreds of $\mu$s after IBD, producing a 2.2 MeV or 8 MeV event respectively, by desexcitation of the nucleus through gamma ray emission. The light of the capture process is again detected by the photomultipliers and is called delayed event. The signal of a neutrino event is, therefore, a coincidence of a prompt and a delayed event in a pre-defined time window. After IBD the positron is emitted nearly isotropic, while the neutron preserves a memory of the neutrino incoming direction. While the positron contains the information on the neutrino energy, one can use the neutron to reconstruct the neutrino incoming direction. Alternatively, one could also have used elastic scattering on electrons, quasi-elastic scattering on a proton or deuteron or even on a nucleus to detect the antineutrinos from a reactor. The choice of the IBD was driven by the fact that elastic scattering on electrons has a lower cross section, because the interaction with deuterium atoms has a too high energy threshold of 2.2 MeV and because the interaction on a nucleus is hardly detectable (a few keV of nucleus recoil energy). But the main argument for using the IBD is that one can use the coincidence measurement of the prompt and delayed event to considerably reduce the background.

The neutrino energy can be reconstructed by assuming that the proton is initially at rest and that the nucleons are infinitely heavy compared to the antineutrino and the positron. Using $c = h = 1$ notation,

$$E_{\bar{\nu}_e} = E_{e^+} + 1.293 \text{ [MeV]}, \tag{3.3}$$

where 1.293 MeV is the difference of the proton and neutron mass. If the energy seen in the detector is $E_{\text{prompt}} = E_{e^+} + 0.511$ [MeV], from the annihilated positron, then

$$E_{\bar{\nu}_e} = E_{\text{prompt}} + 0.782 \text{ [MeV]}. \tag{3.4}$$

The existence of the 1.8 MeV threshold in the detection process, automatically ensures that only $\bar{\nu}_e$'s from large Q-value, and hence, short half-life $\beta$ decays are detected. Thus the observed $\bar{\nu}_e$ signal tracks closely in time the power excursions in the reactor.

The cross section for neutrino capture on protons to lowest order, assuming infinitely heavy nucleons, is given by

$$\sigma_{\text{IBD}} = \frac{2\pi^2}{m_e^5 f \tau_{\text{n}}} p_{e^+} E_{e^+}, \tag{3.5}$$

where $f$ is a statistical function including the Coulomb correction ($f_{exp} = 1.6857$) and $\tau_{\text{n}}$ is the free neutron mean lifetime [51].
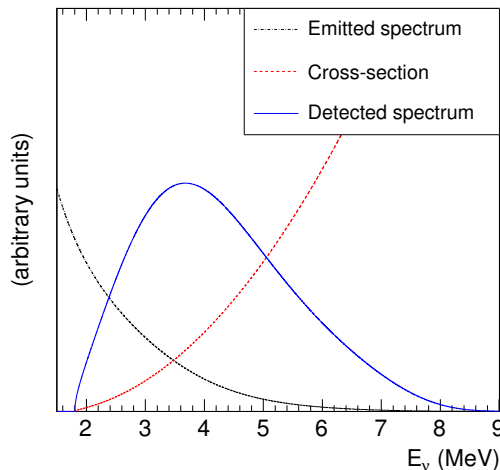
Figure 3.7: The IBD cross section, reactor neutrino flux and the expected detection energy spectrum, calculated as multiplication of both cross section and neutrino flux.

The antineutriono flux decreases with increasing energy, however the cross section increases, creating the detected spectrum shown in figure 3.7. This spectrum begins at the threshold for an IBD reaction, $E_{\bar{\nu}_e} \geq 1.804$ MeV, derived from equation 3.3 for creating a positron at rest.

Finally, since reactor neutrinos has not enough energy for appearance of $\mu$ or $\tau$, one looks for disappearance of neutrinos.

## 3.3 Two Detectors Concept

The method to reduce the uncertainty in the measurement of $\theta_{13}$ that was more accepted by the scientific community was the use of two identical detectors, one near and the other far from a nuclear reactor, as proposed for the first time in [52, 53, 54]. The main reason that this proposal was better accepted was that at that time it shown to be cheaper, easier and faster to be implemented than to build neutrino factories in experiments using hundred or thousand kiloton detectors located a few thousand kilometers from the accelerator neutrino source. In addition, its result would be used as reference for the design of future accelerator based experiments. Figure 3.8 shows the survival probability, defined be equation 2.9, as a function of the baseline.

The advantage of using two detectors is that the absolute normalization uncertainties due to reactor flux and detector efficiency are cancelled out when comparing the rate or spectrum shape of both detectors. For example, an analysis based on the ratio of the total number of events, $N$, detected by each detector running at the same time, can be done as:

$$R = \left( \frac{L_{far}}{L_{near}} \right)^2 \times \left( \frac{V_{near}}{V_{far}} \right) \times \left( \frac{\varepsilon_{near}}{\varepsilon_{far}} \right) \times \left( \frac{N_{far}}{N_{near}} \right). \tag{3.6}$$

where, $L$ is the reactor-detector distance, $V$ the target volume and $\varepsilon$ the detector efficiency. This $R$ value is independent of the exact knowledge of the reactor neutrino flux and energy spectrum. Moreover, the absolute values of detection efficiencies are practically cancelled, remaining only the relative uncertainty. In absence of oscillation, $R$ is equals to 1.

Furthermore, an analysis based on the spectrum shape, $S(E)$ measured simultaneously by the two detectors can be performed. Divided in energy bins, the spectra ratio
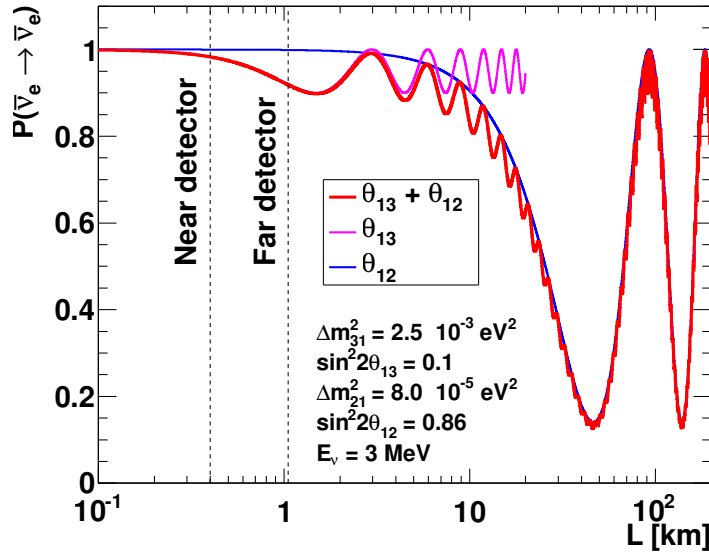
Figure 3.8: Electron antineutrino survival probability as a function of neutrino length of flight, for two (pink and blue) or three (red) neutrinos scenario. For a few km, $\theta_{13}$ has a dominant effect.

is energy independent in case of no oscillation, as shown in equation 3.7.

$$\frac{S(E_i)_{far}}{S(E_i)_{near}} = C\frac{1 - \sin^2 2\theta_{13}\sin^2(1.27\Delta m^2 L_{far}/E_i)}{1 - \sin^2 2\theta_{13}\sin^2(1.27\Delta m^2 L_{near}/E_i)} \tag{3.7}$$

Small deviations from the constant value $C$ are sought for oscillation parameters. This ratio also does not depend on the exact knowledge of the reactor power, absolute neutrino flux and energy spectrum, burnup effects, absolute values of target and detection efficiencies, reducing significantly the systematics uncertainties.

## 3.4 Double Chooz Detector

The Double Chooz detector is a set of five concentric cylinders submerged in the ground and topped with an outer muon veto, as shown in figure 3.9. This design was inspired by the original Chooz design and includes multiple layers in order to reduce backgrounds. At the center is the Neutrino Target, surrounded immediately by the Gamma Catcher, and then the Buffer Vessel which contains the photomultiplier tubes (PMTs) used to detect the neutrino signal. Surrounding theses three volumes is the Inner Veto followed by steel shielding. Each of the vessels has an opening at the top for a chimney attached to the Target vessel to extend through. At the top of this chimney is a Glove Box to enable access to the Target volume for calibrations. Finally, the Outer Veto is located below the glove box.

### 3.4.1 Inner Detector

Collectively the Neutrino Target (NT), Gamma Catcher (GC) and Buffer volumes are referred as the Inner Detector (ID). A picture taken before the ID top lid closure is shown in figure 3.10, where is possible to see the three volumes and the PMTs.

**Calibration Glove Box**
**Outer veto (OV)**
• **Plastic scintillator strip**
• **Far: 6.4 x 12.8 m² / Near: 11.0 x 12.8 m²**
**Stainless Stell Shield**

**Neutrino detector**
**Inner veto   (IV, 90 m³ liquid scintillator)**
• 78 PMTs (8-inch, Hamamatsu R1408)

**Inner detector (ID)**
  **Buffer        (110 m³ mineral oil)**
• 390 PMTs (10-inch, Hamamatsu R7081MOD)
  **γ catcher** (22.3 m³ liquid scintillator)
  **ν target      (10.3 m³ liquid scintillator with Gd)**
• **Number of protons = (6.738±0.020 x 10²⁹)**

Figure 3.9: A CAD cutaway view of the Double Chooz detector design.
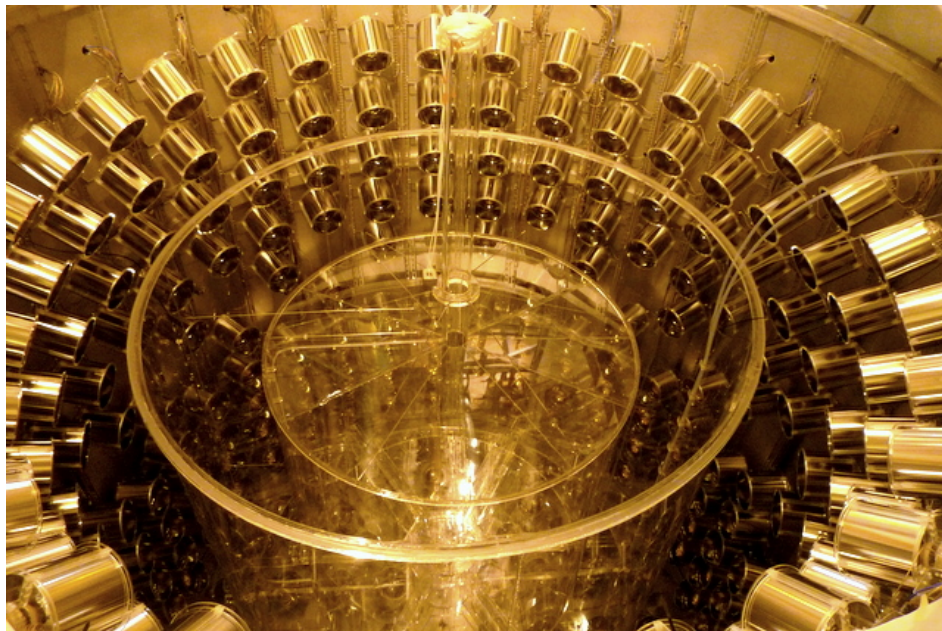


Figure 3.10: A picture of the ID before the top lid closure. From the center to the outermost part of the figure is possible to see the NT, GC and Buffer (equipped with the side and bottom mu-metal assembled PMTs), respectively.

### 3.4.1.1    Neutrino Target

The Neutrino Target (NT) is the innermost volume of the detector and the effective fiducial volume for $\bar{\nu}_e$ interaction. Its vessel is an acrylic cylinder of 2.46 m height, 2.30 m diameter and 8 mm thickness filled with 10.3 m$^3$ of organic liquid scintillator, almost twice that of the original Chooz experiment. The acrylic vessel is transparent to ultraviolet and visible photons with wavelengths above 300 nm. The liquid scintillator in the target has been newly-developed for Double Chooz, with design emphasis on long-term chemical stability [55]. It is composed of 20% ortho-phenylxylylethane (o-PXE), $C_{16}H_{18}$, and of 80% n-dodecane ($C_{12}H_{26}$), thus the number ratio of C:H is approximately 1:2. Both PXE and dodecane are aromatic molecules which get easily excited or ionised by energy deposition. The admixture of the dodecane reduces the light yield, but it improves the chemical compatibility with the acrylic and increases the number of free protons in the neutrino target. The fluors PPO (2,5-diphenyloxazole), 7 g/l, and Bis-MSB (4-bis-(2-methylstyryl)benzene), 20 g/l, are added as wavelength shifters to prevent the re-absorption of the scintillation light and to shift the scintillationg light frequency to match the PMT quantum efficiency range. The target also contains Gadolinium (Gd) as it has a very large capture cross-section for neutrons roughly $8 \times 10^9$ times larger than hydrogen.

To ensure time stability of the Gd-doped liquid, the Gd atoms are encapsulated in a meta-$\beta$-diketone, Gd(thd)$_3$, or Gd(III)-tris-(2,2,6,6-tetramethyl-heptane-3,5-dionate) molecule (structure shown in figure 3.11), for an efficient dissolving in the scintillator and a durable transparency. The absorbance of the scintillator was monitored for 180
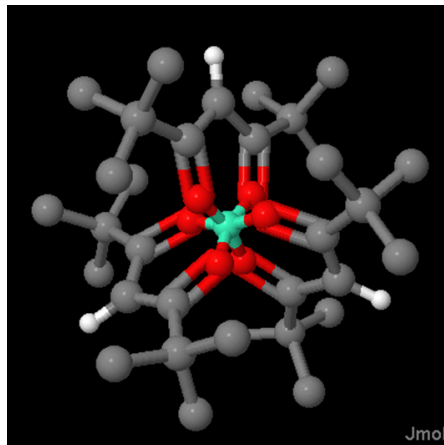


Figure 3.11: A 3D view of the structure of Gd compound used for dissolve Gd in the liquid scintillator.

days as shown in figure 3.12, confirming its long term stability, being suitable for use in the experiment. This complex metal-organic compound has been found to exhibit higher solubility in organic solvents, lending itself to long-term chemical stability. The high vapor pressure of the molecule also allowed purification by sublimation, reducing radioimpurities due to U, Th, and K chains.

The optical stability of the liquid scintillator is granted by the stability of the energy peak of neutron capture on Gd, which has been found stable within 1% over about one year. This is one of the main improvement with respect to the Chooz experiment, which was limited in sensitivity because the optical instability of its liquid scintillator. The proton number in the target (i.e. the absolute number of H nuclei) and its associated error are crucial parameters for the experiment. The error on the proton number is minimised by using a well defined and pure chemicals in combination with a precise
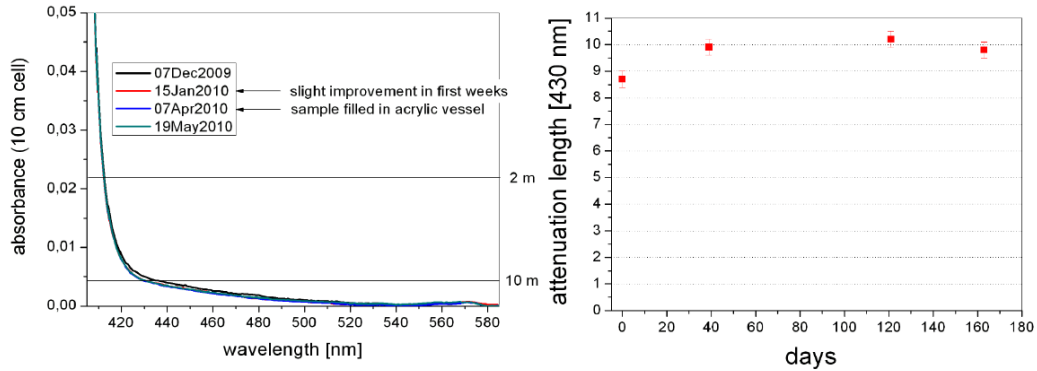
Figure 3.12: Liquid scintillator asorbance and attenuation length stability. The left plot shows the scintillator absorbance as a function of wavelength for various periods. The right plot shows the stability of attenuation length at 430 nm.

knowledge of the weights of each chemical added in the scintillator production. The amount of scintillator in the target has been determined upon liquid thermalisation by weight measurement, with a precision of 0.04%. The Hydrogen fraction in the target scintillator is known with a 0.3% precision, leading to a number of proton in the target liquid of $(6.747 \pm 0.020) \times 10^{29}$ [55].

With the used concentration of 1 g/l (0.123%) roughly 80% of the neutrons in the target will be captured on Gd. Adding Gd in the target scintillator has the followings advantages:

- The total energy released by the capture of a neutron on Gadolinium is 8 MeV, far above the energy range contaminated by natural radioactivity, which extends to 2.6 MeV (due to $^{208}$Tl). For comparison, neutron capture on Hydrogen yields 2.2 MeV.

- Gadolinium has a high cross section for neutron capture - 254 kbarn at 0.0253 eV on $^{157}$Gd (15.65% natural abundance) and 61 kbarn at 0.0253 eV on $^{155}$Gd (14.80% natural abundance), as shown in figure 3.13. This large neutron cross-section of Gd reduces the neutron capture time from about 180 $\mu$s, for Hydrogen, to roughly 30 $\mu$s allowing more restrictive cuts between the prompt and delayed event and thus again reduces the background to antineutrino rate.

The disadvantage of a reduced light yield by adding Gd is, thus, by far compensated.

The Gd-loaded scintillator for both far and near detectors was produced together to assure identical proton per volume concentrations in both detectors, and to assure that if there are any ageing effects, they are more likely to be the same.

### 3.4.1.2   Gamma Catcher

The Gamma Catcher (GC) volume surrounds the NT. It is formed by a acrylic vessel with a thickness of 12 mm and a total volume of 22.4 m$^3$. It contains a liquid scintillator which, contrary to the NT liquid, is not loaded with Gd. Although the Gd-loading does not affect the density of the liquid significantly, it makes the light yield 10-20% smaller than non Gd-loaded one due to some quenching effects. Although, it is possible to adjust the light yield by changing the PXE and dodecane ratio, it will modify the liquid density. Therefore, to increase the detector response uniformity, matching the CG with the NT scitillator in light yield and density, a commercial mineral oil (Ondina909) is added in addition to PXE and dodecane. The final composition consists of 30% dodecane, 66%
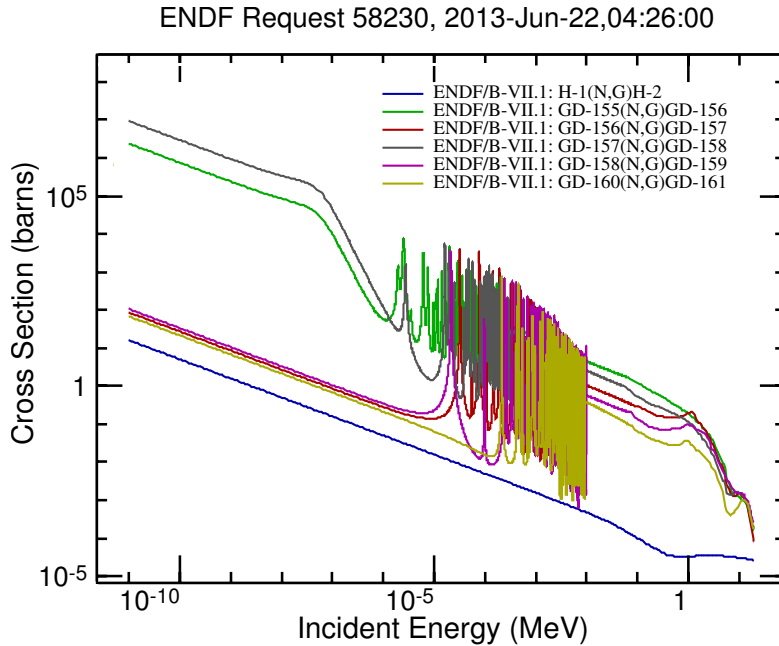
Figure 3.13: Neutron capture cross section for the most natural abundant isotopes of Gadolinium, and for Hydrogen.

mineral oil, 4% PXE, 2 g/l of PPO and 20 mg/l of Bis-MSB, where the ratio of PPO and Bis-MSB were also adjusted to give the same light yield as the NT [56]. The density of GC liquid was measured to be $0.8041 \pm 0.010$ kg/l at $15\,^\circ$C [55]. The Hydrogen fraction in the GC scintillator is $14.6 \pm 0.15\%$, leading to a number of proton in the GC liquid of $(1.578 \pm 0.019) \times 10^{30}$.

The purpose of the GC is rather literal - it is designed to ensure that the energy of the gammas produced in the NT is fully absorbed in the scintillating volumes, thus enhancing the efficiency for detecting neutron captures at the edges of the NT, and improving the uniformity of the detector response. It also acts as a buffer to fast neutrons entering the detector from outside. Only the NT includes Gd which is used for antineutrino detection, providing a well defined fiducial volume, without loss of calorimetric precision near the edge of the fiducial volume. This eliminates the need for a volume cut on antineutrino events, which can increase the overall systematic uncertainty. However, there occur a so called "Spill In" events, if an IBD takes place in the gamma catcher but the neutron travels into the target and is captured there on Gd. Such an event appears in the analysis as a target event. It can happen the way around that neutrons from IBD in the target reach the gamma catcher and, therefore, can not be detected, called "Spill Out". Both effects do not cancel each other and one observes a net spill in current. This phenomenon will be discussed in sections 4.6.5 and 4.6.6 in more detail.

### 3.4.1.3  Buffer

The Buffer vessel is made from the low background stainless steel 304L, and has enough long term tightness for ten years operation. In addition, it has chemical compatibility with mineral oil of the buffer region and liquid scintillator in the inner veto. This vessel optically isolates the ID from the IV and serves as support for the 390 ID photomultiplier tubes. It has a 105 cm thick layer of non scintillating mineral oil, resulting in a volume of 114 m$^3$. This oil main function is to shield the NT and GC scintillating liquids from radioactivity naturally present in the PMTs, steel vessel, and surrounding rock.

Its composition is a mixture of a commercial mineral oil (53%), Ondina917, and n-alkane (47%), CobersolC70, chosen for its transparency, low aromaticity, compatibility with the acrylics and PMTs, and to have the same density (0.804 kg/l at 15 °C) as the scintillator, to protect the thin GC's acrylic vessel. Use of the buffer is one of the significant improvements of the Double Chooz detector over the previous design of Chooz experiment, and a picture of it before the GC and NT installation is shown in figure 3.14.
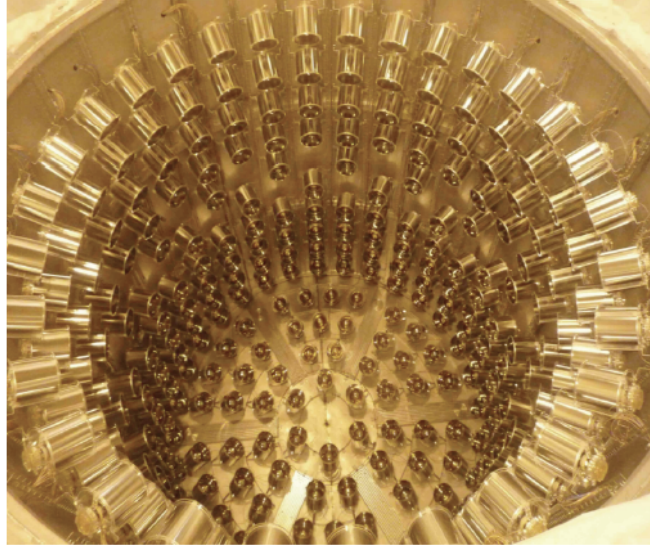


Figure 3.14: The Buffer volume, after the side and bottom PMTs assembling and before the GC and NT acrylic vessels installation.

### 3.4.1.4 Light Production

As it was said in the previous sections, the liquids for the Double Chooz detector are a mixture of three organic chemicals that are mainly responsible for the production of light: PXE, PPO, and bis-MSB. PXE is aromatic compound that serves as a solvent with high density (0.988 g/cm$^3$) and high flash point (145 °C), which is advantageous from safety and self-shielding points of view. The solvent is responsible for the bulk of energy absorption. The excited molecules of PXE then transfer the energy to the light emission, either through radiative or non-radiative mechanisms. The existence of non-radiative transfer is an advantage since the light absorption is high at the PXE emission peak. Excited molecules of PPO fluoresce when they return to the ground state. Due to a shift of the light wavelength between absorption and emission spectra, wavelength of the emitted photons get larger, so that it is not likely to be absorbed by PPO again. The emission spectrum is still not soft enough to be in the optimal photo-cathode quantum efficiency region of the Double Chooz PMTs, neither is in the region where the attenuation length is large enough for the light to reach the PMTs effectively. The absorption band of Bis-MSB matches well the emission profile of PPO, and therefore the resulting spectrum is effectively shifted further, yielding peaks at 420 - 430 nm, where the PMT photocathode sensitivity is maximum, and the total attenuation length is of the order of meters. The liquids' chemical components and properties for the neutrino detector are summarized in tables 3.2 and 3.3, while figure 3.15 shows wavelength spectra of the scintillators as inputs for the detector simulation.

Table 3.2: Composition of the Double Chooz detection liquids

| Volume | Solvent | Primary Solution | Secondary Solution | Gd(thd)$_3$ |
|---|---|---|---|---|
| NT | dodecane (80%) : PXE (20%) | PPO (7 g/l) | Bis-MSB (20 mg/l) | 1 g/l Gd |
| GC | dodecane (30%) : PXE (4%) : Mineral Oil (66%) | PPO (2 g/l) | Bis-MSB (20 mg/l) | - |
| Buffer | Mineral Oil (53.5%) : n-alkanes (46.5%) | - | - | - |
| IV | LAB (50%) : n-alkanes (50%) | PPO (2 g/l) | Bis-MSB (20 mg/l) | - |

Table 3.3: Properties of the Double Chooz detection liquids

| | $\nu$-Target | $\gamma$-Catcher |
|---|---|---|
| Density [kg/l] @ 15°C | $0.8035 \pm 0.0010$ | $0.8041 \pm 0.0010$ |
| Attenuation Length @ 430 nm [m] | $7.8 \pm 0.5$ | $13.5 \pm 1.0$ |
| Refractive index @ 405 nm (18°C) | 1.47 | 1.46 |
| Light yield [% BC-505] | $48.1 \pm 0.5$ | $46.6 \pm 1.0$ |
| Potassium [ppb] | $< 2$ | $< 2$ |
| Gd [wt.%] | $0.123 \pm 0.002$ | - |
| Hydrogen [wt.%] | $13.60 \pm 0.04$ (calc.) | $14.6 \pm 0.2$ (meas.) |
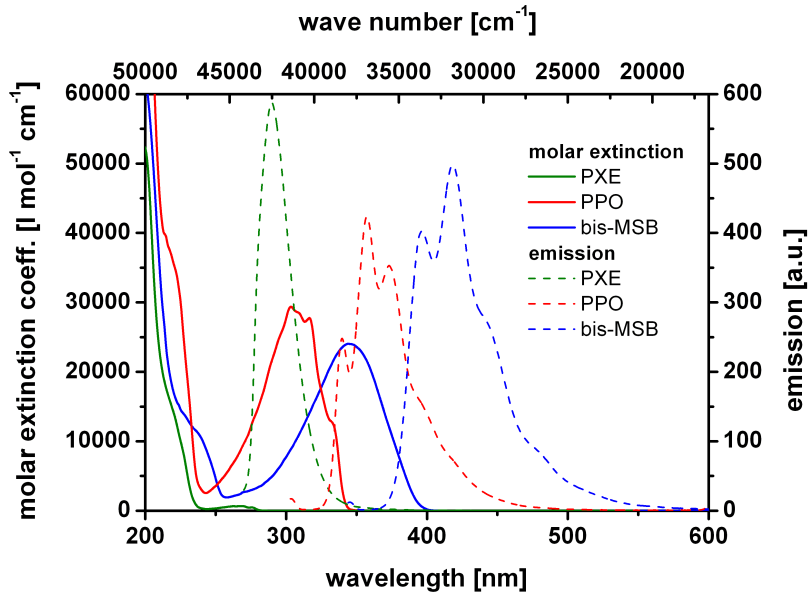


Figure 3.15: Wavelength spectra for the light absorbed and emitted from the scintillator of the neutrino target as inputs for the detector simulation. The doted lines show the probability of light emission for the scintillator of the neutrino target.

### 3.4.1.5 Light Detection

To collect the scintillation light produced by neutrino interactions, the detector is equipped with 390 PMTs mounted on a dedicated support structure, inside the buffer volume. From this number, 270 are held on buffer tank side walls and the rest are equally divided in the buffer tank bottom and top lid. These PMTs have 10 inches low radioactive glass bulb and were developed by Hamamatsu Photonics K. K., based on Hamamatsu R7081 model. Its glass is formed with platinum coating to reduce contamination of radioactive isotopes, such as $^{238}$U. To protect the PMT electronics from the buffer oils, an epoxy glue was used to envelope the PMT base. Figure 3.16 shows a picture of a single Double Chooz PMT and its technical drawing, and table 3.4 summarises its basic specifications.
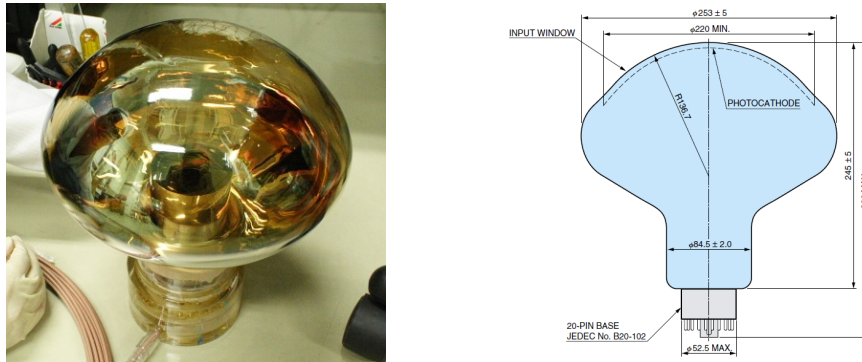


Figure 3.16: Picture of a Double Chooz 10" Hamamatsu R7081 PMT on the left and its technical drawing on the right. The PMT electronics, on the left figure, is already covered by epoxy and connected with signal cable.

Table 3.4: Basic specifications of Hamamatsu R7081 PMT

| Property | values |
| --- | --- |
| Wavelength region | 300 nm $\sim$ 650 nm |
| Photocathode | Bialkali |
| Peak wavelength | 420 nm |
| Diameter | 253 mm |
| Number of dynodes | 10 |
| Glass weight | 1.15 kg |

The number of PMTs was determined based on the required energy resolution and the light output of the NT scintillator. The required energy resolution is less than $10\%/\sqrt{E}$ (FWHM), where E is in MeV. This implies a light yield bigger than 100 photoelectrons per MeV. The NT and GC liquid scintillator light yields were measured before the detector filling to be around 6500 photons per MeV of energy deposition, so only about 1.5% of this is actually required to be collected.

The detection efficiency of single photon on the PMT ($\varepsilon_{\mathrm{Ph}}$) is defined as the product of quantum efficiency ($QE$) and photo-coverage (PC), or the fraction of the Buffer inner surface covered by the PMTs, i.e.,

$$\varepsilon_{\mathrm{Ph}} = QE \times PC. \tag{3.8}$$

The collection efficiency of the ID PMT with quantum efficiency was measured before installation as shown in the right of figure 3.17 [57]. The QE of the Double Chooz PMTs

is 21% on average and the total PC of the PMTs is around 13%. It means that total detection efficiency for scintillation photons is estimated to be 3%. Thus, the energy resolution is calculated to be $7\%/\sqrt{E[\text{MeV}]}$, which is smaller than the requirement.
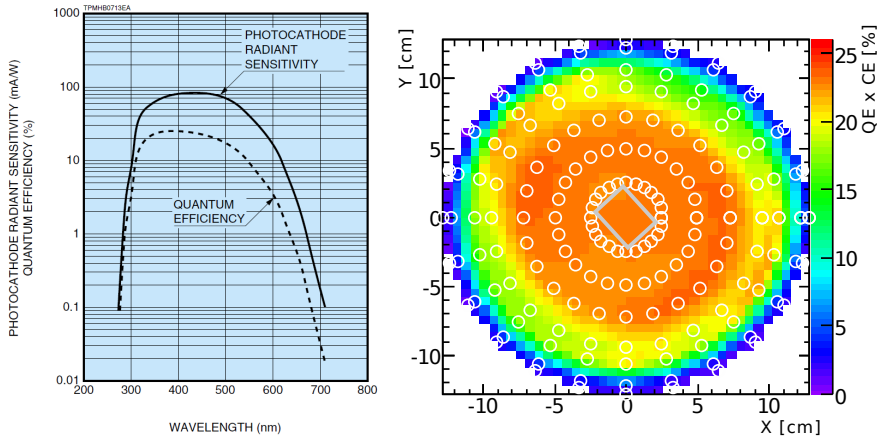


Figure 3.17: Quantum efficiency of PMT R7081 measured by Hamamatsu Photonics [58], on the left, and average collection efficiency maps [57] including the PMT surface.

Finally, each PMT is shielded by a mu-metal cylinder to suppress effects from magnetic fields. The angular positions of the PMTs were optimized in order to guarantee a uniform detector response at the center of the detector.

### 3.4.2   Inner Veto

The Inner Veto (IV) is an active liquid scintillator detector surrounding the ID. Its main purposes is to tag incoming muons and muon-induced backgrounds, such as fast neutrons, entering the detector from the outside and shields the ID against low energy radioactive background. The IV is optically isolated from the ID and can actually be considered a separate detector. It should be noted that the IV does not actively veto muon events, but values for the energy deposited in this volume are included for each event, allowing for an offline discrimination between muon and non-muon events. The IV vessel has a diameter of 6.5 m, a height of 6.85 m and holds 90 $m^3$ of liquid scintillator. The scintillator is monitored by 78 Hamamatsu R1408 8" PMTs arranged around the sides (12 PMTs), bottom (48 PMTs), and top (24 PMTs) of the cylinder, with different orientation, maximizing the uniformity of light collection. These PMTs and their bases are enclosed within a conical mu-metal structure to shield from magnetic fields, and they were previously used in the IMB and Super-Kamiokande experiments [59]. The volume between the PMT and the mu metal is filled with mineral oil. The IV liquid scintillator composition is 48.4% LAB, 51.6% CobersolC70, 2 g/L PPO, 20 mg/L bis-MSB [55]. Since the total photo coverage for the IV is 0.6%, the walls of this vessel are made from steel and is painted in white to increase reflectivity. The outside of the Buffer vessel, which forms the other wall in this volume is coated with a thin polymer film (VM2000), a material highly reflective in the wavelength range 300 - 700 nm. Including this material approximately doubles the light collection. A photo of the IV is shown in figure 3.18.

### 3.4.3   Steel Shielding

The IV is surrounded by 15 cm of low activity demagnetized stainless steel. The main purpose of this layer is to shield the detector against naturally occurring gamma radiation in the rock and cavern surrounding the detector. The thickness and the shape

Figure 3.18: Photograph of the Inner Veto vessel, on the left, from its PMT installation period. On the right it is a picture taken after the ID installation, where the Buffer vessel and its reflective wall can be seen.

of the shield was determined by a full detector simulation of the natural radioactivity backgrounds from the rocks. Due to the limited size of the access tunnel, the shield was divided into about 50 pieces with a 60 degrees "V" shape interface to match two consecutive pieces, as shown in figure 3.19. This shape is efficient to prevent gamma
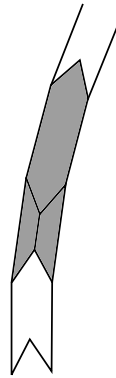


Figure 3.19: Design of the steel shield pieces. The 60 degrees shape prevents gamma radiation leaking into the detector.

radiation entering the detector through the shield cracks between neighbour pieces. This is a major improvement with respect to Chooz experiment, which used low radioactivity sands to shield the active part of the detector. In order to access the ID, the top part of the shield is assembled in halves and can be moved to the side of the pit as shown in figure 3.20.

### 3.4.4 Outer Veto

Another further improvement with respect to the Chooz experiment is the Outer Veto (OV). It is a system of overlapping plastic scintillator strips which is installed above the stainless steel shield. The purpose of the OV is to tag muons, that could cause background events through muon correlated physics. Such detector allows to track the coordinates for muons passing through an area of 12.8 m × 6.4 m centred on the detector chimney, as shown in figure 3.21. The dimensions for the near detector is designed to be larger ($11.0 \times 12.8$ m$^2$) than the one in the far detector due to higher rate of cosmic muons. With two layers of strips in orthogonal directions, both muon timing and position information are available. A smaller upper OV installed above the
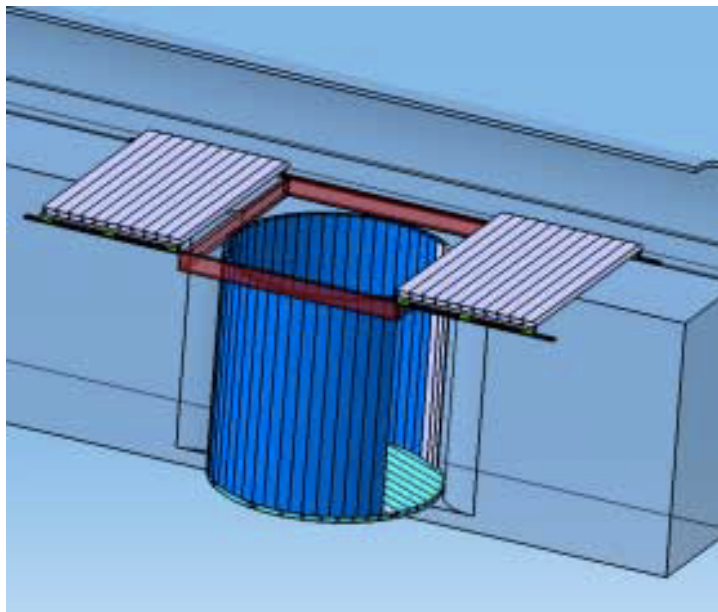
Figure 3.20: A 3D view of the steel shielding. Its top part opens into two halves to access the ID. After the detector installation, the top part is closed and the outer veto is placed above it.
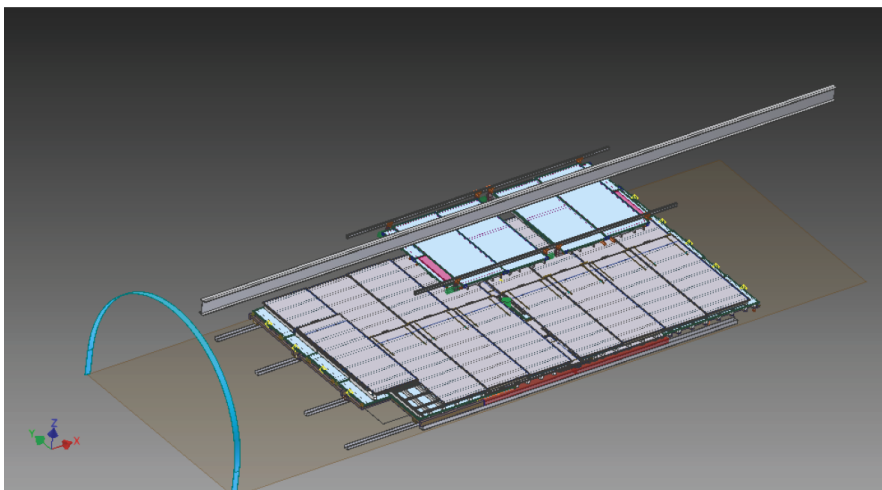


Figure 3.21: Design of the alignment of the OV planes. The upper and lower OV module planes are shown as light-blue and light gray boxes, respectively.

chimney allows to cover an area of 1.1 m × 0.30 m left open around the chimney. The OV consists of 64 plastic scintillator strips of $5 \times 1 \times 320$ cm coupled to 1.5 mm diameter and 360 cm long wavelength shifting optic fibers that are connected to 64 channel multi-anode PMT (Hamamatsu H8804). The strips are superimposed to form $x$ and $y$ plane of 32 strips each. To be noticed that the OV dimensions extend beyond the IV diameter to allow the tagging of near-by muons not entering in the detector, which could cause muon correlated physics in the ID. A picture of the far laboratory taken after the OV and before the Glove Box installation can be seen in figure 3.22.



Figure 3.22: Inside of the Double Chooz far hall, before installation of the Glove Box, where the lower OV modules can be seen.

### 3.4.5 Calibration Systems

For a near and far detectors scheme, the dominant source of systematic uncertainty is the differences in detector responses between the two detectors (energy scales and efficiencies of selection cuts). The goal of the Double Chooz experiment is a relative error, between the detectors, on detection efficiency of about 0.5%. Thus, it is important to determine accurately the scintillator response, the detector optical model, the energy scale and time offset, and the PMTs gain, which can be checked using calibration sources. In order to monitor the detector response, determine the energy scale and trigger efficiency, several embedded and deployable calibration systems are used, such as: untagged radioactive sources, laser diffuser balls, light injection systems and natural sources. Each one is described on the following sections, together with their method of use. All the calibration sources will be the same for the two detectors.

#### 3.4.5.1 Untagged Sources

Source deployment on the detector is essential to evaluate the detector responses against physics interactions, as the absolute energy scales and neutrino detection efficiency. The sources were designed and fabricated specifically for the Double Chooz experiment and are very small (approximately 0.3 cm in length and radius of 0.08 cm, as shown in figure 3.23) in order to reduce absorption of emitted radiation and shadowing of the light by the materials of the deployment system and the capsule itself. The same source can be used in all active regions of the detector and are encapsulated to preserve scintillator chemical integrity. In addition, the outer encapsulation of the sources contains a threaded part that allows attachment of the same source to different calibration systems.
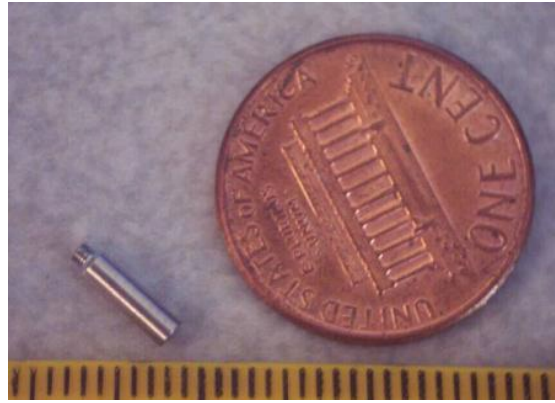
Figure 3.23: AmBe source next to a one US cent coin.

The following gamma and neutron sources are available for the detector calibration and neutron detection efficiency determination:

- **Am-Be**: Americium-241 emits an alpha particle that can interact with a $^{13}$Be nucleus to produce $^{13}$C in an excited state, which de-excites by neutron emission. The energy spectrum of AmBe neutrons extends up to, approximately, 11 MeV, and has an average of, approximately, 4 MeV. In roughly 60% of the cases, the neutron emission will leave the $^{12}$C nucleus in its first excited state, which will then de-excite by a single 4.43 MeV gamma. The emission of a mono-energetic gamma following a neutron is advantageous as it allows one to "tag" the neutron emission and use the source to determine the absolute neutron detection efficiency;

- $^{68}$**Ge**: Germanium-68 decays by electron capture to $^{68}$Ga, which suffers a $\beta^+$ decay, converting to stable $^{68}$Zn.[1] The annihilation gammas from the positron emitted by this source correspond to the minimum prompt signal for IBD reaction, thus allowing to calibrate the efficiency of the trigger threshold at different positions to make sure all IBD positrons are accepted;

- $^{252}$**Cf**: Californium-252 undergoes into spontaneous fission with emission of several neutrons with average multiplicity of 3.76, known to about 0.3%. It can be used to study neutron efficiency at different positions, in particular close to the boundary between target and gamma catcher. The neutron energy spectrum of $^{252}$Cf is softer than the one of the AmBe source and has an average of approximately 2.1 MeV;

- $^{137}$**Cs**: Caesium-137 emits 0.662 MeV mono-energetic gamma that can be used to calibrate the scintillator energy scale;

- $^{60}$**Co**: Cobalt-60 emits 1.173 and 1.333 MeV gammas.

Two type of deployment systems have been developed for the Double Chooz experiment. One is the *z-axis* system to insert calibration sources into the NT and the other one is the *guide tube* system for the GC. Both of them can be seen in figure 3.24.

Deployment using the *z-axis* is performed directly in the NT volume, along the symmetry axis, using a micro-step motor and pulley-and-line system, which is connected through the ID chimney to a light tight Glove Box, sitting above the detector. The Glove Box (left of figure 3.25) is continually flushed with nitrogen and kept at the same pressure as the ID, in order to maintain a clean and radiopure detector conditions while in use. The source capsule is attached on the edge of a weight, which is tied to the deployment

---

[1]in 3% of cases, there is a 1.077 MeV gamma emission from an excited state of $^{68}$Zn
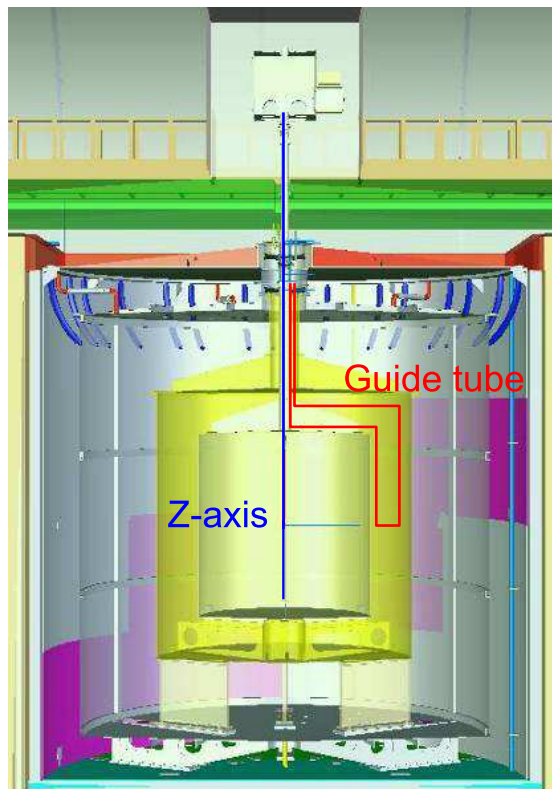
Figure 3.24: Scheme of the Double Chooz deployment systems. The blue line shows the positions accessed by the *z-axis* system, while the red line is for the *guide tube* system.



Figure 3.25: Picture of the Double Chooz Far Detector Glove Box, on the left, and *z-axis* deployment system, on the right.

system string. The deployment range span from 1 cm above the NT bottom up to the chimney, with 1 mm precision, allowing fine control over the position of the source. The system is useful to determine the absolute energy scale at the center of the detector and its position dependence along the central axis. At the top and bottom regions of the NT, it is also possible to estimate fraction of neutrons which escape from the neutrino target.

The *guide tube* is a thin rigid hermetic stainless steel tube embedded in the GC. Deployment with this system is performed using a motor driven wire, guided through the rigid looped tube. It traverses the GC passing near the boundaries of the target and the buffer, as shown in figure 3.26. The source position is known within 1 cm precision
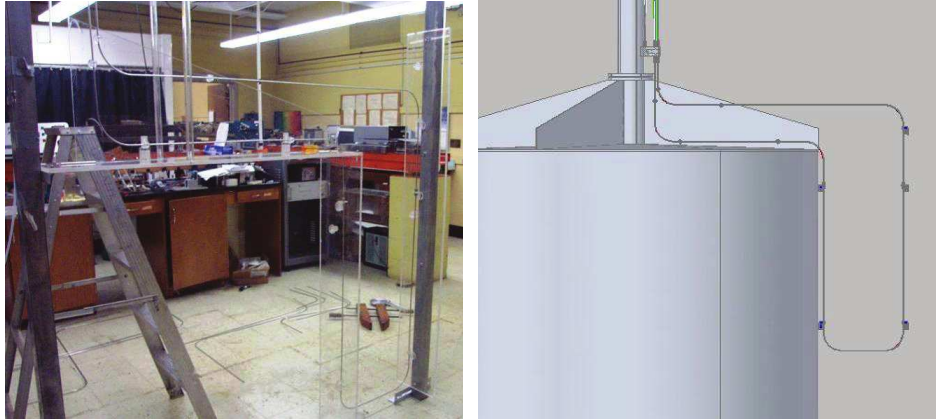


Figure 3.26: Two views of the Double Chooz *guide tube*. *Left*: In the laboratory, before installation. *Right*: CAD drawing of its position in the GC volume.

along the loop and the perpendicular distance between the source and the target wall is known within 2 mm. This system allows sources to be deployed just outside of the NT vessel wall or just inside the GC wall, making possible the measurement of neutron capture at the edge of the detector's fiducial volume.

### 3.4.5.2   Light Injection Systems

The Inner Detector Light Injection (IDLI) system consists of a control box and a Light Emitting Diodes (LEDs) flasher box connected with optical fibers. The end points of the fiber cables are connected to attachments, which are mounted on the support structure of the ID PMTs. There are 46 injection points, each one connected with a flasher module in the LED box. These modules have three LEDs with three different wavelengths (385 nm, 425 nm and 470 nm) and a PIN-photo diode as a monitor of LED light intensity. The 385 nm wavelength is expected to excite the scintillator inside the GC vessel and isotopic light is generated by absorption and re-emission process in the scintillator molecules. On the other hand, the 427 nm and 470 nm lights do not excite the scintillator so that the lights can directly reach the PMT surfaces on opposite sides, passing though the buffer, GC and NT volumes. Among all injection points, 32 (20 of side wall, 6 of top, and 6 of bottom) are attached with light diffuser plane. Lights though the diffuser planes have a diffusion angle of 22 degrees to spread inside the buffer tank and cover a large fraction of the detector, as exemplified in figure 3.27. Therefore, diffused lights with 425 nm are suitable for gain and timing calibration of each PMT channel. The other 14 points have narrower diffusion angle of 7 degrees, which are mounted at 8 different places on the side wall. The narrow lights with the 385 nm LEDs can make point-like light sources via absorption and re-emission at the
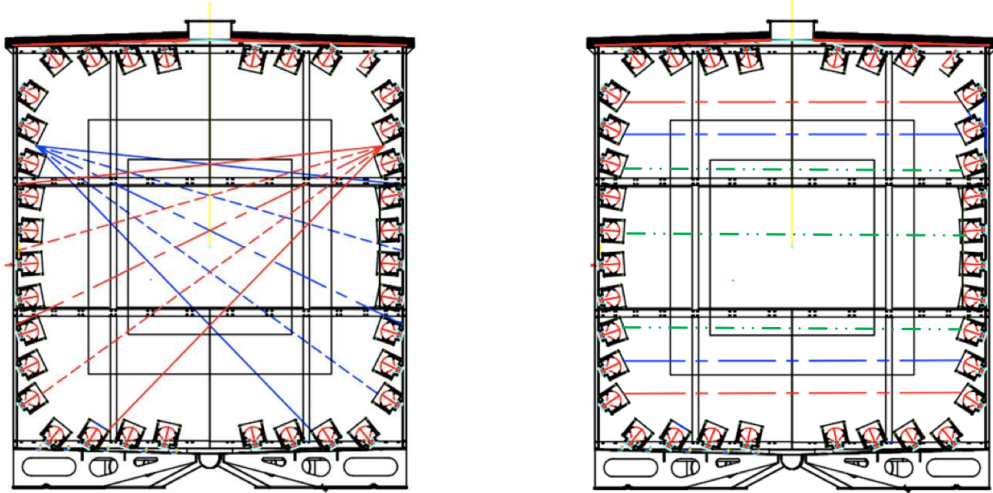
Figure 3.27: Two Double Chooz detector schematics, with typical position of the LEDs for calibration. The left figure shows the diffused light paths while the right figure shows the paths for the pencil beam mode.

boundary around the GC. The LED properties like flash rate, intensity and duration are all remotely controlled.

The Inner Veto Light Injection (IVLI) system have a conceptual design that is quite similar to the IDLI, although its hardware implementation is rather different. The IVLI is responsible to extract the gain of every IV PMT; determine the offsets in the time response of all IV channels, and follow their possible changes as a function of time; and monitor the light transmission inside the IV liquids and their light yield. Gain measurements are performed with weak light pulses analysing charge likelihoods at the single photoelectron (SPE) spectrum. On the other hand, timing measurements are performed with high intensity light. These high intensity runs are also used to monitor the light transmission inside the liquid scintillator, comparing at each time the number of photoelectrons detected. To send light evenly at all the IV channels, light injectors are attached on every single PMT. The light pulses necessary for these calibration runs are produced by a board of LEDs installed outside the detector. The light is carried inside the IV through a network of 1 mm outer diameter (0.6 mm quartz core diameter) and 25 m long quartz fibers (Thorlabs BFH48-600 model), that were chosen because plastic suffers degradation in the liquid scintillator. The LED board has $8 \times 12$ LEDs: 90 LEDs produce blue light (475 nm) while the remaining 6 illuminate in the UV region (365 nm). Like the IDLI the blue light is used to study the light transmission and the attributes of individual PMTs, and the UV light is used to survey the scintillator light yield.

Calibration data taken with these two systems are used to extract conversion factor from integrated charge to number of photoelectrons (PEs) and to correct for relative timing difference for each channel. In addition, they are also useful to check stabilities of the detector and readout hardware since the systems are installed inside the detector. Finally, they are run periodically to monitor the detector, as well as the gain and timing of the PMTs, stability.

### 3.4.5.3   Natural Sources

Natural occurring radioactivity (the U/Th decay chains for example) and cosmic rays can be used as calibration methods for the detectors. Cosmic rays interaction products, such as Michel electrons and cosmogenic isotopes ($^{12}$B for example) can be used to

Figure 3.28: Two fibers attached to an IV PMT.

calibrate the high energy part ($> 7$ MeV) of the IBD energy range, while spallation neutron captures can be tagged by muons entering the detector some $\mu$s before and be used to calibrate the neutron energy scale at 2.2 MeV and 8 MeV. These clear neutron absorptions on H or Gd peaks, can also be used to supervise the detector stability during time.

#### 3.4.5.4   Future Calibration Plans

Future calibrations methods planed for the Double Chooz detectors, seen in figure 3.29, are:

- **Articulated Arm**: This system will allow radioactive sources to be deployed throughout the NT volume. The arm would deploy down the chimney of the NT, and the articulation would allow a calibration source to be placed anywhere within that vessel with high spatial precision. This form of calibration would allow full mapping of detector response as a function of position within the NT, energy, and particle species.

- **Tagged Source**: A tagged $^{252}$Cf source was successfully used in the Chooz experiment to measure absolute neutron efficiency to 0.6%. It was consisted of an ionization chamber with $^{252}$Cf isotope deposited on the external surface of the cylindrical anode. The chamber was filled with Argon (1 atm) and few percent of carbon dioxide. Use of the ionization chamber allowed to detect fission fragments and easily discriminate against alpha decays of $^{252}$Cf that emit roughly 30 times less energy. The signal from the chamber anode constituted an electronic "tag", indicating the a fission has occurred, and hence neutrons were emitted.

- **Laser Diffuser Ball and Central LED Flasher**: Two lasers (470 nm and 380 nm) will be used to determine the PMT time offsets, gain, charge likelihoods (important input for vertex reconstruction), and speed of light. The light produced by the laser heads is guided through the optical fiber into the diffuser ball that is deployed inside the NT along the vertical axis. The diffuser ball is a 80 mm sphere with 53 mm long necks made of 4 mm (for blue laser ball) and 6 mm (UV laser ball) thick acrylic.

(a) Articulated Arm

(b) $^{252}$Cf Tagged Source



(c) Laser Diffuser Ball and Central LED Flasher
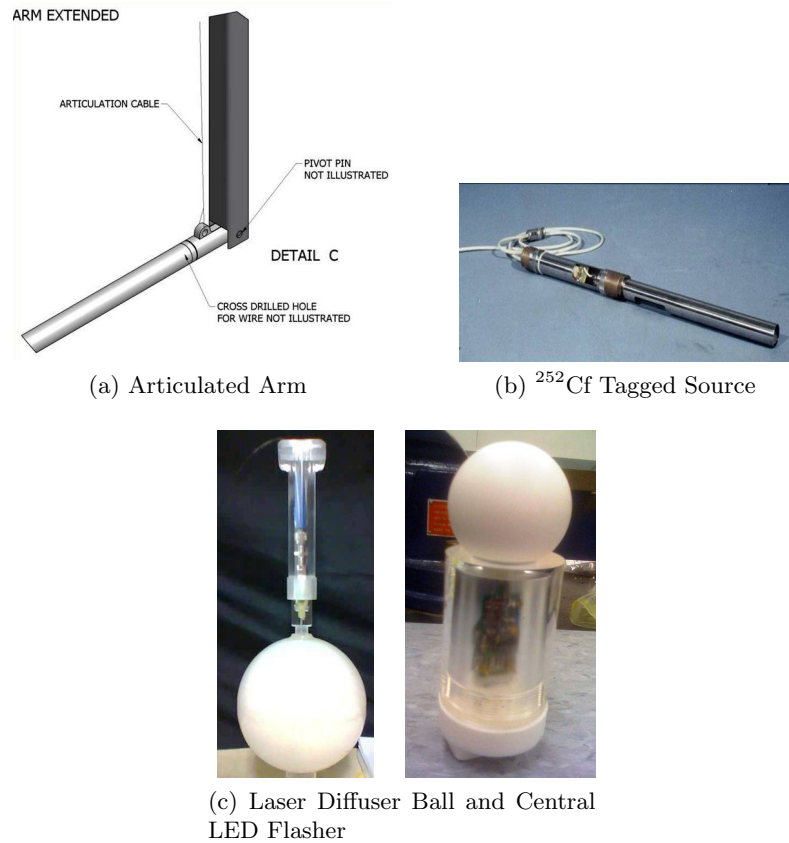
Figure 3.29: Future Double Chooz calibration methods.

A battery powdered hermetically sealed blue LED was deployed before the filling at the center and along the *z-axis* of the empty target vessel to calibrate PMT time offsets independently of the speed of light, as it is accurately known for the air. The flasher automatically cycles through eight light levels, putting out 128 pulses at each level before moving to the next one. The data were used to extract time offsets to about 0.5 ns precision. This system will be also used in the current operational detector in the future.

### 3.4.6  Data Acquisition System

The search of neutrino events is only possible with a high precision data acquisition system (DAQ). Such system is composed of all the electronics and devices to collect the IBD light, convert it in electronic signal, which will be written in readable data for the off line analysis. The Double Chooz experiment has two independent systems, refereed as neutrino DAQ ($\nu$-DAQ) and outer veto DAQ (OV-DAQ). The $\nu$-DAQ is responsible for the ID and IV, while the OV-DAQ handles, as the name suggests, the data from the outer veto system. A global clock (32 ns per clock) is provided by the trigger system of $\nu$-DAQ to the OV-DAQ in order to share the time stamp among the two DAQs. Data from the two systems are merged on a phase of offline event processing for analysis.

The $\nu$-DAQ is a readout system which reads out signals from the 390 ID and 78 IV PMTs. Photons seen by a PMT are converted to an electronic signal, first by producing an electron, called photoelectron, by Photo-Electron Effect at the photocathode, and then it is accelerated by a high voltage potential until it hits an dynode plate, where it will knock out more electrons, which will also be accelerated and hit another dynore, knocking out more electrons. This process occurs across 10 dynodes covering a span of

about 1.5 kV, producing a gain output on the last dynode (anode) of $\sim 10^8$, as shown in figure 3.30. The final signal at the anode is then transported away from the detector
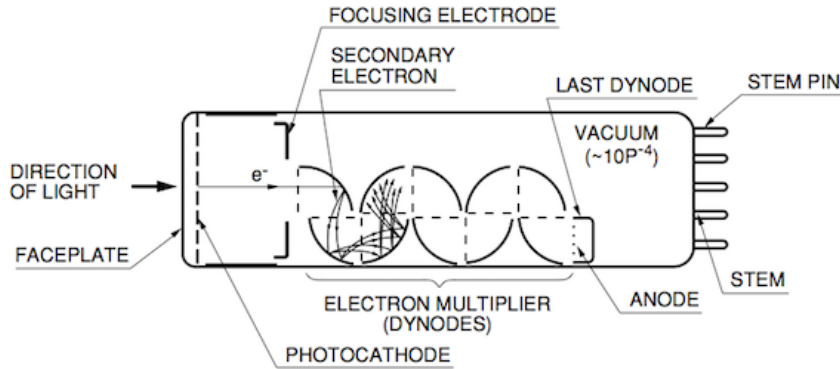


Figure 3.30: Scheme of electrical signal produced by a PMT. The incident light reaches the photocathode ejecting a electron by photoelectron effect, which will be accelerated through the high voltage and collide in the first dynode, producing more electrons by elastic scattering. After an avalanche effect in each dynode, the initial signal is multiplied by a factor of $\sim 10^8$ in the final dynode (anode).

trough 40 m cables.

The PMTs are powered by positive high voltages (HV) using HV crates and modules produced by CAEN [60]. To limit the total amount of material inside the detector, one cable was used per PMT for both the incoming high voltage and for the outgoing event PMT signal. These cables terminate at a high voltage custom made splitter (passive filter) box, shown in figure 3.31, where the small (mV order) signal is decoupled from the input voltage. From the splitter boxes, the signal is sent to the front end electronics
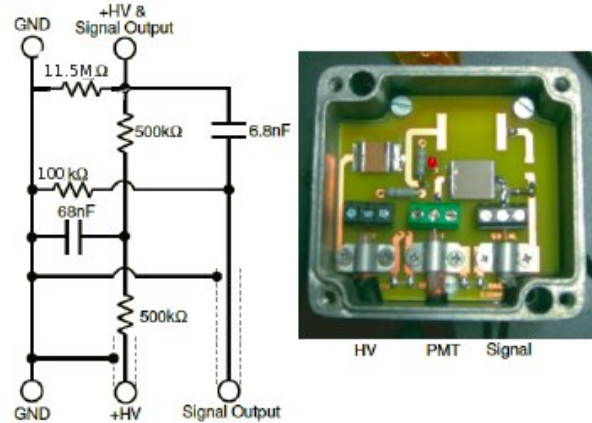


Figure 3.31: High voltage splitter used to separate the high voltage supplied to the PMTs from the outgoing signal. By using a splitter, only one cable per PMT is necessary which reduces the amount of extraneous material inside the detector, thus reducing backgrounds.

(FEE). Up to about 3 MeV of deposited energy, a single photoelectron (SPE) pulse is produced per channel, having pulses with an amplitude of about 5 mV after 40 m of cable and reaches the FEE. The FEE modules works as pulse shaping amplifier and also

provides stretcher signal to create a trigger. The sum of the stretcher signals are sent to a trigger system, which generates trigger NIM signals if the pulse amplitude exceeds the threshold, and provides them to all flash analogue-to-digital converter (FADC) modules. The FADC digitizes and records waveforms of the signals pulse. Both FADC and trigger modules are mounted on 5 VME crates. Four of the 5 crates have only the flash-ADC modules and the last crate has both the trigger modules and the FADCs. A CPU board, Motorola MVME3100, is mounted on each VME crate to read both digitized waveforms and trigger information via VME64 bus, passing to a readout computer though 10 Gbps Ethernet cables. An outline of this system is shown in figure 3.32.
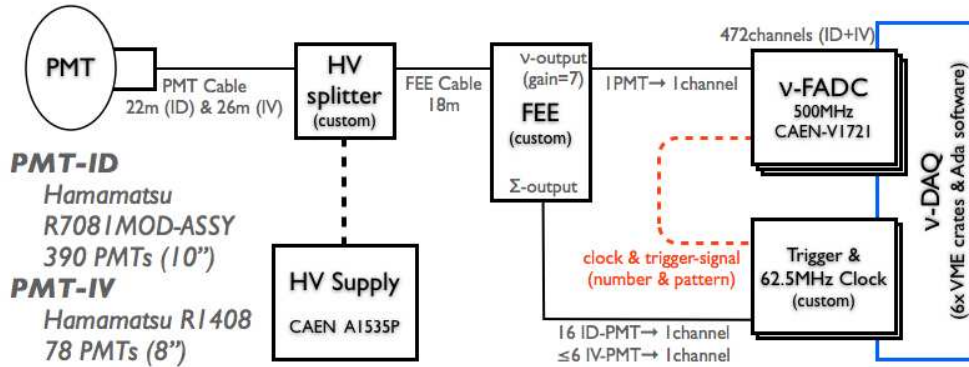


Figure 3.32: Diagram of the electronic readout system configuration for the Double Chooz detector.

### 3.4.6.1   High Voltage Supply

High voltage (HV) system [61], supplies the ID and IV PMTs with the necessary voltage. It is important in order to ensure stability of the PMT gain. The Double Chooz experiment adopted the HV crate model SY1527LC (figure 3.33), that posses a CPU and Ethernet connectors. Thus, the HV supply is controlled remotely via the



Figure 3.33: Pictures of a CAEN's HV module (A1535SP model, on the left) and crate (SY1527LC, on the right).

Internet. The crate integrates the HV modules (A1535SP), which supply a high voltage from 0 to 3.5 kV, each having 24 output channels. Two HV crates and 19 modules are operating at the Double Chooz far laboratory. Deviation on the HV are monitored with a precision of 0.1%, which affects about 0.8% of the PMT's gain deviation. The HV values are tuned to provide a PMT gain of about $10^7$. In addition, the HV system is controlled by a software made of three components that communicates with each other

via network: the HV crates, a control server and a Graphical User Interface (GUI). The control server is based on C++ and uses an API library, provided by CAEN, to control the HV crate. This library has several functionalities for network access of the crate via Transmission Control Protocol (TCP) sockets. The control server sets the HV values and maximum limits of the current, and monitors theses values, recording them into a MySQL [62] databases, which are use in the common online monitor system. The control server also connects to the common notification system so that it can send error and warning messages. The control GUI is written in Sun Java 5, which shows details of status of the HV crates and has functionalities to modify settings of the crates via the control server. This GUI is used in case of emergency shutdown or to test with different HV settings.

### 3.4.6.2  Front End Electronics

The Front End Electronics (FEE) combine signals from individual PMTs and stretch the summed signal for the analogue trigger. The hardware of the FEE module is contained in a standard NIM module. There are 8 analogue inputs and 16 outputs for waveform digitizers. Eight of the output channels are used for the $\nu$-DAQ and the remaining channels are saved for future upgrades. The main purpose of the FEE is to match the signals with the dynamic range of the FADCs. It also provides stretcher pulse output, which are summed and used to create a trigger. The tasks performed by the FEE can be divided in:

- **Noise rejection**: There are two types of noise sources between outputs of the PMTs and input connectors of the FEE modules. One is the 40 m PMT cable, which can pick up radiative noise. A 4.7 $\mu$F capacitor is inserted between the shielding on the cables and ground of the modules to short the noise greater than 6.7 kHz to ground. The other is common-mode noise and the first gain stage of the FEE, an instrumentation amplifier, is designed to remove this type of noise.

- **Baseline restoration**: The baseline of the output can drift after a large pulse, such as a muon. The baseline drift must be solved as soon as possible to suppress DAQ dead time. This issue is treated with two inverting operational amplifiers and an operational transconductance amplifier.

- **Amplification**: Pulse height of input signals range from 4 to 5 mV/p.e., which is too small for the FADCs and the trigger system so that the FEE amplifies the signals by a factor of 7.8. On the other hand, it attenuates higher energy signals such as those from muon events by a factor of 0.55.

- **Clipping**: For higher energy events that are too large for the amplifier, the FEE clips the voltage once it reaches 1.2 V, however the pulse shape is retained.

### 3.4.6.3  Trigger System

The trigger system generates triggers to make FADCs of the $\nu$-DAQ to read their buffers and also provides global timing clocks for both $\nu$- and OV-DAQ. It consists of two types of VME modules: one master board (left of figure 3.34) and three trigger boards (right of figure 3.34). Two triggers boards receive a sum of the stretched signal from the ID PMTs and one for the IV PMTs. Different trigger conditions are used for the ID trigger boards and the IV trigger boards. However, all three boards are connected to a single trigger master board which initiates a readout of all ID and IV PMTs whenever a trigger condition in any of the three boards is satisfied.
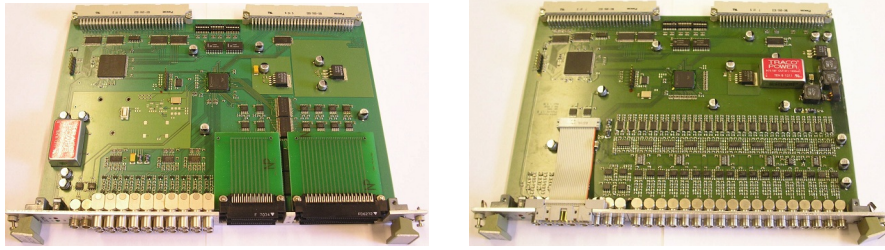
Figure 3.34: Picture of the trigger system boards: the master board on the left and the trigger board on the right.

Each ID trigger board is connected to half of the ID PMTs evenly distributed throughout the detector. The FEE sums the PMT pulses in 12 groups of 16 PMTs and one group of three PMTs for each ID trigger board. The total summed PMT signal as well as the summed PMT signal for each group is discriminated against different programmable thresholds. The neutrino threshold for the total summed PMT signal is set at a 400 keV. Another threshold for the total summed PMT signal is set at a 200 keV equivalent energy threshold and pre-scaled such that only 1/1000 of the triggers above this threshold are read out. This is done since the event rate below the neutrino threshold is too high to be handle individually.

The IV trigger board is connected to all 78 IV PMTs arranged in 5 groups of 3 to 6 PMTs. Because the main purpose of the IV is to tag cosmic muons, a threshold scan was performed of the summed PMT signal discriminator and a suitable threshold was chosen to be higher than 5 MeV. The IV trigger condition is satisfied when both the summed PMT signal and at least one PMT group sum is above this threshold (scaled to the number of PMTs).

Finally, trigger signals from the light injection calibration systems and clock triggers can be handled with the trigger system and records them as "external trigger". A diagram of the trigger system is shown in figure 3.35.
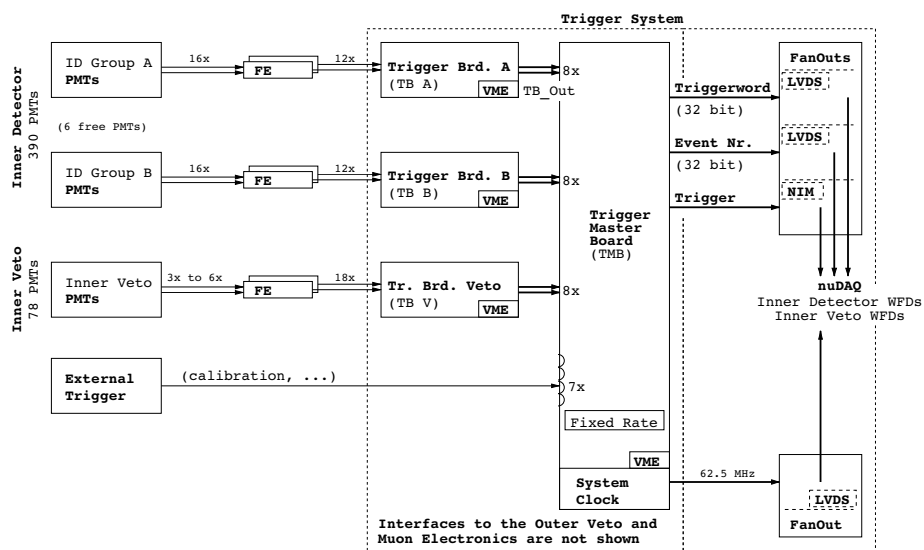


Figure 3.35: Diagram of the Double Chooz detector trigger system [63].

**Trigger Efficiency**

The trigger efficiency of the ID was measured by selecting a sample of events which passed the pre-scaled, low-energy threshold and counting how many of these events also passed the neutrino threshold. The definition of the efficiency is the ratio between the number of events with both pre-scaled and neutrino triggers, and the number of events with the pre-scaled trigger. Figure 3.36 shows the trigger efficiency as a function of

**Double Chooz Trigger Efficiency of Singles**
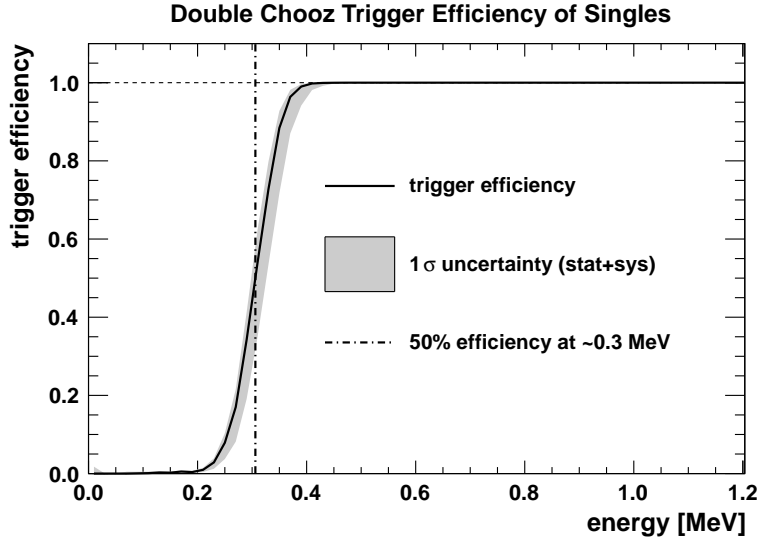


Figure 3.36: The trigger efficiency, in black, as a function of the reconstructed visible energy in the ID. The grey region represents the 1 $\sigma$ uncertainty.

reconstructed visible energy, where the efficiency is 50% at 400 keV and increases to 100% at 700 keV, which is used for the IBD prompt energy analysis threshold.

Complementary, a conservative estimate of the trigger inefficiency can be calculated. The trigger system has a 64 to 128 ns dead-time after each trigger. The inefficiency due to any trigger dead-time is given by $R \times T$, where $R$ is the the 120 Hz trigger rate and $T$ the dead-time is the known 64 to 128 ns trigger dead-time. The resulting inefficiency is found to be $0.15 \times 10^{-4}$. In fact the 256 ns flash-ADC readout window allows most of the triggers in this 64 to 128 ns window to be recovered and so the actually inefficiency is much smaller than this and can be neglected. As a cross check, dedicated tests were performed with the IDLI during commissioning to measure any trigger dead-time for for light levels similar to those of IBD candidate events. No trigger dead-time was observed.

### 3.4.6.4   Flash-ADCs

The waveform digitizer, neutrino FADC ($\nu$-FADC), receives signals that have been amplified previously by FEE. This system (V1721 model, with basic specifications summarized in table 3.5) was co-developed by CAEN [60] and the Double Chooz Collaboration, as the readout system for the ID and IV PMTs. The $\nu$-FADC consists of 60 modules (figure 3.37), each one with 8 analogue input channels with a dynamic range of 1000 mV and 8 bit resolution. Its sampling rate of 500 MHz gives a timing resolution of 2 ns, thus the data can be reprocessed offline and refined pulse shape discrimination (PSD) studies are also possible. Each channel has 2 MB memory split into rotating buffers, or pages, that works as a FIFO (first-in-first-out), where the number of pages is adjustable. In case of 1024 pages, each one can store 2048 samples for a total of 4 $\mu$s of digitized data.

Table 3.5: Basic specifications of the V1721 FADC.

| Property | Values |
| --- | --- |
| Number of Channels | 8 per module |
| Sampling Rate | 500 MHz |
| Time resolution | 2 ns |
| Number of Samples | 2048 per event |
| Resolution | 1 Vpp per 8 bit |
| Buffer size | 1024 events per ch |
| Buffer memory | 2 MB |
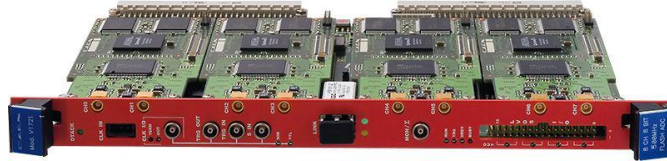


Figure 3.37: Picture of the CAEN FADC module V1721.

The $\nu$-FADC continuously writes data in the current page (indicated by the "write index"), until it receives a signal from the trigger system. On a first clock after the trigger detection (all $\nu$-FADCs receive a 62.5 MHz clock from the trigger), the last ADC sample is written into the current write index and the write index is incremented so the subsequent samples are written into the next page, while the first becomes available for read-out, as exemplified in figure 3.38. The earliest page that has not yet been read
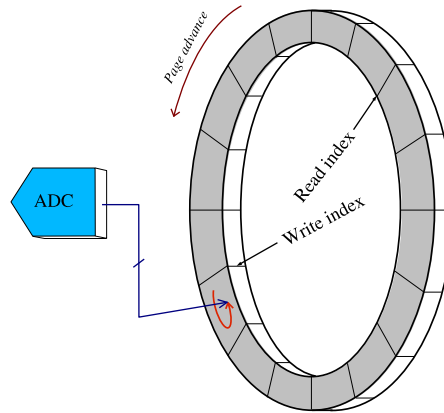


Figure 3.38: Operation of the Waveform Digitizer as a FIFO [64].

out through the VME bus is marked by the "read index". As long as the write index never catches up with the read index from the previous cycle, the system will have zero dead time. In case the write index is just below the read index, for example, the $\nu$-FADC writes to the $1024^{\text{th}}$ page and if the first page has not yet been read out, the trigger command is ignored, introducing a certain amount of dead-time. In addition, it is possible to read only a part of the page, and for the normal physics data taking, in order to suppress data size, only 128 samples around trigger timing (i.e. 256 ns of time window, that contains most of the released scintillation light) are transferred to the readout computer. The data read out from the $\nu$-FADC buffers into the VME crate controllers can optionally be processed by a software based data reducer that decides how much information to store. For the first period of data taking the data reducer is switched off. In addition to the pulses from the PMTs, the stretcher signals to the

trigger system and NIM signals of the external triggers (such as triggers of the light injection systems) are recorded as digitized waveform for offline data quality checks.

A muon flash-ADC ($\mu$-FADC), designed to receive higher energy and attenuated signals from from the FEE, is planned to be add in the near future.

### 3.4.6.5   $\nu$-DAQ Software

To read and store the data from the $\nu$-FADC, the Double Chooz experiment makes use of six Read Out Processor (ROP) and Event Building Processor (EBP). The 256 ns read from the FADCs is saved as binary file and converted to ROOT format [65]. Only after that the data is transferred to off site computers. A diagram of the readout software is depicted in figure 3.39. Both the on-board CPUs and the readout machine works with a
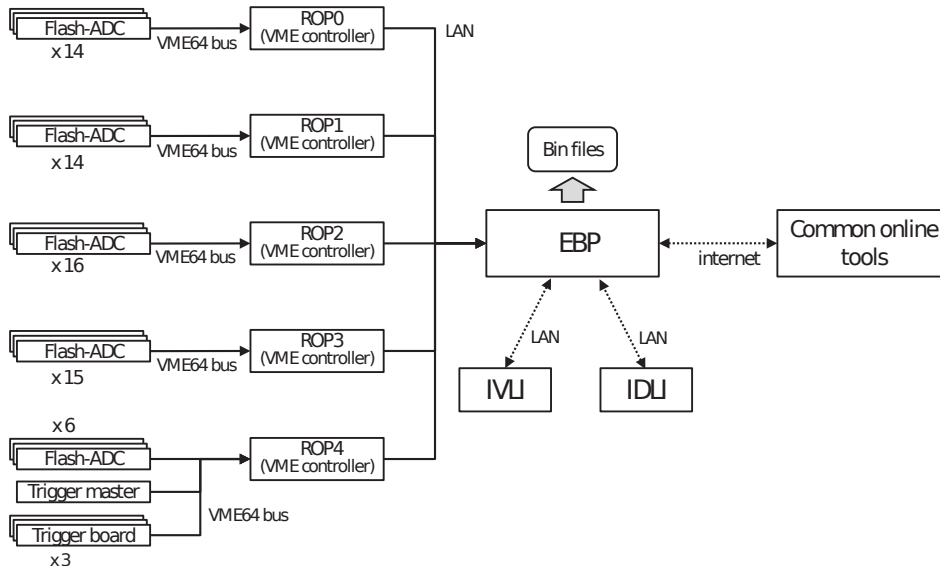


Figure 3.39: The $\nu$-DAQ diagram.   Each box represents the hardware or software components of the system, while the solid arrows indicate the direction of the data stream. The dashed arrows show the paths of control messages [66].

Linux Operational System (OS) Debian (version Lenny 5.0) distribution [67]. The ROP runs on the on-board CPU, which manages the VME modules mounted on the same crate. On the other hand, the EBP, which is running on the readout machine, manages the ROP and the interface with others online systems. Both processors are implemented with Ada object oriented programming language [68]. Five ROP works in parallel and communicates with the EBP via TCP/IP connections. The $\nu$-DAQ is controlled and monitored via the Double Chooz common online systems. Basically, the ROP works as a bridge between VME bus and Ethernet connections. Each processor handles about 15 FADC modules so that the data size per processor is about 17 kB per event. Since the EBP has connections to both the ROP and the common online systems, its main task is to merge the information, including digitized waveforms, from the ROP, and to write down the information into binary files on the disk. The processor also provides several command messages such as run start / stop and run configuration to the ROPs in order to control the status of data taking. The $\nu$-DAQ is controlled by the common run control system. Monitoring of the $\nu$-DAQ is also done with the common online data monitor systems and the common notification system. In addition, the EBP also communicates with a calibration interface process to send configurations to the two light injection calibration systems.

### 3.4.6.6   Outer Veto DAQ

The data acquisition system for the OV has been developed on USB-based readout system. Each multi-anode PMT (MAPMT) of the plastic scintillator plane is connected to a readout module in the same way as the OPERA experiment, based on Macro2 [69], which reads 64 analogue signals from the MAPMT to convert them into digitized charge and hit time. The front end boards are connected via CAT-5 cables in up to 6 different daisy-chains, which are read out via USB data streams and the data is stored into different files from chain to chain. The binary files are passed to an event builder which merges the data, and finally, the OV data is combined with data from the $\nu$-DAQ by the offline event processing. The whole OV DAQ system is also controlled and monitored via the common online systems.

### 3.4.6.7   Event Processing

The Double Chooz event processing has two steps, as shown if figure 3.40. The first step
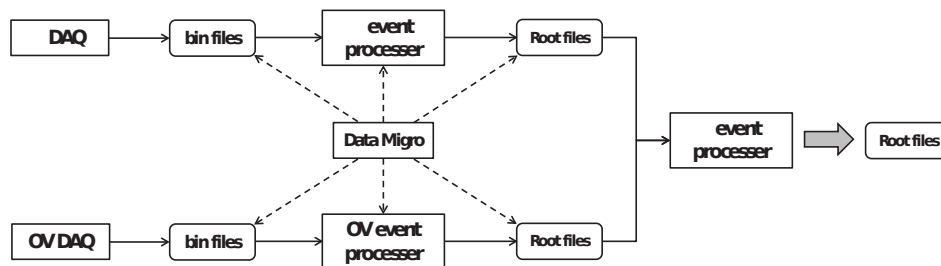


Figure 3.40: Flowchart of the Double Chooz event processing. The solid lines represent the direction of the data stream, while the dashed lines indicates the paths of control messages [66].

is performed on computers at the experimental site and the second one is carried out on computer clusters of IN2P3 [70] at Lyon after the data transfer. All operations of event processing and data transfers are managed by a daemon software named "DataMigro" [71], written in Python programming language. Firstly, the binary files are converted into ROOT files. During this process, a basic analyses, for data quality check with digitized waveforms, is also performed. This analysis results are summarized on a web page to be used for data quality checks. The binary and ROOT files are transferred to the computer cluster based in Lyon, which uses iRODS [72]. Finally, after transferring the data, several higher level analyses, such as vertex reconstruction and energy calibration, are performed and both data files (from $\nu$-DAQ and OV-DAQ) are combined. All files are stored into the High Performance Storage Systems (HPSS) [73], also at Lyon.

### 3.4.6.8   Common On Line System

The Double Chooz experiment online systems are interfaces between the online components and the person in charge of the data taking and are distributed in the local area network (LAN). Since the far detector is placed inside the Chooz nuclear power plant, access to it is limited. Therefore, four types of common software tools was developed in order to help access to the DAQ systems via the Internet: run control, online data monitor, notification monitor, and process control. Figure 3.41 shows overview of the online systems in the Double Chooz experiment from viewpoint of the network. The online systems in the experimental site consist of four computer systems: $\nu$-DAQ, OV-DAQ, file storage, and a machine for common tools. Almost all
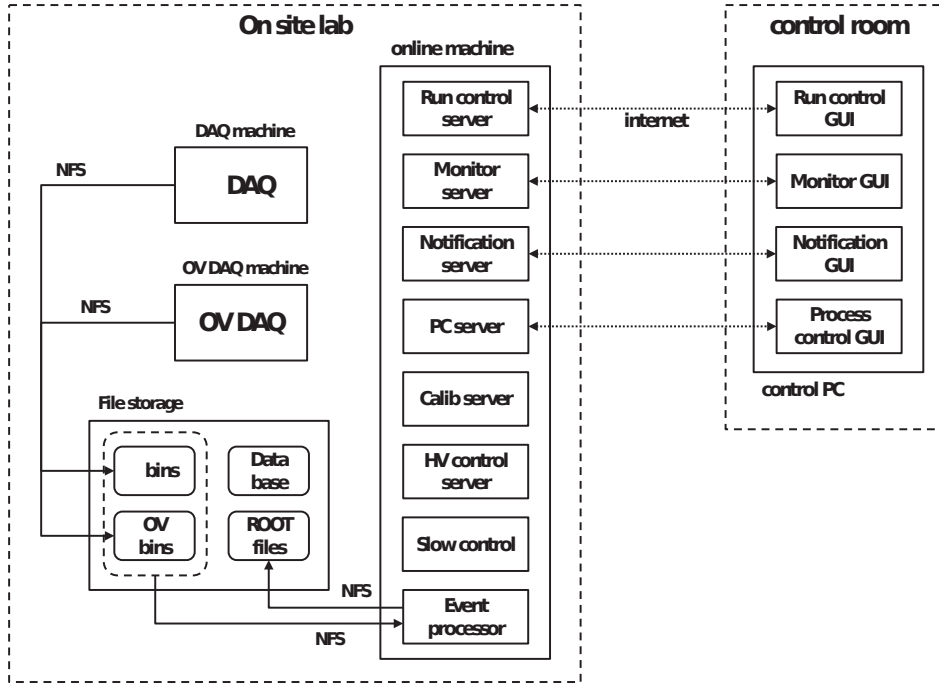
Figure 3.41: Flowchart of the Double Chooz online systems. The solid lined boxes indicate the online components working on the on-site computers. The solid arrows represents the paths of data stream, while the dashed lines represents paths of command and state messages. The dashed lined boxes show the experimental site and control room, each other connected via Internet [66].

online components are collaboratively working on the experimental site, connected with the control room via the Internet, using the common tools. Graphical user interfaces (GUIs) of the common tools display status of the online components and transfers several operation commands to the components. Server processes of the common tools are designed to work on Linux OS and these implementations are based on C++ programming language. On the other hand, the GUIs are written in Java 5 [74] (also available with Java 6) since the they are assumed to be operated remotely with several different environments such as Windows, Max OS and Linux. Detailed information about each common tool can be found in [66].

## 3.5    Backgrounds

In a experiment like the Double Chooz, which main purpose is to study the disappearance of electron antineutrinos, it is of vital importance to understand and estimate all the possible background sources that would mimic a true IBD signal. If not understood well, the background will be interpreted as a neutrino interaction signal, and a disappearance probability smaller than the real value is measured. In the following subsections a general description of each background source is given, while the details of their estimation is described in section 4.7. As schematic representation of the main three background source is presented in figure 3.42.

### 3.5.1    Accidentals

Accidental background are random uncorrelated triggers that can pass all the neutrino selection cuts, mimicking a delayed coincidence. One example of accidental background

(a) Accidental                (b) Correlated                (c) Cosmogenic
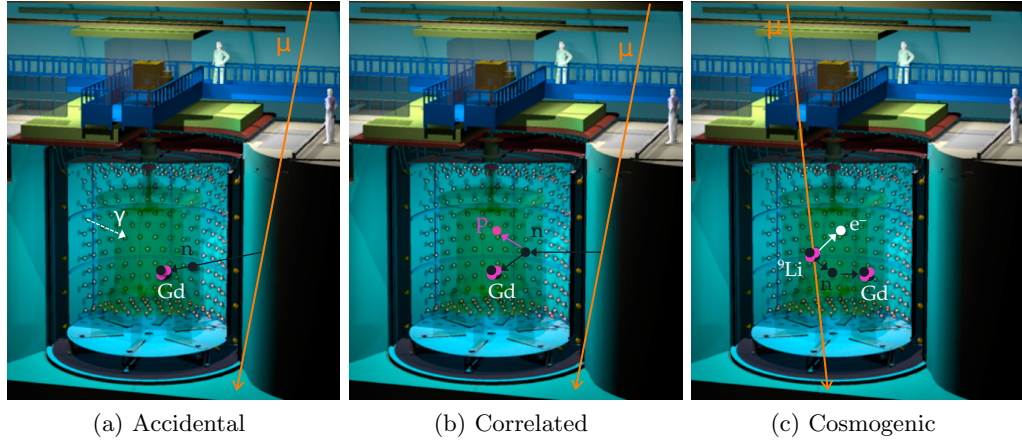
Figure 3.42: Schematic representation of the three main background sources, that can mimic an IBD event.

is shown if figure 3.42a. An environmental gamma radiation with a energy similar to a IBD positron, and a environmental neutron that is capture by Gadolinium or Hydrogen. If both events occurs within the time window of the IBD selection cut, it will be tagged as a true neutrino signal. All parts used to build up the Double Chooz detectors were chosen based on the criteria of reducing as much as possible the natural radioactive emissions, in order to reduce the accidentals coincidences.

### 3.5.2   Correlated

Correlated background are muons that decays in the target volume or spallation neutrons produced by muon interaction with the rocks surrounding the detector. These neutrons can enter the detector and collide with a proton. After the collision, there is a probability of the neutron being absorbed in the delayed coincidence time window, faking a true neutrino signal, as shown in figure 3.42b. Moreover, a low energy muon can deposit all its energy until it stops inside the detector and decay, producing a Michel electrons. Since this electrons have a energy spectrum ranging from 0.511 MeV up to 52.8 MeV, it can produce an neutrino like event, also because of the muon has a short life time of 2.197 $\mu$ [33].

### 3.5.3   Cosmogenic

Cosmogenic background is referred to radioactive elements produced inside the detector by cosmic muon interactions. High energetic muons crossing the detector volume can interact with the liquid scintillator's $^{12}$C via spallation processes, creating $^{8}$He or $^{9}$Li. These elements are beta and neutron emitters, and their decay, as shown in equations 3.10 and 3.9, will produce a delayed coincidence-like signal.

$$^{8}\text{He} \; \rightarrow \; ^{7}\text{Li} + e^{-} + n \; [16\%, \tau = 119 \text{ ms}, \; Q = 8.618 \text{ MeV}] \tag{3.9}$$

$$^{9}\text{Li} \; \rightarrow \; 2 \; ^{4}\text{He} + e^{-} + n \; [50.8\%, \tau = 178 \text{ ms}, \; Q = 11.941 \text{ MeV}] \tag{3.10}$$
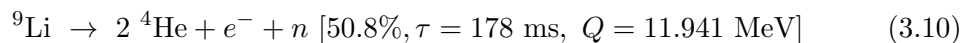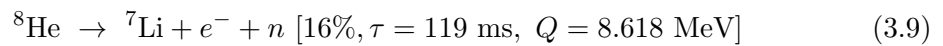
On figure 3.42c a schematic view of the cosmogenic background is presented. Since many of the background events in IBD detection originate from cosmic ray muons, the detectors are placed underground to suppress as much as possible the muon flux, i.e., the rock above the detector shields it against a large fraction of the muons and other cosmic ray showers.

### 3.5.4   Light Noise

During the far detector commissioning period an unexpected high trigger rate was observed. Investigation with the detector showed that this rate was directly related to some PMTs with HV applied or not. Off-site measurements were performed with spares PMTs and it showed the same behaviour and it was found that the source of this extra noise was coming from electrical discharges between electrodes of the cathode and the first-anode, where the potential difference is highest, on the PC board of the PMT base circuit, that sporadically flashes light. This problem was also reported by Super-K, Daya Bay and RENO experiments, and hereafter it is referred as Light Noise, or simply LN events.

After examining a separated base during operation with a thermographic camera, the observed temperatures were not high enough to characterize the light emission as thermal emission. Others Off-site measurements also showed that the LN has a strong HV dependence on rate and pulse amplitude, a temperature dependence, and it is unstable through time. In addition, these measurements also established that the time scale associated with light noise events were generally longer than the time scale associated with PMT pulses from real particle detection. Since these events have different signature from the events that excite the scintillator, it is possible their identification. Moreover, the LN does not effect on the PMT electronic signal.

However, a test with a PMT base with capacitors and resistors not covered by the epoxy showed that it is not possible to induce the light emission with values of temperature and voltage much bigger than the operative conditions, what is an indication that the PMT epoxy plays an important role on the LN mechanism. When a small piece of epoxy was place between the two pins of a resistor and HV was applied a clear bright spot was evidenced. In a cracked epoxy, the light production was also observed, and interpreted as corona discharges. Dielectric properties of the epoxy used for sealing the PMTs bases, can explain the light emission process, in which photons can be produced by the glowing of trapped gas, during the mixing of the components.

In the scope of the Double Chooz detector, due to large solid angle, a significant amount of the light which is generated by a PMT base reflects off the buffer vessel surface as well as the inner wall of its own mu-metal shield and reaches its own photocathode, as represented by figure 3.43. Consequently, the majority of the light is seen by the
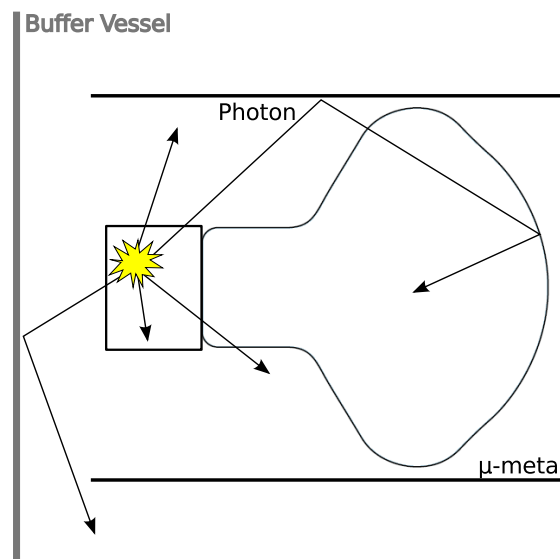


Figure 3.43: Scheme of LN event produced by a Double Chooz Far Detector PMT.

PMT which produces it. This reflection effect was confirmed in lab tests and also by MC simulations. The LN visible energy extends from hundreds of keV to several tens of MeV, and the trigger rate contribution in the beginning of the data taking was of 20 Hz. Thus, a proper handle of this events is necessary, and it is further discussed in section 4.4.1.

## 3.6   Double Chooz Software

The Double Chooz software suite is called DOGS (Double Chooz Online Group Software) and consists of a collection of software designed for storing, simulating, and analysing data for the experiment. The schema for the software stack is shown in figure 3.44. Each stage in the figure covers the aspect of the detector to be understand through
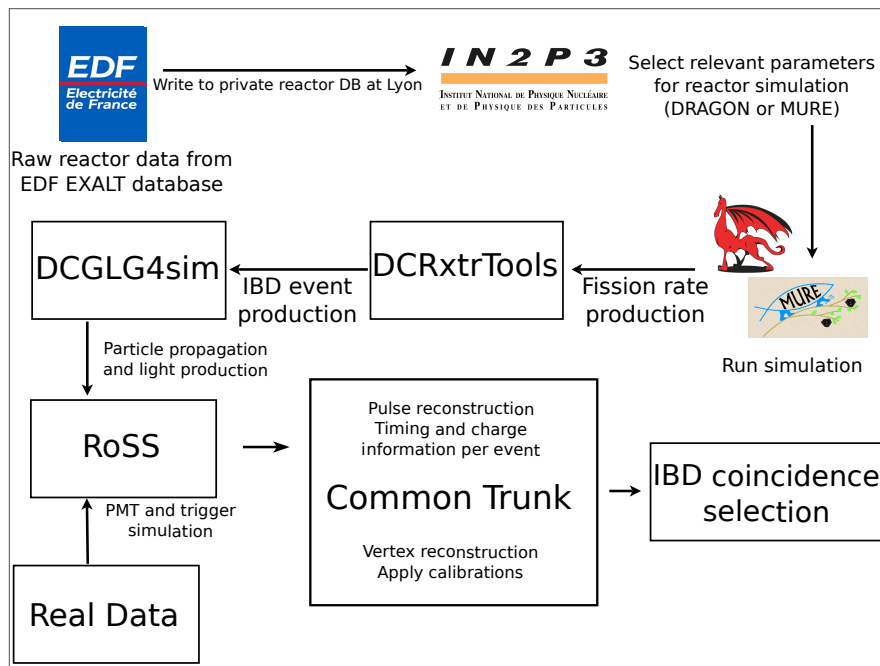


Figure 3.44: The Double Chooz software components.

simulations:

- **Raw Reactor Data**: EDF reports over 3000 variables for each reactor and stores them in a private database called EXALT. As the database is updated, authorized members of the Double Chooz Reactor Group can perform a retrieval. EXALT stores information on Excel spreadsheets. These are transformed into MySQL databases, and several quality checks are performed to ensure continuity of the data. Then the contents are stored on a private IN2P3 collaboration database, which contains data at a granularity of one minute and includes information such as the thermal power, the boron concentration, and the positions of the control rods in the reactor.

- **Reactor Simulations**: Double Chooz collaboration uses two reactor codes for simulations: DRAGON [75] and MURE [76]. MURE, a reactor evolution code based on Monte Carlo N-Particle Transport Code (MCNP), provides the reactor fission rates as a function of time. These fission rates are crucial ingredients to compute the antineutrino flux without oscillation. DRAGON, a deterministic

lattice code, computes assembly-level fission rates much more quickly than MURE and is used as a cross-check to the MURE simulations.

- **IBD Event Generation**: The DCRxtrTools package, reads the fission rate information from the private collaboration database and generates IBD neutron-positron pairs, including their energies, momenta, and positions. It provides a connection between the reactor simulations and the detector database.

- **Scintillation Light Simulation**: This is carried out by the DCGLG4sim package, which adapts the GLG4sim package [77]. GLG4sim, or "Generic Liquid-scintillator Anti-Neutrino Detector (GenericLAND) Geant4 simulation", was derived from the KamLAND experiment. The package takes IBD candidate events and simulates the light production in the liquid scintillator. The output consists of photoelectrons produced by PMTs.

- **Readout Simulation**: The RoSS (Read-out Simulation Software) package simulates the PMTs output, and creates FADC and trigger output in the same format as real data.

- **Event Reconstruction and Calibration**: The Common Trunk contains several modules that perform pulse reconstruction and calibration, event reconstruction, and quality control.

## 3.7   Double Chooz Current Status

The Double Chooz collaboration decide to make a two phase experiment, first using only the the far detector and later using both near and far detectors, because the use of the Chooz experiment laboratory for the Double Chooz far detector reduces civil construction time and costs. This allowed a single-detector measurement of $\theta_{13}$ while the near detector is being constructed. Once the near detector is operational, the far detector will have already accrued significantly more data than if it were simultaneously started with the near detector, improving the initial near-far measurements.

The far only analysis gave many results so far, being the first experiment, among the three current ones, to:

- Retrieve a positive signal of neutrino disappearance, presented in November 9th, 2011 at LowNu11 conference, which was later published on [29];

- Perform a spectral analysis [30];

- Give a consistent result of $\theta_{13}$ based on neutron capture on Hydrogen [78];

- Make a precise measurement of background, using periods when both Chooz reactors were not operational [79];

- Study a Lorentz violation possibility with reactor neutrinos [80].

By the time of this dissertation writing, the near detector laboratory hall excavation and laboratory construction were finished. Some cabling and the inner veto installation were about to start. The data taking with the near detector is expected in less than a year.

# Chapter 4

# Double Chooz Data

> Oh, there's my missing neutrino.
>
> *Sheldon Cooper*

The Double Chooz experiment started to take data with its far detector only, in $13^{\text{th}}$ of April of 2011. The period used in this dissertation, is the same as used in [30, 78], spanning since the first day of data taking until $30^{\text{th}}$ of March of 2012, which corresponds to 333 days of data taking. Figure 4.1 shows a data taking summary of this period. This
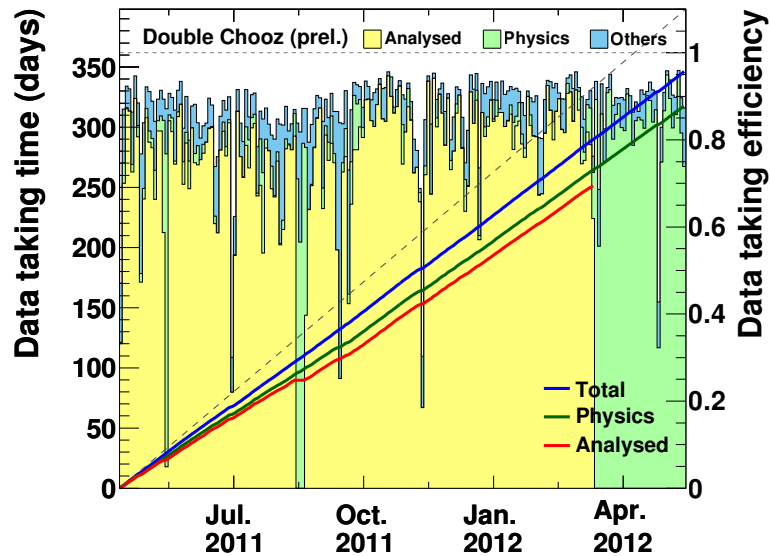


Figure 4.1: Summary of the data taking over the considered period for analysis. Besides the physics runs for neutrino data, calibration and test run were also taken.

chapter is dedicated to the analysis of these data, concerning the estimation of neutrino events, the event information reconstruction method, the neutrino event selection and the background estimation and measurements.

## 4.1 Event Prediction

When a neutrino detector is placed in the vicinity of a nuclear reactor, the expected flux is

$$N_\nu^{\text{exp.}}(s^{-1}) = \frac{1}{4\pi L^2} N_p \epsilon \frac{P_{th}}{\langle E_f \rangle} \langle \sigma_f \rangle \tag{4.1}$$

63

where $N_p$ is the number of targets, $\epsilon$ the detector efficiency, $L$ the detector-reactor distance (baseline), $P_{th}$ the thermal power, $\langle E_f \rangle$ the mean energy release per fission, and $\langle \sigma_f \rangle$ the mean cross-section per fission. The first three terms depend on the detector and are constant. On the other hand, the last three terms depend on the reactor operation. Here the thermal power and isotopic composition of the core are instantaneous values, or mean values of the considered period of time.

Since the Double Chooz experiment currently consists of one detector and two reactors, equation 4.1 must be changed to a more general form, as:

$$N_\nu^{\text{exp.}}(s^{-1}) = \frac{1}{4\pi} N_p \epsilon \sum_{R1,R2} \frac{1}{L_R^2} \frac{P_{th}^R}{\langle E_f \rangle_R} \langle \sigma_f \rangle_R \qquad (4.2)$$

where the index $R$ refers to the two Chooz B reactors.

**Reactor Thermal Power**

The instantaneous thermal power of each reactor core is provided by EDF and is evaluated over time steps of one minute. This information and other important variable for the reactor core modelling are downloaded every two weeks and stored in a database. The instantaneous thermal power is derived from in-core instrumentations measuring the temperature of the water in the primary cooling loop. The thermal power in-core measurement is cross-checked and calibrated though heat balance in the secondary cooling loop. Since the accuracy of the thermal power measurement determines the maximum power at which the reactor can operate, EDF has performed a detailed study of the uncertainty in this measurement [94], resulting in the maximum thermal power of $P_{\text{th}} = 4250.0 \pm 12.2$ MW (0.4% at 95% CL). The thermal power for both Chooz reactors is shown in figure 4.2 as a function of the day since the FD data taking has started. During the data taking period, both Chooz B reactors were at their fuel cycle 12, and
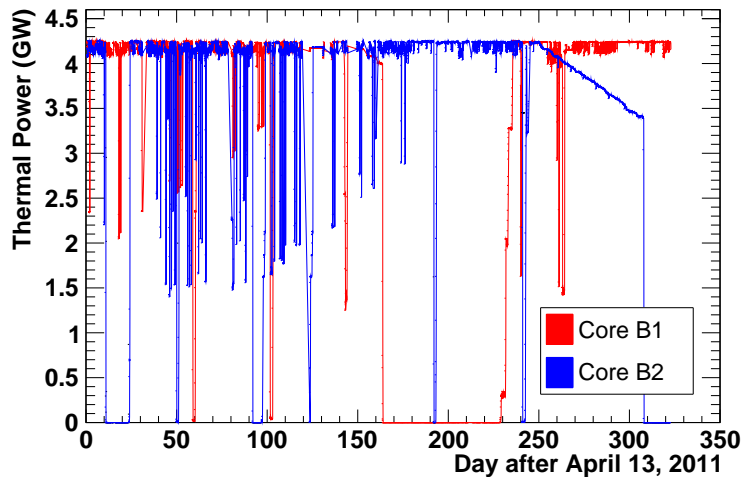


Figure 4.2: Thermal power history for both Chooz B reactors, measure by EdF, since the start of data taking with the far detector. Periods with only one reactor in operation are also present. Reactor B1 stopped for two months in order to renew its fuel. Reactor B2 stopped for the same reason almost one month before the end of data set. During the refuelling of B1, B2 stopped for one day for programmed tests, when background measurements were performed.

the B1 reactor had fuel exchanged and started its cycle 13. The cycles start and stop time were:

- **Core B1**: Cycle 12 → 26th of August of 2010 — 24th of September of 2011;

- **Core B1**: Cycle 13 → 27th of November of 2011 — Operational until the end of data set;

- **Core B2**: Cycle 12 → 15th of November of 2010 — 15th of February of 2012

**Mean Cross-Section per Fission**

The mean cross-section per fission is the averaged cross-section over the $\bar{\nu}_e$ spectra from each fissile isotope, defined as

$$\langle \sigma_f \rangle_R = \sum_k \alpha_k^R \langle \sigma_f \rangle_k^R = \sum \alpha_k^R \int_0^\infty S_k(E)\sigma_{\mathrm{IBD}}(E)dE \tag{4.3}$$

with $\alpha_k$ the fraction of fission rate of the $k^{\mathrm{th}}$ fissile isotope, $S_k(E)$ the referece antineutrino spectrum of the $k^{th}$ isotope and $\sigma_{\mathrm{IBD}}(E)$ the interaction cross-section.

The $\bar{\nu}_e$ spectrum of each fissile isotope and the IBD interaction cross-section are given in section 3.1 and 3.2 respectively.

**Energy per Fission**

The associated mean energy per fission is given by

$$\langle E_f \rangle_R = \sum_k \alpha_k^R \langle E_f \rangle_k, \tag{4.4}$$

and the values for $\langle E_f \rangle_k$ can be found in table 4.1.

Table 4.1: Mean thermal energy released per fission for each fissile isotope [81]

| Isotope | $\langle E_f \rangle_k$ [MeV/fission] |
|---|---|
| $^{235}$U | $201.92 \pm 0.46$ |
| $^{239}$Pu | $209.99 \pm 0.60$ |
| $^{238}$U | $205.52 \pm 0.96$ |
| $^{241}$Pu | $213.60 \pm 0.65$ |

**Fission Rates**

The fission rates $(f_k^R)$ evolve in time depending on the reactors thermal power and the evolution of the fuel assemblies. The thermal power for a given fission is relatively insensitive to the specific fuel composition since the mean energy released per fission differs by less than 6% among the different isotopes. However the detected number of $\bar{\nu}_e$ directly depends from the different spectra of the isotopes and their time-dependent rate of fission.

The $f_k^R$ are heavily dependent upon the amount of each fuel isotope within the reactor's instantaneous fuel inventory, as well as the instantaneous thermal power of the reactor. Two complementary simulation codes have been used to model the reactor cores evolution, MNCP Utilities for Reactor Evolution - MURE [76] and DRAGON [75]. MURE is a Monte Carlo code which use a statistical approach to solve the neutron transport equation in a 3-dimensional reactor core. DRAGON uses a deterministic approach to solve, with some approximations, the neutron transport equation in a 2-dimensional core. Example results from the MURE calculations can be seen in figure 4.3.

(a) Reactor B1                                    (b) Reactor B2
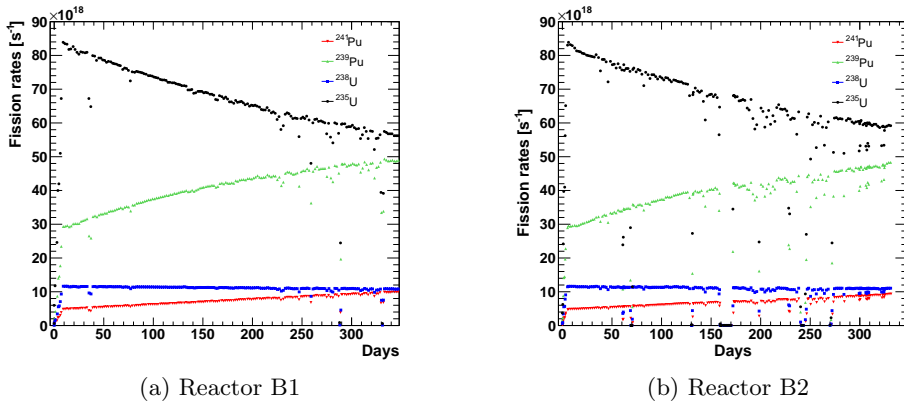
Figure 4.3: Fission rates for the Chooz reactors, as calculated by simulations with MURE, for each of the four main fuel nuclides [82]. The lack of smooth evolution in time is due to fluctuations of the thermal power in each reactor. Note the decrease of $^{235}$U due to burn-up over time, and the increase of $^{239}$Pu and $^{241}$Pu as those isotopes are bred from fertile fuel.

The performance of the codes are compared against each other [83] and the validation against data was carried out by comparisons of simulation results to destructive fuel assay data from a cycle of the Japanese Takahama-3 reactor [84], and to the results of simulations using the same data by other code packages.

In practice, the MURE simulation calculates the fission rates at 48 hours steps in the reactor fuel cycle based on data acquired from the reactor management company - EdF. The data includes reactor operating parameters such as the thermal power, concentration of boron in the moderator water, and control rod positions within the core. In addition, for each fuel cycle, EdF provides initial burn-up of the assemblies. The simulation uses these parameters to determine the mass inventory of each fuel nuclide at the beginning of each time step. With the mass inventory known, the number of fissions of each nuclide is determined using the mean energy per fission $\langle E_f \rangle_k$ from each nuclide $k$ and its subsequent daughters.

The fractional fission rate of each fissile isotope is defined as

$$\alpha_k^R = \frac{f_k^R}{\sum_{k=1}^4 f_k^R} \tag{4.5}$$

where the index $k$ runs over the four principle fissile isotopes: $^{235}$U, $^{238}$U, $^{239}$Pu, and $^{241}$Pu. Plots of these quantities are shown in figure 4.4 for all three reactor fuel cycles considered in the Double Chooz analyses and the averaged values are summarised in table 4.2.

Table 4.2: Mean value of the fission rate fraction of each main fissile isotope

| Isotope | $\langle \alpha_k \rangle$ |
|---|---|
| $^{235}$U | $0.469 \pm 0.016$ |
| $^{239}$Pu | $0.351 \pm 0.013$ |
| $^{238}$U | $0.087 \pm 0.006$ |
| $^{241}$Pu | $0.066 \pm 0.007$ |

In figure 4.5 the time evolution of $\alpha_k$ is presented with the error bars, for a single fuel cycle. The systematic uncertainty on the fission rates are obtained by varying
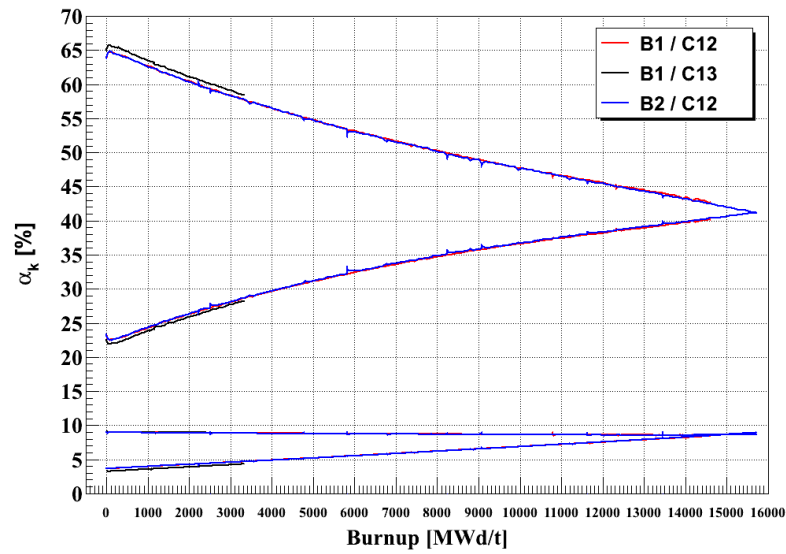
Figure 4.4: Fractional fission rates as a function of the fuel burn-up as calculated by simulations of the Chooz reactors using
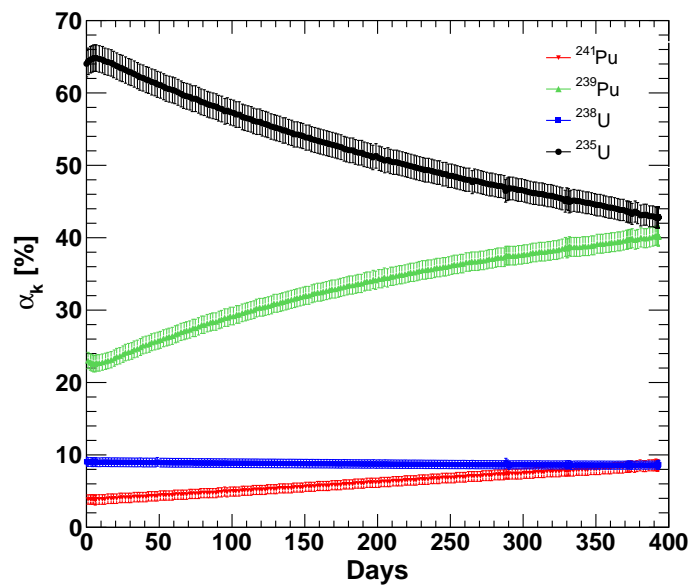


Figure 4.5: Fission rates for each of the main fuel isotopes of the Chooz B1 reactor as a function of days since the start until the end of cycle 12.
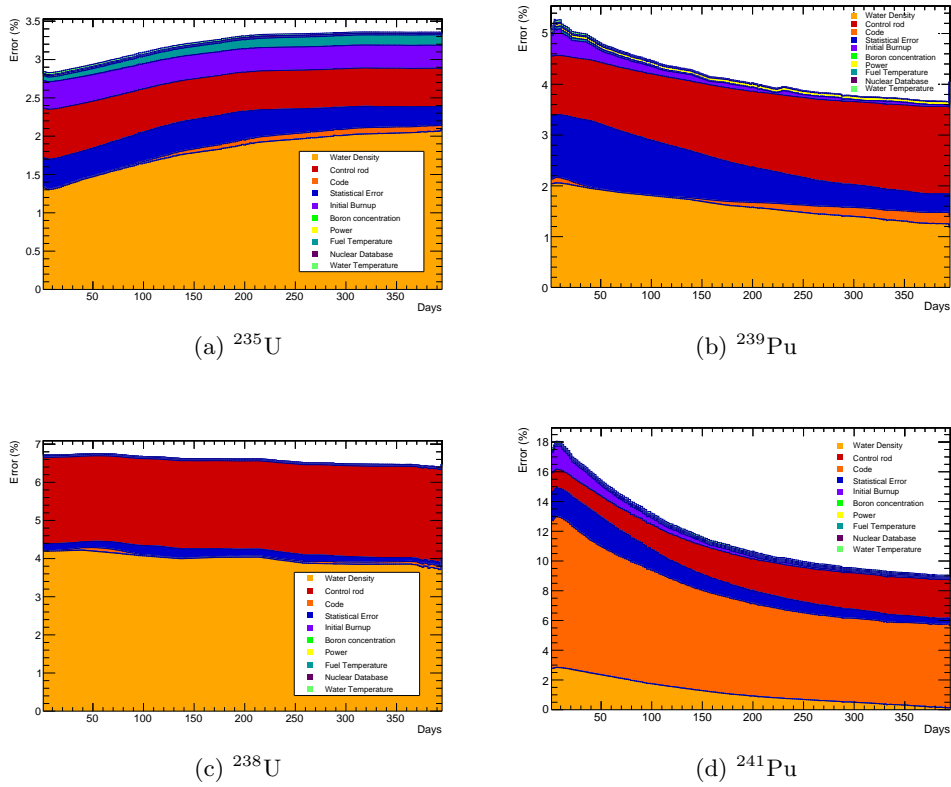
Figure 4.6: The fission rate error budget for each of the main fuel fissile isotopes as a function of days since the start of the reactor B1 cycle 12.

different input parameters of the simulation, such as the thermal power, the boron concentration, the water and fuel temperatures, the mean energy released per fission and the geometrical parameters of the cores. The maximum discrepancies observed comparing the two different simulation code are also included in the fission rate systematic error. The breakdown of uncertainties for each fissile isotope is shown in figure 4.6.

**Bugey4 Normalization**

Even with recent recalculation, the neutrino reference spectrum carries an uncertainty on their normalization of about 2.5%. Measurement of the total corss-section per fission from a nuclear reactor have been made to better degrees of precision. In particular, the Bugey4 experiment measures $\langle \sigma_f^{\text{Bugey}} \rangle = (5.752 \pm 0.081) \times 10^{-43}$ cm$^2$ / fission 15 m far from a PWR with a nominal fractional fuel composition namely $^{235}$U : $^{238}$U : $^{239}$Pu : $^{241}$Pu = 0.538 : 0.078 : 0.328 : 0.056 [85]. This measurement provides a better constraint on the expected flux from an identical reactor. The measurement can be used as an "anchor point" to constrain fluxes from other reactors by redefining $\langle \sigma_f^{\text{R}} \rangle$ in equation 4.2 to account for differences in the fuel composition with respect to that of the Bugey4 reactor ($\alpha_k^{\text{Bugey}}$). Thus,

$$\langle \sigma_f^{\text{DC}} \rangle = \langle \sigma_f^{\text{Bugey}} \rangle + \sum_k \left( \alpha_k^{\text{DC}} - \alpha_k^{\text{Bugey}} \right) \langle \sigma_f \rangle_k. \tag{4.6}$$

Since the correction term is small $(0.9 \pm 1.3)\%$, the uncertainties on the reference spectra are suppressed and the dominant uncertainty comes from the Bugey4 measurement, of

about 1.4%. Using the Bugey4 measurement as anchor point, the overall contribution of the reactor related systematics decreases from 2.7% to 1.7%. The breakdown of the different contribution to the prediction of the reactor $\bar{\nu}_e$ rate uncertainty is shown in figure 4.7.
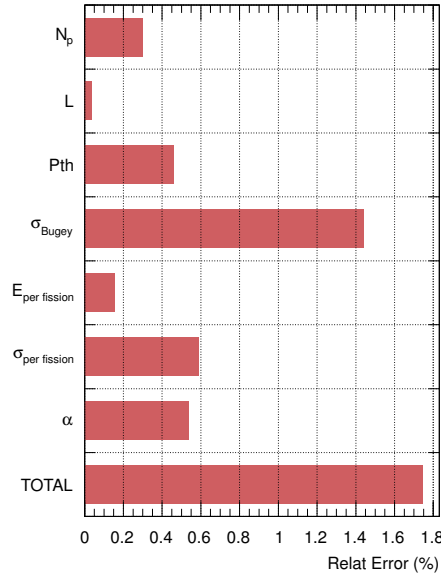


Figure 4.7: Breakdown of uncertainties on reactor $\bar{\nu}_e$ rate prediction from equation 4.2. The main contribution to the total uncertainty comes from the normalisation of the mean cross section per fission to the Bugey4 measurement, of about 1.4%. Nevertheless, the use of the Bugey4 measurement as anchor point reduces the overall systematics from 2.7% to 1.7%.

### 4.1.1 IBD Event Generation

Knowing all the variables that are input for equation 4.2, one can calculate the expectation rate of interactions in the detector, as showed if figure 4.8. Once the total expected rate of $\bar{\nu}_e$ events is known, the production of the IBD interaction events as inputs for the detector simulation is performed by the generation of random numbers. The first step is to draw an integer number of events to generate. This is done using the know expected rate as an argument for a Poisson distribution, that will be used as a probability function to draw a random number of events. Then, for each event, the following steps are carry out:

1. Select one of the fuel isotopes randomly, weighting the mean fission rates of the isotopes;

2. Generate a neutrino energy using the selected isotope cross-section weighted spectrum $\langle \sigma_f \rangle_k$;

3. Obtain a $\bar{\nu}_e$ interaction point inside the reactor cores with random 3-dimensional distribution;

4. Obtain a vertex of the IBD interaction randomly generated inside the detector, with weighting by the proton densities of the detector materials;
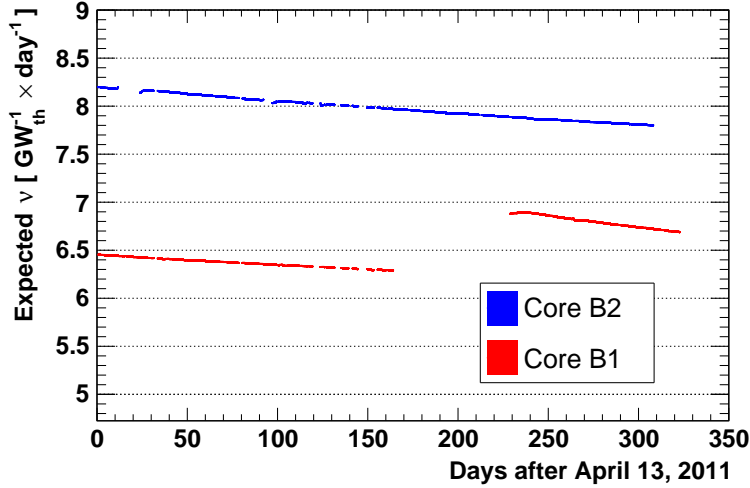
Figure 4.8:  Daily mean expected neutrino rate as calculated by equation 4.2 and normalized for reactor power, for each Chooz B reactor, versus calendar date. Burn-up effect is clearly notice on this plot.

5. Using the $\bar{\nu}_e$ energy and the vector connecting the creation and interaction points, the kinematic quantities of the resulting neutron and positron are calculated.

The neutron and the positron are used as inputs for an event of the detector simulation.

### 4.1.2   Systematic Uncertainties from $\bar{\nu}_e$ Prediction

The predicted $\bar{\nu}_e$ rate, describe by equation 4.2, can be divide in energy ranges between $E_i$ and $E_i + \Delta E_i$ in the following way

$$N_i^R = \frac{N_p \epsilon}{4\pi L_R^2} \frac{P_{th}^R}{\sum_k \alpha_k^R \langle E_f \rangle_k} \sum_k \alpha_k^R \langle \sigma_f \rangle_k^i, \qquad (4.7)$$

where

$$\langle \sigma_f \rangle_k^i = \int_{E_i}^{E_i + \Delta E_i} S_k(E) \sigma_{IBD}(E) \mathrm{dE}. \qquad (4.8)$$

The uncertainty of all the variables that constitute equation 4.7, contribute to the uncertainty in the prediction of the $\bar{\nu}_e$ spectrum. Since these variables are independent of each other, they are assumed to be uncorrelated. These uncertainties are propagated using a covariance matrix $M_{ij}$ relating the predictions in energy bins $i$ and $j$.

The matrix $M_{ij}$ representing the total systematic uncertainty on the signal prediction can be built as a sum of the uncorrelated components $M_{ij}^A$, from different uncertainty contributors $A$, as follows

$$M_{ij}^{\text{total}} = M_{ij}^{\epsilon} + M_{ij}^{L} + M_{ij}^{N_p} + M_{ij}^{P_{\text{th}}} + M_{ij}^{\langle E_f \rangle} + M_{ij}^{\langle \sigma_f \rangle} + M_{ij}^{\alpha_k}. \qquad (4.9)$$

Each independent matrix $M_{ij}^A$ is constructed using the Jacobian formalism, based on partial derivatives. Fro uncertainty contributors governed by one parameter $\sigma_A$ (e.g. $Np$, $\epsilon$, $L_R$, $\langle \sigma_f \rangle^{\text{Bugey}}$ and $P_{\text{th}}^R$), $M_{ij}^A$ is constructed as

$$M_{ij}^A = J_i^A (\sigma_A)^2 J_j^A, \qquad (4.10)$$

where $J_i^U$ is the Jacobian:

$$J_i^A = \left( \frac{\partial N_i}{\partial A} \right) \tag{4.11}$$

For uncertainty contributors governed by a number of correlated parameters $\{A\} = A_\beta$ (e.g. $\langle \sigma_f \rangle_k^i$ and $\alpha_R^k$) the matrix construction requires summing over the potential cross-terms of those parameters, as

$$M_{ij}^{\{A\}} = \sum_{\beta\gamma} J_i^{A_\beta} m_{\beta\gamma}^{\{A\}} J_j^{A_\gamma}, \tag{4.12}$$

where $m_{\beta\gamma}^{\{A\}}$ is the covariance matrix relating the parameters $A_\beta$.

Finally, the total uncertainty on the prediction can be written as,

$$\delta N = \sqrt{\sum_i \sum_j M_{ij}^{\text{total}}}. \tag{4.13}$$

The contribution of each input variable to the predicted IBD are the ones showed in figure 4.7.

### 4.1.3 Uncertainty Propagation to the Prompt Energy Spectrum

The uncertainties of the $\bar{\nu}_e$ prediction described in the previous sections are related to the $\bar{\nu}_e$ energy spectrum (38 energy bins) while the oscillation analysis is performed with the reconstructed visible energy of the IBD prompt signal which is divided into 18 bins. Therefore, it is necessary to propagate the uncertainties in the prediction into the reconstructed IBD energy spectrum. The propagation of the uncertainties and calculation of the $18 \times 18$ covariance matrix, $M^{\text{pred}}$, is performed based on by the following steps:

1. A function of the energy spectrum, $f^{\text{mean}}(E_\nu)$, is created by interpolating the binned neutrino energy spectrum, $N_i$, with linear functions.

2. The covariance matrix for the neutrino energy spectrum is decomposed by an unitary matrix $U$ as follows

$$M^{\text{total}} = US^2U^T, \text{ with } S_{ij}^2 = \delta_{ij}\tilde{\sigma}_i^2 \ (\tilde{\sigma} > 0). \tag{4.14}$$

   Using random numbers, $V_i$, generated according to a Gaussian distribution with $\tilde{\sigma}$, the fluctuation of the neutrino energy spectrum, $\delta N_i$, can be obtained by

$$\delta N_i = \sum_j U_{ij}^T V_j. \tag{4.15}$$

   Then, a fluctuated spectrum is obtained as $N_i + \delta N_i$.

3. A function of the fluctuated energy spectrum, $f(E_\nu)$ is created by a linear interpolation of the fluctuated spectrum.

4. The MC samples passed by the IBD selection is refilled into the reconstructed prompt energy histogram with weighting by a ratio of $f(E_\nu)/f^{\text{mean}}(E_\nu)$. And a covariance for the prompt spectrum is given by

$$m_{ij}^k = \Delta n_i^k \Delta n_j^k, \tag{4.16}$$

   where $k$ is repeat count fluctuation and $\Delta n_i^k$ is the difference of numbers of events between the mean and fluctuated spectrum.

5. Repeating the step 2 to 4 (10000 times in this thesis), the covariance matrix of the $\bar{\nu}_e$ prediction related to the reconstructed prompt energy is obtained as an average of equation 4.16 as follows

$$m_{ij}^{\text{pred.}} = \frac{1}{10000} \sum_k^{10000} m_{ij}^k. \tag{4.17}$$

## 4.2  Detector Simulation

The Double Chooz Monte Carlo simulation (**DCGLG4sim**) is based on the **Geant4** tool-kit [86], an application widely used in particle and nuclear physics to simulate the passage of particles through matter. In general, DCGLG4sim constructs the simulated Double Chooz detector and its immediate surroundings, defines the list of particle interactions to be modelled by Geant4, and includes custom models of scintillation light emission and PMT optical surfaces. The detector simulation includes a detailed description of detector geometry and materials, as shown in figure 4.9. Measured or
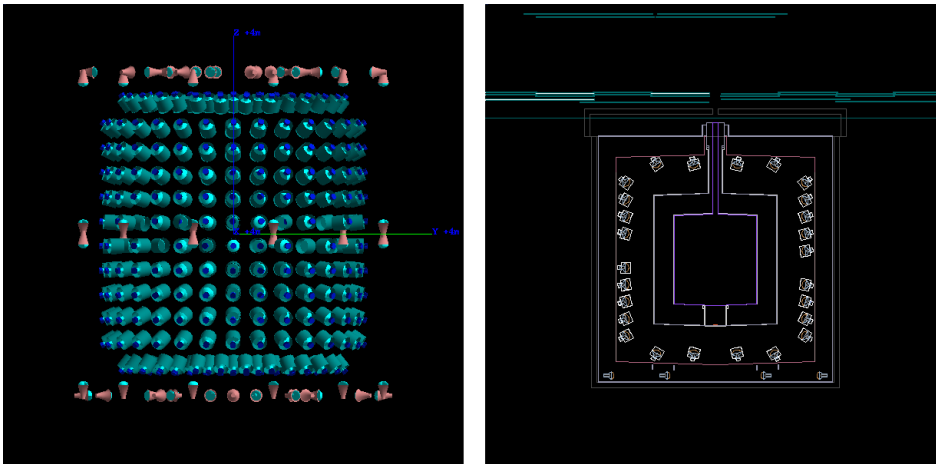


Figure 4.9: Visualizations of the Double Chooz detector built using Geant4. On the left, ID and IV veto PMTs arrangement. On the right, Double Chooz geometry simulation.

calculated values of the molecular composition and densities of the liquids and acrylic vessels are used to calculate the interaction cross sections and energy loss. In addition, Geant4 tracks the particles step-by-step as they propagate through the detector medium. At each step, the energy loss of a particle is simulated according to a process chosen from the list of defined interactions. If any secondary particles are created, then Geant4 begins to track these particles as well. The process continues until all particles have been absorbed, depositing all their energy to the detector, or left the tracking volumes. The IBD delayed coincidence signal consists of a prompt positron followed by a delayed neutron capture. Therefore, properly modelling electromagnetic and neutron interactions at low energies ($E < 10$ MeV) is essential for reproducing the observed data.

### 4.2.1  Electromagnetic Interactions

Three interactions are defined which describe the energy loss of gammas in detector material: the photoelectric effect, Compton scattering, and electron-positron pair production. Parametrized models are used to compute cross-sections and generate final state particles which can then be tracked by Geant4.

The electromagnetic interactions defined for both electron ($e^-$) and positron ($e^+$) are ionization due to inelastic collisions with atomic nuclei, elastic Coulomb scattering off of nuclei, and bremsstrahlung radiation. In addition, positrons annihilation with atomic electrons is simulated both in flight and at rest.

Above a certain minimum secondary particle kinetic energy, $T_{cut}$, $e^\pm$ ionization energy loss is simulated via the explicit production of gamma particles from Moeller ($e^- e^-$) or Bhabha ($e^+ e^-$) scattering which Geant4 then begins to track. Below $T_{cut}$, ionization is simulated as a continuous energy loss of the incident $e^\pm$ according to the Berger-Selzter formula [87]. Fluctuations around this mean energy loss are then drawn from an energy straggling function.

$T_{cut}$ is defined as the energy for which the $e^\pm$ stopping range is $< 10$ $\mu$m. The stopping range is computed as

$$R(T) = \int_0^T \frac{1}{dE/dx} dE, \tag{4.18}$$

where $T$ is the kinetic energy of the $e^\pm$ and $dE/dx$ is the energy loss per unit length due to ionization and bremsstrahlung. For the target scintillator, $T_{cut} = 10.5$ (10.3) keV for electrons (positrons).

Similarly, above some minimum photon energy $k_{cut}$, $e^\pm$ radiation energy loss is simulated via the explicit production of bremsstrahlung gamma particles. Below $k_{cut}$, bremsstrahlung is simulated as a continuous energy loss of the incident $e^\pm$. Here, $k_{cut}$ is defined as the energy for which $L_{int} = 2\mu$m, where $L_{int}$ is defined as the interaction length for the photoelectric effect, Compton scattering, or $e^+ e^-$ pair production. For the target scintillator $k_{cut}$ is below the default Geant4 value. Therefore, this default Geant4 value of $k_{cut} = 990$ eV is used instead. Again, fluctuations around the mean energy loss are drawn from an energy straggling function.

### 4.2.2   Neutron Interactions

Neutron transport in Geant4 is described by a high precision, data-driven model, which simulates the interactions of neutrons from 20 MeV all the way down to thermal energies. The model includes elastic scattering, inelastic scattering, radiative capture, and fission. Cross sections, angular distributions, and final state information are taken from the Geant4 evaluated neutron data library (G4NDL) derived primarily from linear interpolations of processed ENDF/B-VI evaluated nuclear data from the National Nuclear Data Center [88].

One major issue of the Double Chooz Geant4 neutron transport model is that it does not include the effects of molecular bonds on neutron elastic scattering. Molecular binding energies are typically of order 1 eV, and so we expect these effects to become important for neutron energies of 1 eV. This is well above the energy (25 meV) at which neutrons become thermal. Thus, The Double Chooz experiment has developed a MC package, named "NeutronTh", with modelling for low energy neutron which takes into account Hydrogen molecular bonds in neutron elastic scattering with neutron energy below than 4 eV. In the NeutronTh package, the molecular bonds were modelled for Hydrogen in dodecane. The molecular structures of all other liquid oil molecules are similar to dodecane and their cross section were assumed to be the same as for dodecane. Dodecane and dodecane-like liquid oil molecules make up the largest fraction in the Double Chooz scintillators and dominate the neutron elastic scattering physics.

### 4.2.3  Optical Model

Optical photons in the detector are produced either by Čerenkov radiation or scintillation light emission. Typically, the measured scintillation light yield per unit length produced by a particle passing through scintillator is proportional to its ionization energy loss. However, for highly ionizing particles quenching can occur, in which there is an increase in scintillation inefficiency and the linear scaling breaks down. This effect is described semi-empirically by Birk's Law [89]

$$dL/dx(E) = \frac{L_0 dE/dx}{1 + k_B dE/dx} \tag{4.19}$$

where $L_0$ is a light yield without quenching and $k_B$ is an empirical parameter which is related to impacts of the quenching and should be measured for each particle. Values of $L_0$ and $k_B$ for electrons and alpha particles were determined by measurements for scintillators of the NT and the GC before installation. However the absolute scale of the measurements is difficult to determine and the scintillation light yields were tuned with calibration data, especially with radioactive sources inside the detector.

The simulation includes a detailed model of scintillation light emission based on a suite of laboratory measurements, namely:

- Wavelength-dependent attenuation lengths

- Scintillation light yield

- Scintillation light resolution

- Scintillation light spectra

- Re-emission probability

Optical photons are generated according to the quenched energy deposition in the scintillating volumes given by equation 4.19 or via Čerenkov radiation. They are then tracked and propagated by Geant4. Both the effects of absorption and re-emission at longer wavelengths are included in the optical model. Polarization dependent reflection and refraction are simulated at the boundaries between dielectric materials. At metal surfaces such as the buffer wall or PMT mu-metal shields, optical photons can be absorbed or reflected according to specular and diffusive reflectivity parameters. Optical photons incident on the PMT optical surface are handled by a dedicated PMT model, simulating position-dependent collection efficiency based on the measurement performed before installation as shown in the right-hand plot of figure 3.17. If the optical photon is absorbed by the photocathode, a photoelectron is generated with some probability shown in the left plot of figure 3.17. For each event, the PE hit times and PMT channel numbers are aggregated and passed to the detector readout simulation.

### 4.2.4  Readout System Simulation

The Geant4 based detector simulation gives as output the time that each photon strikes the photocathode of each PMT, producing a photoelectron, and the deposited charge. The Readout System Simulation (RoSS), converts these informations into a format identical to the raw detector data. RoSS accounts for the response of elements associated with detector readout as the PMTs, FEE, FADC and trigger system. The simulation relies on the measured probability distribution function (PDF) to empirically characterise the response to each single PE as measured by the full readout chain. A dedicated set up consisting in one readout channel was built to measure most of the

necessary PDFs and to tune the design of the full readout chain. Variation channel-to-channel such as gains, baselines, noise and SPE width are considered, including dispersion effects. In this way the simulation exhibit non-linearity effects as observed in the data. For each event, the measured data format consists of trigger information and a waveform for each PMT representing the digitized current response recorded by the FADC.

## 4.3   Event Reconstruction

As previously explained, energy is deposited in the detector by particle interactions that produce scintillation light which is detected by the PMTs. The PMTs, in turn, will convert these light into electric signals that are recorded as digitized pulses by the FADCs. Therefore, in order to reconstruct the energy of the primary particle, defined as visible energy, one need to extract the charges from the PMTs pulses. Then, a correction is applied concerning the differences among the PMTs and the charge is converted into number of photoelectrons. Finally, the visible energy is calculated multiplying the total number of photoelectrons, got from all PMTs, by the energy scaling factor. Moreover, the timing information is used to reconstruct the interaction vertex. Both data and MC are subjected to the same reconstruction process, performed by the common trunk (CT). The CT takes place at CCIN2P3 as soon as the MC generation ends or the data files are transferred from on site. Details of each reconstruction step are given in the followings subsections.

### 4.3.1   Pulse Reconstruction

The pulse reconstruction is performed by a custom code called "DCRecoPulse", a collection of generic algorithms and tools meant to perform pulse charge and timing reconstruction as well as baseline analysis, from the digitized waveforms. For each PMT channel, DCRecoPulse performs the following three procedures: waveform baseline calculation; search for a time window which maximizes the pulse charge; and extraction of the pulse charge and hit time. The pulse charges are recorded as integrated FADC counts, called Digitized Unit of Charge, or simply DUQ. While the pulse hit time is not used directly in the energy reconstruction, it is used for the vertex reconstruction, which in turn is used as inputs for reconstruction energy position dependent corrections.

**Baseline**

The estimation of the baseline is the first step to be performed toward charge reconstruction, since it needs to be subtracted to obtain the actual signal. To determine the FADC baselines, two estimation methods are used: the *external baseline method*, which calculates the baseline from the event's full time window (256 ns), with external triggers rate of 1 Hz, and the *floating baseline method*, which obtains the baseline from the first 20 ns samples in each digitized waveform. The first method gives a stable and robust baseline independent of the signal shape and hit timing, while the second is not valid for light noise events, since theirs signals may arise at the beginning of the time window. On the other hand, the external method is known to be biased if the external trigger happens after a large energy deposition, such as muons. Thus, a hybrid scheme is adopted.

The floating method is chosen as default, but if the baseline RMS obtained by this method is larger than the one obtained by the external method ($\text{RMS}_{\text{floating}} - \text{RMS}_{\text{external}} > 0.5\,\text{DUQ}$), the later is employed for the channel.

**Pulse Charge**

The pulse charge of a PMT signal is obtained by integrating the waveform after the baseline subtraction, using an algorithm called "sliding window". The maximum value of the integrated charge is searched in a fixed 112 ns time window by shifting the window position, as shown in figure 4.10. The maximum value is compared with a
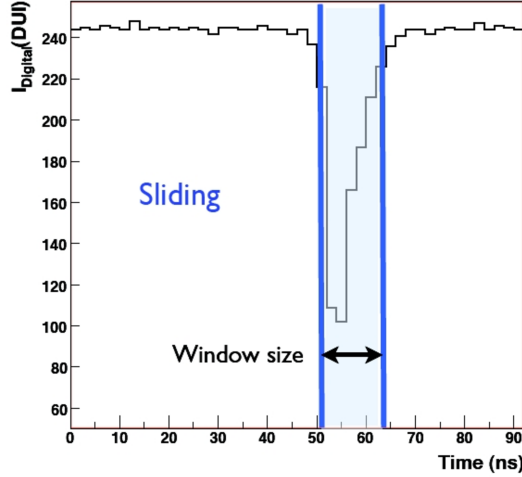


Figure 4.10: Illustration of the reconstruction of pulse charge by the sliding window method. The y-axis is in DUI, an arbitrary unit that stands for digital unit of current.

charge threshold to ensure the reconstructed pulse actually comes from PE signal and not from pedestal fluctuation. This threshold on the measured charge is set as:

$$q_{\min} \equiv \sigma_{\mathrm{RMS}} \times \sqrt{N_{\mathrm{tw}}}, \tag{4.20}$$

where $\sigma_{\mathrm{RMS}}$ is the baseline deviation and $N_{\mathrm{tw}}$ is the number of samples in the integration time window. If the maximum charge is larger than the threshold $q_{\min}$ and the maximum amplitude of the pulse is higher than two FADC counts, the value is stored as a PMT charge. Otherwise, the pulse charge is discarded.

**Timing**

Once non-zero value of the PMT charge is calculated, the pulse hit time is also obtained from the time difference between the beginning of the FADC time window and the time in which the pulse amplitude exceeds 20% of the maximum amplitude.

### 4.3.2   PMT and Electronics Calibration

The 390 PMTs and electronics channels of the Double Chooz ID are affected by several sources, such as charge gain and hit timing offsets, that will cause differences on the responses of the observed photoelectrons. The IDLI system is used to calibrate both gain and timing offset of these PMTs.

**Gain**

The gain is defined as the conversion factor from the number of PEs to DUQ, including gain of PMTs, amplitudes in the FEE, digitization of FADC, and effect of the pulse reconstruction. This relation between the number of PE, $n_{\mathrm{pe}}^{i}$, and the observed charge

$q_i$ for the $i$-th ID PMT can be expressed by

$$n_{\text{pe}}^i = \frac{q_i}{g^i(q^i)}, \qquad (4.21)$$

where $g^i$ is the gain.

The gain depends on the reconstructed charge due to the non-linearity of the PMT gain and characteristics of the electronics as will be shown. Therefore, the gain is measured as a function of the observed charge to correct for this non-linearity. The function of the gain for each channel is parametrized by three following parameters

$$g(q) = \begin{cases} g_0 & \text{if } q \geq q_0 \\ g_0 - s(q - q_0) & \text{otherwise} \end{cases} \qquad (4.22)$$

where $g_0$ is the gain constant in the linear part, $s$ is the slope in the non-linear part, and $q_0$ is the intersection between the linear and the non-linear parts.

In order to estimate the gain with the non-linearity, it is required to extract the gain with various charges for each PMT channel. A gain calibration method, called "multi PE calibration" has been developed to extract the gains from various charge input. Generally, a variation $\sigma$ of the observed charge distribution can be expressed by

$$\sigma^2 = \sigma_{\text{poisson}}^2 + \sigma_{\text{spe}}^2 + \cdots . \qquad (4.23)$$

In the equation above, the term $\sigma_{\text{poisson}}$ is a variation related to statistical fluctuation to the number of detected PEs, which should obey a Poisson distribution and can be approximated by a Gaussian distribution when the light intensity is relatively high. In this case, $\sigma_{\text{poisson}}$ can be defined as $\sigma_{\text{poisson}}^2 \approx g^2 N$, where $N$ is the number of PEs. the second term, $\sigma_{\text{spe}}$ is a resolution of a single PE peak which can also be expressed by Gaussian distribution as $\sigma_{\text{spe}}^2 = \alpha^2 g^2 N$, where $\alpha$ is a relative variation of SPE charge. In case that others contributions to $\sigma$ are negligible, the gain can be obtained from the following relation between the mean charge, $\mu$, and $N$: $\mu = gN$, where

$$g = \frac{\sigma^2}{\mu} \frac{1}{1 + \alpha}. \qquad (4.24)$$

The two parameters of this equation, $\sigma$ and $\mu$, are the RMS and mean value of the charge distribution as shown in the left plot of figure 4.11. The charge distributions are acquired using various light intensities and injection points.

On the other hand, $\alpha$ cannot be determined by the multi PE calibration method. Therefore, another calibration method, called "single PE calibration", is used to determine the gain at single PE level and to get $\alpha$. The single PE calibration method uses observed charge distribution with low light intensity, which gives peak of a single PE in the charge distribution as shown by the right plot in figure 4.11. The charge distribution can be modelled by a convolution of Poisson and Gaussian functions as given by

$$F(q) = \sum_{n=1} \frac{N e^{-\mu} \mu^n}{\sqrt{2\pi n}\sigma} \exp\left(\frac{q - gn}{\sigma\sqrt{n}}\right), \qquad (4.25)$$

where $N$, $g$, $\sigma$ and $\mu$ are the number of single PEs, single PE peak position (i.e. the gain), resolution of single PE peak, and the expected number of occurrences based on the Poisson statistics, respectively. These values are obtained by a fit to the charge distribution data as shown in the right plot of figure 4.11. Through the data taking period, $\alpha$ is uniquely determined using all ID PMT. Its value is optimized to make the average gains, estimated by both multiple and single PE methods, consistent with each other at high light intensity calibration runs.

Finally, correlation between the gain and the mean observed charge is obtained from the data taken with various light intensities. An example of the correlation for one channel is shown in figure 4.12.
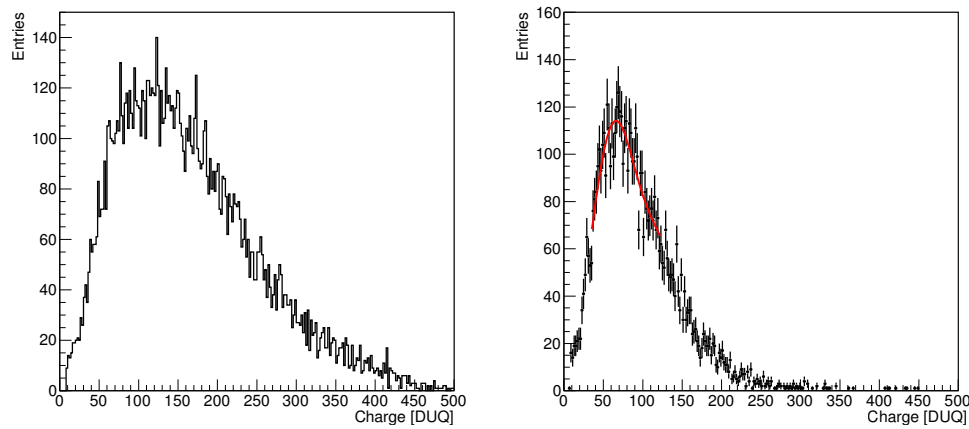
Figure 4.11: Charge distribution of a typical ID PMT channel taken with the IDLI system for the multi (left) and single (right) PE methods. The red line on the right plot was obtained by fitting with equation 4.25
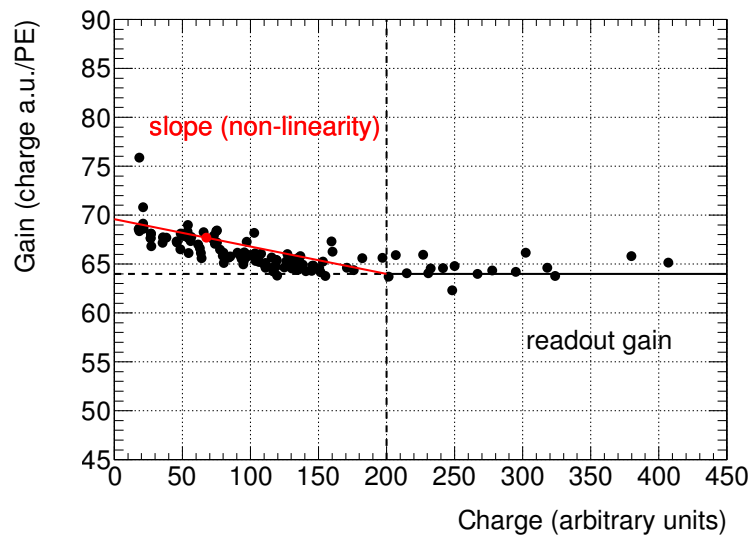


Figure 4.12: Correlation between gain and mean observed charge for a typical PMT channel. The black point are the extracted gains by the multi PE method. The black line shows the constant part of the gain, $g_0$, while the red line shows its slope term.

**Timing Offset**

Due to latency of the electronics responses, pulse hit timing should have an offset from the true hit timing and it generally differs from each other channel. The timing offset calibration is performed to cancel the time offsets. For the cancellation, data taken with the IDLI system is also used. Figure 4.13 shows a distribution of pulse hit timing for
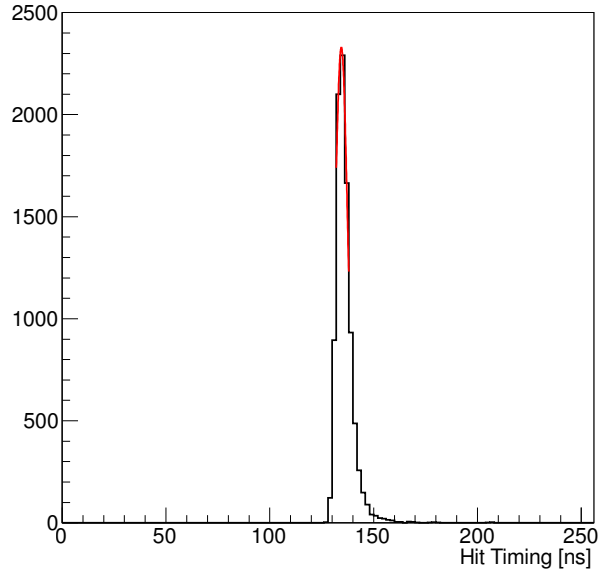


Figure 4.13: A typical distribution of the pulse hit timing for one PMT channel. The red line shows the fitting result with a Gaussian function.

a typical PMT channel, in which mean value of the hit time can be obtained by fitting with a Gaussian function.

The dependence of the pulse hit timing by the distance from the injection points to the PMT surface is measured for each PMT channel using the data taken with the IDLI system injecting the light from various injection points. Figure 4.14 shows the correlation for 8 injection points and the pulse hit timing $t$ can be modelled by

$$t = t_0 + \frac{r}{c_n}, \tag{4.26}$$

where $t_0$ is the timing offset, $r$ is the distance between the PMT and the injection point, and $c_n$ is the effective light speed in the detector. the timing ofsset for the $i$-th PMT channel is obtained as a difference between the measured pulse hit time, $t_i$, and the expected time, $r_i/c_n$, calculated as

$$t_i^{\text{offset}} = t_i - \frac{r_i}{c_n}. \tag{4.27}$$

### 4.3.3   Vertex Reconstruction

The vertex reconstruction is based on charge and time maximum likelihood algorithm using hit/no-hit probability for each PMT. The event is assumed to be a point like source of light characterised by $\mathbf{X} = (x_0, y_0, z_0, t_0, \Phi)$, where $(x_0, y_0, z_0)$ represent the event position within the detector, $t_0$ is the event time and $\Phi$ is the light strength (number of photons per sr). The amount of light and the arrival time at the $i$-th PMT is predicted as:

$$\mu_i = \Phi \times \epsilon_i \times \Omega_i \times A_i \ \text{ and } \ t_i^{\text{pred.}} = t_0 + \frac{r_i}{c_n}, \tag{4.28}$$
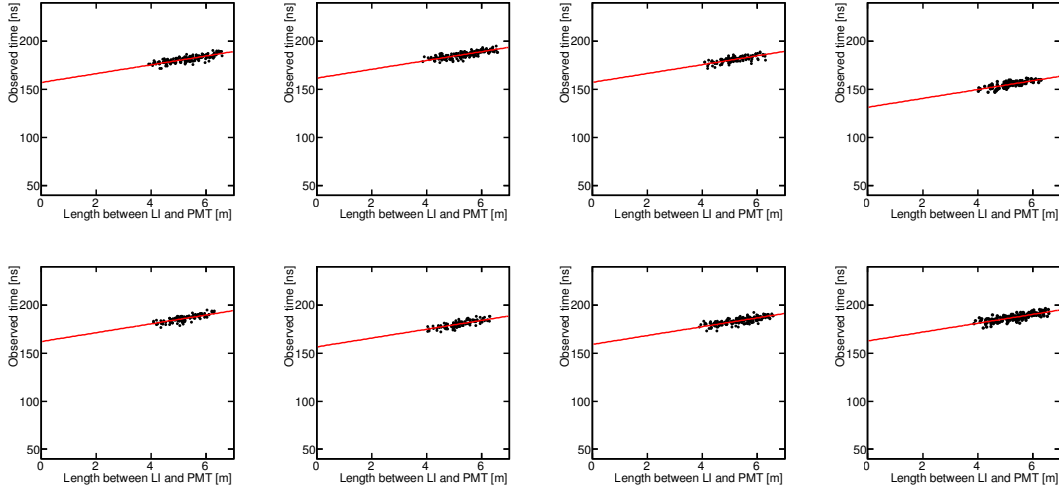
Figure 4.14: A typical plots for the dependence of pulse hit timing by the distance between the PMT and the injection point, for 8 different points. Each black point in the plots is the result from a light injection run. The red lines are the fit result using equation 4.26.

where $\epsilon_i$ is the $i$-th PMT quantum efficiency, $\Omega_i$ is the solid angle subtended by the PMT at a distance $r_i$ from the event vertex, $A_i$ is the light transmission amplitude, and $c_n$ is the effective speed of light in the medium.

The event likelihood is defined as

$$\mathcal{L}(\mathbf{X}) = \prod_{q_i=0} f_q(0, \mu_i) \prod_{q_i>0} f_q(q_i, \mu_i) \times f_t(t_i, t_i^{\text{pred.}}, \mu_i). \qquad (4.29)$$

The first product in this equation concerns only PMTs that have not been hit, while the second concerns the remaining PMTs that have been hit, i.e., non-zero charge $q_i$ reconstructed at time $t_i$. The two function $f_q$ and $f_t$ are the charge and time probability density function (PDF) obtained from MC simulation and validated against physics and calibration data. The event reconstruction consists to find the set of event parameters $\mathbf{X}_{\text{max}}$ which maximizes equation 4.29.

The vertex reconstruction accuracy was evaluated using calibration sources (section 3.4.5.1) deployed at know position with the z-axis and along the guide-tube systems. The reconstructed position had a resolution of 32 cm for $^{137}$Cs, 24 cm for $^{60}$Co and 22 cm for $^{68}$Ge.

### 4.3.4   ID Energy Reconstruction

The energy reconstruction is performed using the following scaling and corrections terms

$$E_{\text{vis}} = f_{\text{E}_{\text{scl.}}} \times \left( \sum_i^{\text{PMTinID}} n_{\text{pe}}^i \right) \times f_{\text{uniformity}}(\vec{x}_{\text{reco}}) \times f_{\text{stability}}(t) \times \frac{N_{\text{PMT}}^{\text{ID}}}{N_{\text{goodPMT}}^{\text{ID}}}, \qquad (4.30)$$

where $n_{\text{pe}}^i$ is the observed number of PEs for the $i$-th PMT (see section 4.3.2), $\vec{x}_{\text{reco}}$ is the reconstructed interaction vertex, $t$ it the event time and $f_{\text{E}_{\text{scl.}}}$ is a factor to convert the number of observed PEs into MeV energy unit. The other three terms on the equation are corrections factors. The first one, $f_{\text{uniformity}}$ corrects for the non-uniformity over the detector volume, and the second $f_{\text{stability}}$, accounts for the time stability. The MC has no time-dependence for energy scale and therefore, $f_{\text{stability}}(t) \equiv 1$ for all events. The number of the operating ID PMTs varies over the data taking period

due to malfunction of electronics or switching off channels due to strong light noise. The last term, $N_{\text{PMT}}^{\text{ID}}/N_{\text{goodPMT}}^{\text{ID}}$, is a ratio of the number of the ID PMTs over the number of ID PMT available for the energy calculation, which is applied to correct for the difference of the number of available PMTs.

### Absolute Energy Scale

The energy scale factor $f_{\text{E}_{\text{scl.}}}$ is established with radioactive source deployments along the z-axis system, during calibration campaigns. Simulation of the same sources was also used to determine the MC's energy scale. From these methods, the absolute energy scale was determined to be 229.9 and 227.7 PE/MeV for data and MC respectively, at the center of the detector, for $t_0$.

### Relative Non-Uniformity

From several studies with deployment source calibration data, it turned out that the detector response is not uniform across the detector volume due to the detector geometry. A correction map for detector response non-uniformity is introduced as a function of cylindrical coordinates of the reconstructed vertices ($\rho = \sqrt{x^2 + y^2}, z$), which corrects the visible energy into the one at the center of the detector ($\rho = 0, z = 0$). For the estimation of the uniformity correction map, the full volume of the NT and the GC was divided into 108 sub volumes according to the reconstructed vertices and the visible energies of neutron capture peak on Hydrogen were extracted for each sub volume as shown in figure 4.15. Cosmogenic spallation neutron and $\bar{\nu}_e$ MC samples are used to
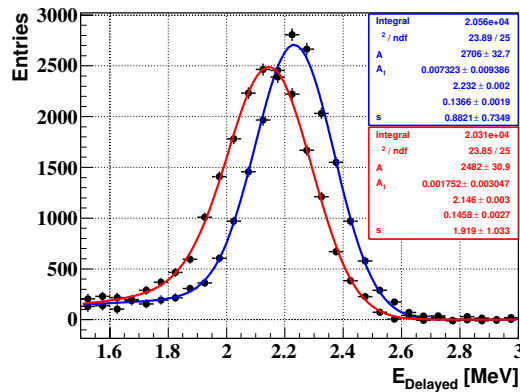


Figure 4.15: Two example of energy distributions of neutron capture on hydrogen in different sub volumes using data. The spectrum with the blue line is obtained for a sub volume around the center of the detector while the one with the red line is obtained around the boundary of the NT.

generate the correction maps for the observed data and MC, respectively. Finally, the correction maps were obtained by normalizing the values at the center of the detector to be one. The detector response correction map for the data is shown in figure 4.16, where the largest deviation in the NT is estimated to be up to about 5%. The similar correction map was also obtained for the MC. Difference between the data and MC correction maps is used to estimate the non-uniformity systematic uncertainty to be 0.43%. If the volume region is extended for the GC, as is the case for the neutron capture in Hydrogen analysis, the non-uniformity uncertainty was found to be 1.33%. The estimation of this value is conservative, since it was taken form the largest discrepancy when comparing the data
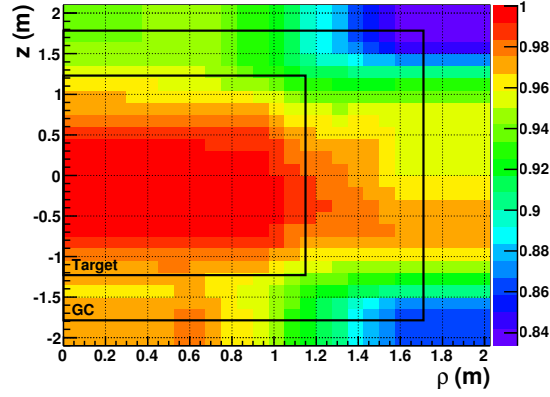
Figure 4.16:   The detector response non-uniformity correction map, in cylindrical coordinates.

and MC neutron capture on Hydrogen peak from the deployment of $^{252}$Cdf source on the z-axis and guide-tube.

These results are consistent with the analysis of all radioactive sources deployed along the z-axis for the NT and the guide tube for the GC.

### Relative Instability

The detector response stability was found to vary in time due to variations of electronics gain or scintillator response. This variation has been measured to be within 2.2%, increasing over 1 year from the neutron capture on gadolinium using spallation neutrons, as shown in figure 4.17a. The stability calibration is relative to a specific reference time, which is defined as the day of the first $^{252}$Cf source deployment, on August, 2011. The instability correction factor as a function of event time $t$ is defined as a ratio of the neutron capture peaks given by

$$f_{\text{stability}}(t) = \frac{\mu_{\text{Gd}}(t_0)}{\mu_{\text{Gd}}(t)}, \tag{4.31}$$

where $\mu_{\text{Gd}}(t)$ is the peak position of neutron capture on Gadolinium. In practice, the correction factor was extracted for each 5 days of data and applied the same value to all events over the 5 days. Instability after the correction was studied with spallation neutrons captured on Hydrogen as shown in figure 4.17b and the systematic uncertainty of associated with the time instability was estimated as 0.61%.

### Total Uncertainty

The total uncertainty associated with the visible energy reconstruction, based on each correction explained on the previous subsection, is estimated to be 0.81% and 1.64% for the Gadolinium and Hydrogen methods, respectively. Moreover, the corrections are considered to be uncorrelated. The contribution of each source of uncertainty is summarized in table 4.3.

### Uncertainty Propagation

Energy scale uncertainties only affect those event types which rely on the Monte Carlo for energy reconstruction: the $\bar{\nu}_e$ signal prediction, and the $^9$Li prediction. The uncertainty prescription combines contributions from the three sources described in
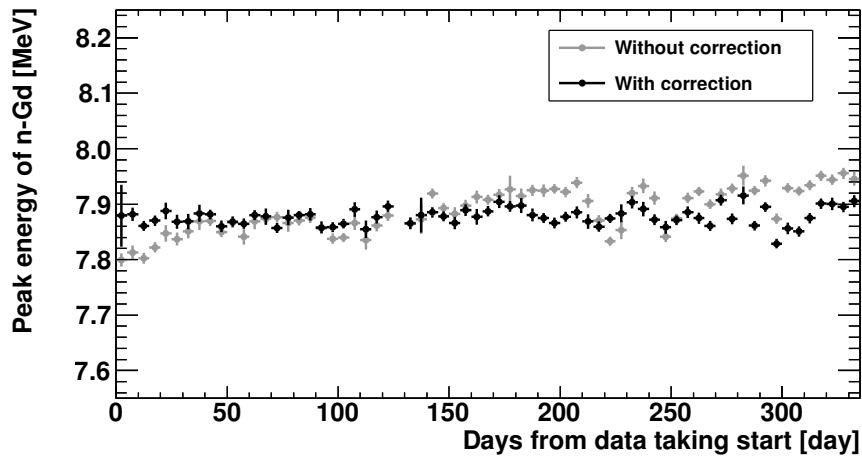
(a) Gadolinium
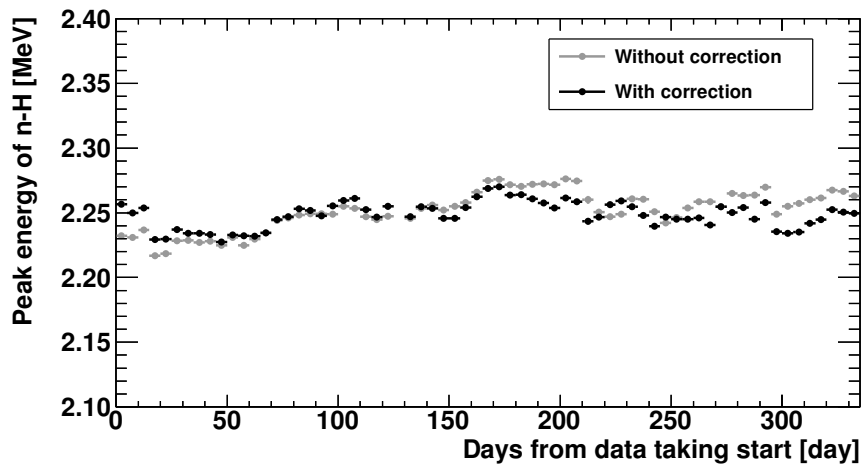


(b) Hydrogen

Figure 4.17: Time evolution of the ID energy scale, measured from neutron capture peaks on Gadolinium and Hydrogen using spallation neutrons. The left axis shows the deviation of energy peak from the value measure at the day of the first $^{252}$Cf source deployment calibration in the target, on August 2011.

Table 4.3: Summary of the reconstruction energy method uncertainties.

| Source | n-Gd [%] | n-H [%] |
|---|---|---|
| Relative non-linearity | 0.85 | 0.85 |
| Relative non-uniformity | 0.43 | 1.33 |
| Relative instability | 0.61 | 0.61 |
| Total | 1.13 | 1.69 |

the previous subsections: non-uniformity of detector response, instability of detector response, and relative non-linearity. While one of the contributions is due to non-linearity, all contributions are presumed to effect a linear shift in the energy scale.

Traditionally, the energy scale is modulated in the final oscillation fit as a parameter $P_E$ which scales the energy $E_{\text{vis}}^0$ of some events comprising the Monte Carlo prediction:

$$E_{\text{vis}} = P_E \times E_{\text{vis}}^0. \tag{4.32}$$

This scaling is only applied to events whose energies $E_{\text{vis}}^0$ are determined by the Monte Carlo reconstruction, and not by measurement in data (e.g. IBD signal events and $^9$Li events, but not fast neutrons/stopping muons or accidentals). As tabulated in table 4.3, three sources of uncertainty combine to give a relative interval $\sigma_{P_E} P_E = 0.81\%$ (1.64%) for Gadolinium (Hydrogen) analysis.

The energy scale covariance matrix is constructed using a **MultiSim**[1] method. Sets of $u = [1, \ldots, U]$ random Gaussian throws $P_{Eu}$ are made on the energy scale parameter $P_E$ and the correlated random bin deviations $\{\delta N_i^{\text{pred.}}\}_u = \{N_i^{\text{pred.}}\}_u - \{N_i^{\text{pred.}}\}_{P_E=1}$ are used to construct an average covariance matrix, $M_{ij}^{\text{escale}}$, as follows

$$M_{ij}^{\text{escale}} = \frac{1}{U} \sum_{u=1}^{U} \left( \{\delta N_i^{\text{pred.}}\}_u \times \{\delta N_i^{\text{pred.}}\}_u \right). \tag{4.33}$$

The fractional energy scale covariance matrix is obtained from the full energy scale covariance matrix using the MC signal plus $^9$Li background energy spectrum. The fractional covariance matrix is then passed to the final oscillation fit codes where the full covariance matrix is reconstituted using the total MC signal plus background prompt energy spectrum before being included in the $\chi^2$) (see section 5.1).

### 4.3.5 IV Energy Reconstruction

The visible energy in the IV is roughly reconstructed from the integrated charge observed by the IV-PMTs as

$$E_{\text{vis,IV}} = \frac{1}{2000 \, [DUQ]} \sum_i^{\text{IV PMT}} q_i, \tag{4.34}$$

where $q_i$ is the charge extracted from the pulse observed in the $i$-th IV-PMT.

## 4.4 Data Sample

As it was said in the beginning of this chapter, the data sample used for the present analysis correspond to 333 days of data taking from 13$^{\text{th}}$ of April of 2011 to 30$^{\text{th}}$ of March of 2012. The total run time over the whole period is 251.27 days. Every energy deposition above ID trigger threshold (0.5 MeV) or IV trigger threshold (4 MeV) are readout and written to file. The data taking started only with the ID and IV and the OV detector started its operation about 100 days later, thus 69% of data contains information of both $\nu$- and OV-DAQ.[2] The run time, defined as the amount of time the data acquisition system was actively acquiring data, is shown in figure 4.18 as a function of the data taking day.

The events observed in the detector can be divided into the following categories: IBD candidates, detector noise (or Light Noise), cosmic muons and radioactive background.

---

[1]The name for this MC-based error propagation technique is taken from the MiniBooNE experiment.

[2]Although the upper OV has been installed recently, it was not operational during the data set used here.
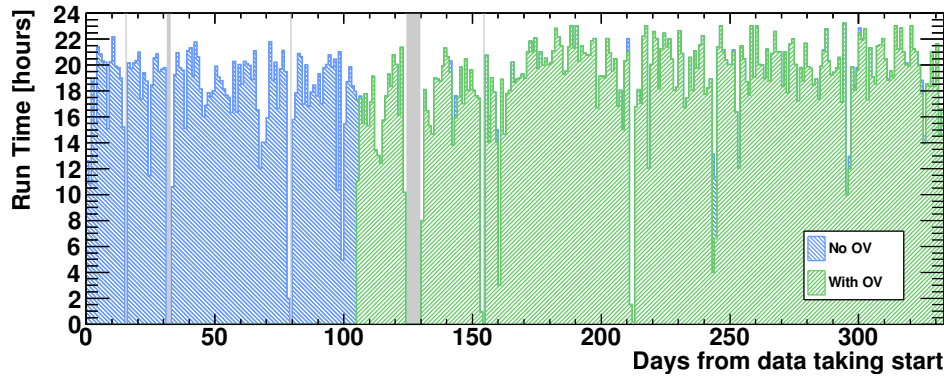
Figure 4.18: Run time of each day of data taking used for analysis. The blue histogram shows daily run times without the OV while the green histogram shows daily run times with the OV. The gray region shows periods with no physics data taking due to some extra works such as calibration or modification of the data acquisition system.

The IBD candidates contains true neutrino interaction and background as well, therefore, the aim of the neutrino selection analysis is to remove as much background as possible. For this purpose, a pre-analysis is performed to create a sub sample of the dataset, rejecting events not related to neutrino (signal) or neutrino-like (background). The methods to reject these events, mainly cosmic muons and LN, are described in the following sections.

### 4.4.1   Light Noise Rejection

As described in section 3.5.4, Light Noise (LN) events are related to light being produced in the base of some ID PMTs. Since the glow PMT tend to have $> 10\%$ of total charge, a Maximum Charge over Total Charge ($Q_{max/tot}$) quantity is defined to select LN events. The $Q_{max/tot}$ cut makes use of the fact that the light-emitting PMT generates much large signals than average of the other PMT signals and it is defined as the ratio of the maximal charge on a PMT over the total charge, i.e.:

$$Q_{max/tot} \equiv \frac{max_i^N(Q_i)}{\sum_i^N Q_i}, \tag{4.35}$$

where $N$ is the number of available PMTs and $Q_i$ is the charge of the $i$-th PMT. For a true neutrino signals, the $Q_{max/tot}$ ratio is determined by the solid angles of the PMTs viewed form the point of the event and it is unlikely that a single PMT will receive more than $5\%$ of the total light. Based on what was before mentioned, the $Q_{max/tot}$ is an effective (high rejection power) and safe (no loss of true events) selection method, consisting of simple calculation, and it does not require wave-form nor position reconstruction.

Also mentioned in section 3.5.4, the LN events generally are much longer (about 100 ns) than $\gamma$ signals, also presenting many spikes. Therefore, it is possible to define another quantity as a LN discrimination method: the $T_{start}^{\mathrm{RMS}}$. This variable is the Root Mean Square (RMS), or standard deviation, of the distribution of starting time on each PMT, i.e.:

$$T_{start}^{\mathrm{RMS}} \equiv \sqrt{\frac{1}{N_{hit}^{\mathrm{ID}}} \sum_i^{N_{hit}^{\mathrm{ID}}} (T_i - \bar{T})^2}, \tag{4.36}$$

where $N_{hit}^{ID}$ is the number of hit PMTs, $T_i$ is the hit time of the $i$-th PMT and $\bar{T}$ is the average of $T_i$ in the ID PMTs. The hit timing is determined as the start time of the pulse in the FADC.

Taken together, these two cuts introduce a physics rejection factor of $< 0.8\%$ base on calibration data, using $^{252}$Cf source. MC simulations indicate that the rejection factor is even lower than this ($< 0.1\%$) for IBD events and so can be neglected.

However, since the trigger rate were higher than expected during detector commissioning, a series of actions was performed in order to decrease it, such as: turn off the 14 most noisy PMT; reduce the voltage on the remaining PMTs to lower the probability of noise emission (gain is 5/6 of the original value); and apply a multiplicity condition at trigger level. The fourteen most noisy PMTs were identified from the distribution of the PMTs with maximum charges for events with $Q_{max/tot} > 0.1$ and with reconstructed energies in the delayed energy range ([6,12] MeV). This action did not introduce any anisotropy in the detector response, since the PMTs were randomly distributed (figure 4.19). In addition, after about 110 days of operation, the detector
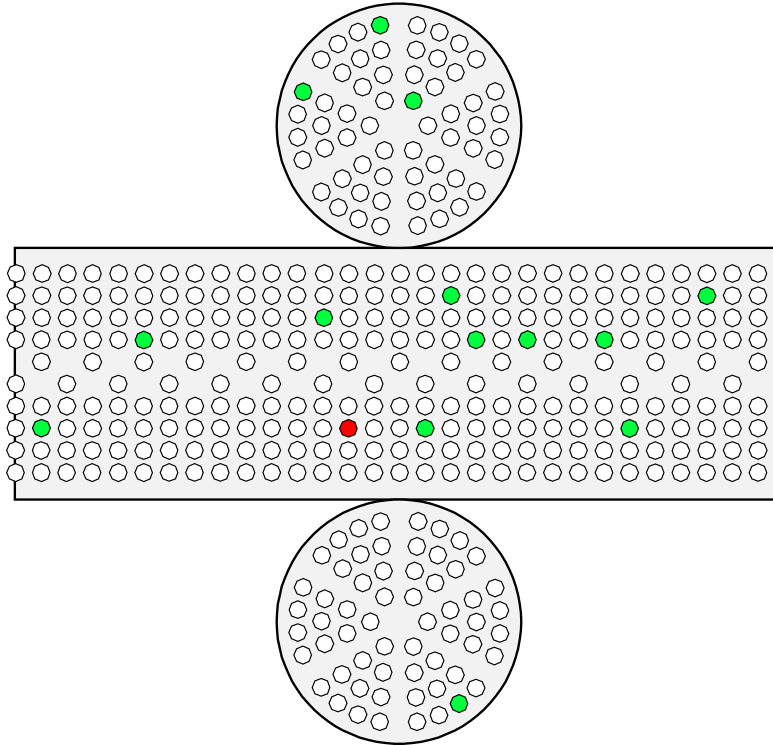


Figure 4.19: Double Chooz ID PMT position map. The 14 most noisy PMTs are in green and the PMT 263 is in red.

trigger and accidental rate started to increase. This was due to an increase of the LN rate of PMT 263. The total single rate in delayed energy range showed to be correlated with the single rate when the PMT 263 had the maximum event charge, as showed in figure 4.20.

A cut was defined as $7 \times 10^{-3}$ Hz in order to reject the bad runs. In figure 4.21 it is shown that after this PMT was turned off, the accidental rate returned to its nominal value.
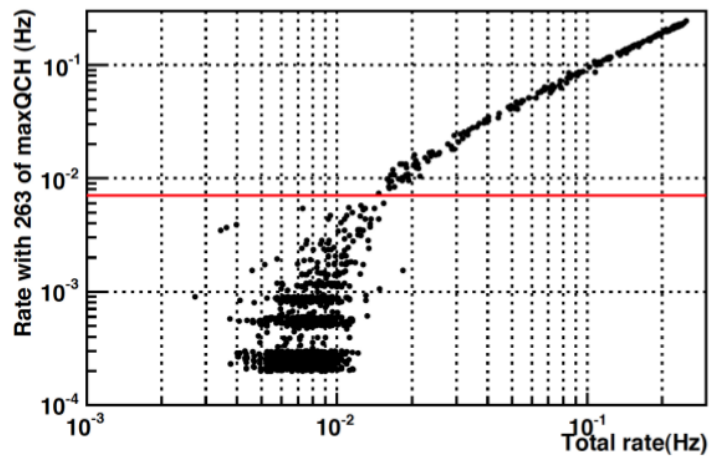
Figure 4.20: Correlation between single rate on delayed energy range and single rate when PMT 263 had the maximum event charge.
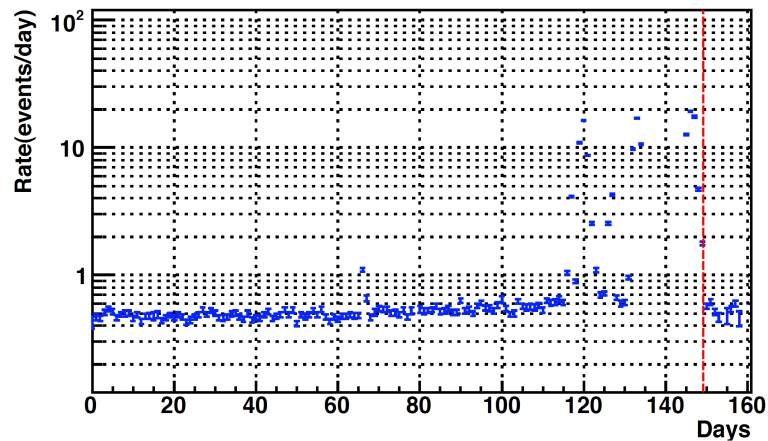


Figure 4.21: Accidental rate before (left side of the vertical red line) and after (right side of the vertical red line) the PMT 263 was switched off.

In order to understand better the LN on the far detector, a series of runs with different HV configuration where taken, as showed in table 4.4. For the normal data taking, the detector is configured with Gain 50 and 15 PMT off, corresponding with Run 4, in the table. Figure 4.22 shows the distribution of the maximum charge PMT for

Table 4.4: Special LN Run Configuration

|       | Gain | PMT    |
|-------|------|--------|
| Run 1 | 40   | All on |
| Run 2 | 40   | 15 off |
| Run 3 | 50   | All on |
| Run 4 | 50   | 15 off |
| Run 5 | 60   | All on |
| Run 6 | 60   | 15 off |

all the runs applying the prompt and delayed energy range cut. On that distributions,
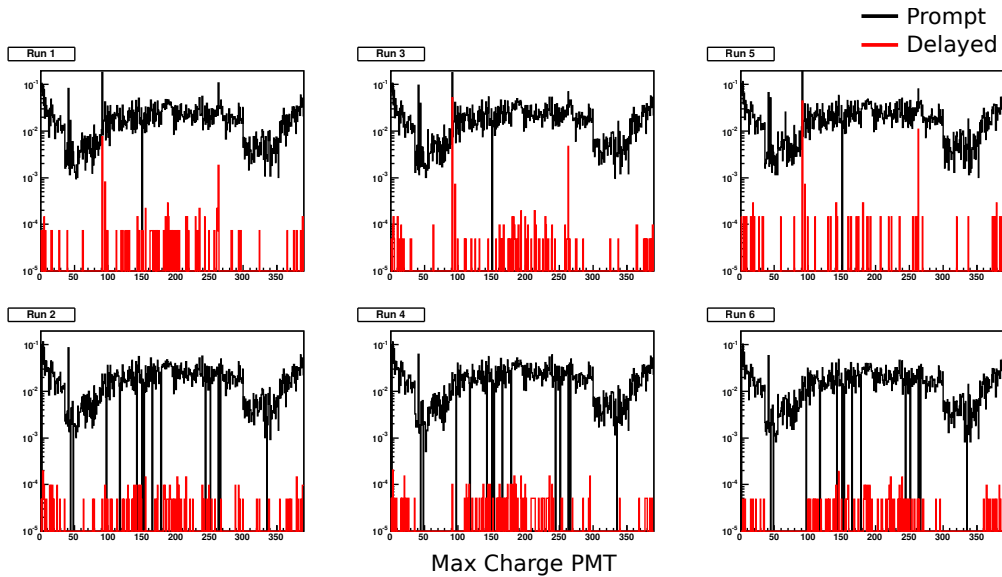


Figure 4.22: Max charge PMT distribution for prompt and delayed energy cuts for the LN test runs.

for all the runs which all the PMTs are on, the bigger contribution on the delayed cut, comes from two PMTs: 91 and 263. Ignoring the events tagged by these two PMTs the single rates go to their nominal values, even when the other thirteen PMTs are on, as showed in figure 4.23. Therefore, turning off only these two PMTs have the same effect of turning off all the fifteen, once the contribution from the others does not pass the current LN cuts.

**LN Status and Future**

Currently, an increase of the total trigger rate has being observed at the far detector. However it did not impacted the neutrino selection analysis, since the LN cuts are still efficient. But it has an impact on the DAQ crash rate, due to the rates reaching the ceiling of the readout capacity. Improvement on the DAQ software are being implemented to handle this increase.

The main strategy to reduce LN events in the near detector is to cover the PMT bases with black sheet that is opaque, radio-pure and chemically compatible with the
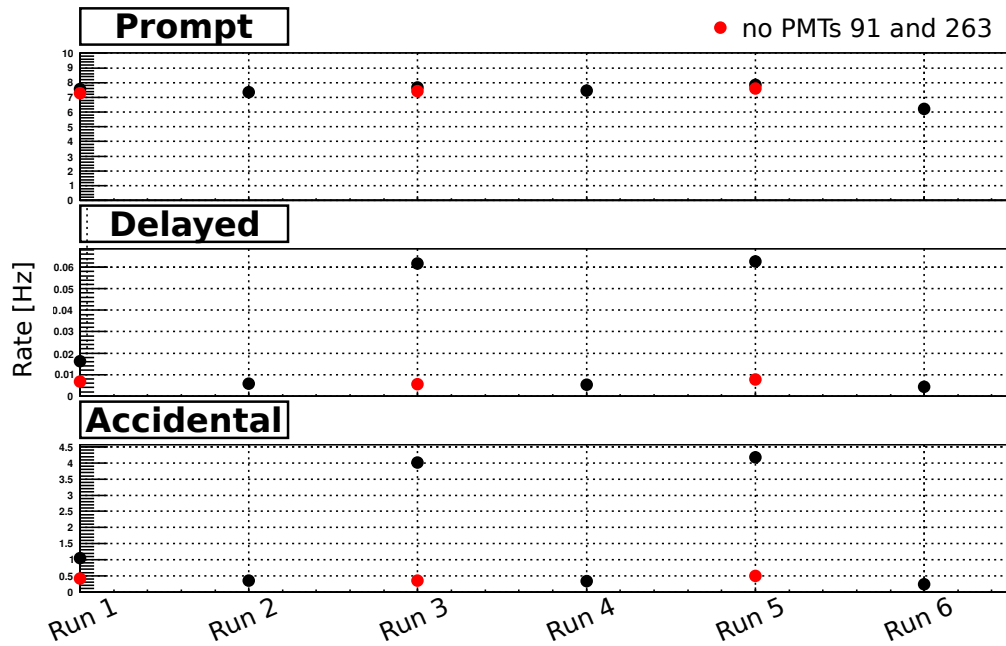
Figure 4.23: Rate of Prompt, Delayed and Accidental Singles before and after special LN runs cut.

experiment liquids. Laboratory measurements showed that there are a reduction of light being emitted by the base of 99.88%. However, it does not eliminate completely the emitted light, since there is no way to block the light going through the PMT to the front and which can be detected by the own glower PMT and/or exit through the PMT window. At laboratory tests, when a PMT is placed in front of a glower PMT, it detection ratio of LN events went from 91%, when the base is not covered, to 47% when the base is covered by the black sheet. Therefore, although the rate of the glowing events coming from the front of the PMT is still considerable, the amount of light is strongly reduced by the black sheet, which make the $Q_{max/tot}$ selection method more powerful.

### 4.4.2    Muon Veto

The events in the ID correlated to a muon crossing the detector is rejected by a veto time upon a tagged muon. This events can induce a delayed coincidence signal, mimicking an IBD candidate, when a muon produces multiple neutrons inside the detector by spallation process. These neutrons can make a delayed coincidence in case one is captured by Hydrogen or Gadolinium followed by another capture. Another effect is the large deposit of light by muons, that can flood the detector with light. This temporarily destabilizes the detector due to after pulses of the PMTs.

Muon are tagged using the energy deposited in the IV or ID. Assuming that muons deposits 2 MeV by each cm traversed in the detector, the lowest energy deposition in the IV is roughly 5 MeV (or $10^4$ DUQ). Moreover, events with energy above 30 MeV in the ID are also identified as muons even if there is no signal in the IV, since muons can pass through the ID chimney. Thus, a muon is tagged assuming $E_{\text{vis}} > 30$ MeV or $E_{\text{vis,IV}} > 5$ MeV. However, there are still low energy muons that can pass through the chimney, stop inside the detecto and decay to an electron, leaving less than 30 MeV. These stopped muons are treated as backgrounds, having a dedicated analysis for their rate estimation, as described in section 4.7.2.

An muon veto time can be determined by observing the number of events detected as

a function of the time passes since the last tagged muon, $\Delta T_\mu$. Figure 4.24 shows that as $\Delta T_\mu$ approaches to zero, a higher event rate is observed, manly with $\Delta T_\mu < 1\ \mu$s. These
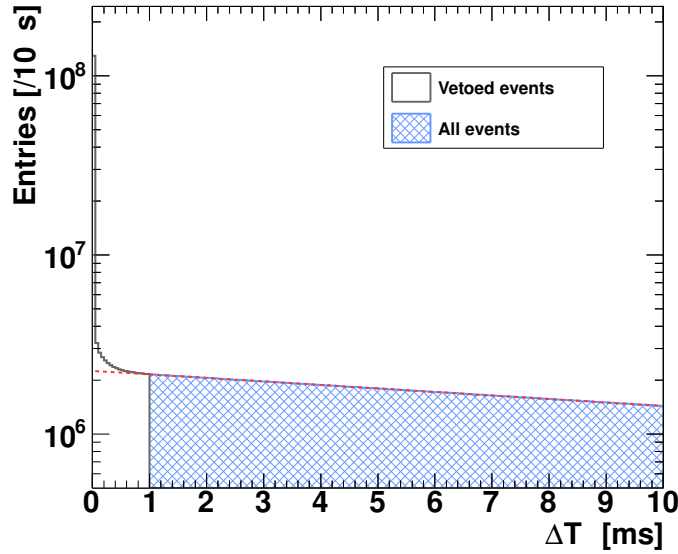


Figure 4.24:  Time difference between a muon tagged and $E_{\mathrm{vis}} > 0.5$ MeV events distribution. Events that occurs before 1 ms after a muon are rejected. The red dashed line corresponds to the function $\exp(R_\mu \Delta T_\mu)$ with $R_\mu = 45.2$ Hz.

events are due to the muons products, as described in the beginning of this section. After $1\ \mu$s, the event rate decreases exponentially, and the muon rate, $R_\mu$, can be determining by fitting this region with the $\exp(R_\mu \Delta T_\mu)$ function, returning $R = 45.2 \pm 0.024$ Hz, which agrees with the measured muon veto rate. Therefore, this 1 ms is used as a muon veto, where the increase of correlated background is negligible ($< 0.2\%$). This muon veto introduces a detector dead time time of 4.4%. with respect to the run time, giving a data taking live time of 240.17 days.

## 4.5   Neutrino Event Selection

The inverse beta decay delayed coincidence signal is defined by a prompt positron event and a delayed neutron capture on Gadolinium or Hydrogen, in a characteristic time window, $\Delta T$. After applying the Muon Veto, depending on which analysis is being used, Gadolinium or Hydrogen, the selection cuts performed in the data to search for the neutrino signals changes. Although the Double Chooz experiment was design to have neutron capture on Gadolinium as the main analysis, this work uses both data set. Therefore, details of each analysis is presented in the following subsections.

### 4.5.1   Gadolinium Selection

For the neutron capture on Gadolinium, the following cuts are applied, where a detailed description of each one is given afterwards:

- **Prompt Event**

    - $0.7 \leq E_{\mathrm{vis}} \leq 12.2$ Mev
    - $Q_{max/tot} \leq 0.09$ and $T_{start}^{\mathrm{RMS}} \leq 40$ ns

- **Delayed Event**

  - $6 \leq E_{\text{vis}} \leq 12$ Mev
  - $Q_{max/tot} \leq 0.055$ and $T_{start}^{\text{RMS}} \leq 40$ ns

- **Coincidence**

  - $2 < \Delta T < 100$ $\mu$s

- **Isolation Cut Window**

  - 100 $\mu$s before and 400 $\mu$s after the prompt signal

- **Extra Muon Veto**

  - Veto events in a time window of 0.5 s, after a muon with $E_{\text{vis}} > 600$ MeV
  - Veto events coincident with an OV trigger

### Prompt Selection

The prompt energy cut is defined to fully cover energy range of the positron generated by the IBD. The lower limit of the prompt energy cut is set to be 0.7 MeV, which is well below 1.022 MeV, i.e. the minimum energy of the prompt signal, from two gamma rays from positron-electron annihilations, and where the trigger efficiency is still 100%. The upper limit of the prompt energy window, 12.2 MeV, was chosen to be well above the 9 MeV endpoint of the IBD spectrum. This introduces fast neutrons, stopping muons, and cosmogenic background events with prompt energies between 9 and 12.2 MeV into the IBD candidate sample. However, given some knowledge of the energy distribution of each of these backgrounds, these high energy events are used to constrain the backgrounds at lower energies, where a clean measurement of the backgrounds is not possible. Precise knowledge of these backgrounds at low energies is important because this is where spectral distortions in the IBD signal are expected to occur.

### Delayed Selection

The presence of a GC in the Double Chooz design ensures that the energy from neutron capture events on Gadolinium is fully absorbed most of the time. However, the neutron capture on Gadolinium visible energy distribution has a tail that extends down to energies of 4 MeV. The lower limit of the delayed energy window was chosen to cut at a relatively flat part fo the spectrum to suprpress teh systematic uncertainties associated with the energy cut efficiency. On the other hand, the upper limit was conservatively chosen to be 12 MeV, since this energy is well above the full absorption peak of neutron capture on Gadolinium and has negligible inefficiency for selecting IBD candidates. In addition, for delayed events a more aggressive LN cut can be placed than on the prompt, since events which deposit more energy in the ID tend to have smaller values of $Q_{max/tot}$.

### $\Delta T$ Cut

The time difference, $\Delta T$, between the prompt and delayed signals is related to neutron capture time in the NT which is approximately 30 $\mu$s. The $\Delta T$ distributions for IBD candidate events and accidental coincidences of uncorrelated events satisfying the prompt and delayed event energy cuts show that events with a $\Delta T > 100$ $\mu$s are dominated by accidental coincidences. IBD candidate events with $\Delta T > 2$ $\mu$s were shown to have reconstructed positions uniformly distributed throughout the target, while those with $\Delta T < 2$ $\mu$s were not, having most of the vertexes, reconstructed around the detector chimney, as shown in figure 4.25. This is an indication of stopping muon background.
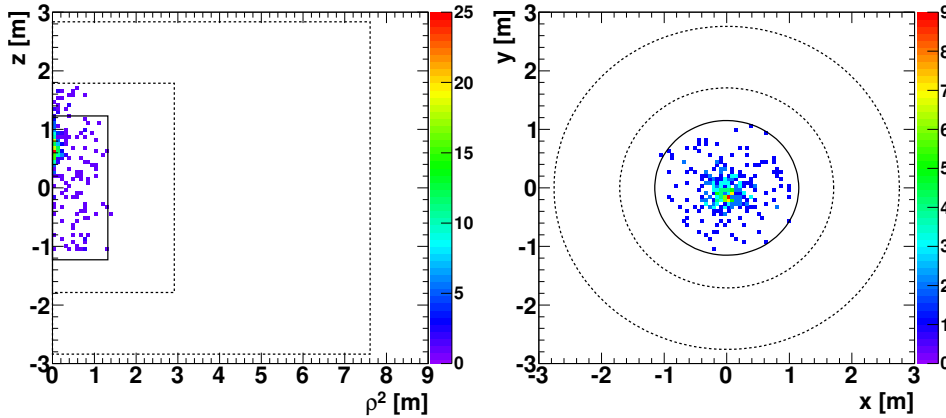
Figure 4.25: Reconstructed vertexes of the prompt signals within $0 < \Delta T < 2$ $\mu$s, in cylindrical coordinates. The lines indicates the boundaries of each detector volume.

## Isolation Cut

In order to suppress correlated backgrounds coming from chimney muons, an isolation cut is also imposed. IBD candidates with an additional trigger with a visible energy bigger than 0.5 MeV in the 100 $\mu$s preceding a prompt event or the 400 $\mu$s following the prompt event are discarded. This isolation cut removes events in the neutron capture peaks of both H and Gd, what indicates that the isolation cut is effective in rejecting double neutron capture events, as explained in section 4.4.2.

## Extra Muon Veto

In order to reduce the background contamination in the sample, two extra muon related veto time are applied. First, candidates within a 0.5 s window after a muon with energy larger than 600 MeV are tagged as cosmogenic isotope events and rejected, increasing the effective veto time to 9.2%. Second, candidates whose prompt signal is coincident with an OV trigger are also excluded as correlated background. Applying these extra vetoes yields an analysis live time of 227.93 days.

## Summary of Gd IBD Selection

Applying all the cuts described above, 8249 IBD candidates were selected which gives an averaged rate of $36.2 \pm 0.4$ events per day. A number of 8439.6 events were expected (without considering any background estimation). Figures 4.26, 4.27, and 4.28 summarizes the main quantities of these selected events.

### 4.5.2   Hydrogen Selection

To select IBD candidates with neutron capture on Hydrogen atoms, a few changes must be apply on the method used for the Gadolinium selection. Concerning the muon veto cut, the same 1 ms and OV coincidence are applied, however in the cosmogenic veto is not. The prompt energy cut is also kept the same. The main modifications are in the values of the remaining cuts and the inclusion of an addition cut on $\Delta R$, the spatial separation between the prompt and the delayed reconstructed vertices. A summary of the cut are presented below, where a detailed description of each cut is given afterwards.

- **Prompt Event**

    - Same for Gd analysis

(a) Prompt vs. Delayed Energy Spectrum                    (b) $\Delta$T Distribution
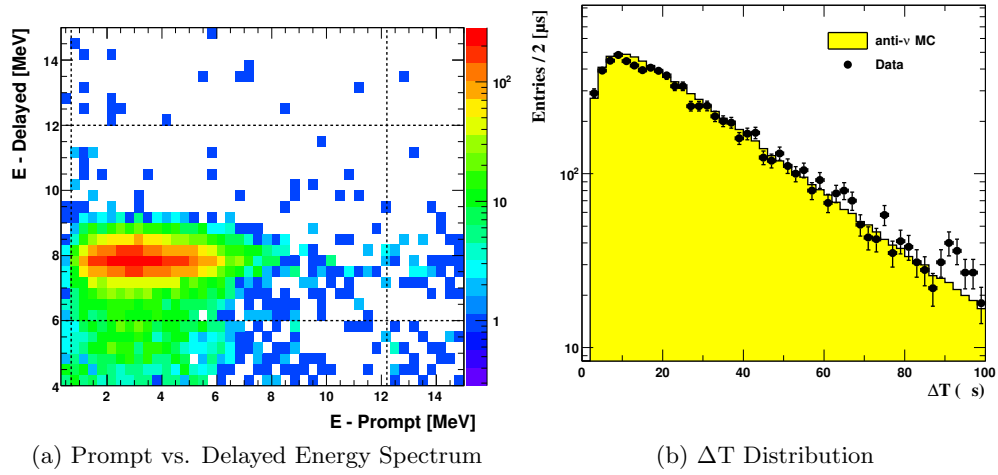
Figure 4.26: Energy correlation between prompt and delayed events on the left. Y-axis shows the Gd-peak between [7,9] MeV and its Compton edge extending to low energies. On the right is the time correlation between the prompt and delayed. Both data (black points) and MC (yellow histogram) agrees with each other, and it shows the fast neutron thermalization time ($\sim 5$ $\mu$s), and the slower neutron capture by Gd time ($\sim 30$ $\mu$s).



(a) Prompt $z\rho^2$ position                               (b) Delayed $z\rho^2$ position
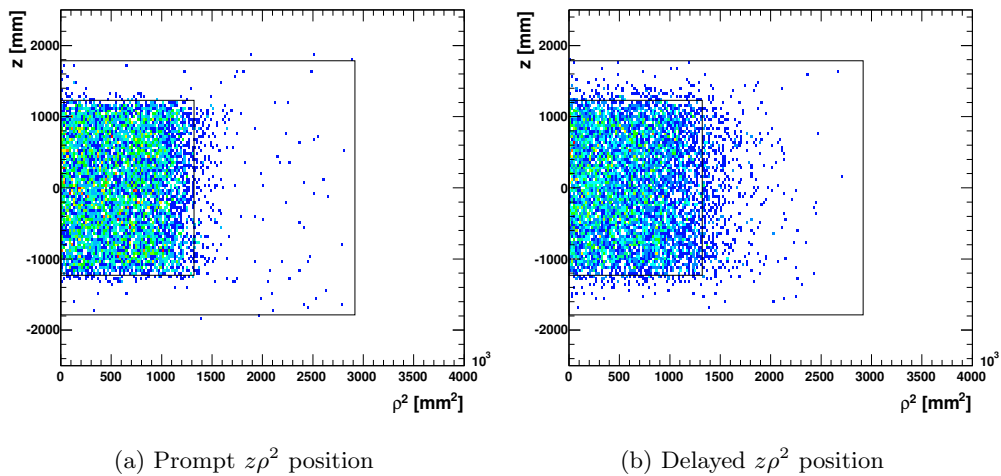
Figure 4.27:  Vertex distributions for the prompt (left) and delayed (right) IBD candidates. The vertices are limited in the NT by the presence of Gd, which implicitly define the target as the fiducial volume.
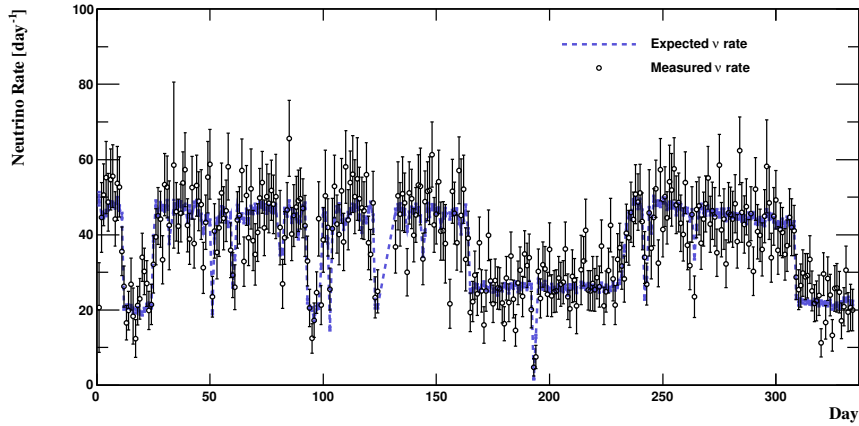
Figure 4.28: Observed (black points) and expected (blue doted line) IBD rate as a function of data taking day. The background is not subtracted from the data. The fluctuation of the rate is due to fluctuations of the reactors thermal power, as showed in figure 4.2.

- **Delayed Event**

    - $1.5 \leq E_{\text{vis}} \leq 3.0$ Mev
    - $Q_{max/tot} \leq 0.9$ and $T_{start}^{\text{RMS}} \leq 40$ ns

- **Coincidence**

    - $10 < \Delta T < 600$ $\mu$s

- **Spatial Separation**

    - $\Delta R < 900$ mm

- **Isolation Cut Window**

    - 600 $\mu$s before and 1000 $\mu$s after the prompt signal

- **Extra Muon Veto**

    - Veto events coincident with an OV trigger

**Delayed Selection**

The energy window has been moved to account for the Hydrogen's neutron capture peak at 2.22 MeV. The window from 1.5 to 3.0 MeV contains the majority of neutron capture by Hydrogen throughout the NT and GC volumes.

**$\Delta T$ Cut**

The coincidence time cut was modified to accommodate the longer capture time in the GC and to reject backgrounds. The upper bound of 600 $\mu$s was chosen to be well above the capture time constant of 200 $\mu$s in the GC, where most neutron captures on Hydrogen occur. The lower bound of 10 $\mu$s was chosen to reject both stopping muons and time-correlated light noise.

**Spatial Separation**

The spatial correlation cut, $\Delta R$, is added to efficiently reject accidental background. Accidentals are quantified using the off-time selection, as is explained in section 4.7.1. Figure 4.42 shows the ratio of $\bar{\nu}_e$ candidate statistics over the accidentals statistics as a function of $\Delta R$ cut value. It is possible to see on this figure that, around 900 mm, the spectrum has a contribution mainly due to accidentals. This is one motivation of using 900 mm as the upper bound of the $\Delta R$ cut. In addition, this value keeps the systematic error from the $\Delta R$ cut small.

**Isolation Cut**

For the Gadolinium analysis, the time window to the past of the prompt is extended to -100 $\mu$s, which is about three times larger than the neutron capture time in the NT. However, for the Hydrogen analysis, the large fraction of the signal comes from the GC volume where the neutron capture time is about 200 $\mu$s. Therefore the multiplicity time window is extended to 600 $\mu$s toward the past of the prompt event, which is roughly three times the neutron capture time in the GC. Also the multiplicity time window is extended to 1000 $\mu$s after the prompt event for a similar reason.[3]

**Summary of H IBD Selection**

Applying all the cuts described above, 36284 IBD candidates were selected which gives an averaged rate of 151.14$\pm$0.79 events per day. A number of 17690 events were expected (without considering any background estimation). Figures 4.29 and 4.30 summarizes the main quantities of these selected events.

## 4.6 Efficiency of IBD Selection

Since the current phase of the Double Chooz experiment involve the its far detector only, the efficiencies related to the data selection are naturally taken into account comparing data with MC expectation, performing an identical selection on the MC. Important quantities are the remaining discrepancies between data and MC that need to be assumed as systematic uncertainties. In the following sections a description of the relevant selection efficiency and related systematics is provided.

### 4.6.1 Muon Veto Efficiency

As described in section 4.4.2, the muon veto of 1 ms introduces an IBD selection inefficiency of 4.4%. However, this inefficiency must be corrected to account for muons whose veto windows overlap and for the time correlation between the IBD delayed coincidence pair. For example, if two muons are separated by a time window ($\Delta T_{\mu\mu}$) smaller than 1 ms, then the total veto time for these overlapping muons is actually $\Delta T_{\mu\mu} + 1$ ms. Therefore, a correction of -0.2% is applied to the above inefficiency to account for this overlapping muon effect based on the measured $\Delta T_{\mu\mu}$ distribution for the run period.

In addition the effective muon veto time window is actually larger than 1 ms for delayed coincidence pairs, because both the prompt and delayed events must fall outside the veto window. Thus, this effects leads to a further correction of +0.1% for IBD events with an approximately exponential $\Delta T$ distribution with a time constant of about 26 $\mu$s.

---

[3]This time is 5 times neutron capture by Hydrogen time in the GC

(a) Delayed Energy Spectrum



(b) $\Delta T$ Distribution



(c) Prompt $z\rho^2$ position
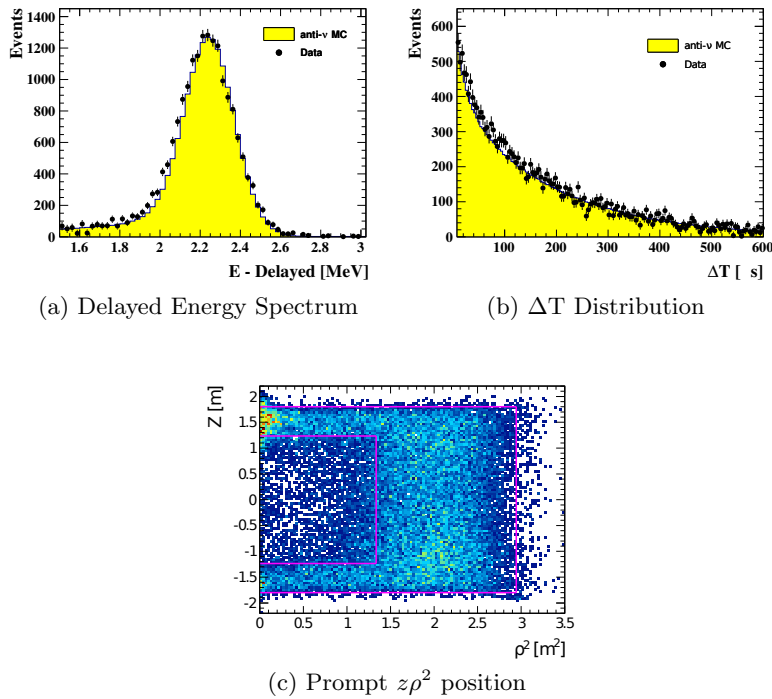
Figure 4.29: Delayed energy distribution shows the H-peak between [1.5,3.0] MeV and its Compton edge extending to low energies. The time correlation between the prompt and delayed shows that both data (black points) and MC (yellow histogram) agree with each other, and it shows the slower neutron capture by H time ($\sim 100\ \mu$s). For both energy and $\Delta T$ distribution the accidentals, as calculated in section 4.7.1.2, are subtracted. Vertex distributions for the prompt IBD candidates concentrated in the GC as expected.
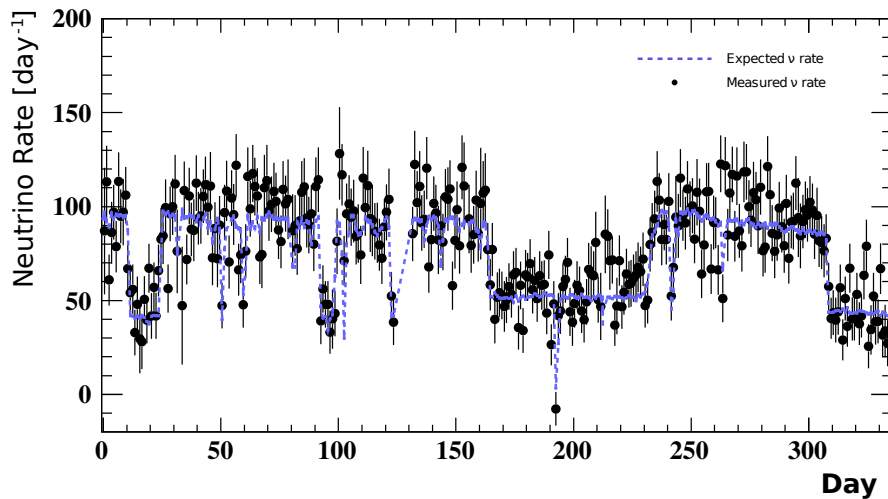


Figure 4.30: Observed (black points) and expected (blue doted line) IBD rate as a function of data taking day for the Hydrogen analysis. The accidental background, calculated in section 4.7.1.2, is subtracted from the data. The fluctuation of the rate is due to fluctuations of the reactors thermal power, as showed in figure 4.2.

(a) Prompt Selection Cut



(b) Delayed Selection Cut
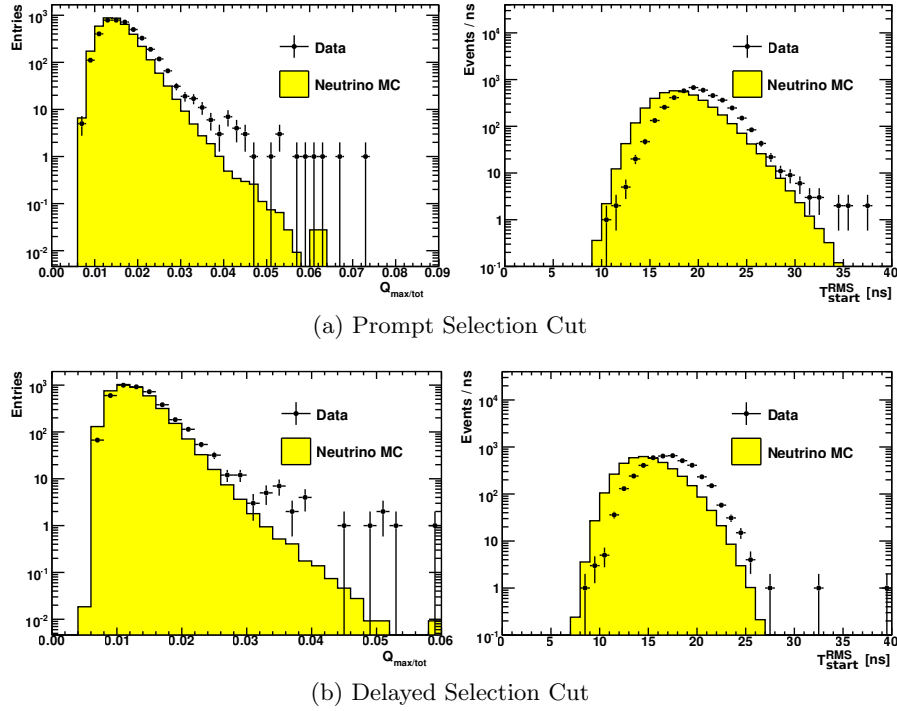
Figure 4.31: Data and MC distributions of $Q_{max/tot}$ (left) and $T_{start}^{RMS}$ (right), for both prompt and delayed selection cuts of the Hydrogen analysis.

In summary, the muon veto introduces an IBD selection inefficiency of 4.3% in the data. A correction factor of 0.957 must be applied to the MC, in which no muons are simulated. Because the resolution of the trigger clock is 16 ns ($<< 1$ ms), the uncertainty on the muon veto correction factor is negligible.

### 4.6.2 Light Noise Cut Efficiency

Light noise cuts were chosen to have negligible inefficiency for selecting IBD events. Figure 4.31 shows the $Q_{max/tot}$ and $T_{start}^{RMS}$ distributions for the prompt and delayed event of IBD candidates (signal and background) in data and MC. There is a slight shift of the data with respect to the MC in both distributions, but in all cases the LN cut is well separated from the distribution of IBD candidate events and induces negligible inefficiency.

### 4.6.3 Isolation Cut Efficiency

The isolation cut introduces an IBD selection inefficiency due to the random coincidence of a trigger with $E_{vis} > 0.5$ MeV within 100 $\mu$s before or 400 $\mu$s after the prompt event of an IBD delayed coincidence pair. This inefficiency can be accurately determined from the data by measuring the rate of triggers which satisfy the isolation cut energy threshold and multiplying by the 500 $\mu$s isolation window. The isolation cut IBD selection efficiency for the data is found to be 99.5% with negligible uncertainty. Therefore, the IBD signal MC must be corrected to account for this inefficiency since it contains no backgrounds.

### 4.6.4 Prompt Energy Cut Efficiency

The minimum visible energy for the prompt event of an IBD delayed coincidence is 1.022 MeV coming from the 2 positron annihilation gammas and well above the 0.7 MeV

low energy prompt selection cut. As described in section 3.4.5.1, the $^{68}$Ge calibration source also produces two positron annihilation gammas totalling 1.022 MeV which is used to tune the detector MC. Based on the good agreement of data and MC for the $^{68}$Ge calibration source, the IBD signal MC is used to determine the inefficiency of the prompt low energy cut. The inefficiency is found to be < 0.1% and therefore negligible.

### 4.6.5  Neutron Detection Efficiency - Gadolinium

The most significant source of inefficiency is the one related to the neutron detection. The efficiency related to the identification of the delayed events coincides with the neutron detection efficiency, $\varepsilon_{\text{neutron}}$, and it can be factorized in the following terms:

$$\varepsilon_{\text{neutron}} \equiv \varepsilon_{\text{Gd}} \times \varepsilon_{\Delta T} \times \varepsilon_{E_{\text{delayed}}}, \tag{4.37}$$

where $\varepsilon_{\text{Gd}}$ is the fraction of neutron captures on Gd, $\varepsilon_{\Delta T}$ is the fraction of neutron capture within the coincidence window $\Delta T$, and $\varepsilon_{E_{\text{delayed}}}$ is the fraction of captures in the delayed cut energy range, and $\varepsilon_{\Delta R}$ is the fraction of captures in the spacial separation cut range. All the terms in equation 4.37 are evaluated comparing data and MC for $^{252}$Cf calibration source deployed along the detector z-axis and in the guide tube. Since $^{252}$Cf also undergoes spontaneous fission, emitting neutrons and also gammas up to 30 MeV, the following selection cuts on the data, similar to IBD selection, can be applied:

- Muon veto and LN reduction: same as IBD selection

- **Prompt**

    - Time isolation: $\Delta T > 1.5$ ms from the last event
    - Energy cut: $0.5 < E_{\text{vis,prompt}} < 30$ MeV

- **Delayed**

    - Time correlation: $\Delta T > 1$ ms
    - Energy cut: $0.5 < E_{\text{vis,delayed}} < 20.5$ MeV

Figure 4.32 shows the energy spectra of prompt and delayed signals, the time difference between the prompt and delayed signals and multiplicity of delayed neutrons in comparison with the MC simulation. The data is in agreement with the MC except for the prompt energy distribution. The prompt energy spectrum is not well reproduced by the MC simulation for $^{252}$Cf fission due to the difference of the MC event generation but it does not affect other features since the delayed signals are independent from the prompt energy. In addition, due to the neutron multiplicity of 3.76 per fission, peaks for simultaneous captures of two neutron on Gd an H ($\sim 10$ MeV) and two captures on Gd ($\sim 16$ MeV) are also observable in figure 4.32b.

#### Fraction of Neutron Capture on Gd

The Gd-fraction, $\varepsilon_{\text{Gd}}$, is the ratio of the number of captured neutrons on Gd, $N_{\text{n}-\text{Gd}}$, to the sum of those on H, $N_{\text{n}-\text{H}}$, and Gd defined as follows

$$N_{\text{n}-\text{Gd}} = \frac{N_{\text{n}-\text{Gd}}}{N_{\text{n}-\text{Gd}} + N_{\text{n}-\text{H}}}. \tag{4.38}$$

For the Gd analysis, the delayed event cut efficiency depends directly on the fraction of neutrons which are captured on Gd, instead of H. The calculation of the fraction of captured neutrons were performed by a fit with three Gaussian functions (H: 2.2 MeV

(a) Prompt Energy

(b) Delayed Energy

(c) $\Delta T$

(d) Multiplicity of neutrons per fission
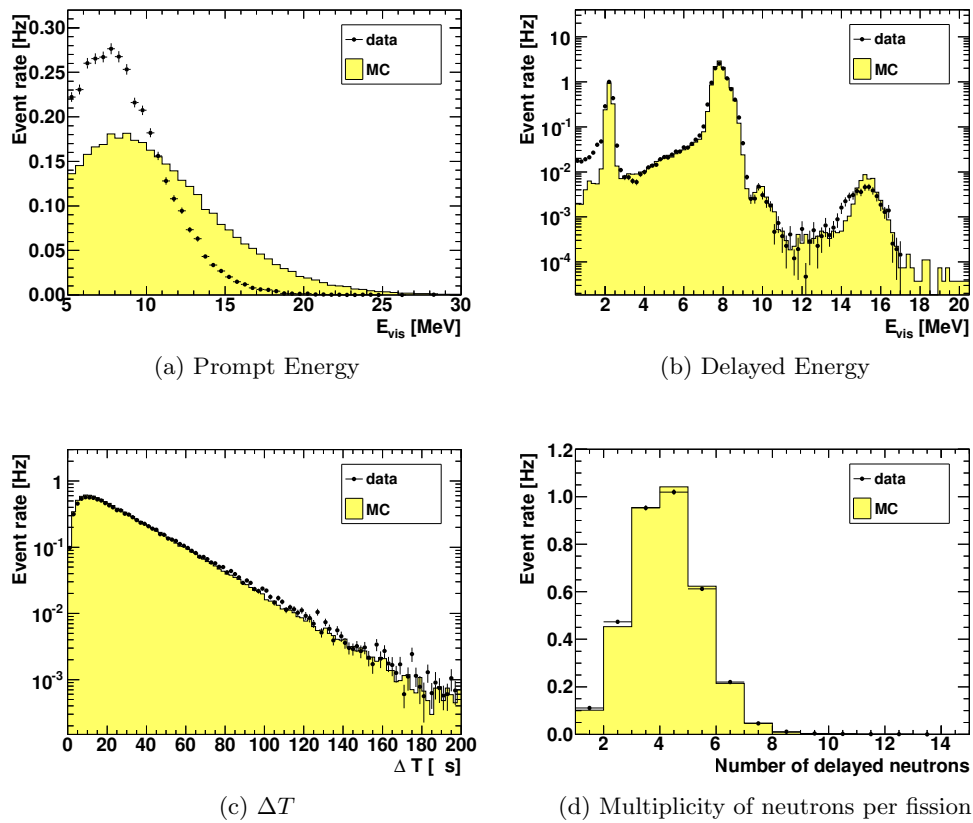
Figure 4.32: Distribution for the prompt and delayed energy, time difference and multiplicity of neutrons per fission with $^{252}$Cf deployed at the center of the NT.
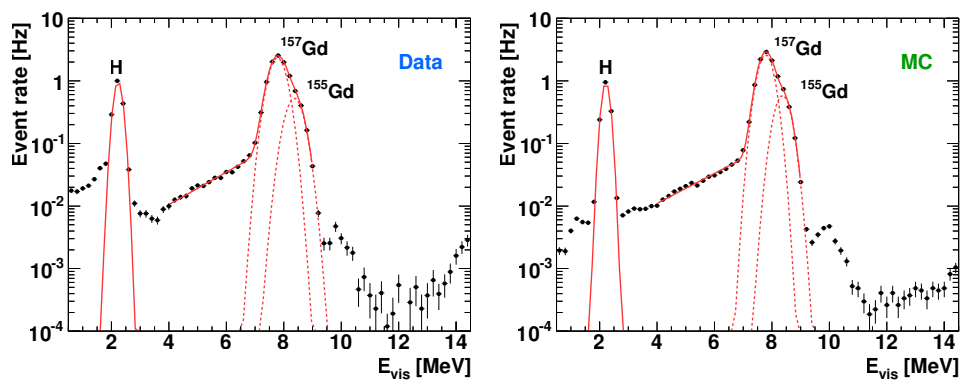


Figure 4.33: Delayed signal spectra with $^{252}$Cf for data (left) and MC (right) with fitting results represented by the red lines.

Gd: 7.94 MeV for $^{157}$Gd and 8.54 MeV for $^{155}$Gd) at the delayed energy spectrum, with $^{252}$Cf deployed at the center of the NT and integrating the functions for both the data and MC independently. Results of the fit is shown in figure 4.33. Applying this method, the Gd fraction is $86.4 \pm 0.15\%$ for the data and $88.0 \pm 0.09\%$ for the MC. The data over MC ratio is $0.982 \pm 0.002$ and, consequently, the MC is corrected by this factor.

### $\Delta T$ Cut Efficiency

The $\Delta T$ cut efficiency represents the fraction of neutron captures within the [2, 100] $\mu$s time window. The efficiency is calculated as a ratio between the events in [2, 100] $\mu$s and the events in [0, 200] $\mu$s as function of the $^{252}$Cf source position along the z-axis as shown in the left plot of figure 4.34, since almost all neutrons are captured on Gadolinium within 200 $\mu$s. The overall efficiency, averaged over the detector volume, is found to be
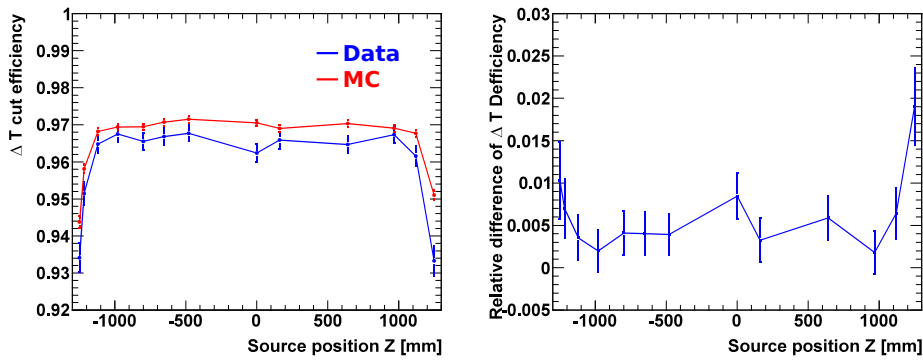


Figure 4.34: $\Delta T$ cut efficiency (left) and data/MC discrepancy (right) as a function of the $^{252}$Cf source position along the z-axis.

96.4% and 96.7% for data and MC, respectively. The uncertainty are estimated from the discrepancies between data and MC simulation, preformed with a custom Geant4 code to properly account for the low energy neutron physics. Standard Geant4 MC, in fact, assumes neutron capture on free-H, when it is known the Hydrogen is in a molecular bound state. The effect is a shorter live time than the observed ones. The data are found in good agreement with MC as shown in the right plot of figure 4.34, resulting in a systematic uncertainty of 0.5%. This figure also shows the normalized efficiency weighted by the Gd fraction.

### Energy Cut Efficiency

The lower bound of the delayed energy selection introduces some inefficiency if a gamma from the Gd capture escapes from the detector active volume. The efficiency due to the energy containment is evaluated to be 94.1% by the ratio between the events selected in [6,12] MeV and the events in [4,12] MeV, with $^{252}$Cf data deployed along the z-axis and guide tube. The energy containment efficiency as a function of the source position in the detector is shown in figure 4.35 for the z-axis. The systematic uncertainty is estimated by the data/MC discrepancy to be 0.7%. Data/MC discrepancies are shown in the right plot of figure 4.35, as a function of the source position. The energy cut efficiency, as well as the energy resolution, decreases around the boundary to the GC because the increase of the gamma rays fraction that escapes from the scintillator region.

A change in the energy scale affects the efficiency of both the prompt and delayed energy cuts. This effect is modelled in the Final Fit framework, so it does not need to be included explicitly in the detection efficiency uncertainty.
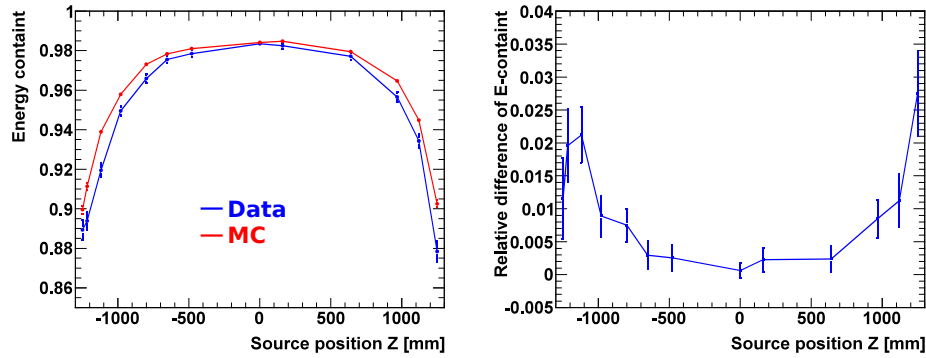
Figure 4.35: $\Delta E$ cut efficiency (left) and data/MC discrepancy (right) as a function of the $^{252}$Cf source radial position along the ID z-axis

**Spill-in / out**

Neutrons are captured on Gd once their energy become thermal. The thermalization process happen through multiple elastic scattering between the neutron and the nuclei of the atoms of the scintillator, the characteristic time is of about 30 $\mu$s. During the thermalisation process, the neutron is diffused in the scintillator. If an IBD occurs in the NT, its neutron could reach the GC volume and be captured on H. On the other hand, the neutrino could interact in the GC and the neutron be captured on Gd in the NT volume. Such effects are called *spill-out* and *spill-in* respectively. Such effects have to be taken into account since they do not compensate precisely, resulting in a net spill-in current which impacts on the normalisation of the MC simulation. Due to the presence of Gd in the NT liquid, the mean live time of a neutron in the target volume is shorter ($\tau_{\mathrm{Gd}} \sim 30$ $\mu$s) than the one in the GC ($\tau_{\mathrm{H}} \sim 100$ $\mu$s). So the spill-in probability is expected to be larger than the spill-out. The spill-in/out effect is studied with $\bar{\nu}_e$ MC sample and the systematics effect due to the MC model (0.22%), the concentration of Gd in the target (0.10% wt.) and the concentration of H in the GC (negligible effect) are taken into account. The variation due to spill-in/out was estimated to be 1.35$\pm$0.30(sys.)$\pm$0.04(stat.) % [90], to the number of selected IBD candidates. Although spill-in / out does not require a MC correction, as the MC was believed to accurately model neutron migration between the detector volumes, its systematic uncertainty is accounted to the overall efficiency uncertainty in the IBD prediction.

### 4.6.6   Neutron Detection Efficiency - Hydrogen

In the Hydrogen analysis, a different approach was used for calculation of neutron detection efficiency. The uncertainties on neutron detection efficiency and on the number of protons ($N_p$) in each detector volume are grouped together because both factors contribute to an overall signal normalization uncertainty, and both factors have different magnitudes in each of the detector volumes. Thus, the expression $\varepsilon N_p$ in equation 4.37 becomes the sum of three proton number weighted efficiencies, as follows

$$\varepsilon N_p = \varepsilon_{\mathrm{neutron,NT}} \times N_{p,\mathrm{NT}} + \varepsilon_{\mathrm{neutron,GC}} \times N_{p,\mathrm{GC}} + \varepsilon_{\mathrm{neutron,Spill}} \times N_{p,\mathrm{Spill}}, \qquad (4.39)$$

where $N_{p,\mathrm{NT}}$ is the proton number in the NT, $N_{p,\mathrm{GC}}$ is the proton number in the GC, $N_{p,\mathrm{Spill}}$ is an effective number of protons for spill events, and $\varepsilon_{\mathrm{neutron,Spill}}$ is an effective efficiency of spill events. These "effective" numbers come from the spill-in/out studies, which combine values from different event classes (spill from NT to GC, from acrylics into the scintillator liquids, etc.) into a common proton number and neutron efficiency.

The neutron efficiency for each volume is then calculated in an analogue way as equation 4.37:

$$\varepsilon_{\text{neturon,NT}} = \varepsilon_{\text{H,NT}} \times \varepsilon_{\Delta T,\text{NT}} \times \varepsilon_{E_{\text{delayed}},\text{NT}} \times \varepsilon_{\Delta R,\text{NT}}, \tag{4.40}$$

$$\varepsilon_{\text{neturon,GC}} = \varepsilon_{\text{H,GC}} \times \varepsilon_{\Delta T,\text{GC}} \times \varepsilon_{E_{\text{delayed}},\text{GC}} \times \varepsilon_{\Delta R,\text{GC}}, \tag{4.41}$$

where the $\Delta R$ cut efficiency, $\varepsilon_{\Delta R}$, was added since this cut is applied for the Hydrogen analysis. These efficiencies can be treated separately since the correlation among them are small (< 1 %) [91]. Moreover, the $^{252}$Cf deployment data with same cuts that was used for the Gadolinium analysis is used here to estimate the efficiencies and their uncertainties.

**Fraction of Neutron Capture on H**

The fraction on neutrons captured in the NT volume, can be estimated by subtracting the capture fraction of Gadolinium from 1, i.e.,

$$\varepsilon_{\text{H}}^{\text{Data}} = 1.0 - \varepsilon_{\text{Gd}}^{\text{Data}} = 13.60 \pm 0.15\% \tag{4.42}$$

$$\varepsilon_{\text{H}}^{\text{MC}} = 1.0 - \varepsilon_{\text{Gd}}^{\text{MC}} = 12.00 \pm 0.10\% \tag{4.43}$$

The remaining tail of $^{12}$C capture below 4 MeV is considered to be negligible since the total fraction of $^{12}C$ captures is about 0.1 %. As the peak of the capture energy distribution is 4.95 MeV, any tail below 4 MeV can be ignored.

For the GC volume, the Hydrogen capture fraction efficiency estimation is performed by analysing the $^{252}$Cf source deployment in teh guide tube at the GC positions, in order to reduce the escape of neutrons into the NT, where the fraction is considerably different. The data and MC spectra are shown in figure 4.36, and both agrees well, including the tails of the hydrogen capture peak which are dominated by energy being lost into the Buffer volume. The efficiency in data is 99% and 98.8% in the MC. Therefore, the
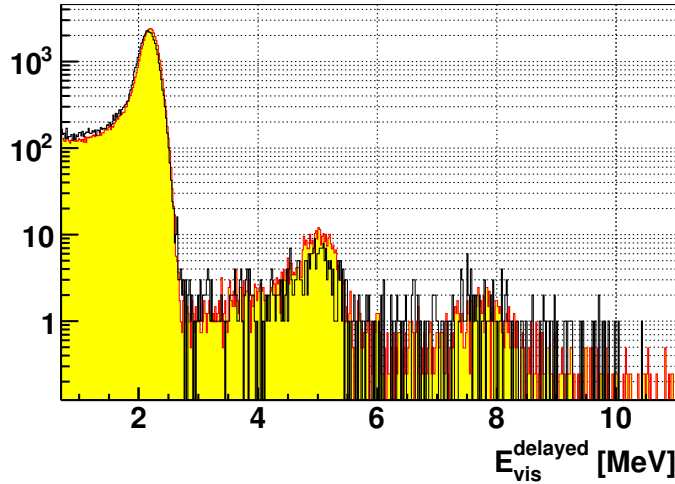


Figure 4.36: Delayed visible energy spectrum of $^{252}$Cf (data in black, MC in yellow). Several runs far away from the NT have been combined.

data/MC ratio is $100.20 \pm 0.3$ %.

**$\Delta T$ Cut Efficiency**

The $\Delta T$ cut efficiency for the Hydrogen analysis is estimated in a similar way as for the Gadolinium. It is calculated as a ratio between the events in [10, 600] $\mu$s and the events

in [0, 1000] $\mu$s as function of the $^{252}$Cf source position along the z-axis, as follows

$$\varepsilon_{\Delta T} = \frac{1.5 < E_{\mathrm{vis}} < 3.0 \text{ MeV} \otimes \Delta R < 900 \text{ mm} \otimes 10 < \Delta T < 600 \ \mu s}{1.5 < E_{\mathrm{vis}} < 3.0 \text{ MeV} \otimes \Delta R < 900 \text{ mm} \otimes 0 < \Delta T < 1000 \ \mu s} \qquad (4.44)$$

The position dependence in the z-axis and guide-tube, for data and MC, is shown in figure 4.37. The data efficiency was found to be $(69.55 \pm 1.24)\%$ and $(90.41 \pm 0.15)\%$
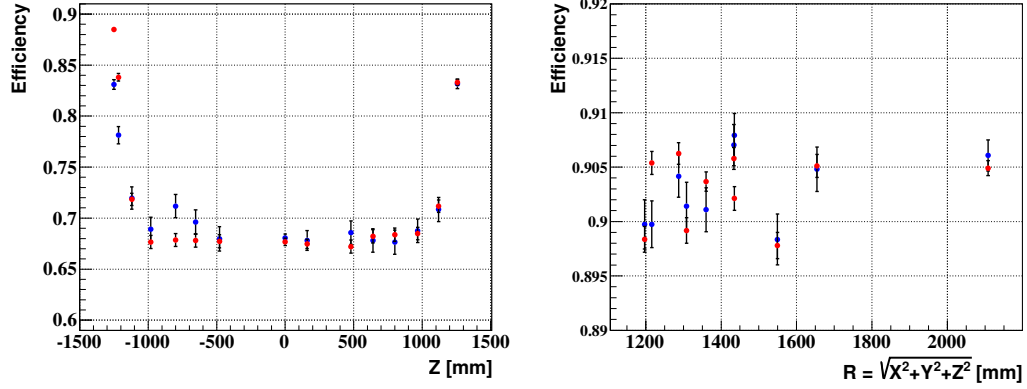


Figure 4.37: Data (blue points) and MC (red points) for the $\varepsilon_{\Delta T}$ in the NT (left) and GC (right) volumes.

for the NT and GC volumes, respectively.

### $\Delta R$ Cut Efficiency

Similarly to the $\Delta T$ cut, the $\Delta R$ cut efficiency is calculated as the ratio between events that are selected by and cut and all the events, as follows

$$\varepsilon_{\Delta R,\mathrm{NT}} = \varepsilon_{\Delta R,\mathrm{GC}} = \frac{\Delta R < 900 \text{ mm} \otimes 1.5 < E_{\mathrm{vis}} < 3.0 \text{ MeV} \otimes 10 < \Delta T < 600 \ \mu s}{1.5 < E_{\mathrm{vis}} < 3.0 \text{ MeV} \otimes 10 < \Delta T < 600 \ \mu s} \tag{4.45}$$

The position dependence in the z-axis and guide-tube, for data and MC, is shown in figure 4.38. The data efficiency was found to be $(93.61 \pm 0.48)\%$ and $(95.84 \pm 0.18)\%$
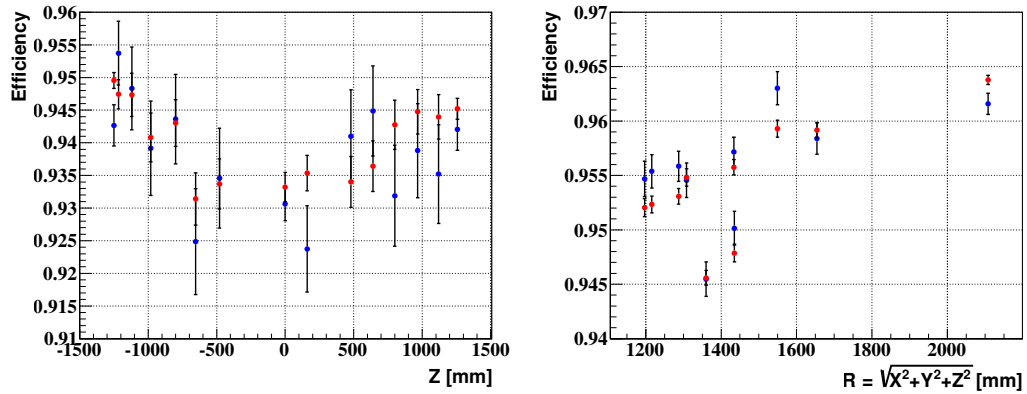


Figure 4.38: Data (blue points) and MC (red points) for the $\varepsilon_{\Delta R}$ in the NT (left) and GC (right) volumes.

for the NT and GC, respectively.

**Energy Cut Efficiency**

Finally, the same approach taken for the $\Delta T$ and $\Delta R$ efficiencies is used to estimate the delayed energy cut efficiency, following the expression

$$\varepsilon_E = \frac{1.5 < E_{\text{vis}} < 3.0 \text{ MeV} \otimes \Delta R < 900 \text{ mm} \otimes 10 < \Delta T < 600 \ \mu\text{s}}{0.7 < E_{\text{vis}} < 3.0 \text{ MeV} \otimes \Delta R < 900 \text{ mm} \otimes 10 < \Delta T < 600 \ \mu\text{s}} \tag{4.46}$$

The lower bound for the full containment (0.7 MeV in the dominator) is based on the 100% trigger efficiency threshold. The upper bound for the energy cut is set high enough to fully contain the neutron capture peak by Hydrogen events.

The data efficiency was found to be $(96.79 \pm 0.28)\%$ and $(92.20 \pm 0.21)\%$ for the NT and GC, respectively.

**Spill-in / out**

In the Hydrogen analysis, the spill-in / out studies is considerably richer compared to Gadolinium, since all the neighbouring sub volumes of the fiducial volume (NT + GC) contribute to spill events: NT, GC, Buffer, and both acrylics vessels, including their feet and stiffener. When quantifying the data / MC uncertainty due to spill events, an additional uncertainty beyond the efficiency and proton number uncertainty can arise from an imperfect MC modelling of the molecular bindings in the detector liquids and in the neutron interaction with theses liquids, which leads to uncertainties of the number of events migrating from one sub volume to another, leading to an uncertainty in the total number of selected neutrino events.

Following the strategy for the Gadolinium analysis, the Hydrogen concentration in the GC scintillator, the acrylic target vessel geometry and thickness, the neutron mobility model and the Gadolinium concentration of the NT scintillator were examined as the mains sources of uncertainty. Among these uncertainties, the neutron mobility model has been the major source of uncertainty, where the other sources had a negligible impact on the spill in / out uncertainty. A comparison with two MC data set were performed, where the thermal neutron transport model was switched off in one of them ("NeutronTH Off"). Since this "NeutronTH Off" models the slow neutron physics imperfectly, the discrepancy of the two model were taken into account to estimate the model uncertainty. Overall, the relative uncertainty on the total number of events due to imperfections in the understanding of the neutron mobility is 1.17% [92].

**Summary**

Combining all the results presented so far, table 4.5 summarizes the neutron detection efficiency estimation for each detector volume.These numbers yield the following absolute efficiencies:

$$\varepsilon_{\text{neutron,NT}} = 8.64 \pm 0.18 \ \% \ \text{ and } \ \varepsilon_{\text{neutron,GC}} = 78.53 \pm 0.36 \ \%. \tag{4.47}$$

Table 4.5: Summary of Hydrogen fraction as well as cut efficiencies from $^{252}$Cf source calibration study for NT and GC volumes.

| Detector Volume | H Fraction | $\varepsilon_{\Delta T}$ | $\varepsilon_{\Delta R}$ | $\varepsilon_{E_{\text{delayed}}}$ |
|---|---|---|---|---|
| NT | $0.1342 \pm 0.0015$ | $0.6955 \pm 0.0124$ | $0.9361 \pm 0.0048$ | $0.9679 \pm 0.0028$ |
| GC | $0.9830 \pm 0.0030$ | $0.9041 \pm 0.0015$ | $0.9584 \pm 0.0018$ | $0.9220 \pm 0.0021$ |

Finally, a relative uncertainty of 1.04% on the detection efficiency and 0.9448 as the MC correction factor was found. Considering the additional uncertainty coming form the number of spill-in/out events of 1.17%, the relative total uncertainty on the total number of events, due to detection efficiency, is 1.57%.

## 4.7 Background Estimation

As explained in section 3.5, the backgrounds that can mimic a true neutrino signal must be understood and estimated with the best precision as possible. In this section the methods used to estimate each background, together with their results, are described. These methods can be similar or not for the Gadolinium and Hydrogen analysis, and the differences will be mention when necessary.

### 4.7.1 Accidentals

There are two ways to estimate the accidental rate background: the off-time window and the analytical methods. While the first is the main estimator, the later is used as a cross-check method, for both Gadolinium and Hydrogen analysis. These methods are adapted for each analysis and their details are described in the following sections.

#### 4.7.1.1 Gadolinium

Accidental is the source of background that contributes the least, since the event rate in the delayed energy range is low. Using the off-time window method is possible to estimate the accidental rate and prompt spectrum, and by the analytical method, the rate is cross-checked.

**The Off-Time Window Method**

The off-time window method is the main one to estimate the accidental contribution as a background source. Since accidentals are uncorrelated signals that pass all the neutrino selection cuts, one would expect its $\Delta T$ distribution as flat, and a prompt spectrum similar to the detector's single triggers one. The flat time distribution is due to the fact that both prompt and delayed signals are uncorrelated, and no time window is expected to be preferred among the others. In this way, the accidental candidates search follows the steps:

- Selection a prompt candidate, where no trigger should be present around it (Isolation);

- Open a time window interval (off-time), where the prompt signal would be. This position on the time scale is referred as a virtual prompt and the time distance between the virtual and the real prompt is defined as:

$$T_n = T_{\text{initial}} + (n - 1) \times \Delta T_{\text{ws}} \tag{4.48}$$

  where $T_{\text{initial}}$ is a initial size of when the windows should start on the time scale, $n$ is the number of a current window that can vary from 1 to any desirable number ($N$), and $\Delta T_{\text{ws}}$ is the size of each time window, defined by the size of the multiplicity cut;

- Search for a delayed trigger in the $n_{th}$ (equation 4.48) window in a $\Delta$T interval;

- Apply the isolation cut around the virtual prompt, where only the delayed candidate should be present.

If many intervals $N$ are used, the number of select events is increased, decreasing the statistical uncertainty. This method is ilustraded in figure 4.39.
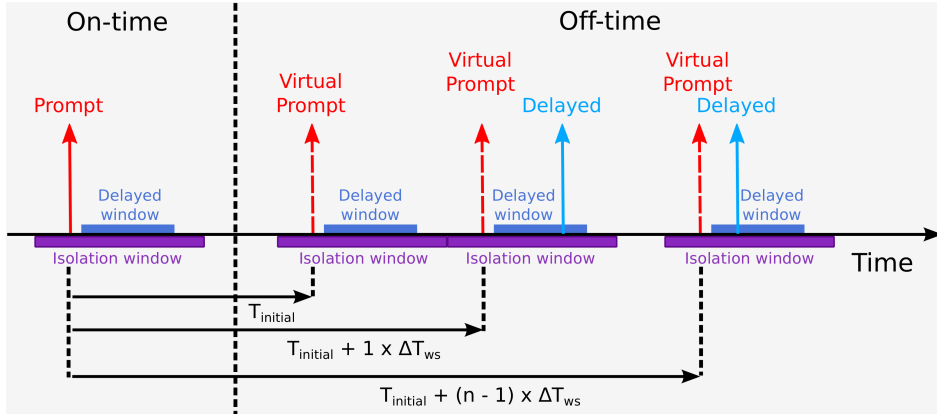


Figure 4.39: On-time and off-time event selection scheme methods

A one second offset for $T_{\text{initial}}$ is adopted to exclude coincidences by long lived bet emitters such as $^{12}$B ($\tau = 29.14$ ms, $Q = 13.4$ MeV). A total of 198 off-time windows, each separated by 500 $\mu$s, are used.

The cuts applied to select the events are the same as presented in section 4.5.1. However, since the prompt and delayed events are separated by a time window bigger than 1 ms, the two separate isolation windows are used for each event. For the 228.15 days of detection live time, 11771 events were selected, that are converted to a rate value as follows

$$R_{\text{acc.}} = \frac{\text{Acc. Candidates}}{\text{LiveTime} \times N}. \tag{4.49}$$

This leads to an accidental rate of $0.261 \pm 0.002$ events per day. Figure 4.40 shows that the accidental prompt energy distribution agrees with the detector singles and that the time distribution is flat, as expected.

**The Analytical Method**

The other way to calculate the accidentals rate is the analytical method, which consists of the product of the single rate of each candidate (prompt and delayed) times the cut



(a) Prompt spectrum                                    (b) $\Delta$T
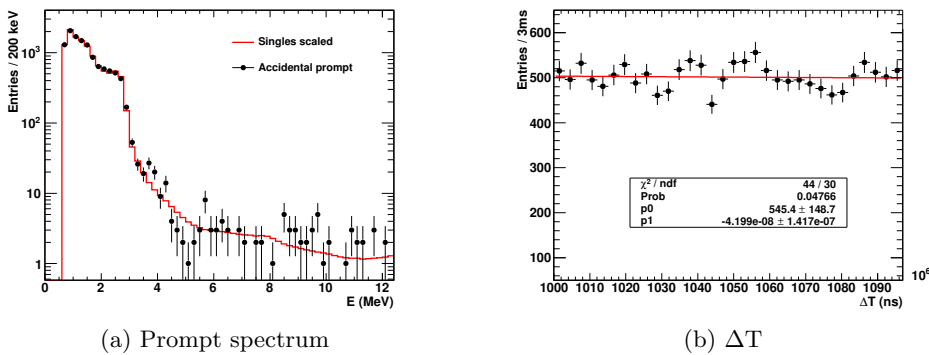
Figure 4.40: Accidentals distributions for the prompt energy, where the dots are the data acquired using the off-time method, and the scaled detector valid triggers spectrum is represented in red. The $\Delta T$ distribution is flat, as expected for uncorrelated events.

conditions and corrections, as defined in the following equation:

$$R_{\text{acc.}}^{\text{analytical}} = R_{\text{prompt}} \times R_{\text{delayed}} \times \Delta T_{\text{coinc.}} \tag{4.50}$$

where $R$ is the single rate for the prompt and delayed selection cut and $\Delta T_{\text{coinc.}}$ is the time interval used to search the delayed signal. For the period concerning the data set, the single rates were

$$R_{\text{prompt}} = 7.6025 \pm 0.0006 \text{ Hz} \ \ \text{and} \ \ R_{\text{delayed}} = 0.00412 \pm 0.00002 \text{ Hz}, \tag{4.51}$$

which, considering the 98 $\mu$s of delayed coincidence time window, gives a rate of $0.262 \pm 0.002$ events per day, in good agreement with the off-time method.

### 4.7.1.2   Hydrogen

Contrary to the Gadolinium, accidentals gives the large contribution to background in the Hydrogen analysis, since the energy range of the delayed event, [1.5,3.0] MeV, is located at the same region with high environmental radioactivity, increasing the probability of uncorrelated delayed coincidences. Thus, the accidental on the Hydrogen analysis needs to be investigated in more details, than it was performed for the Gadolinium analysis.  In the following subsections the changes on the off-time and analytical methods are described.

**Off-Time Method**

Initially, the off-time method is used in the same way as described in the Gadolinium capture case. However, the rate measured by this method is expected to be lower than the real value. This difference occurs because when a window is opened to search for the delayed signal, there is a probability that this signal is not selected, by the extra multiplicity cut (isolation cut inefficiency, $f_{\text{isolation}}^{\text{delayed}}$), or by a muon veto (delayed trigger muon-veto inefficiency, $f_{\mu-\text{veto}}^{\text{delayed}}$). Therefore, the accidentals rate contamination on the neutrino sample is estimated using the following expression:

$$R_{\text{acc.}} = \frac{\text{Acc. Candidates}}{\text{LiveTime} \times N} \times f_{\text{isolation}}^{\text{delayed}} \times f_{\mu-\text{veto}}^{\text{delayed}} \tag{4.52}$$

The $f_{\text{isolation}}^{\text{delayed}}$ correction factor can be estimated by measuring the efficiency of the multiplicity cut for the delayed triggers for all the data. On the other hand, the delayed trigger muon-veto inefficiency has to be estimated from the muon rate. Every accidental candidate has some probability of being vetoed because its prompt or delayed signal occurs too soon after a muon. For a given candidate, the total muon veto probability is the product of veto probability on the prompt signal and on the delayed signal. The veto probability for prompt signals is the same for both on- and off-time analysis: it is equal to the muon veto window (1 ms) times the muon rate. However, the veto probability for delayed events differs between on- and off-time accidentals. For off-time, the delayed veto probability is equal to the prompt veto probability, and is given by:

$$P_{\mu-\text{veto}}^{\text{off-time}} = 1ms \times R_{\mu} \tag{4.53}$$

where $R_{\mu}$ is the muon rate. For on-time accidentals, the delayed veto probability is lower, because the 1 ms window preceding the delayed event overlaps with the 1 ms window preceding the prompt event. When the prompt veto probability is calculated, it is already taking into account the probability of a muon in the overlapping portion. Thus, the delayed veto probability must be calculated using only the non-overlapping

(a) Prompt spectrum

(b) $\Delta$T
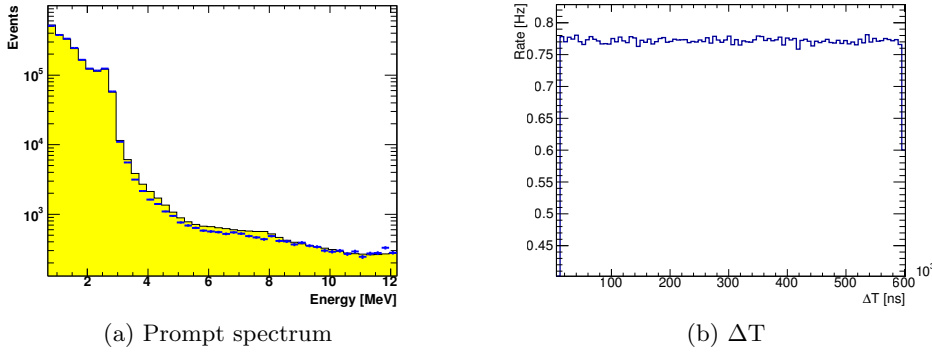
Figure 4.41: Accidentals distributions for the prompt energy, where the dots are the data acquired using the off-time method, and the scaled detector valid triggers spectrum is represented in yellow. The $\Delta T$ distribution is flat, as expected for uncorrelated events.

portion of the time window. Following this logic, the muon veto probability for off-time delayed signals is:

$$\mathrm{P}_{\mu-\mathrm{veto}}^{\mathrm{on\text{-}time}} = \int_{T_0}^{T_1} \frac{t \times R_\mu}{T_1 - T_0} dt = R_\mu \times \frac{(T_1 + T_0)}{2} \tag{4.54}$$

where $T_0$ and $T_1$ are initial and final time of the coincidence window respectively. Note that the "muon rate" in equation 4.53 and 4.54 is not actually the rate of muons passing through the detector but instead the rate of "muon veto windows", since two coincident muons have the same veto potencial as a single muon. Therefore, the correction factor is:

$$f_{\mu-\mathrm{veto}}^{\mathrm{delayed}} = \frac{1 - \mathrm{P}^{\mathrm{on\text{-}time}}}{1 - \mathrm{P}^{\mathrm{off\text{-}time}}} \tag{4.55}$$

The number of selected candidates, the measured correction factors and the rate, calculated using equation 4.52, are shown in table 4.6. In figure 4.41 are present the

Table 4.6: Accidental results of the off-time method for the Hydrogen analysis

| Variables | Values |
|---|---|
| Candidates | 2096406 |
| $f_{\mathrm{isolation}}^{\mathrm{delayed}}$ | $1.01941 \pm 0.00002$ |
| $f_{\mu-\mathrm{veto}}^{\mathrm{delayed}}$ | $1.03137 \pm 0.00005$ |
| $R_{\mathrm{acc.}}$ | $73.45 \pm 0.05$ day$^{-1}$ |

prompt energy spectrum and $\Delta T$ distribution estimated using this method.

One way to cross-check the value of correction parameter ($f_{on/off}^{\mathrm{corr}} = f_{\mathrm{isolation}}^{\mathrm{delayed}} \times f_{\mu-\mathrm{veto}}^{\mathrm{delayed}} = 1.05139 \pm 0.00005$) is to compare both $\Delta R$ distributions of the on-time selection and the non corrected off-time method, for higher values where a pure sample of accidentals takes place, as showed in figure 4.42 for the hydrogen sample. The region with $\Delta R$ bigger than 1100 mm is considered to be composed purely by accidental events. Therefore, a fit of the on-time and off-time ratio is done up to 3500 mm in order to check the excess. The result is presented in figure 4.43, where the fit output of $1.051 \pm 0.002$ is compatible to the correction factor measured from data. The larger uncertainty obtained by this method is due to the large statistical uncertainty present on the on-time sample. Thus, a conservative approach is assumed, assigning the 0.2% as a systematic uncertainty
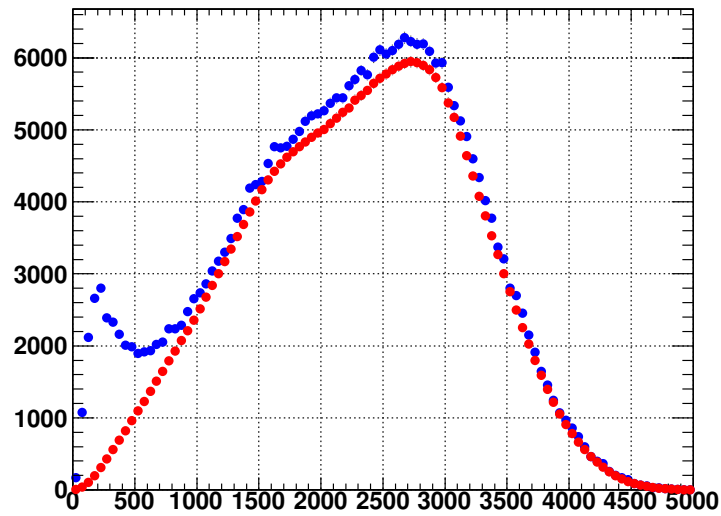
**ΔR Distribution**



Figure 4.42: On-time (in blue) and off-time (in red) $\Delta R$ distributions.
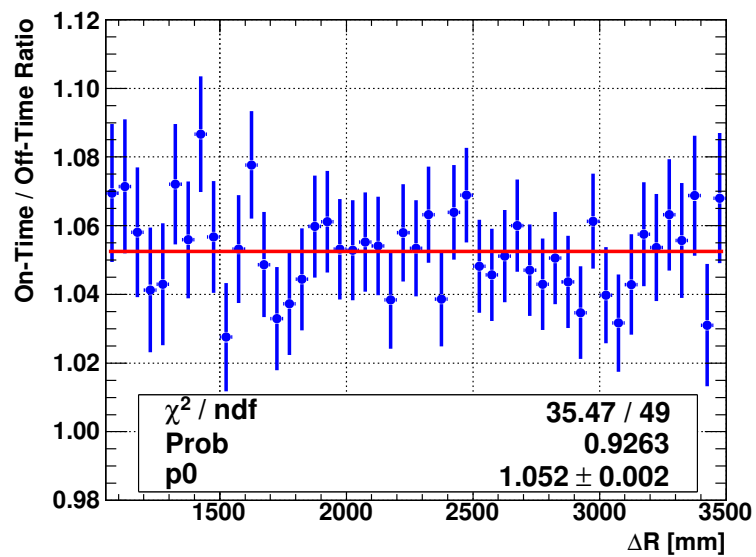


Figure 4.43: Ratio of the on-time and off-time $\Delta R$ distribution.

in the accidental rate estimation using the off-time sample, resulting in the final number of:

$$R_{\text{acc.}}^{\text{H}} = 73.45 \pm 0.05 (\text{stat.}) \pm 0.15 (\text{sys.}) \text{ day}^{-1}.$$

Since this "systematic error" is dominated by statistical uncertainty of the on-time sample in the 1100 mm $< \Delta R <$ 3500 mm region, it would became smaller with more statistics.

**Analytical Method**

To adapt the analytical method for the Hydrogen analysis, as it was performed in the off-time method, the cut condidtions and corrections need to be consider, as follows:

$$R_{\text{acc.}}^{\text{analytical}} = R_{\text{prompt}} \times R_{\text{delayed}} \times \Delta T_{\text{coinc.}} \times \varepsilon_{\mu-\text{veto}}^{\Delta T} \times \varepsilon_{\text{isolation}}^{\text{prompt}} \times \varepsilon_{\Delta R} \times f_{\mu-\text{veto}}^{\text{delayed}} \quad (4.56)$$

where $R$ is the single rate for the prompt and delayed selection cut, $\Delta T_{\text{coinc.}}$ is the time interval used to search the delayed signal, $\varepsilon_{\mu-\text{veto}}^{\Delta T}$ is the efficiency of muon anti-correlation, $\varepsilon_{\text{isolation}}^{\text{prompt}}$ is the efficiency of the isolation cut on prompt candidates, and $\varepsilon_{\Delta R}$ is the efficiency of the prompt to delayed events spatial separation. The parameters measured for the analytical method can be seen on table 4.7. This table also shows the result of this method, which agrees with the one measured by the off-time method.

Table 4.7: Inputs and final result of the analytical method for accidental (equation 4.56) estimation on Hydrogen analysis

| Variables | Values |
|---|---|
| $R_{\text{prompt}}$[Hz] | $8.1972 \pm 0.0006$ |
| $R_{\text{delayed}}$[Hz] | $2.9908 \pm 0.0004$ |
| $\Delta T_{\text{coinc.}}$ [$\mu$s] | 590 |
| $\varepsilon_{\mu-\text{veto}}^{\Delta T}$ | 0.955412 |
| $\varepsilon_{\text{isolation}}^{\text{prompt}}$ | $0.98131 \pm 0.00002$ |
| $\varepsilon_{\Delta R}$ | $0.06079 \pm 0.00004$ |
| $R_{\text{acc.}}^{\text{analytical}}$ [day$^{-1}$] | $73.46 \pm 0.05$ |

In figure 4.44 is shown the time evolution of the accidental rate and all variables used for its estimation. Again it is possible to see in figures 4.44g and 4.44h that both off-time and analytical methods agree in a daily basis as well.

### 4.7.2  Correlated

Most of the correlated backgrounds are rejected by 1 ms muon veto after each tagged muon, as explained in section 4.4.2. The remaining events arise from cosmogenic events whose parent muon either misses the detector or deposits an energy low enough to scape the muon tagging. Two contributions have been found: fast neutrons (FN) and stopping muons (SM). Details on theirs rate and shape estimation for each Gadolinium and Hydrogen analysis are given in the following subsections.

#### 4.7.2.1  Gadolinium

Study of the FN and SM backgrounds is accomplished by examining IBD candidates in the energy region $12 < E_{\text{vis}} < 30$ MeV where no IBD signal events are expected. The spectrum is then extrapolated down into the IBD signal region $0.7 < E_{\text{vis}} < 12.2$ MeV. In order to allow independent study of each, the components of this background are

(a) Prompt Rate

(b) Delayed Rate

(c) Efficiency of Muon Anti-correlation

(d) Prompt Isolation Efficiency

(e) Efficiency of $\Delta R$ Cut

(f) Delayed Trigger Muon-Veto Inefficiency

(g) Accidental Rate

(h) Ratio of Off-time and Analitycal Methods
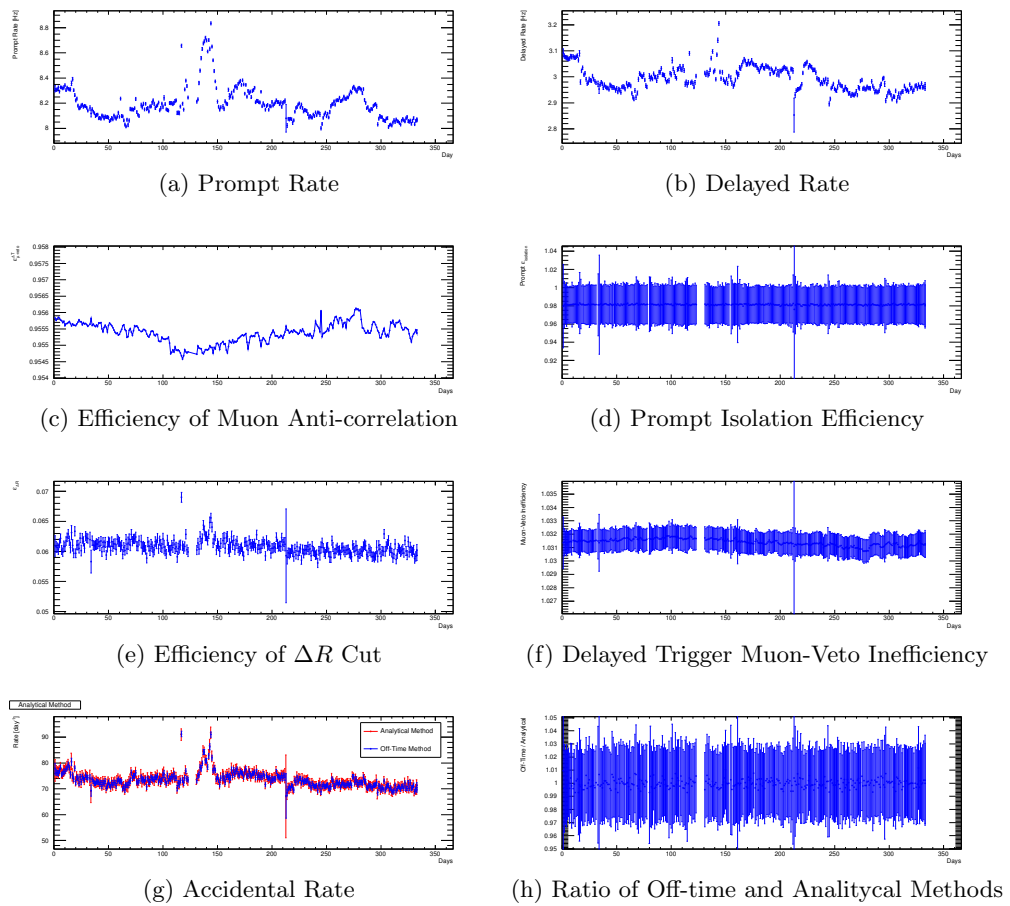
Figure 4.44:   Time evolution of the parameters used to estimate the accidental background by the analytical method on Hydrogen Analysis.

divided using a cut on the time difference $\Delta t$ between the prompt and delayed parts of the events in this high energy sample. As shown in figure 4.45, the $\Delta t$ profile of SM is driven by capture of the muon, with a characteristic time of 2.2 $\mu$s, while FN events follow a $\Delta t$ profile with the same 30 $\mu$s characteristic time as IBD events. Thus,
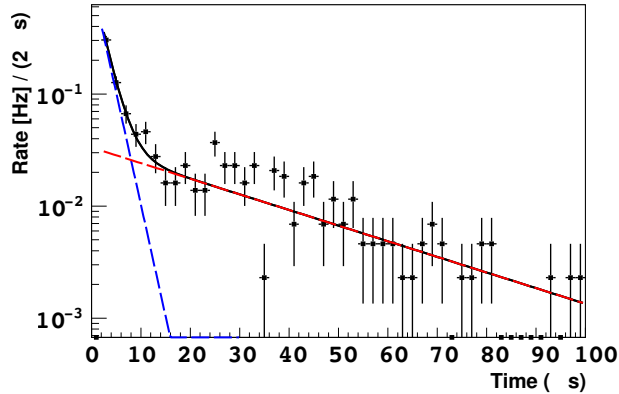


Figure 4.45: Distribution of time separation between prompt and delayed signal components of background events with $12 < E_{\mathrm{vis}} < 30$ MeV. The two exponential fit represents populations of SM (blue dashed) with 2.2 $\mu$s time constant, and FN recoil (red dashed) with 30 $\mu$s time constant.

stopping muon events are selected as having $\Delta t < 10$ $\mu$s, while fast neutron recoils are those events with $\Delta t > 10$ $\mu$s. In combination with independent measurements of tagged samples of each background component, these two rate measurements allow for a measurement of the FN and SM background energy spectral shape without making prior assumptions regarding combined spectral shape.

### Stopping Muons

The SM sample is due to some low energy muons that can sneak through the detector chimney, avoiding tagging by the IV, and then decay. These muons are considered backgrounds themselves, and a pure sample of these events is tagged by selecting events where the delayed component of the coincidence is certainly from the Michel electron produced in muon decay. This is achieved by using a delayed energy window of $20 < E_{\mathrm{vis}} < 60$ MeV. In this energy regime, the largest background is from high energy spontaneous light noise. The light noise events are subtracted from the measured stopping muon spectrum by use of a large off-time window: $1000 < \Delta t < 1100$ $\mu$s, with the measured off-time spectrum scaled down to the 10 $\mu$s window of the SM selection. The background subtracted prompt spectrum of the stopping muon population is then fit to a linear hypothesis. The upper OV, as shown in figure 3.21, is going to be installed over the chimney and the Glove Box in order to tag such events more efficiently.

### Fast Neutrons

A pure sample of FN recoils events is isolated by selecting events which are coincident with a low energy deposition in the IV. This strategy is based on the assumption that FN recoils are often produced by neutrons from showering muons, where the multiplicity of neutrons produced by the muon is high. Non-IBD neutrons interact within the IV by proton recoil, or capture on Hydrogen. However, this type of event has large "background" contributions due to: true IBD interactions in the ID, coincident with a neutron capture in the IV; IV interactions by gamma rays from natural radioactivity

or dark noise in the IV PMTs. The dark noise background is suppressed by requiring that at least two IV PMTs produce charge as part of the tagged event. The other backgrounds are tagged by use of spatial criteria: a requirement that the prompt and delayed components of the IBD-like signal occur within 150 cm of each other rejects interactions by gamma rays in the IV; a requirement that the IV and ID PMT signals occur within a [-2, 95] ns window of each other rejects coincidental antineutrino events. The remaining background subtracted spectrum is then fit to a linear hypothesis to determine the final background estimate.

**Background Combination**

The total FN/SM background spectrum is found by summing the final spectra produced by the methods described above. The background subtracted spectra produced in each section are summed, and fit to a linear hypothesis. The fit spectrum is extrapolated into the IBD signal region, and scaled to the summed measured rates of each background component. The total expected background rate from FN and SM is $0.93 \pm 0.26$ per day, before any OV-based veto is imposed. The break-out of FN and SM populations and their uncertainties is given in table 4.8.

Table 4.8: FN and SM population break-out, before use of OV based veto condition.

| Component | Rate w/o OV [day$^{-1}$] | Rate w/ OV [day$^{-1}$] | Reduction [%] |
|-----------|--------------------------|-------------------------|---------------|
| Fast Neutron | $0.33 \pm 0.16$ | $0.30 \pm 0.14$ | $9 \pm 6$ |
| Stopping Muon | $0.60 \pm 0.22$ | $0.34 \pm 0.18$ | $43 \pm 28$ |
| Total | $0.93 \pm 0.26$ | $0.67 \pm 0.20$ | $28 \pm 11$ |

**Inclusion of OV**

As described in section 4.5, the Gadolinium IBD candidate selection criteria requires an anti-coincidence of the prompt event with the OV. This measure was found to decrease the rate of FN and SM events by 9% and 43%, respectively, as indicated in table 4.8. Most of the vetoed events were reconstructed near the center top of the detector, consistent with the majority coming from stopping muons entering near the chimney, as shown in figure 4.46. The prompt spectrum of the anti-coincident events is
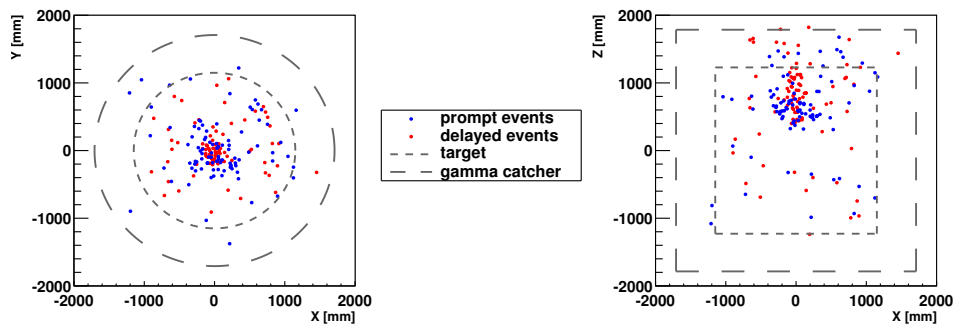


Figure 4.46: Reconstructed positions of selected IBD candidates, in coincidence with an OV event, projected in the $xy$ (left) and $xz$ (right) planes.

shown in figure 4.47, and it displays a distribution that is consistent with a flat spectrum.

The final combined rate for the background was found to be $0.67 \pm 0.20$ per day, including the OV anti-coincidence. The OV anti-coincidence condition was also used to
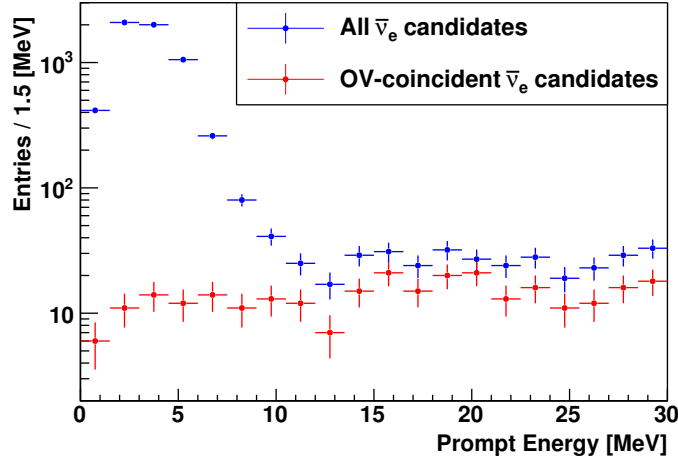
Figure 4.47: Prompt spectrum of all selected IBD candidates using the Gd cuts (blue points) and spectrum of IBD candidates coincident with a signal in the OV (red points).

establish the propagated uncertainty on the slope of the FN/SM spectrum: a rescaled version of the spectrum without the anti-coincidence requirement was used to define the $1\,\sigma$ deviation for the spectral shape, as showed in figure 4.48.
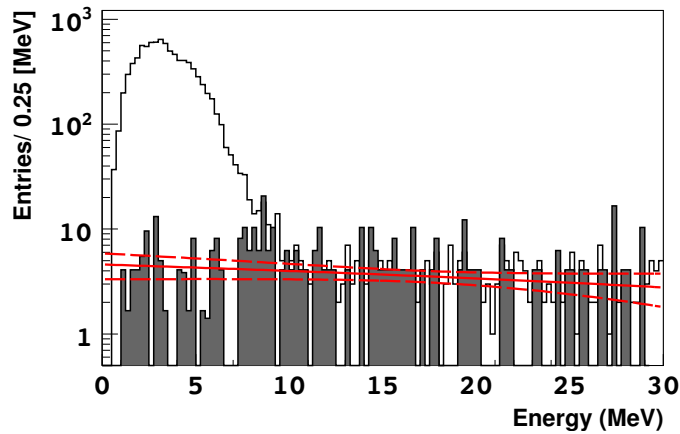


Figure 4.48: FN and SM combined spectral model best fit (solid red line) with $\pm1\,\sigma$ uncertainty (dashed red lines), energy distribution of tagged FN and SM population, and IBD spectrum.

#### 4.7.2.2   Hydrogen

Understanding the FN and SM backgrounds is especially important for the Hydrogen analysis because their rate are expected to be larger than in Gadolinium, not only because of the increased fiducial volume, but also because of the decreased shielding in the GC. The same method used in for the Gadolinium is applied to the Hydrogen analysis to estimate the correlated background rate.

The delayed coincidence time difference, employed in the neutron capture on Hydrogen IBD selection, of $10 < \Delta T < 600\ \mu$s and the OV veto remove essentially all SM. The $\Delta T$ distribution has contributions from four different components: the exponential component from neutron capture on Hydrogen in the NT; the exponential with a different time constant from neutron capture in the GC; an exponential component from SM decay; and a flat accidental component. To show that the SM rate is all completely removed by the $\Delta T$ cut, a fit to the off-time subtracted $\Delta T$ distribution

with an analytical function that includes the three exponentials is performed. However, the decay times need to be beforehand estimated.

For this analysis an independent SM sample is obtained using the default Hydrogen IBD selection cut, changing the prompt and delayed energy cuts to [0,60] MeV and [12.60] MeV respectively, and no OV coincidence is used. In addition, an off-time sample is selected using an offset of one second. Subtracting the off-time $\Delta T$ distribution from the SM one, and using an exponential decay curve to fit the remaining distribution, a SM decay of $2.12 \pm 0.14$ $\mu$s is obtained, as shown in figure 4.49, being in a good agreement with the well measured $\tau_\mu$. $^{252}$Cf source deployment in the NT center is used to estimate
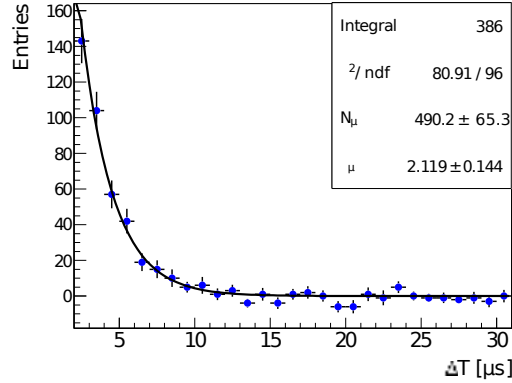


Figure 4.49: $\Delta T$ distribution of the SM data sample after subtraction of the off-time sample. The function (black line) used for the fit assumes a pure exponential decay.

the NT neutron capture time, and for the GC a simple exponential fit on the neutrino sample with $\Delta T \in [150, 600]$ $\mu$s. The obtained decay time constants are summarized in table 4.9. These constants are used to perform a fit on the modified SM / FN candidate

Table 4.9: Decay time constants obtained for the $\Delta T$ distribution fit for correlated background rate estimation.

| Event Type | Decay Time Constant [$\mu$s] |
|---|---|
| Muon Decay | $2.12 \pm 0.14$ |
| n-H in NT | $26.72 \pm 0.42$ |
| n-H in GC | $194.46 \pm 8.33$ |

sample. In this fit, in order to enhance the error due to the time constants extracted from the different data sample, the following $\chi^2$ with penalty terms is used:

$$\chi^2 = \chi^2_{\text{Pearson}} + \sum_i^{\mu,\text{NT,GC}} \left( \frac{\Delta \tau_i}{\sigma_{\tau_i}} \right)^2 . \qquad (4.57)$$

The triple exponential fit yields a fairly small $\chi^2$ value, and the SM rate is estimated using the normalization from the SM component. Using the data sample live time, ($T_{\text{Live}}$), the SM rate is

$$R_{\text{SM}} = \frac{1}{T_{\text{Live}}} \times \int_{2\ \mu\text{s}}^{600\ \mu\text{s}} N_\mu \exp\left( -\frac{t}{\tau_\mu} \right) dt = 1.66 \pm 0.28 \, \text{day}^{-1}, \qquad (4.58)$$

where the uncertainty includes statistics from $N_\mu$ and systematics from $\tau_\mu$ coming from the fit. If the low integration limit is set as 10 $\mu$s, the SM rate becames $0.1 \pm 0.1$ events per day, what is negligible, justifying the $\Delta T$ values cut for IBD events selection.

As in the Gadolinium analysis, the FN shape and rate is estimated by the IV tag analysis. The selection of a FN sample is performed applying the same IBD selection cuts, but changing the prompt energy range to [0.7,30] MeV. In order to reduce the low energy background of this sample an off-time analysis was employed as well a condition requiring a minimum of 2 IV PMT to have non zero charge. The efficiency of this IV cut, $\varepsilon_{\text{IVhit}} = 0.337 \pm 0.018$, is obtained using a sample subset with prompt energy on the [12,30] MeV range. Moreover, the IV and ID PMTs first pulse separation distribution also gives a Gaussian plus flat component, and a requirement that the IV and ID signals occurs within the [-90,150] ns time window, rejects the remaining background, IBD coincident events, from the sample.

To fit the FN spectrum shape, an exponential with a constant off-set was used, due to an increase of low energy events, as one can see in figure 4.50. Integrating this function
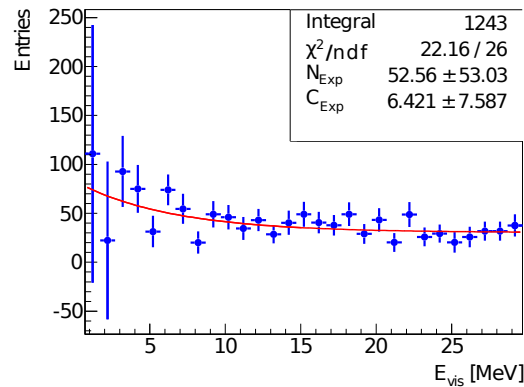


Figure 4.50: Final FN shape (in blue), after subtracting the background. An exponential plus offset function (in red) is used to fit the data, and is renormalized by taking the IV tagging inefficiency into account.

over the IBD prompt energy range gives a FN rate of $2.50 \pm 0.47$ events per day.

### 4.7.3  Cosmogenic

The cosmogenic radioisotopes $^9$Li and $^8$He are produced by cosmic muon spallation on $^{12}$C in the liquid scintillator, as explained in section 3.5. Since these elements have a relatively long lifetime ($\sim$200 ms), it is difficult to reject by a muon veto, however, they can be identified from the time and space correlation to their parent muon. In the following subsections this background source estimation methods are given for both Gadolinium and Hydrogen analysis.

#### 4.7.3.1  Gadolinium

Since the $^9$Li and a muon events have correlation in time and space, the $^9$Li rate is obtained by searching for triple fold coincidences between an $\bar{\nu}_e$-like candidate and a suitable parent muon in a 20 s long time window (about 80 times the $^9$Li life time) and fitting the time difference, $\Delta t_\mu$, distribution with an exponential and a flat components. For a true neutrino event, the time distribution should be flat, while the $^9$Li events should have the exponential time distribution with its decay constant. Thus, the function, $f(\Delta t_\mu)$, used for such a fit is defined as

$$f(\Delta t_\mu) = \frac{N_{^9\text{Li}}}{\tau} e^{-\Delta T_\mu / \tau} + C, \tag{4.59}$$

where $\tau$ is the $^9$Li lifetime, $N_{^9\mathrm{Li}}$ is proportional to the rate and $C$ is the constant background.

From the experience of previous experiments, KamLAND in particular, it is known that the more energetic, sometimes called "showering", muons that mostly contribute to the cosmogenic isotope production [93]. Double Chooz, being a smaller detector, is less well equipped for identification of the showering muons, compared to KamLAND, but one can still attempt to discriminate against the lower energy muons by applying an energy cut.

The $^9$Li rate produced by high energy muons ($E > 600$ MeV, muons crossing both NT and GC) is obtained directly by a fit of the $\Delta T$ distribution as shown in figure 4.51. A precise rate of $(0.95 \pm 0.11)$ events per day is obtained.
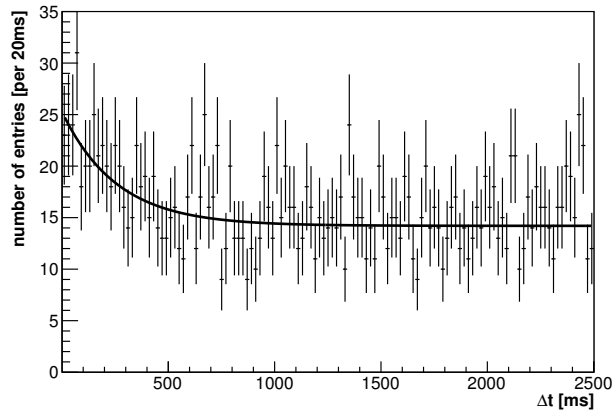


Figure 4.51: $\Delta T_\mu$ distribution for muons with $E > 600$ MeV preceding IBD candidates fit by equation 4.59.

For mid-range energy muons ($E$ in [275,600] MeV, muons crossing GC and a fraction of the NT), the $^9$Li rate for events near to the muon track ($d < 0.8$ m) is obtained directly from the fit of the $\Delta t$ distribution while the rate for events far from the muon track is extrapolated based on the lateral distance profile between muon and $^9$Li candidate observed for high energy muons. A rate of $1.08 \pm 0.44$ events per day is obtained.

Lastly, the $^9$Li rate produced by low energy muons ($E < 275$ MeV, muons crossing the buffer and fraction of the GC) is estimated from the fit of the $\Delta t$ distribution and it is found compatible with zero. An upper limit of $< 0.3$ events per day is established by the fit of the $\Delta t$ distribution for events near the muon track ($d < 0.8$ m).

Finally, studies have been conducted to estimate the systematic uncertainties coming from the inclination of the background of random coincidences in the $\Delta t$ fit and the necessity to accommodate a small fraction $(10 \pm 10)\%$ of $^8$He in the selected $^9$Li data sample. Combining the results obtained from the three muon energy ranges and accounting for the systematic uncertainties of the fitting method, the total $^9$Li rate is $2.05^{+0.62}_{-0.52}$ events per day. High energy muons with $E > 600$ MeV showering into the detector, have been found as the most likely parents of $^9$Li isotopes. For this reason the 0.5 ms veto is applied to the $\bar{\nu}_e$ selection, after a showering muon of energy above 600 MeV. The definition of parent muon and the veto condition were varied to obtain the maximum veto efficiency for a fixed dead exposures of 5%. The reduced $^9$Li background rate is $1.25 \pm 0.54$ events per day. The result of asimilar analysis based on the IV muon tracking agrees within the uncertainty.

It should be noted that contamination from another cosmogenic isotope, $^{12}$B with a life time of 29 ms, is removed from the measured cosmogenic rate in this analysis by

requiring a maximum distance between prompt and delayed events of the IBD-like event of 90 cm. This cut has a small inefficiency of about 1%.

It is known that the prompt spectrum of $^9$Li has a different shape from the spectrum of the IBD interaction so that it is possible to use this information for a better constrain in the IBD shape analysis. Due to lack of statistics on the data, the prediction of $^9$Li spectrum shape is performed using MC simulation. A MC event generator to simulate $^9$Li beta decay is written according to recent nuclear data [94]. On 50.8% of the cases, the produced $^9$Li will suffer a beta decay into a exited estate of $^9$Be, that has two major branches of neutron emission: $^9$Be $\rightarrow$ $^5$He $+ \alpha$, $^5$He $\rightarrow$ $n + \alpha$ and $^9$Be $\rightarrow$ $^8$Be$+n$, $^8$Be $\rightarrow 2\alpha$, as depicted in figure 4.52. The decay process is selected event-
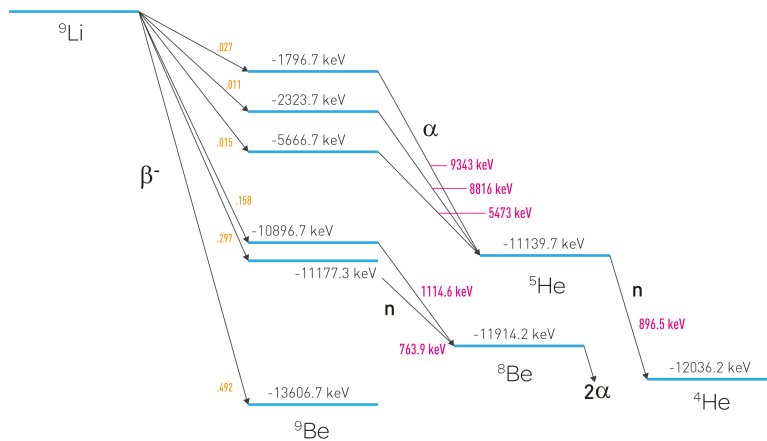


Figure 4.52: $^9$Li decay scheme. 50.8% of the times the $^9$Li nucleus decays into alpha particles, with beta and neutron emission, mimicking the characteristic antineutrino signal.

by-event according to the measured branching ratios. Finally, the prompt spectrum is given through the detector and readout simulation as shown in figure 4.53. Because
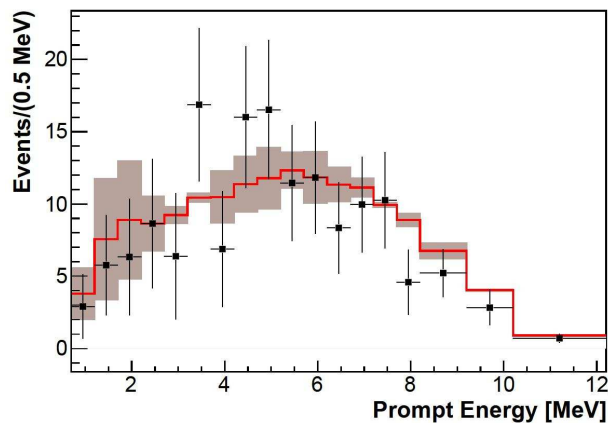


Figure 4.53: The $^9$Li spectrum from data (black points) and MC (red histogram). The data sample is obtained by selecting a purer sample of events subtracting backgrounds. The shaded region represents the systematic uncertainty on the shape prediction.

the alpha particle contributes the prompt energy and the energy of the alpha from $^9$Be

is different than ones from $^8$Be, the uncertainty of the branching ratios is considered as a shape uncertainty of the predicted spectrum, which is calculated by the difference between two models of the branching ratio: the model with the measured values and the model with only the branch into $^8$Be. These uncertainty is shown as the bars on figure 4.53. Moreover, this figure shows the $^9$Li spectrum obtained by selecting a purer sample of $^9$Li events subtracting the $\bar{\nu}_e$ background through off-time selection. The sample was obtained for muons with energy > 620 MeV, a distance cut of 0.7 m and a $\Delta T_\mu$ cut of 600 ms. The obtained spectrum is then compared with MC simulation of the possible $^9$Li decay branches. The $\chi^2$ test performed between data and MC spectra give an excellent agreement with a $\chi^2_{\min} = 16.8$ for 18 energy bins.

### 4.7.3.2 Hydrogen

As explained previously, the energy deposition on the ID was used to determine the muon track, in the Gadolinium analysis. However, this method is not suitable for the Hydrogen analysis, because there are muons passing only through the buffer volume or by the GC edges, that contribute for $^9$Li event rate, but has a small light yield. This makes it difficult to understand the muon tracking performance. Thus, another method, the IV tracking, is used. In addition, also for the Hydrogen analysis, the event sample following muons contains a large amount of background events, such as accidental and IBD events, what makes it very difficult to perform an accurate $\Delta T_\mu$ fit to estimate the $^9$Li signal rate. Therefore, it was required to have the short *distance of closest approach* (DCA) between a prompt candidate and muons, since the $^9$Li event and corresponding muon have correlation in space.

The threshold of DCA is calculated to have the strongest separation power. In order to calculate the best threshold value, a MC sample was used for both muon and $^9$Li events. While the $^9$Li events were generated with the Double Chooz customised tool, muons events were created using **MUSIC** [95] code with the specific hill profile of the far laboratory site, as shown in figure 4.54. Then, the two events are combined with
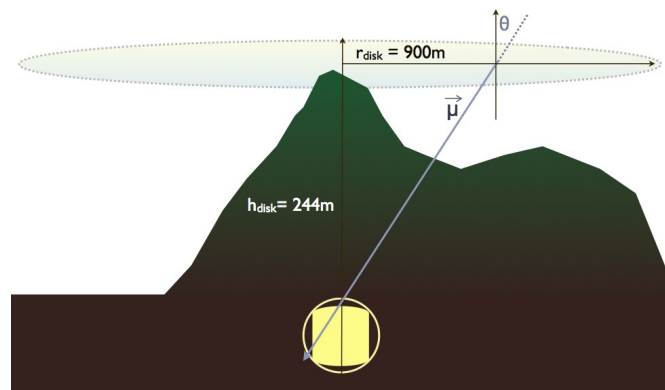


Figure 4.54: The Double Chooz far detector drawing inside the surrounding mountains. The detector is situated under a hill which is sharply peaked on one side. Muons are generated at random locations uniformly distributed on an imaginary disk just above the hill. The region of interest is a sphere surrounding the actual Double Chooz far detector [96].

correlations of DCA and decay time, from the muon. The decay time is set to 257.3 ms from the muon and the DCA$^{\text{true}}$ between the muon track and $^9$Li event follows an exponential function with a mean value of 10 cm.

The event selection is performed in two steps. First a pre-selection requires the event

passes the cuts used for the Hydrogen neutrino selection. Then, the second step requires the presence of at least one muon in the window of $20 < \Delta T_\mu < 8000$ ms preceding the prompt candidate. Those muons were also required to have a track reconstructed by IV information, which requires $Q_{IV} > 10000$ DUQ and at least 5 IV PMT to have non-zero charge. Events with no energy deposition on the ID are also rejected, therefore, only muons passing through both ID and IV are selected. Moreover, it was required a short DCA between the prompt and muon events, where the threshold was obtained to have the strongest separation power, from the DCA distribution obtained from the MC sample. The background distribution due to other muons coming accidentally or due to neutrinos are obtained from data which $\Delta T_\mu$ has to be greater than 1000 ms. Figure 4.55 shows the DCA distributions for both signal and background of $^9$Li rate estimation. The
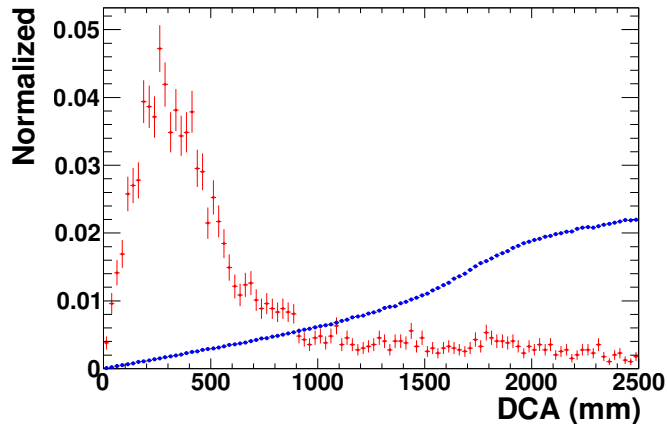


Figure 4.55: DCA distribution for both signal (red) and background (blue) of $^9$Li rate estimation. The signal distribution is obtained from MC with DCA$^{\text{true}}$ equals to 10 cm, while background from data to be $\Delta T_\mu > 1000$ ms. The distribution of other DCA$^{\text{true}}$ does not looks so different, since the signal distribution is smeared due to the position and tracking resolution.

signal and background efficiencies, $\varepsilon_{\text{sig}}$ and $\varepsilon_{\text{bkg}}$ respectively, as a function of DCA, are shown in the left plot of figure 4.56. The separation power, defined as $\varepsilon_{\text{sig}}/\sqrt{\varepsilon_{\text{bkg}}}$, is
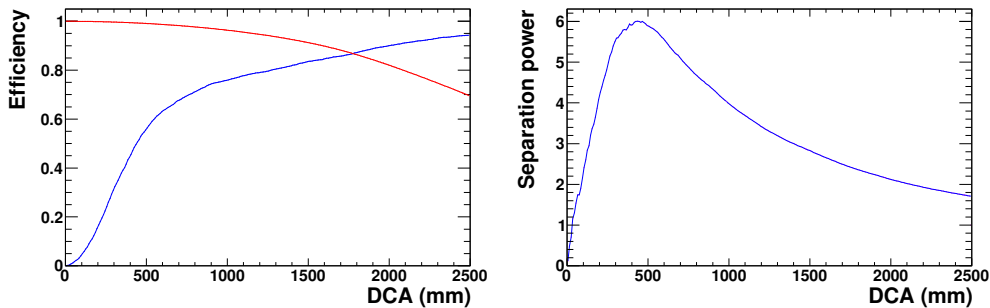


Figure 4.56: The signal efficiency (left - blue), background rejection (left - red), and the separation power (right) as a function of DCA cut value.

used to estimate the optimal threshold on DCA cut, and is represented by the right plot of figure 4.56. Thus, the DCA is required to be less than 43.5 cm, where the separation power has a peak, corresponding to an efficiency of 48.2%.

After selecting the muon candidates, the $\Delta T_\mu$ distribution is created for all the candidates. In order to remove accidental backgrounds, which accounts for almost a half of backgrounds with another half from neutrinos, the $\Delta T_\mu$ distribution is subtracted by

the off-time candidates. The final $\Delta T_\mu$ distribution, blue dots on figure 4.57, is used to perform a fit, using equation 4.59 to extract the $^9$Li rate of $2.84 \pm 0.53$ events per day, after the efficiency correction of $48.2 \pm 0.8\%$.
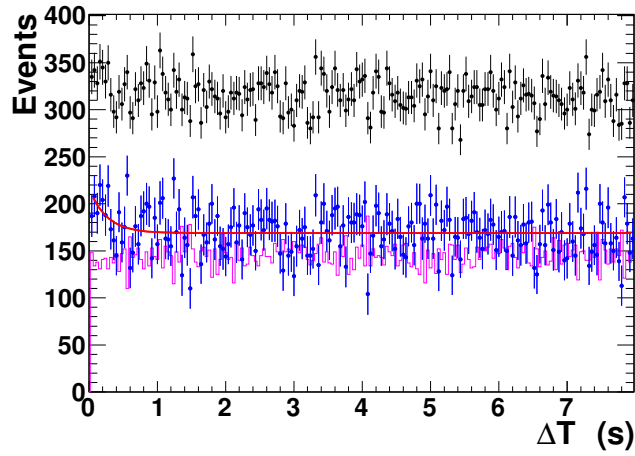


Figure 4.57: $\Delta T_\mu$ distribution for $^9$Li rate estimation. The black dots are on-time sample, while the pink histogram is from off-time sample. The blue dots are the histogram of which on-time is subtracted by off-time, and the red curve is equation 4.59 with best fit value.

When systematics uncertainties on MC flight distance model and statistics, off-time subtraction, and fitting condition (binning) are taken into account, the most conservative assumption leads to a total cosmogenic rate of $2.84 \pm 1.15$ events per day. This value was cross checked by scaling the cosmogenic rate obtained for the Gadolinium analysis. Scaling by the difference of number of $^{12}$C in the NT and GC, and detection efficiency of $^9$Li ($R_{\mathrm{H/Gd}} = 1.86 \pm 0.01$), a rate of $3.81 \pm 1.16$ events per day is obtained, in agreement with the IV tracking method.

For the Hydrogen analysis, the cosmogenic background spectrum shape is also generated from a MC sample that accounts for all the beta decay branches and that are uniformly distributed over all the ID volumes, including the buffer region.

### 4.7.4   Correlated Light Noise

Although the LN events are well understood for the Gadolinium analysis and avoided by the default cuts, during the data taking, specifically after October $20^{\mathrm{th}}$ of 2011 (day 190), it was notice the appearance of low energy events that are time and space correlated, and whose vertices are reconstructed at the center of the detector [97]. The exponential time constant measured is $14.1 \pm 0.9$ $\mu$s, and it fits the shape very well. $\Delta R$ distribution peaks at around 0.4 m, and it continues to about 1 m. Hence neither of our default $\Delta T$ or $\Delta R$ cut reduces this background source. Thus, these events are called Correlated Light Noise (CLN). The $Q_{max/tot}$ cut does not reduce it while the $T_{start}^{\mathrm{RMS}}$ start cut reduces some fraction. Yet the most efficient cut to reduce this background turned out to be the multiplicity cut. One could see a very small yet a remaining fraction of this BG in figure 4.58. The figures are made by selecting event samples from the data taken after day 190, to enhance its existence.

The remaining contamination were investigated by using a vertex cut, dividing the ID into three regions to compare and estimate the amount of CLN, as shown below.

1. $-0.8 < Z < 0.3$ m and $0 < \rho^2 < 0.2$ m$^2$;

2. $-0.8 < Z < 0.3$ m and $0.25 < \rho^2 < 0.45$ m$^2$;
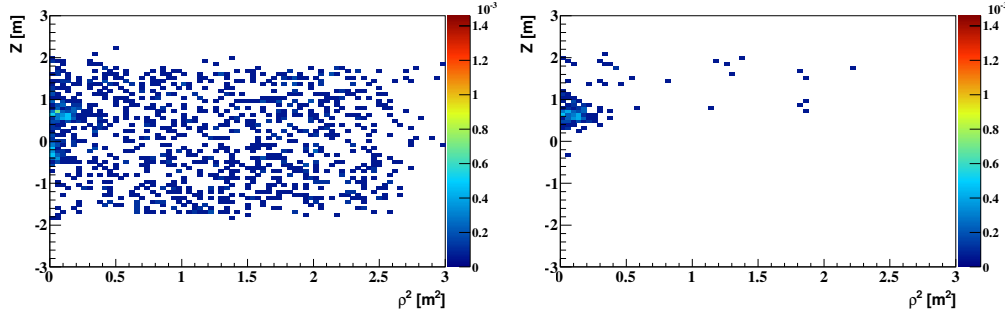
Figure 4.58: Vertices distribution of IBD selected events with $\Delta T < 15$ $\mu$s after day 190 and with (right) and without (left) OV correlation. While the OV tagged events are SM, the ones that are not tagged are correlated LN contamination.

3.  $-0.8 < Z < 0.3$ m and $0.45 < \rho^2 < 0.65$ m$^2$.

While the first vertex cut isolates where the increase of CLN occurred, the second and third ones are sued to quantify the excess seen in one by spectral comparison. The $\Delta T$ spectrum was created for each sample, where the accidentals were removed from the $152 < \Delta T < 250$ $\mu$s period. The excess was quantified by fitting an exponential curve to the $\Delta T$ distribution of (1-2) and (1-3), since both should yield a comparable exponential fit parameters. The $\Delta T$ distribution of (2-3) should be flat, since no time correlation is expected. The three distributions and respective exponential fit are shown if figure 4.59. The exponential time constant for (1-2) and (1-3) are $13.88 \pm 3.92$ $\mu$s and
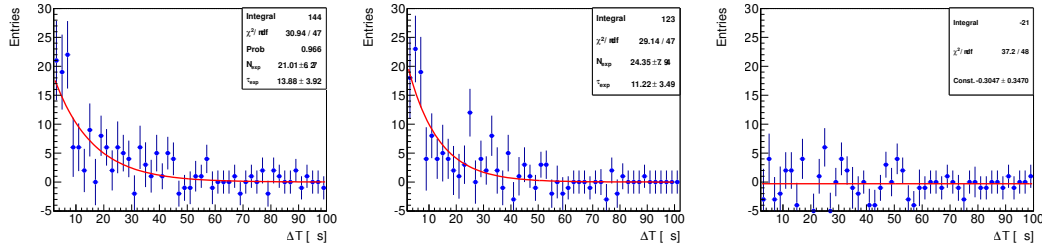


Figure 4.59: CLN $\Delta T$ distribution for three volume cuts. The left figure shows the subtracted distribution of volume (1-2); the middle is (1-3); and the right is (2-3). The right plot is consistent with a flat distribution with no offset.

$11.22 \pm 3.49$ $\mu$s respectively. In addition, the (2-3) distribution is consistent with a flat shape, as expected. Therefore, the volumes (2) and (3) have a similar distribution while (1) contains the CLN sample.

The CLN rate is obtained by integrating the sample spectrum in the range from 10 to 600 $\mu$s, to avoid any SM contamination. This method yields a rate of

$$R_{\text{CLN}}^{(1-2)} = 0.32 \pm 0.07 \text{ day}^{-1} \text{ and } R_{\text{CLN}}^{(1-3)} = 0.25 \pm 0.07 \text{ day}^{-1}. \qquad (4.60)$$

Again, the rate estimated using the two cuts are in agreement. The rate got using (1-2) volumes is chosen, because (2) should be less affected by an accidental subtraction, since accidentals are populated toward the outside of NT, to which volume (3) is closest.

The CLN $E_{\text{prompt}}$ spectrum is obtained also form (1-2) sample, since it does not show considerable difference from (1-3). The spectrum is represented in figure 4.60.
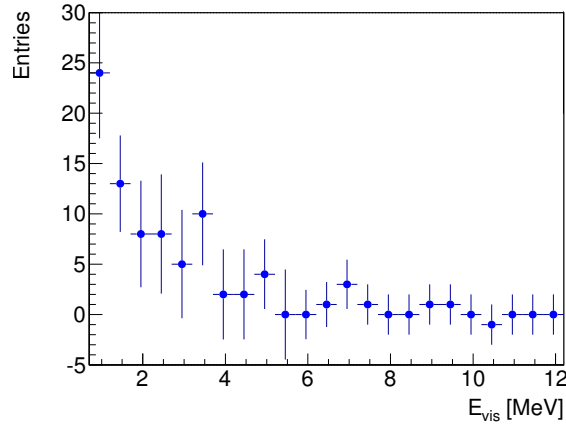
Figure 4.60: CLN energy spectrum obtained from (1-2) volume.
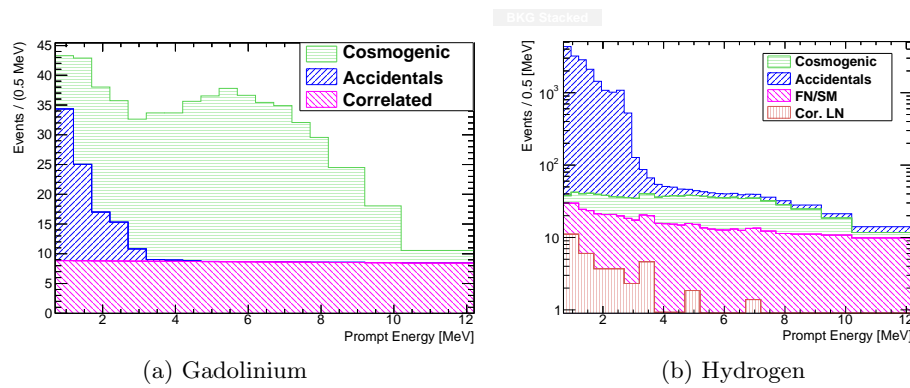


(a) Gadolinium



(b) Hydrogen

Figure 4.61: Stacked Estimated Background Spectra

### 4.7.5   Background Summary

A summary of all backgrounds rate estimation is present in table 4.10 and their spectra on figure 4.61.

Table 4.10:   Summary of the background rate estimations.

| Analysis Type | Accidentals [day$^{-1}$] | Cosmogenic [day$^{-1}$] | FN/SM [day$^{-1}$] | Corr. LN [day$^{-1}$] |
|---|---|---|---|---|
| Gd | $0.261 \pm 0.002$ | $1.25 \pm 0.54$ | $0.67 \pm 0.20$ | - |
| H | $73.45 \pm 0.16$ | $2.84 \pm 1.15$ | $2.50 \pm 0.47$ | $0.32 \pm 0.07$ |

## 4.8   Background Measurements

The background estimations described in the previous section can be cross checked by two different methods: a direct background measurement during periods of time when both reactors are near zero, or completely stopped; or by an extrapolation of background rates from the measured rate of observed events as a function of the reactor power. Due the simple two reactors configuration of the Double Chooz experiment, these background evaluations are a particular feature that is unlikely to be performed by the other reactor neutrino experiments.

### 4.8.1   Observed Candidate Rate vs. Expected $\bar{\nu}_e$ Rate

Plotting the observed IBD candidate rate versus expected event rate is loosely equivalent to plotting the IBD candidate rate versus average reactor power. At the minimal expected rate, where both reactors are at or near zero thermal power, the irreducible backgrounds dominate the observed IBD candidate rate. Thus, a linear fit to these data allows a measurement of the sum of all irreducible backgrounds to be made by extrapolation. This is the linear fit depicted on figure 4.62, and gives a best fit value for the background rate of $2.8 \pm 1.5$ events per day, consistent within uncertainties with the combined background estimate of $2.18 \pm 0.58$ events per day, for the Gadolinium data set. This linear fit also allows for a measurement of $\sin^2 2\theta_{13}$ based on the slope of the
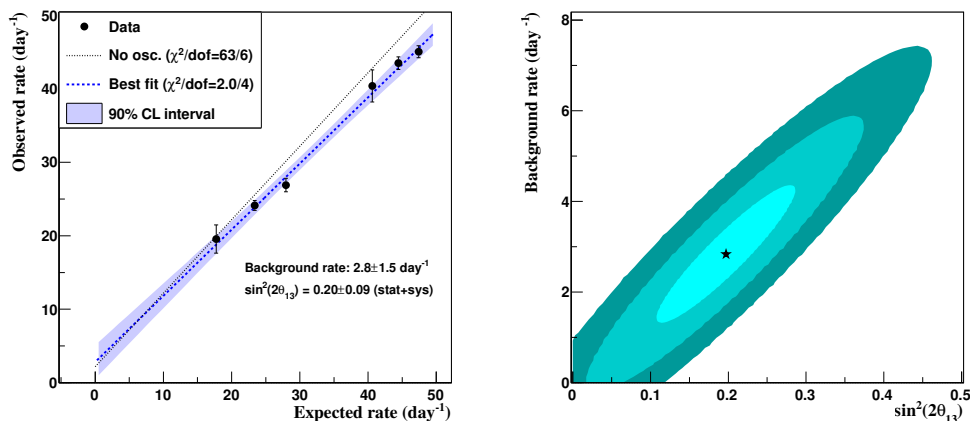


Figure 4.62: Daily number of observed IBD candidate events versus the expected number of $\bar{\nu}_e$. On the left plot, dashed blue line shows the best fit to the data, with blue region giving the 90% confidence level band, and dotted line shows the expectation from the no-oscillation scenario. On the right plot the 1, 2 and 3 $\sigma$ contour plot is shown for the $\sin^2 2\theta_{13}$ vs. total background rate [98].

line. The linear best fit of the data corresponds to a value of $\sin^2 2\theta_{13} = 0.20 \pm 0.09$ at the MINOS value for $\Delta m^2_{31}$ [23]. This value is in agreement within uncertainties with those values found by the fitting methods described in section 5.1.

### 4.8.2   Measured Candidate Rate with Both Reactors Off

On October of 2011, both reactors B1 and B2 were shut down for a period of about 24 hours. This yielded a physics data live time of 0.84 days (22.5 hours) during which the dominant sources of expected IBD candidates are the irreducible backgrounds. Fewer than 0.3 residual $\bar{\nu}_e$ events are expected during this time period from long lived residual radioactive decays. Three events were found which passed the first four IBD candidate selection cuts listed in section 4.5.1, compared to a background prediction of about 2.18. Two of these events were found to have prompt energies of 4.8 MeV and 9.4 MeV, and were reconstructed within 30 cm and 240 cm of the closest energetic muon. The second candidate was found to be rejected by the "$^9$Li reduction" showering muon veto. These factors suggest that these IBD candidates were cosmogenic $^9$Li background events. The third candidate was found to have a prompt energy of 0.8 MeV, with its prompt and delayed components reconstructed 3.5 m distance from each other. This is suggestive of an accidental coincidence.

In June of 2012, a maintenance shut down of reactor B1 occurred during the scheduled refuelling shut down of reactor B2, allowed another 6 days live time of data

with both reactors off. While these data were not included in the analysis of this work, they are described in more detail in [79] and the data and expectation spectra for the gadolinium selection method is shown in figure 4.63. Applying this measurement and the
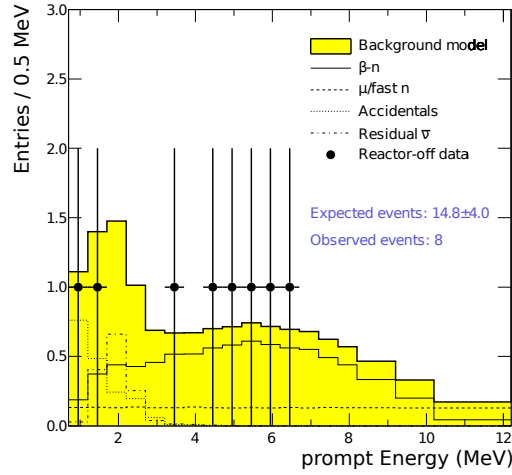


Figure 4.63: $\bar{\nu}_e$ candidates in the reactor-off data sample, with breakdown by components. The black points represents the data and the yellow histogram shows the background plus $\bar{\nu}_e$ expectation.

hydrogen selection method to the observed candidate rate vs. expected $\bar{\nu}_e$ rate analysis, described in the previous subsection, gives a better constrain on the background and $\sin^2 2\theta_{13}$, as it can be seen in figure 4.64. The linear best fit of the data corresponds
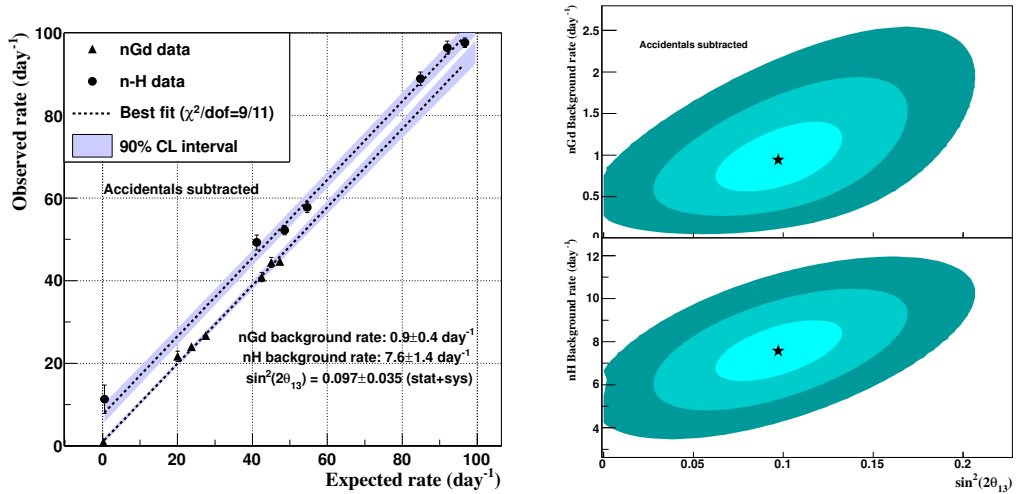


Figure 4.64: Daily number of observed IBD candidate events versus the expected number of $\bar{\nu}_e$, with hydrogen data and off-off measurement. On the left plot, dashed blue line shows the best fit to the data, with blue region giving the 90% confidence level band. On the right plot the 1, 2 and 3 $\sigma$ contour plot is shown for the $\sin^2 2\theta_{13}$ vs. total background rate, where the upper plots concerns the gadolinium data and the bottom plot the hydrogen data [98].

to a value of $\sin^2 2\theta_{13} = 0.097 \pm 0.035$ with a accidental subtracted background rate of $0.9 \pm 0.4$ ($7.6 \pm 1.4$) events per day for the gadolinium (hydrogen) analysis, again with a good agreement with the other numbers.

# Chapter 5

# Measurement of Neutrino Oscillation Parameters

As stated before, the Double Chooz experiment was developed with the main purpose of improve the knowledge about the last unknown neutrino oscillation mixing angle, $\theta_{13}$, by measuring the $\bar{\nu}_e$ survival probability at a $\sim 1$ km distance. The disappearance of $\bar{\nu}_e$ indicates a non-zero $\theta_{13}$. An analysis of the neutrino reactor data, based on the baseline dependence, gives information about the squared effective mass difference $\Delta \tilde{m}^2_{31}$. In this chapter, the methods used to analyse the data in order to measure the value of both reactor neutrino oscillation parameters are presented.

## 5.1 Measurement of $\theta_{13}$

To measure the neutrino survival probability, one need to compare the neutrino flux at a near detector with the flux at a far detector. The use of a near detector can be avoided if enough knowledge about the flux prediction is provided. Since the Double Chooz Near Detector is not operational by the time of this dissertation conclusion, the Far Detector data is compared with the prediction in case of no oscillation and possible oscillation scenarios. Considering the survival probability defined by equation 2.14, with $\Delta m^2 = 2.32 \times 10^{-3}$ eV$^2$, $\sin^2 2\theta = 0.1$ and $L = 1050$ m, one would expect a distortion in the Double Chooz Far Detector spectrum corresponding to the oscillation probability shown in figure 5.1.

A prediction of the observed number of signal and background events is constructed for each energy bin as follows,

$$N_i^{\text{predic.}}\left(\sin^2 2\theta_{13}\right) = \sum_{R=1,2}^{\text{Reactors}} P\left(\bar{\nu}_e \rightarrow \bar{\nu}_e\right) N_i^{\text{expec.,R}} + \sum_{b}^{Bkg} N_i^b, \qquad (5.1)$$

where $P\left(\bar{\nu}_e \rightarrow \bar{\nu}_e\right)$ is the oscillation probability, as described in equation 2.27, $N_i^{\text{expec.,R}}$ is the events expectation at the $i$-th energy bin due to reactor $R$ and $N_i^b$ is the background prediction of source $b$ also at the $i$-th energy bin.

The method used to measure the value of $\sin^2 2\theta_{13}$ and its uncertainty consist of a
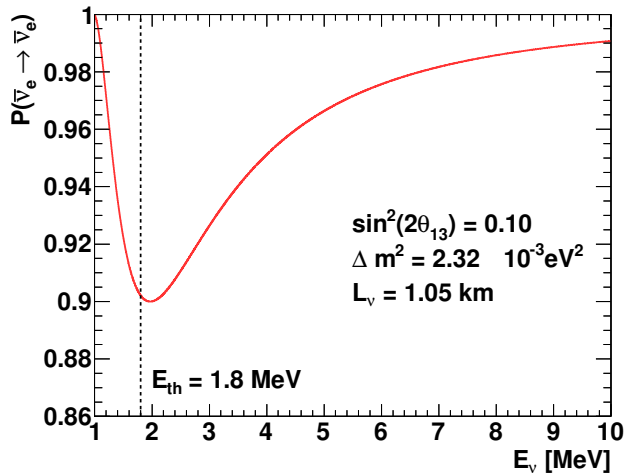
Figure 5.1: The electron antineutrino survival probability as a function of the energy, assuming some values for the oscillation parameters. The dashed line represents IBD threshold energy.

minimization of a $\chi^2$ function, defined as:

$$\chi^2 = \sum_{ij} \left[ N_i^{\mathrm{data}} - N_i^{\mathrm{predic.}} \left( \sin^2 2\theta_{13} \right) \right] \times M_{ij} \left( \sin^2 2\theta_{13} \right)^{-1}$$
$$\times \left[ N_j^{\mathrm{data}} - N_j^{\mathrm{predic.}} \left( \sin^2 2\theta_{13} \right) \right], \tag{5.2}$$

where $N_i^{\mathrm{data}}$ is the measured number of IBD candidate events in the prompt energy bin $i$, $N_i^{\mathrm{predic.}} \left( \sin^2 2\theta_{13} \right)$ is the predicted number of IBD candidate events with oscillations in the prompt energy bin $i$, and $M$ is the covariance matrix describing the uncertainties in the predicted number of events. The reconstructed prompt energy, ranging from 0.7 to 12.2 MeV, was divided into 18 variable-width bins for the Gadolinium analysis fit: 15 bins from 0.7 to 8.2 MeV with width of 0.5 MeV, two bins from 8.2 to 10.2 MeV with a width of 1 MeV, and one bin from 10.2 to 12.2 MeV with a width of 2.0 MeV. For the Hydrogen analysis, since a larger statistics is observed, narrower bins is used in the 0.7 to 7.2 MeV energy range (0.25 MeV width), and the same binning as for Gadolinium is used for higher energies, totalling 31 bins. Although true IBD candidates are not expected with energies larger than 8 MeV, this energy range is useful for a better background constrain of the measurement.

The value of $\sin^2 2\theta_{13}$ which gives the minimum $\chi^2$, $\sin^2(2\theta_{13})_{\mathrm{best}}$, is chosen as the one that describes the neutrino oscillation. In order to define the uncertainty of $\sin^2(2\theta_{13})_{\mathrm{best}}$, the $\Delta\chi^2$ distribution is analysed. The $\Delta\chi^2$ test statistic is defined as the excursion of the $\chi^2$ about its minimum as a function of $\sin^2 2\theta_{13}$:

$$\Delta\chi^2 \left( \sin^2 2\theta_{13} \right) \equiv \chi^2 \left( \sin^2 2\theta_{13} \right) - \chi^2_{\mathrm{min}} \left( \sin^2(2\theta_{13})_{\mathrm{best}} \right) \tag{5.3}$$

In the large sample limit, $\sin^2(2\theta_{13})_{\mathrm{best}}$ is Gaussian-distributed about the true value of $\sin^2 2\theta_{13}$ and $\Delta\chi^2 \left( \sin^2 2\theta_{13} \right)$ follows a $\chi^2$ distribution with one degree of freedom [33]. The 1 $\sigma$, or 68% confidence interval, for $\sin^2 2\theta_{13}$ is then determined by the range of values of $\sin^2 2\theta_{13}$ for which $\Delta\chi^2 \left( \sin^2 2\theta_{13} \right) < 1$. In addition, the minimum value of $\chi^2$ can also be used to evaluate the goodness-of-fit for the oscillation hypothesis. If the predicted number of events in each reconstructed prompt energy bin $i$ is sufficiently large, the minimum of equation 5.2 follows a $\chi^2$ distribution with *N-1* degrees of freedom [33], where $N$ is the number of bins.

A mathematically equivalent method of minimizing the $\chi^2$ given in equation 5.2, is to minimize a related pulls-based $\chi^2$ in terms of $\sin^2 2\theta_{13}$ and one or many systematic parameters or "pulls" [99]. The advantage of the pull-based approach is that one learns the value of the pulls at the $\chi^2$ minimum giving an indication of how the data constrains the systematic parameters and how each systematic parameter contributes do the overall $\chi^2$. Therefore, the default $\chi^2$ function, used in this section, to be minimized is defined as:

$$\chi^2 = \sum_{ij} \left[ N_i^{\text{data}} - N_i^{\text{predic.}} \left( \sin^2 2\theta_{13} \right) \right]$$
$$\times M_{ij} \left( \sin^2 2\theta_{13} \right)^{-1} \times \left[ N_j^{\text{data}} - N_j^{\text{predic.}} \left( \sin^2 2\theta_{13} \right) \right] \quad (5.4)$$
$$+ \frac{\varepsilon_{\text{cosmo}}^2}{\sigma_{\text{cosmo}}^2} + \frac{\varepsilon_{\text{cor}}^2}{\sigma_{\text{cor}}^2} + \frac{\left( \Delta m_{31}^2 - \left( \Delta m_{31}^2 \right)_{\text{MINOS}} \right)^2}{\sigma_{\text{MINOS}}^2},$$

where $\varepsilon$ refers to the pull term for the cosmogenic or correlated rate uncertainty, and $\sigma$ its the rate uncertainty. The value of $\Delta m^2$ is also constrained by a pull term.

### 5.1.1 Covariance Matrix Determination

The covariance matrix $M$ is used to encode the knowledge of the uncertainties in $N_i^{\text{predic.}}$ and background events in the prompt energy bin $i$, as well as the correlations between the bins. The six major sources of uncertainty that contribute to our definition of $M$ are:

- $M^{\text{stat}}$: the statistical uncertainty in the predicted number of events;

- $M^{\text{reac}}$: the systematic uncertainty in the predicted reactor neutrino flux and IBD cross-section, described in sec. 4.1.2;

- $M^{\text{escl}}$: the systematic uncertainty in the relative energy reconstruction differences between data and MC, described in sec. 4.3.4;

- $M^{\text{eff}}$: the systematic uncertainty in the relative efficiency for selecting IBD events in the data and the MC, described in sec. 4.6;

- $M^{\text{b,rate}}$: the rate uncertainty in the predicted number of events for the $b$-th background, described in sec. 4.7;

- $M^{\text{b,shape}}$: the spectral uncertainty in the predicted number of events for the $b$-th background, described in sec. 4.7;

The above mentioned sources of uncertainty are all uncorrelated. Thus, the total covariance matrix is just the sum of the covariance matrices describing each of these sources of uncertainty:

$$M_{ij}^{\text{total}} = M_{ij}^{\text{stat}} + M_{ij}^{\text{reac}} + M_{ij}^{\text{escl}} + M_{ij}^{\text{eff}} + M_{ij}^{\text{b,rate}} + M_{ij}^{\text{b,shape}}. \quad (5.5)$$

Each term $M_{ij}^A = cov(N_i^{\text{pred}}, N_j^{\text{pred}})$ on the right-rand side of equation 5.5 represents the covariance of $N_i^{\text{pred}}$ and $N_j^{\text{pred}}$ due to uncertainty $A$. In the following subsections further details of the construction of these matrices are given.

### 5.1.1.1 Statistical Uncertainty

The statistical uncertainty in each energy bin is assumed completely uncorrelated with each other. Thus, it is considered as a diagonal matrix:

$$M_{ij}^{\text{stat}} = (N_i^{\text{predic.}} \left( \sin^2 2\theta_{13} \right)) \delta_{ij}. \tag{5.6}$$

The statistical uncertainty matrices are represented in figures 5.2a and 5.3a.

### 5.1.1.2 Neutrino Flux Prediction Uncertainty

The covariance matrix concerning the IDB prediction for the detector is obtained from the covariance matrix for the reactor neutrino prediction, $m_{ij}^{\text{pred}}$, calculated in Section 4.1.3, correcting for the number of MC events:

$$M_{ij}^{\text{reac}} = \frac{N_i^{\nu}}{n_i^{\nu}} \frac{N_j^{\nu}}{n_j^{\nu}} m_{ij}^{\text{pred}}, \tag{5.7}$$

where $N_i^{\nu}$ is the expected number of IBD signal given by equation 4.2 and $n_i^{\nu}$ is the number of the MC events with no oscillation given by the same equation. The total flux prediction uncertainty matrix are shown in figures 5.2b and 5.3b.

### 5.1.1.3 Detector Efficiency Uncertainty

Since corrections are used to account for differences in the relative efficiency for selecting IBD events in the data and MC as well their associated uncertainties, the relative uncertainty between data and MC enters into the fit as an overall normalization uncertainty. Thus, a combination of the relative efficiency uncertainty of all sources of normalization uncertainty, discussed in section 4.6, is performed. The normalization covariance matrix that describes this uncertainty is defined as:

$$M_{ij}^{\text{eff}} = \sigma_{\text{eff}}^2 N_i N_j, \tag{5.8}$$

where $N_i$ is the predicted number of signal IBD candidate events in energy bin $i$. The detector efficiency covariance matrix can be seen in figures 5.2c and 5.3c.

### 5.1.1.4 Energy Scale Uncertainty

The energy scale covariance matrix is described in section 4.3.4. Uncertainties in the parameters that model the differences in the energy scales between data and MC induce uncertainties in the shape of the predicted reconstructed positron energy as events migrate between energy bins. However, they can also induce normalization uncertainties by changing the number of selected IBD candidates events in a correlated way.

As described in section 4.3.4, the fractional energy response covariance matrix is converted back to a full covariance matrix using the expected MC IBD signal plus background prompt energy spectrum. Figures 5.2d and 5.3d shows the energy scale covariance matrices.

### 5.1.1.5 Accidental Background Uncertainty

The shape of the accidental background spectrum is measured very accurately from the data, as described in section 4.7.1. Therefore, no systematic uncertainty is assigned to the shape of the accidental spectrum. Moreover, since the accidental rate is accurately

measured for each bin, their correlation is assumed to be zero. The rate systematic uncertainty is expressed by the following diagonal matrix:

$$M_{ij}^{\text{acc}} = \sigma_{\text{acc}}^2 N_i^{\text{acc}} N_j^{\text{acc}} \delta_{ij}, \tag{5.9}$$

where $N_i^{\text{acc}}$ is the number of the accidental events in the $i$-th energy bin and $\sigma_{\text{acc}}^2$ is the uncertainty of the accidental background rate. The accidental matrices are represented in figures 5.2e and 5.3e.

### 5.1.1.6   Correlated Background Shape Uncertainty

As described in Sec. 4.7.2, the primary analysis for the shape of the fast neutron and stopping muon background predicts a flat spectrum, while a second independent analyses predicts a linear spectrum increasing as a function of energy. In order to cover both analyses, the fast neutron and stopping muon background was modelled as a flat spectrum, with a fully correlated shape uncertainty determined from the bin-by-bin differences, $\delta N_i^{\text{corr}}$, between the flat model and the alternative linear hypothesis, in which both were normalized to the predicted rate. Therefore, the correlated background shape uncertainty was included as a covariance matrix of the form:

$$M_{ij}^{\text{corr,shape}} = \delta N_i^{\text{corr}} \delta N_j^{\text{corr}}. \tag{5.10}$$

The correlated background shape covariance matrices are shown in figures 5.2g and 5.3g.

### 5.1.1.7   Cosmogenic Background Shape Uncertainty

Similar to the correlated background the shape uncertainty for the cosmogenic background is treated as fully correlated. Since the cosmogenic spectrum shape uncertainty expectation relies on MC simulations, uncertainties in the MC event generation modelling is considered. As mentioned in section 4.7.3, differences of the reconstructed prompt spectra of two models of the $^9$Li branching ratios is considered and the shape uncertainty is taken as the difference between a central value prediction and the alternative hypothesis, given by

$$M_{ij}^{\text{cosmo,shape}} = \delta n_i^{\text{cosmo}} \delta n_j^{\text{cosmo}}, \tag{5.11}$$

where $\delta n_i^{\text{cosmo}}$ is the difference of numbers of events in the $i$-th energy bin between the two models.

### 5.1.1.8   Correlated Light Noise Uncertainty

The correlated light noise contamination on the Gadolinium sample is negligible and very small for the Hydrogen sample. Thus, its covariance matrix was calculated in the same way as for the accidental background. It can be seen in figure 5.3h.

### 5.1.2   Fit Procedure

For each value of $\sin^2 2\theta_{13}$ the MC expectation and covariance matrices are recalculated and equation 5.4 is minimized for the pull terms, using a custom-built tool kit written in C++ that uses the **ROOT** [65] analysis framework libraries and **MINUIT** [100], a software package for minimization and error analysis. As described in section 4.1.1, MC IBD candidates are generated with a factor 100 more than the predicted for the detector run time. This is made to reduce the uncertainty associated with statistical fluctuation in the MC so that they become negligible compared to the statistical fluctuations in the

(a) Statistical Uncertainty



(b) Flux Prediction



(c) Efficiency



(d) Energy Scale



(e) Accidental Background



(f) Cosmogenic Background Shape



(g) Correlated Background Shape
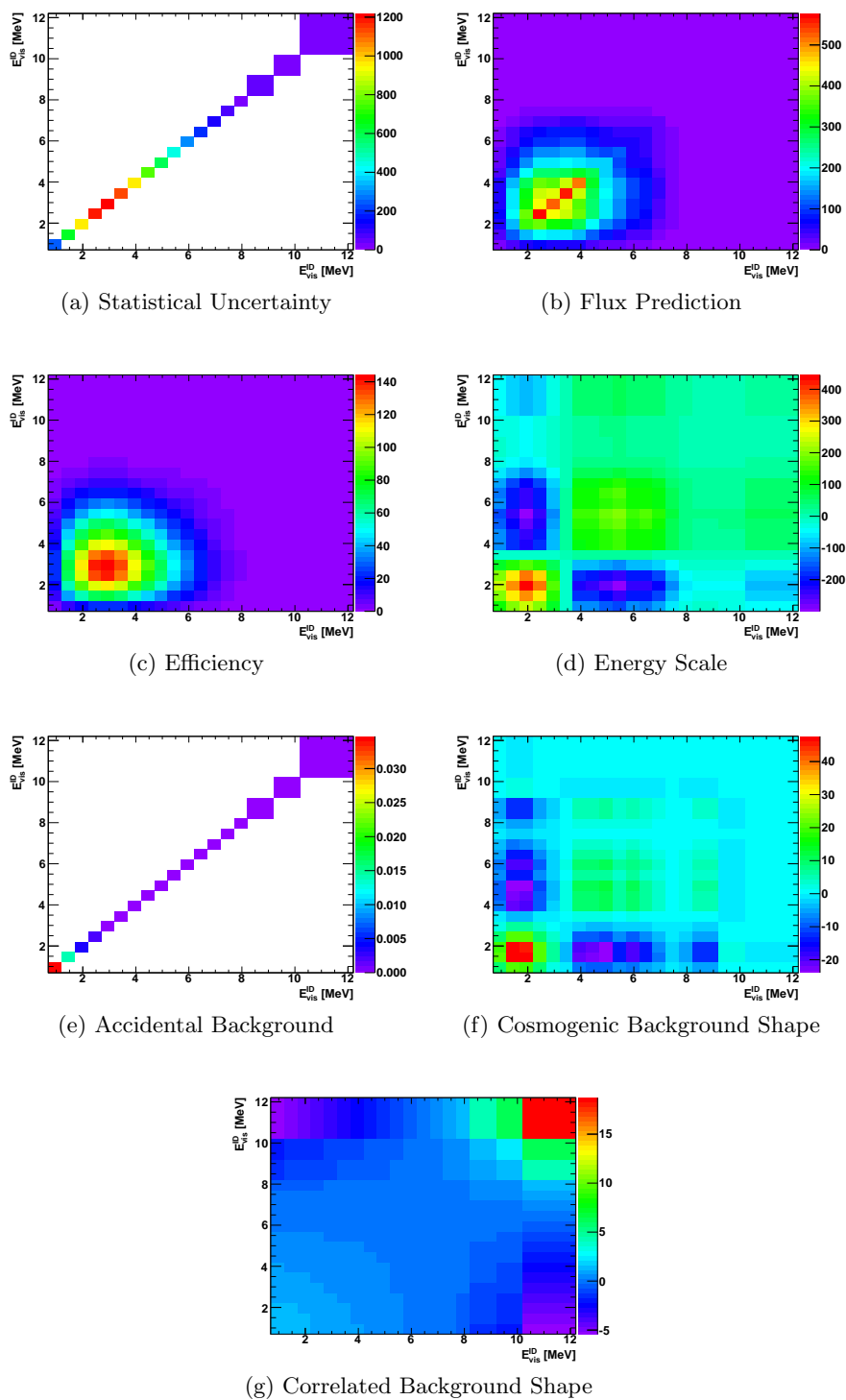
Figure 5.2: Systematic uncertainty covariance matrices of the expected prompt energy spectrum for the gadolinium analysis.

(a) Statistical Uncertainty

(b) Flux Prediction

(c) Efficiency

(d) Energy Scale

(e) Accidental Background

(f) Cosmogenic Background Shape

(g) Correlated Background Shape

(h) Correlated Light Noise
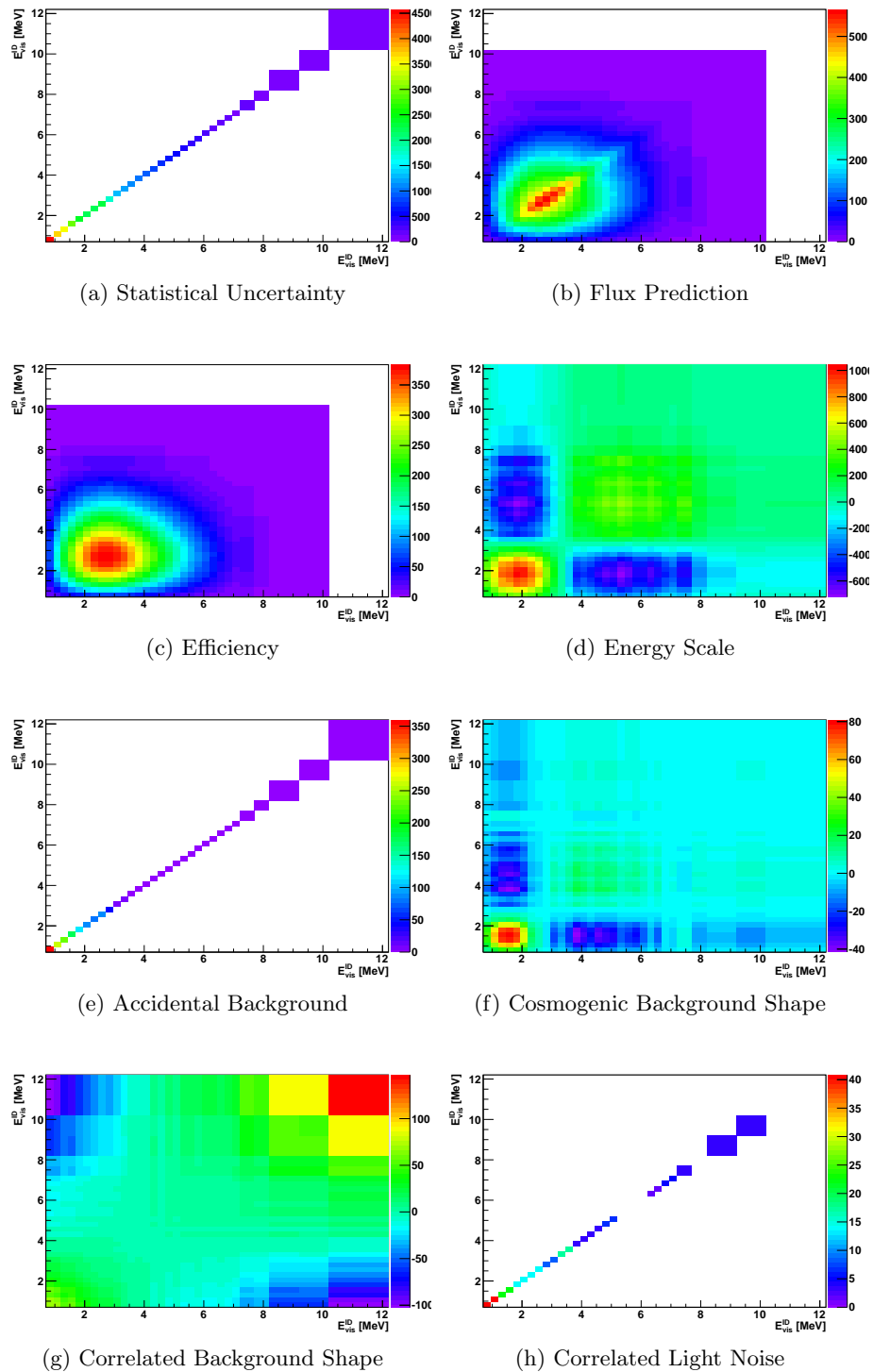
Figure 5.3: Systematic uncertainty covariance matrices of the expected prompt energy spectrum for the hydrogen analysis.

data. The MC events are then re-weighted by a factor 1/100, in order to correspond to the expected number of IBD events in the data. Then, the MC are re-weighted again by a correction that accounts for data/MC differences, and it is discussed in section 4.6.

For each of the backgrounds, estimated in section 4.7, a set of MC background events is generated according to the measured background rate by randomly sampling from the corresponding prompt energy spectrum. The accidental and fast neutron/stopped muon backgrounds use the reconstructed prompt energy spectra measured directly from the data to generate MC background events. For the cosmogenic background, however, the MC prompt energy spectrum shown in figure 4.53 is used to generate MC events since the measured cosmogenic energy spectrum do not have enough statistics, as described in section 4.7.3.

Similar to the MC IBD events, a factor of 100 more MC background events are generated than are predicted for the detector run time corresponding to the data, and these are then re-weighted by a factor of 1/100. However, in contrast to the IBD MC events, the MC background events just consist of random pulls from reconstructed energy spectra. Therefore, they should not be re-weighted by IBD selection efficiency corrections, which are already taken into account by the background estimation itself. Therefore, the MC background events are only re-weighted by an additional factor to correct for the muon veto dead time, whose effect is not included in the MC background simulation.

### 5.1.3  Gd Data Results

For the neutron captured in Gadolinium event selection, the contribution of each uncertainty is summarized in table 5.1 and the covariance matrices are in figure 5.2. The minimization of equation 5.4, described previously, gives the $\chi^2$ distribution as

Table 5.1:  Summary of signal and background uncertainty of the gadolinium analysis

| Source | Uncertainty [%] |
|---|---|
| Reactor Flux | 1.67 |
| Detector Response | 0.32 |
| Statistics | 1.06 |
| Efficiency | 0.95 |
| Accidental | 0.01 |
| Cosmogenic | 1.38 |
| Correlated | 0.51 |
| Total | 2.66 |

function of $\sin^2 2\theta_{13}$, which is showed in figure 5.4. The best fit value found is

$$\sin^2 2\theta_{13} = 0.100^{+0.038}_{-0.039},$$
$$\chi^2_{\mathrm{min}} = 20.84 \,/\, 17 \text{ Degrees of Freedom},$$

which corresponds to a goodness-of-fit of 23.4%. The inputs used for the pull terms, together with their output at best fit value, are in table 5.2, where it is possible to see the good agreement between the numbers.

Figure 5.5 shows the reconstructed prompt energy spectrum for the data and the MC prediction for the case of no oscillation and for the best fit result. The black points are the data shown with statistical errors only. The blue histogram is the no-oscillation MC prediction and the red histogram is the best fit oscillated spectrum, whit total systematic uncertainty represented by the orange band. The residual plot is also shown in the lower panel of this figure.
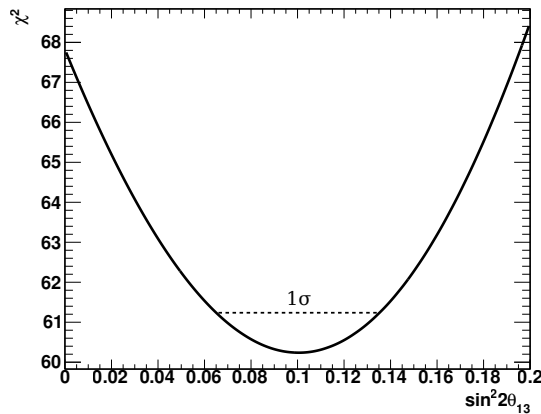
Figure 5.4: $\chi^2$ distribution for the rate plus shape fit using the gadolinium data. The best fit value correspond to $\sin^2 2\theta_{13} = 0.100^{+0.038}_{-0.039}$.

Table 5.2: Input and output of the Gd pull terms

| Pull Term | Input | Output |
|---|---|---|
| Cosmogenic Bkg. Rate | $1.25 \pm 0.54$ | 0.914 |
| Correlated Bkg. Rate | $0.67 \pm 0.20$ | 0.68 |
| $\Delta m^2$ | $2.32 \pm 0.12$ | 2.32 |

### 5.1.4 H Data Results

For the neutron captured in Hydrogen event selection, the contribution of each uncertainty is summarized in table 5.3 and the covariance matrices are in figure 5.3. The minimization of equation 5.4, described previously, gives the $\chi^2$ distribution as

Table 5.3: Summary of signal and background uncertainty of the hydrogen analysis

| Source | Uncertainty [%] |
|---|---|
| Reactor Flux | 1.8 |
| Detector Response | 0.3 |
| Statistics | 1.1 |
| Efficiency | 1.6 |
| Accidental | 0.2 |
| Cosmogenic | 1.6 |
| Correlated | 0.6 |
| Light Noise | 0.1 |
| Total | 3.1 |

function of $\sin^2 2\theta_{13}$, which is showed in figure 5.6. The best fit value found is

$$\sin^2 2\theta_{13} = 0.096^{+0.049}_{-0.048},$$
$$\chi^2_{\min} = 39.85 \,/\, 30 \text{ Degrees of Freedom},$$

which corresponds to a goodness-of-fit of 10.8%. The inputs used for the pull terms, together with their output at best fit value, are in table 5.4, where it is possible to see the good agreement between the numbers.

Figure 5.7 shows the reconstructed prompt energy spectrum for the data and the MC prediction for the case of no oscillation and for the best fit result. The color scheme
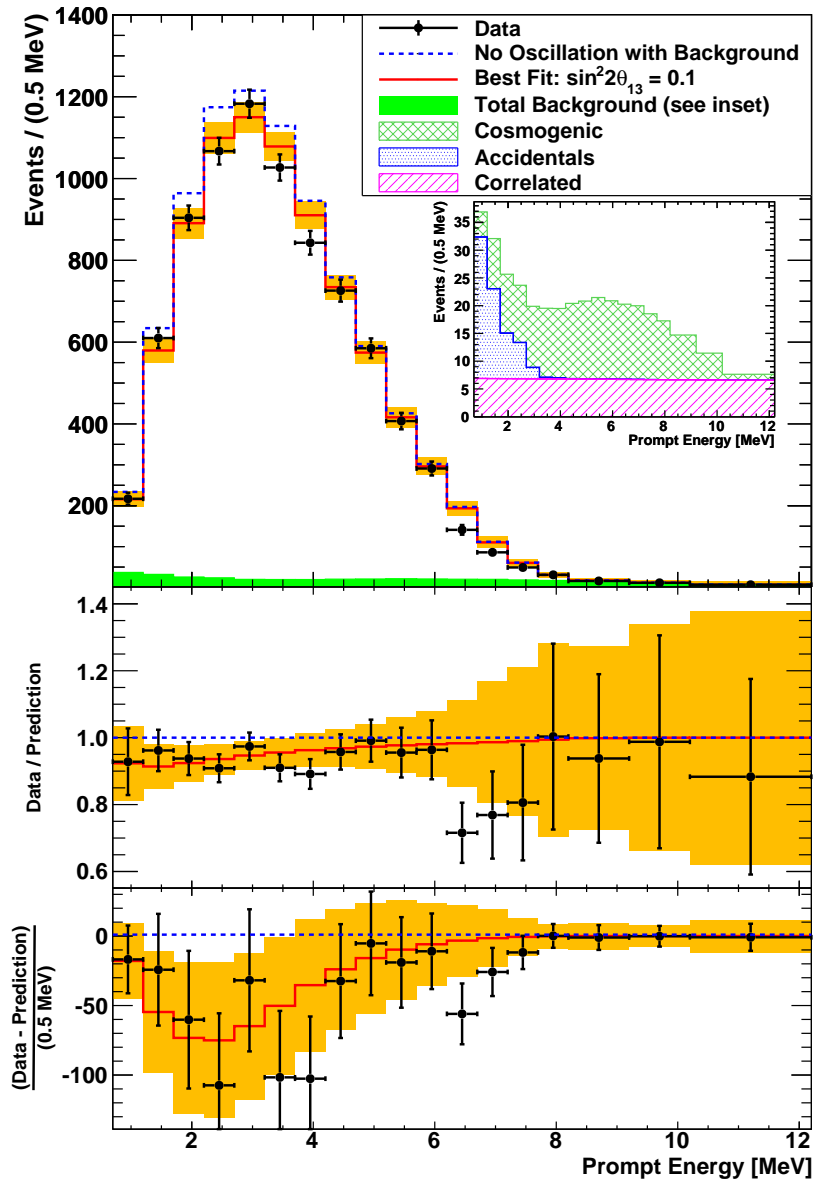
Figure 5.5: Prompt energy spectrum for Gadolinium IBD events. The black pints are the data and its statistical error. The blue curve is the prediction without oscillation and the red histogram shows the best fit spectrum expectation with $\sin^2 2\theta_{13} = 0.100^{+0.038}_{-0.039}$ and the background estimation. The green histogram is the total background with the best fit value, while the inset shows the three main background stacked. The orange region is the 1 $\sigma$ systematic uncertainty of each energy bin of the best fit expectation. The bottom plots are the ratio and difference, respectively, of the data and best fit, compared with the no oscillation expectation.

Table 5.4:  Input and output of the H pull terms

| Pull Term | Input | Output |
|---|---|---|
| Cosmogenic Bkg. Rate | $2.84 \pm 1.15$ | 3.79 |
| Correlated Bkg. Rate | $2.50 \pm 0.47$ | 2.55 |
| $\Delta m^2$ | $2.32 \pm 0.12$ | 2.31 |
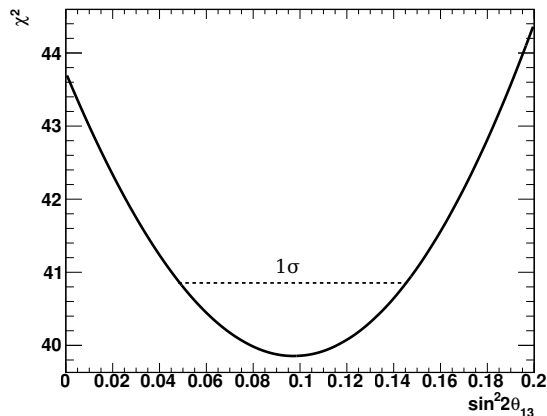
Figure 5.6: $\chi^2$ distribution for the rate plus shape fit using the hydrogen data. The best fit value correspond to $\sin^2 2\theta_{13} = 0.096^{+0.049}_{-0.048}$.

is the same as for figure 5.5. In addition, the spectra showed in this figure have the accidental background subtracted, for a better visualisation, since the contribution of this source is on the order of the signal, as showed in figure 4.61b. The energy spectrum with background and signal expectation is shown in figure 5.8.

### 5.1.5 Combined Gd+H Analysis

In order to perform a combined analysis to extract the value of $\theta_{13}$ using both Gadolinium and Hydrogen data, the correlation, between these two dataset must be accounted for. A zero correlation is not expected since both dataset are under the same detection systematics, with only a few differences on their selection.

The standard definition for the correlation coefficient, between two source of uncertainty, $x$ and $y$, is defined as

$$\rho_{xy} \equiv \frac{\text{Cov}[x,y]}{\sigma_x \sigma_y}, \tag{5.12}$$

and it takes a value in the range $-1 \leq \rho \leq 1$. $x$ and $y$ refer to the value of a specific parameter in the Gadolinium and Hydrogen analysis, respectively, throughout this section.

For each source of uncertainty, the correlation coefficients are summarized in table 5.5. The cosmogenic and FN/SM rate are considered uncorrelated because they are measured using disjoint datasets. For the accidentals, although the method is similar, the rate is also measure directly form disjoint datasets. The correlated light noise is not accounted for the gadolinium analysis, thus it is also uncorrelated. The FN/SM shape uncertainty came from fits to different datasets with different functional forms. The cosmogenic shape uncertainty is derived from the same MC simulation for both dataset, therefore it is considered fully correlated. The reactor uncertainties are also considered fully correlated since the reactor flux is the same for both analysis. Finally the partially correlation of the detection uncertainty and the energy scale are explained in more detail in the following subsections.

#### 5.1.5.1 Efficiency Correlation

This quantity depends mainly on the neutron detection efficiency, since corrections on the MC are applied in order to match the data efficiency. For the both hydrogen and
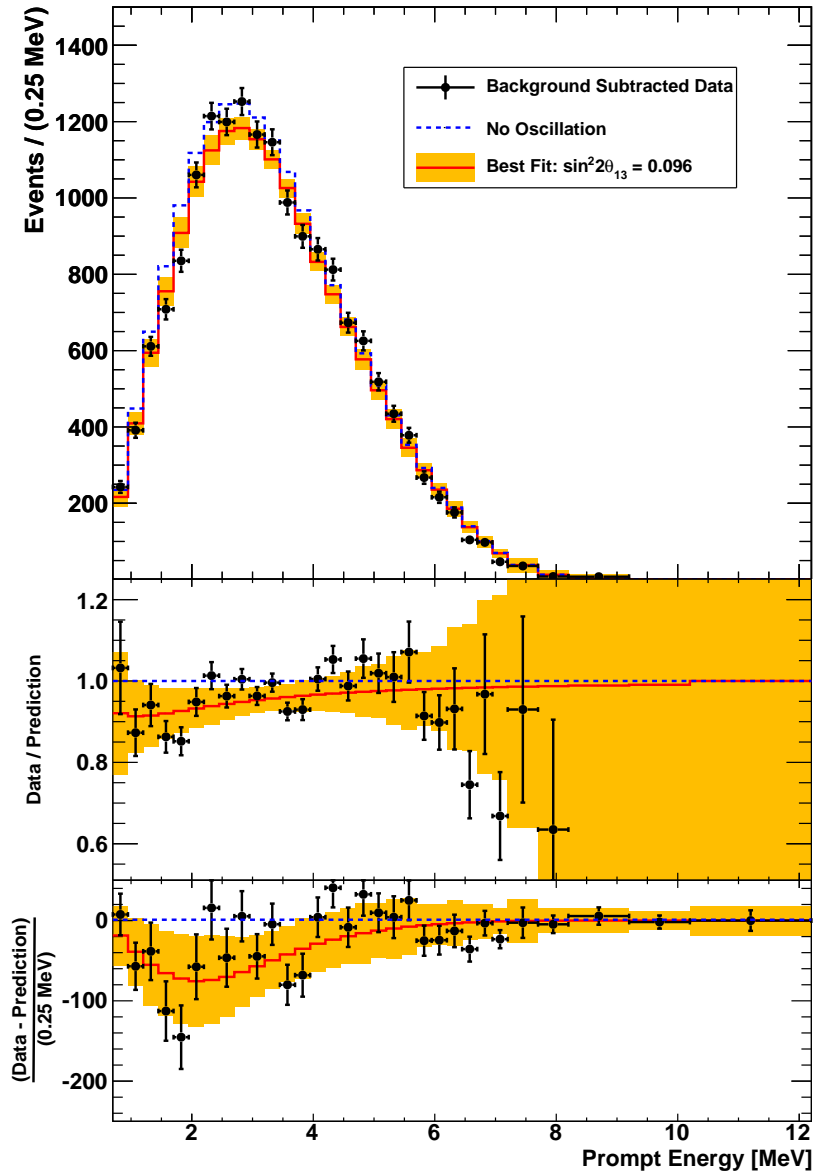
Figure 5.7: Prompt energy spectrum for Hydrogen IBD events. The black pints are the data and its statistical error. The blue curve is the prediction without oscillation and the red histogram shows the best fit spectrum expectation with $\sin^2 2\theta_{13} = 0.096^{+0.049}_{-0.048}$ and the background estimation. The orange region is the 1 $\sigma$ systematic uncertainty of each energy bin of the best fit expectation. The bottom plots are the ratio and difference of the data and best fit, compared with the no oscillation expectation.
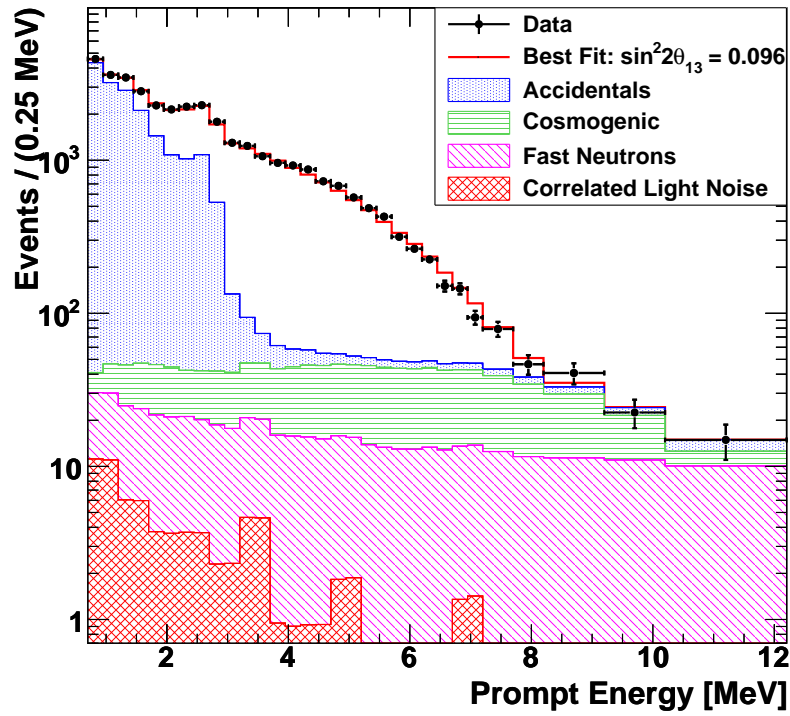
Figure 5.8: Prompt energy spectrum of IBD event candidates without background subtraction. The black points are data with statistical uncertainty, while the red line is the best fit oscillation hypothesis. The contributions from accidentals, $^9$Li, fast neutrons and correlated light noise, are also shown.

Table 5.5:   Correlation factor estimation for each systematic uncertainty for the Gadolinium and Hydrogen data sets.

| Systematic Uncertainty | Correlation Factor |
| --- | --- |
| Statistics | 0 |
| Reactor Flux | 1 |
| Efficiency | 0.09 |
| Energy Scale | 0.39 |
| Accidental Bkg. | 0 |
| Cosmogenic Bkg. Rate | 0 |
| Cosmogenic Bkg. Shape | 1 |
| FN/SM Bkg. Rate | 0 |
| FN/SM Bkg. Shape | 0 |
| Correlated Light Noise Bkg. | 0 |

gadolinium analysis, the MC correction factor accounts for data and MC differences in: $\Delta$t cut efficiency; $\Delta$R cut efficiency; $E_{\text{delayed}}$ cut efficiency; Multiplicity cut efficiency; Gd fraction; number of protons; spill in/out; and electronics. The systematic uncertainty on MC correction factor is included as a signal normalization uncertainty, which includes uncertainty on all factors listed above. To quantify correlation in efficiency uncertainty, the level of correlation of each of the above mentioned uncertainties in Gd and H analysis must be determined. However, these quantities are only possible correlated in the NT volume, since there is no Gd on the GC. For the Hydrogen analysis, 5.39% of the antineutrino interactions occur in the NT, therefore almost all the correlated uncertainties must have their H component re-weighted by this factor. The only exception to this is the uncertainty due to spill events, which must have its NT H component re-weighted by a factor of $1.46/4.58 = 0.319$, which is the fraction of H spill events that migrate between the NT and GC.

The best approximation of the efficiency uncertainty correlations are:

- $\Delta T$ : The $\Delta T$ cut efficiency depends on neutron transport model. It is considered to be uncorrelated because different techniques are used to evaluate the uncertainty: Gd uses a combination of z-axis and guide tube Cf data, while H uses a sampling method with Cf on the z-axis only. Moreover, different physics dominates the uncertainty for different event classes: in Gd ($\Delta T > 2$ $\mu$s) the uncertainty is dominated by neutron thermalization model; in H ($\Delta T > 10$ $\mu$s) the uncertainty is dominated by capture lifetime uncertainty. and is fully correlated in the target region and uncorrelated in the gamma catcher, since it is used only for the Hydrogen analysis.

- $\Delta R$ : There is no $\Delta R$ cut in the Gadolinium analysis, thus it is uncorrelated.

- **Energy Cut** : The efficiency on the $E_{\text{delayed}}$ cut depends on the modelling of $\gamma$'s from neutron capture, that is different for each analysis. In addition, the two analysis have a cut in different region. If there is any correlation, they may already be accounted for by the energy scale correlation, thus it is considered uncorrelated.

- **Gd/H** : The Gd fraction is anti-correlated in the NT region, since an overestimation in Gd causes an underestimation in H, and it is zero for the GC region.

- **Proton Number** : The proton number in the NT is fully correlated between Gd and H analysis, since they share the same measurement for this quantity.

- **Spill In/Out** : The main source of uncertainty in the determination of Spill events is the MC neutron mobility model in the NT and Gd concentration. Since they are measured similarly, NT events have fully correlated spill uncertainty.

Table 5.6 summarizes all the above uncertainties and their correlations.

Because there are correlated and anticorrelated uncertainties, the total correlation coefficient takes the form:

$$\rho_{\text{eff}} = \rho_{\text{corr}} - \rho_{\text{anticorr}}, \tag{5.13}$$

where $\rho_{\text{anticorr}}$ is due to the Gd/H capture fraction uncertainty and $\rho_{\text{corr}}$ is due to the combination of the proton number and spill uncertainties. Re-weighting the Gd/H fraction uncertainty, the anticorrelation coefficient is:

$$\rho_{\text{anticorr}} = \frac{\sigma_{\text{Gd}}^{\text{Gd cap.}} \sigma_{\text{H}}^{\text{H cap.}}}{\sigma_{\text{Gd}}^{\text{tot.}} \sigma_{\text{H}}^{\text{tot.}}} = \frac{0.3\% \cdot (0.0539 \cdot 1.12\%)}{1.101\% \cdot 1.57\%} = 0.01. \tag{5.14}$$

Table 5.6: Efficiency uncertainty for the NT (Gd and H analysis) and GC (H analysis) volumes. The last column shows the correlation between Gd and H analysis in the NT.

| Source | Gd unc. | H unc. (NT) | H unc. (GC) | $\rho$ (NT) |
|---|---|---|---|---|
| Gd/H frac. | 0.3% | 1.12% | 0.31% | -1 |
| $\Delta T$ eff. | 0.5% | 1.78% | 0.17% | 0 |
| $\Delta R$ eff. | - | 0.51% | 0.19% | 0 |
| Energy Cut | 0.7% | 0.29% | 0.23% | 0 |
| Spill In/Out | 0.3% | 1.17% | 1.17% | 1 |
| Proton Number | 0.3% | 0.3% | 1.0% | 1 |
| Total | 1.01% | 1.57% | | |

The spill and proton number uncertainties are the only efficiency uncertainties with positive correlation between the Gd and H analysis, and the correlation coefficient is:

$$\rho_{\text{corr.}} = \frac{\sqrt{0.3\%^2 + 0.3\%^2} \cdot \sqrt{(0.319 \cdot 1.17\%)^2 + (0.0539 \cdot 0.3\%)^2)}}{1.01\% \cdot 1.57\%} = 0.1. \qquad (5.15)$$

Using equation 5.13, the correlation coefficient for the efficiency uncertainty is $\rho_{\text{eff}} = 0.09$.

### 5.1.5.2 Energy Scale Correlation

For both Gadolinium and Hydrogen analysis, the uncertainty on the energy scale has three contributions: Relative Non-linearity; Relative Time Instability; and Relative Non-uniformity. They are assumed in quadrature to get a total uncertainty, as showed in table 4.3. The only component which was re-evaluated for the Hydrogen analysis was the non-uniformity, due the fact that antineutrinos primarily interact in the GC, for this analysis.

Since different methods were used to evaluate the non-uniformity uncertainty in the GC, the energy scale uncertainty is considered to be uncorrelated for this component. While the same value and measurement for non-linearity is used in both analysis, it has been suggested that the energy scale non-linearity may manifest itself differently in the NT and GC. For this reason, a compromise was struck in which the non-linearity was considered 50% correlated between both analysis. Therefore, the correlation coefficient is

$$\rho_{\text{E}_{\text{scale}}} = \frac{\sigma_{\text{Gd}}^{\text{corr.}} \cdot \sigma_{\text{Gd}}^{\text{corr.}}}{\sigma_{\text{Gd}}^{\text{tot.}} \cdot \sigma_{\text{Gd}}^{\text{tot.}}} = \frac{\sqrt{0.5(0.85\%)^2 + 0.61\%^2} \cdot \sqrt{0.5(0.85\%)^2 + 0.61\%^2}}{1.13\% \cdot 1.69\%} = 0.39.$$
$$(5.16)$$

### 5.1.5.3 Results

The correlations described above were used to construct the covariance matrices, that can be seen in figure 5.9. These matrix is used for a similar fit that were performed in the Gd and H analysis, by minimization of equation 5.4. A comparison of the $\Delta\chi^2$ for the three analysis is presented in figure 5.10. From this figure is possible to infer that the addition of the Hydrogen sample, to the Gadolinium one, improves the measurement of $\theta_{13}$, and gives a best fit value of

$$\sin^2 2\theta_{13} = 0.100 \pm 0.034,$$
$$\chi^2_{\text{min}} = 60.24 \, / \, 48 \text{ Degrees of Freedom.}$$

The pull terms input and best fit output, for this combined fit, are summarized in table 5.7.

(a) Statistical Uncertainty

(b) Flux Prediction

(c) Efficiency

(d) Energy Scale

(e) Accidental Background

(f)  Cosmogenic   Background Shape

(g)   Correlated    Background Shape

(h) Correlated Light Noise
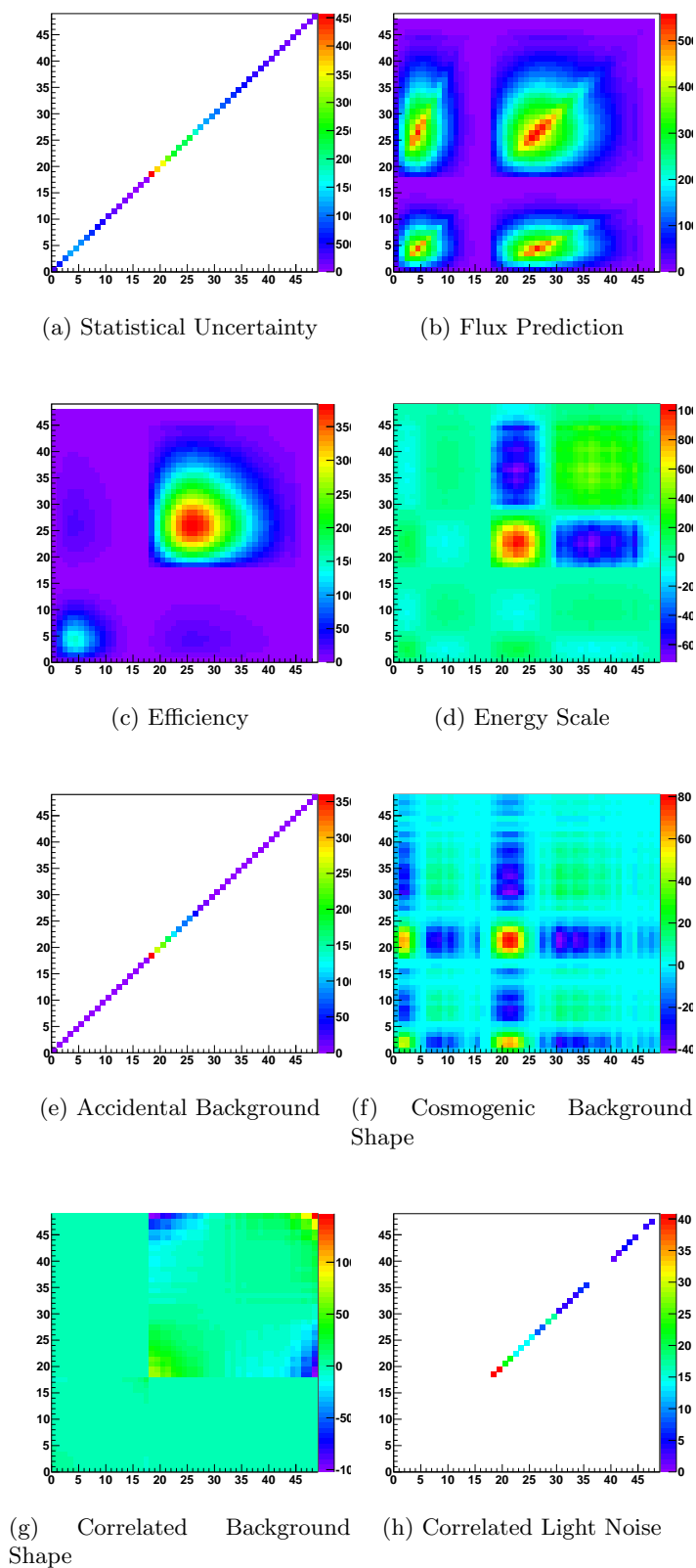
Figure 5.9: Systematic uncertainty covariance matrices of the expected prompt energy spectrum for the combined Gd+H analysis.
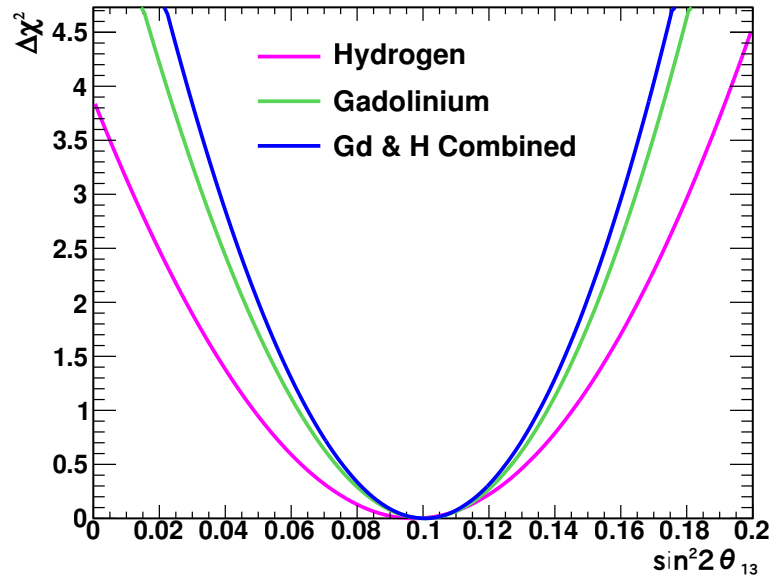
Figure 5.10: $\Delta\chi^2$ distribution for each Gd and H analysis and the combined. The additon of the Hydrogen data makes the combined analysis $\chi^2$ distribution narrower than the Gd only one, showing the improvement on the final result of $\sin^2 2\theta_{13}$

Table 5.7:  Input and output of the combined Gd+H pull terms

| Pull Term | | Input | Output |
|---|---|---|---|
| Cosmogenic Bkg. Rate | Gd | $1.25 \pm 0.54$ | 0.73 |
| | H | $2.84 \pm 1.15$ | 4.13 |
| Correlated Bkg. Rate | Gd | $0.67 \pm 0.20$ | 0.69 |
| | H | $2.50 \pm 0.47$ | 2.61 |
| $\Delta m^2$ | | $2.32 \pm 0.12$ | 2.31 |

#### 5.1.5.4   Summary and Future Sensitivity

The $\theta_{13}$ result acquired in this dissertation can be compared with the other reactor and accelerator experiment results, as showed on the left of figure 5.11. An estimation of the
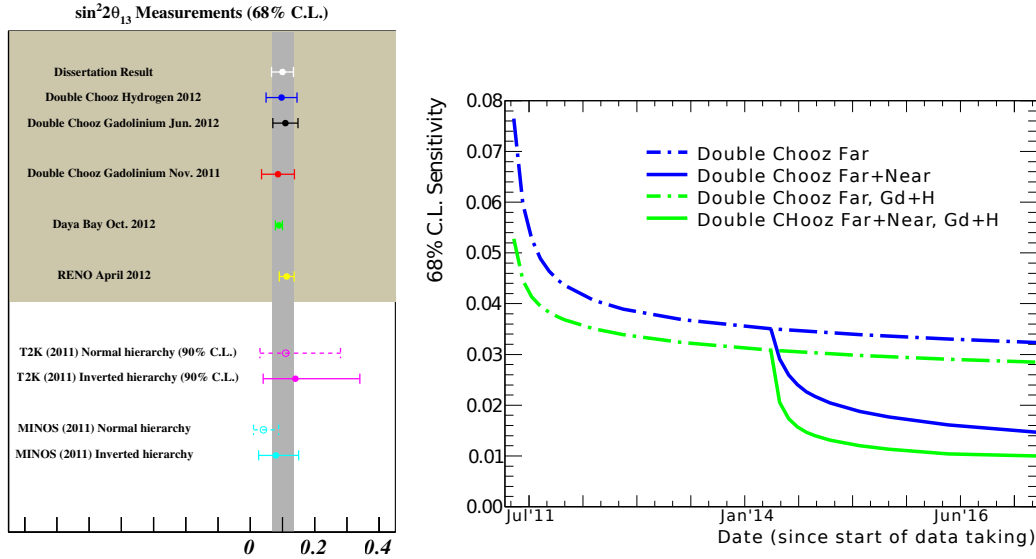


Figure 5.11: $\theta_{13}$ result from all the current experiment and the Double Chooz experiment future sensitivity. On the left plot, the result obtained in this dissertation is compared with the past Double Chooz results and with the current reactor and accelerator based $\theta_{13}$ experiments. On the right, the future sensitivity of the Double Chooz experiment is shown for different analysis scenarios, where the ultimately sensitivity is expected to be $\delta(\sin^2 2\theta_{13}) \sim 0.010$ by 2016.

future sensitivity of the Double Chooz experiment is show on the right of figure 5.11, for different analysis scenarios. This figure shows that by the end of the far detector only stage, a sensitivity of $\delta(\sin^2 2\theta_{13}) \sim 0.030$ will be obtained, and after six months of near and far data, $\delta(\sin^2 2\theta_{13}) \sim 0.015$. The ultimately sensitivity for the experiment is expected to be archived by 2016 with $\delta(\sin^2 2\theta_{13}) \sim 0.010$.

## 5.2   Measurement of $\Delta \tilde{m}^2_{31}$

As explained in section 2.5.4, a measurement of $\Delta \tilde{m}^2_{31}$ can be performed with $E/L$ analysis, i.e., detectors at different baselines or spectral distortion in a single detector. In the followings subsection a description of two methods to retrieved the mass difference by baseline dependence and their results are showed. A briefly discussion on the possibility of measurement by spectral analysis is also given.

### 5.2.1   Weighted Baseline Analysis

To avoid dealing with energy reconstruction uncertainties, a rate analysis using detectors at different locations can be performed to get the value of the effective mass splitting related to disappearance of electron antineutrinos. In order to perform this analysis a combination of Daya Bay and RENO's result together with Double Chooz is required.

The reactor neutrino disappearance probability of each experiment, $P_{\mathrm{d}}$, can be related to the oscillation parameters such as [101],

$$P_{\mathrm{d}} = \sin^2 2\theta \frac{\int_{1.8\mathrm{MeV}}^{8.0\mathrm{MeV}} S_\nu(E)\sigma_{\mathrm{IBD}}(E) \sin^2\left(\frac{\Delta m^2 L}{4E}\right) dE}{\int S_\nu(E)\sigma_{\mathrm{IBD}}(E) dE} \equiv \sin^2 2\theta \Lambda(\Delta m^2 L). \qquad (5.17)$$

where $S_\nu(E)$ is the reactor neutrino energy spectrum and $\sigma_{\rm IBD}$ the interaction cross section.

As already discussed in section 3.1, the energy spectrum of the reactor neutrinos is a sum of the energy spectrum of neutrinos from the four fissile elements,

$$S_\nu(E_\nu) = \sum_{i={}^{235}{\rm U},{}^{238}{\rm U},{}^{239}{\rm Pu},{}^{241}{\rm Pu}} \beta_i f_i(E_\nu), \qquad (5.18)$$

where $f_i(E_\nu)$ is reactor neutrino spectrum per fission from fissile element $i$ and $\beta_i$ is a fraction of fission rate of fissile element $i$. There is a relation $\sum_i \beta_i = 1$. For equilibrium light water reactors, $\beta_i$ are similar and is possible to make the assumption of a nuclear fuel cycle mean values. On this analysis the values in Bugey paper [85], namely ${}^{235}{\rm U} : {}^{238}{\rm U} : {}^{239}{\rm Pu} : {}^{241}{\rm Pu} = 0.538: 0.078: 0.328: 0.056$, are used. Moreover, for simplicity, $f_i(E)$ is approximated as an exponential of a polynomial function which is defined in [46],

$$f_i(E_\nu) \propto \exp(\sum_{j=1}^{6} \alpha_j E_\nu^{(j-1)}). \qquad (5.19)$$

The interaction cross section, defined in equation 3.5, can be written as the following energy dependence function,

$$\sigma_{\rm IBD}(E_\nu) \propto (E_\nu[{\rm MeV}] - 1.29)\sqrt{E_\nu^2 - 2.59E_\nu + 1.4}, \qquad (5.20)$$

where the information of absolute normalization is not necessary (see equation 5.17).

The flux-weighted average baselines of the far detectors, $\langle L \rangle$, for the three reactor experiments are 1.05 km for Double Chooz, 1.44 km for RENO and 1.65 km for Daya Bay, respectively. The average baseline of RENO experiment was calculated using neutrino flux shown in [102] and distances between the far detector and each reactor. Published values are used for Daya Bay and Double Chooz.

From measured disappearance probability, an allowed line can be drawn in $\sin^2 2\theta - \Delta m^2$ parameter space using the relation 5.17. Since the baselines are different for the three reactor neutrino experiments, there are three different allowed lines as shown in figure 5.12(a). The point of intersection indicates the solution of $\Delta \tilde{m}_{31}^2$ and $\sin^2 2\theta_{13}$. In real experiments, due to errors, the three lines do not cross at same point. When combining different reactor results, $\chi^2$ values are calculated by using following formula for each point of the parameter space.

$$\chi^2 = \sum_{k={\rm exp.}} \left( \frac{\sin^2 2\theta \Lambda(\Delta m^2 \langle L \rangle_k) - (P_{\rm d})_k}{\sigma_k} \right)^2, \qquad (5.21)$$

where $k$ is index of the three experiments and $\sigma_k$ is measurement error of experiment-$k$. Figure 5.12(b) shows contour of the significance in case each experiment measures the disappearance with 0.5% accuracy. In this case, $\Delta \tilde{m}_{31}^2$ can be determined with precision of $\sim 23(9)\%$ with two (one) dimensional uncertainty. The large difference between the one dimensional error and the two dimensional error is because the shape of one $\sigma$ contour island has long tail as shown in figure 5.12(b). Since there are two parameters to measure, at least three experiments are necessary to redundantly measure the parameters and test the goodness-of-fit.

In the actual analysis, $P_{\rm d}$ is not directly written in papers and it is calculated from measured $\sin^2 2\theta_{13}$ and flux-weighted mean distance $\langle L \rangle$. In their papers, $\sin^2 2\theta_{13}$ were derived by assuming the MINOS $\Delta \tilde{m}_{32}^2$ [23]. Relations between these parameters and the disappearance probability, and allowed line are shown below.

$$P_{\rm d} = \sin^2 2\theta_{13}\Lambda(\Delta \tilde{m}_{32}^2 \langle L \rangle_{\rm Far}) = \sin^2 2\theta \Lambda(\Delta m^2 \langle L \rangle_{\rm Far}). \qquad (5.22)$$
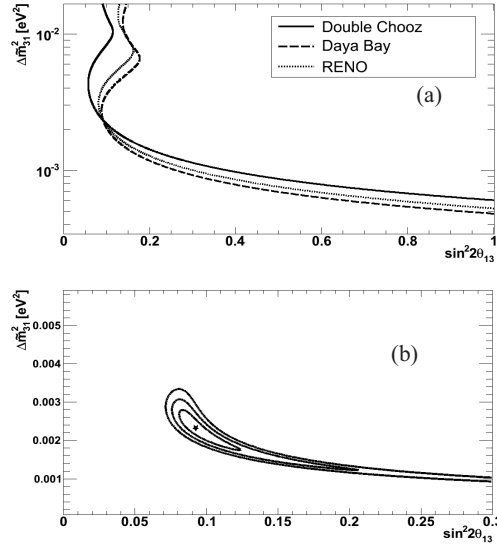
Figure 5.12: Hypothetical sensitivity plots assuming true parameter values are $\Delta m^2 = 2.32 \times 10^{-3}$ eV$^2$ and $\sin^2 2\theta = 0.092$. (a) Allowed lines if disappearance probabilities are measured as expected. (b) Allowed regions after combining the three reactor experiments. The contour lines correspond to, from inner to outer, $1\sigma$, $2\sigma$ and $3\sigma$ significances. Disappearance error of 0.5 % is assumed for each experiment. $\Delta\tilde{m}_{31}^2$ is expected to be measured with $\sim$ 23(9) % accuracy corresponding to two (one) dimensional uncertainty.

The calculated disappearance probabilities are shown in table 5.8 together with the other parameters.

Table 5.8: Parameters of the three reactor neutrino experiments.

| Item | Double Chooz | Daya Bay | RENO |
|------|--------------|----------|------|
| $\langle L\rangle_{\mathrm{Far}}$[km] | 1.05 | 1.65 | 1.44 |
| $\sin^2 2\theta_{13}$ | $0.109 \pm 0.039$ | $0.089 \pm 0.011$ | $0.113 \pm 0.023$ |
| $P_{\mathrm{d}}@\langle L\rangle_{\mathrm{Far}}$ | $5.5 \pm 2.0\%$ | $7.0 \pm 0.9\%$ | $8.2 \pm 1.6\%$ |

The $\sin^2 2\theta_{13}$ were measured using both near and far detector at Daya Bay and RENO but only far detector was used in Double Chooz experiment. It is important to point out that although the reactor experiments assume $\Delta\tilde{m}_{32}^2$ to extract $\sin^2 2\theta_{13}$, this analysis is independent of the assumption for the first order. If the experiments used different $\Delta\tilde{m}^2$, they would obtain different $\sin^2 2\theta_{13}$ but the $P_{\mathrm{d}}$ calculated by the equation 5.22 would be the same. $\Delta\tilde{m}_{23}^2$ was used just as a reference point. Figure 5.13 shows the combination of the three reactor experiments calculated this way. The most probable oscillation parameters and their errors are,

$$\Delta\tilde{m}_{31}^2 = 2.99^{+1.13}_{-1.58}(^{+0.86}_{-0.88}) \times 10^{-3}\mathrm{eV}^2$$
$$\sin^2 2\theta_{13} = 0.089^{+0.071}_{-0.013}(^{+0.014}_{-0.013}), \tag{5.23}$$

where the errors are for two (one) dimensional uncertainty. There are large differences between two (one) dimensional uncertainties because the shape of one $\sigma$ contour island is like a boomerang with a long arm. This result is consistent with $\Delta\tilde{m}_{32}^2$ within one $\sigma$ and 3 flavor oscillation scheme is fine within this accuracy. The most probable $\sin^2 2\theta_{13}$ value coincides with the Daya Bay result but this $\sin^2 2\theta_{13}$ has meaning that it was
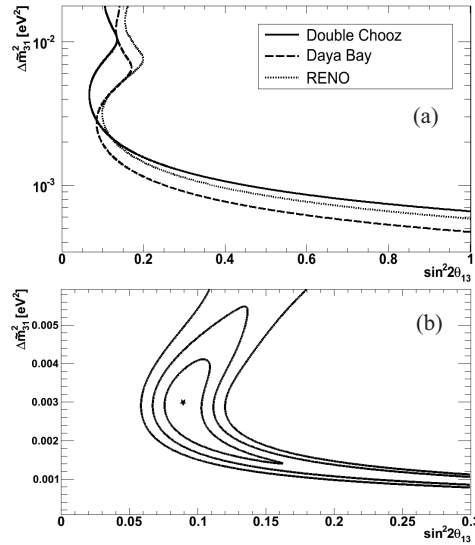
Figure 5.13: Same as figure 5.12 but disappearance probabilities and their errors are calculated from measured $\sin^2 2\theta_{13}$.

derived without assuming $\Delta\tilde{m}^2_{31}$. The minimum $\chi^2$ is 0.43 with one degree of freedom which means that the three reactor experiments are consistent with each other.

Baseline dependence of observed disappearance probability and various expectation lines are shown in figure 5.14.  This figure clearly shows the relation of the calculated disappearance probabilities and expected oscillation patterns. The calculated disappearance probabilities correspond to the values of the expected lines at their flux-averaged baselines. In the near future, errors of the experiments are expected to improve much and the oscillation pattern will be determined much more precisely.

### Future possibilities

It is important to evaluate how precisely we can measure $\Delta\tilde{m}^2_{31}$ since it may resolve the mass hierarchy comparing with $\Delta\tilde{m}^2_{32}$ in the future.  In order to make the most of the reactor complementarity, a fourth experiment addition was studied and the optimum baseline to measure $\Delta\tilde{m}^2_{31}$ by combining with the current three experiments was calculated.  Figure 5.15 shows dependence of the two dimensional uncertainty on baseline of the fourth experiment. The accuracy improves rapidly when $L$ exceeds Daya Bay baselines of 1.6km and reaches to $\sim$7% at 2.5 km. This is because that the tail of the island in the sensitivity contour plot vanishes thanks to the almost perpendicular intersection of the fourth allowed line. Figure 5.16 shows sensitivities with the fourth experiment with baseline 2.5 km. Since the combined allowed region no more has tails, one and two dimensional errors become similar. This baseline is mere 1.5 times of Daya Bay far detector baselines and thus it is not unrealistic.

### 5.2.2   Reactor Neutrino Global Fit Analysis

The method presented in the previous, although robust, is an approximation and it does not take into account particular details of each experiment, such as reactor-detector configuration, and possible correlations. Here a more detailed method, which uses all detectors data of each experiment is presented. Firstly, the Daya Bay and RENO data are re-analysed in order to demonstrate that the analysis methods used in this work are consistent with the publications. The $\chi^2$ used for each experiment will be used to form
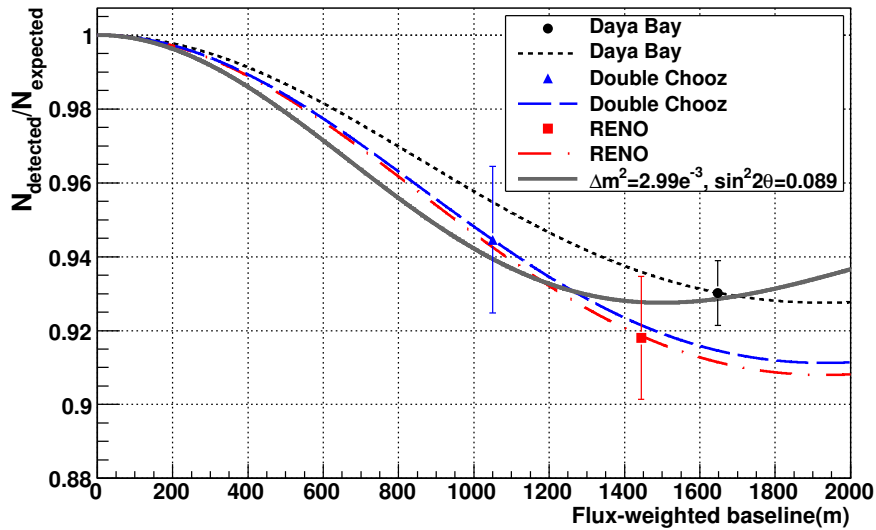
Figure 5.14: Baseline dependence of $\bar{\nu}_e$ survival probabilities. Dashed and/or dotted lines are expected oscillation pattern calculated using $\sin^2 2\theta_{13}$ measured in each experiment and MINOS $\Delta \tilde{m}_{32}^2$. The calculated disappearance probabilities correspond to the values of the expected lines at their flux-averaged baselines. The solid line is expectation from the most probable $\Delta \tilde{m}_{31}^2$ and $\sin^2 2\theta_{13}$ measured by this analysis.
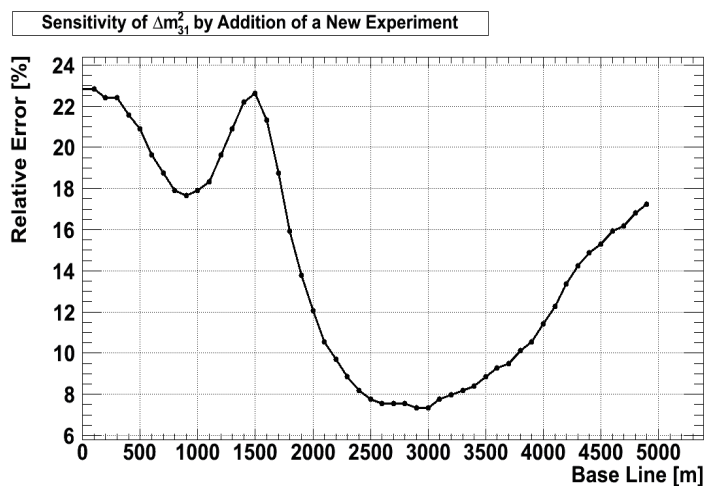


Figure 5.15: Dependence of the two dimensional uncertainty on baseline of fourth experiment.
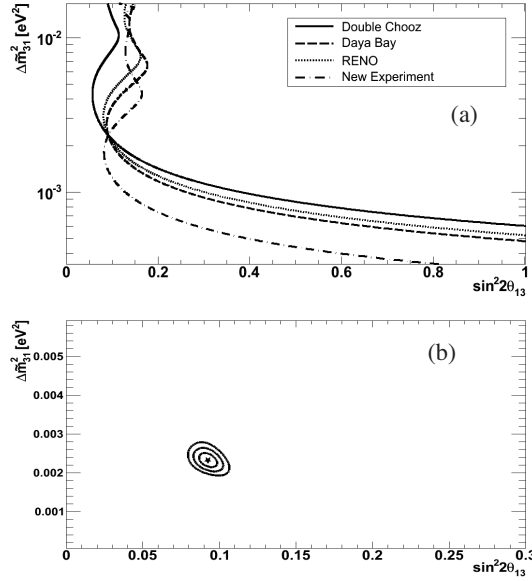
Figure 5.16: Same as figure 5.12 but a hypothetical fourth experiment with baseline 2.5 km is added. $\Delta\tilde{m}^2_{31}$ can be measured with precision $\sim 7\%$.

global $\chi^2$ function.

### 5.2.2.1   Daya Bay

The Daya Bay (DB) reactor neutrino experiment, located on the south coast of Guangdong Province in the People's Republic of China, consists of three experimental halls (EH), containing one or more antineutrino detectors (AD). The AD array sees 6 reactors clustered into 3 pairs: Daya Bay (DB1, DB2), Ling Ao (L1, L2) and Ling Ao II (L3, L4) power stations. Figure 2.10 shows the relative locations of reactors and AD and table 5.9 shows the distance between each combination of reactor and detector. All

Table 5.9: Daya Bay: Baselines, in meters, between each detector and core [103].

|     | DB1  | DB2  | L1   | L2   | L3   | L4   |
|-----|------|------|------|------|------|------|
| AD1 | 362  | 372  | 903  | 817  | 1354 | 1265 |
| AD2 | 358  | 368  | 903  | 817  | 1354 | 1266 |
| AD3 | 1332 | 1358 | 468  | 490  | 558  | 499  |
| AD4 | 1920 | 1894 | 1533 | 1534 | 1551 | 1525 |
| AD5 | 1918 | 1892 | 1535 | 1535 | 1555 | 1528 |
| AD6 | 1925 | 1900 | 1539 | 1539 | 1556 | 1530 |

reactors are functionally identical pressurized water reactors with maximum thermal power of 2.9 GW [28].

In Daya Bay publication, the $\chi^2$ is defined as

$$\chi^2_{\mathrm{DB}}(\theta_{13}, \Delta m^2_{31}) =$$
$$\sum_d^6 \frac{\left[ M_d + \eta_d - T_d \left( 1 + a + \sum_r^6 \omega_r^d \alpha_r + \epsilon_d \right) \right]^2}{M_d + B_d} \tag{5.24}$$
$$+ \sum_r^6 \frac{\alpha_r^2}{\sigma_r^2} + \sum_d^6 \left( \frac{\epsilon_d^2}{\sigma_d^2} + \frac{\eta_d^2}{\sigma_B^2} \right),$$

where $M_d$ are the measured neutrino candidate events of the $d$-th AD with background subtracted, $B_d$ is the corresponding background, $T_d$ is the prediction from neutrino flux, Monte Carlo simulation (MC) and neutrino oscillation. $\omega^d_r$ is the fraction of neutrino event contribution of the $r$-th reactor to the $d$-th AD determined by baselines and reactor fluxes. The uncorrelated reactor uncertainty is $\sigma_r$. $\sigma_d$ is the uncorrelated detection uncertainty, and $\sigma_B$ is the background uncertainty, with the corresponding pull-terms $(\alpha_r, \epsilon_d, \eta_d)$. An absolute normalization factor $a$ is determined from the fit to the data.

The values of $\omega^d_r$ are not shown in Daya Bay publications and was estimated using

$$\omega^d_r = \frac{p_r/L^2_{rd}}{\sum_r (p_r/L^2_{rd})} \quad \text{with} \quad p_r = \frac{w_r}{\sum_r w_r}, \tag{5.25}$$

where $w_r$ is the thermal power of each reactor and $L_{rd}$ is the baseline of $r$-th reactor to $d$-th detector. In this analysis, the value of $p_r$ is considered $1/6$ since all reactors have same nominal thermal power. The calculated $\omega^d_r$ is shown in table 5.10. All the others terms are shown in table 5.11.

Table 5.10: Daya Bay: Contribution to each detector from reactor; $\omega^d_r$.

|     | DB1 | DB2 | L1 | L2 | L3 | L4 |
|-----|--------|--------|--------|--------|--------|--------|
| AD1 | 0.4069 | 0.3854 | 0.0654 | 0.0799 | 0.0291 | 0.0333 |
| AD2 | 0.4089 | 0.3870 | 0.0643 | 0.0785 | 0.0286 | 0.0327 |
| AD3 | 0.0330 | 0.0318 | 0.2676 | 0.2441 | 0.1882 | 0.2354 |
| AD4 | 0.1208 | 0.1241 | 0.1894 | 0.1892 | 0.1851 | 0.1914 |
| AD5 | 0.1201 | 0.1248 | 0.1895 | 0.1895 | 0.1847 | 0.1913 |
| AD6 | 0.1209 | 0.1241 | 0.1892 | 0.1892 | 0.1851 | 0.1914 |

Table 5.11: Daya Bay: Fitting parameters [103].

|                  | AD1 | AD2 | AD3 | AD4 | AD5 | AD6 |
|------------------|------------------|------------------|------------------|-----------------|-----------------|-----------------|
| $\nu$ candidate  | 69121            | 69714            | 66473            | 9788            | 9669            | 9452            |
| $T_{d0}$         | 68613            | 69595            | 66402            | 9922.9          | 9940.2          | 9837.7          |
| BKG total/day    | $13.68 \pm 1.54$ | $13.55 \pm 1.54$ | $10.38 \pm 1.17$ | $3.56 \pm 0.24$ | $3.55 \pm 0.24$ | $3.44 \pm 0.24$ |
| Live Time (days) | 127.5470         | 127.5470         | 127.3763         | 126.2646        | 126.2646        | 126.2646        |
| Efficiency       | 0.8015           | 0.7986           | 0.8364           | 0.9555          | 0.9552          | 0.9547          |
| $M_d$            | 67723.59         | 68334.17         | 65363.96         | 9358.7          | 9240.98         | 9037.24         |
| $\sigma_B$       | 157.43           | 156.86           | 124.65           | 28.95           | 28.94           | 28.93           |
| $\sigma_d$       | 0.002            | 0.002            | 0.002            | 0.002           | 0.002           | 0.002           |
| $\sigma_r$       | 0.008            | 0.008            | 0.008            | 0.008           | 0.008           | 0.008           |

By using equation 5.24 and the data from tables 5.10 and 5.11, Daya Bay's result is reproduced, where $T_d$ was multiplied by the value of the deficit probability ($P^{\text{def}}_{dr}$), as defined in equation 5.17.

$\sin^2 2\theta_{13}$ is extracted by fixing $\Delta\tilde{m}^2_{31}$ as the MINOS $\Delta\tilde{m}^2_{32} = 2.32 \times 10^{-3}$ eV$^2$ [23]. The $\chi^2$ distributions of the Daya Bay paper and this calculation are compared in figure 5.17. The Daya Bay central value and uncertainty is $\sin^2 2\theta_{13\text{DB}} = 0.089 \pm 0.011$ while this analysis showed $\sin^2 2\theta_{13} = 0.090^{+0.011}_{-0.010}$, in good agreement with the published value.

The effect of how different values for the fission rates coefficients of equation 5.18 and different assumptions for equation 5.25 affects the final result, was verified. Dependence on the burn-up values is less than 0.001, by assuming burn-up of Chooz reactors at the beginning and end of reactor cycle. Extreme assumptions on equation 5.25 (one or two reactors off for the whole data period, for example) had an effect of less than 0.002

on the central value, with no change on the sensitivity. Moreover, the good agreement between the $\chi^2$ distributions, shows that the assumptions are reasonable.
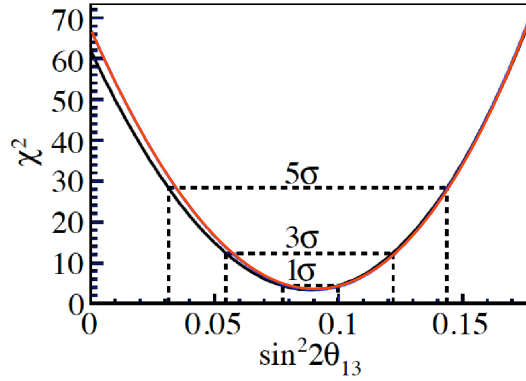


Figure 5.17: $\chi^2$ distribution with respect to $\sin^2 2\theta_{13}$ by fixing $\Delta m^2$ as $\Delta \tilde{m}_{32}^2$ for Daya Bay data. The black curve is the $\chi^2$ distribution shown in their paper [103] with central value and $1\sigma$ uncertainty of $0.089 \pm 0.011$, while the red curve shows the $\chi^2$ distribution calculated in this analysis with central value and $1\sigma$ uncertainty of $0.090^{+0.011}_{-0.010}$.

### 5.2.2.2   RENO

The Reactor Experiment for Neutrino Oscillation (RENO) is located in South Korea and has two identical detectors, one near (ND) and one far (FD) from an array of six commercial nuclear reactors (Yonggwang), as shown in figure 2.11. Together with the distances of each detector reactor pair, the contribution of each reactor flux to each detector for the period of their first analysis is available [102] and are summarized in table 5.12.

Table 5.12: RENO: Baselines and neutrino flux contributions [102].

|                  | R1     | R2     | R3     | R4     | R5     | R6     |
|------------------|--------|--------|--------|--------|--------|--------|
| FD baseline [m]  | 1556.5 | 1456.2 | 1395.9 | 1381.3 | 1413.8 | 1490.1 |
| FD contribution  | 0.1373 | 0.1574 | 0.1809 | 0.1856 | 0.1780 | 0.1608 |
| ND baseline [m]  | 667.9  | 451.8  | 304.8  | 336.1  | 513.9  | 739.1  |
| ND contribution  | 0.0678 | 0.1493 | 0.3419 | 0.2701 | 0.1150 | 0.0558 |

The RENO $\chi^2$ is defined as:

$$\chi^2_{\mathrm{RE}}(\theta_{13}, \Delta m_{31}^2) =$$
$$\sum_d^2 \frac{\left[ N_{\mathrm{obs}}^d + b_d - (1 + n + \xi_d) \sum_r^6 (1 + f_r) N_{\mathrm{exp}}^{d,r} \right]^2}{N_{\mathrm{obs}}^d} \qquad (5.26)$$
$$+ \sum_d^2 \left( \frac{\xi_d^2}{(\sigma_d^\xi)^2} + \frac{b_d^2}{(\sigma_B^b)^2} \right) + \sum_r^2 \frac{f_r^2}{\sigma_r^2},$$

where $N_{\mathrm{obs}}^d$ is the number of observed IBD candidates in each detector after background subtraction and $N_{\mathrm{exp}}^{d,r}$ is the number of expected neutrino events, including detection efficiency, neutrino oscillations and contribution from the $r$-th reactor to each detector determined from baseline distances and reactor fluxes. A global normalization $n$ is taken free and determined from the fit to the data. The uncorrelated reactor uncertainty is

$\sigma_r$, $\sigma_d^{\xi}$ is the uncorrelated detection uncertainty, and $\sigma_d^b$ is the background uncertainty, and the corresponding pull parameters are ($f_r$, $\xi_d$, $b_d$). The values of these variables are shown in the table 5.13.

Table 5.13: RENO: Fitting parameters [104].

|                   | ND              | FD              |
|-------------------|-----------------|-----------------|
| IBD candidates    | 154088          | 17102           |
| $N_{\exp}^d$      | 151723.54       | 17565.72        |
| BKG (total/day)   | $21.75 \pm 5.93$ | $4.24 \pm 0.75$ |
| Live Time (days)  | 192.42          | 222.06          |
| Efficiency        | 0.647           | 0.745           |
| $N_{\mathrm{obs}}$ | 149902.86       | 16160.46        |
| $\sigma_d$        | 0.002           | 0.002           |
| $\sigma_r$        | 0.009           | 0.009           |
| $\sigma_b$        | 1141.05         | 166.54          |

The expected number of events for both detectors are not present in the RENO paper, but the ratio between data and expectation is shown. This ratio and the quantities of table-5.12 were used to calculate the expectation value ($N_{\exp}^{d,r}$).

Using the data in the table 5.13, equation 5.22 and the MINOS $\Delta\tilde{m}_{32}^2$, $\sin^2 2\theta_{13} = 0.111 \pm 0.024$ was obtained, which is in good agreement with their published value of $\sin^2 2\theta_{13\mathrm{RE}} = 0.113 \pm 0.023$. The $\chi^2$ distributions are also very similar as shown in figure 5.18.
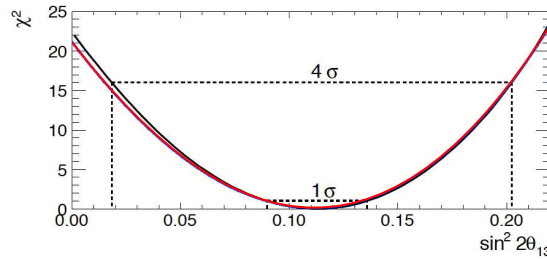


Figure 5.18: $\chi^2$ distribution with respect to $\sin^2 2\theta_{13}$ by fixing $\Delta m^2$ as $\Delta\tilde{m}_{32}^2$ for RENO data. The black curve shows the $\chi^2$ distribution shown in their paper [104] with central value and 1 $\sigma$ uncertainty of $0.113 \pm 0.023$, while the red curve shows the $\chi^2$ distribution calculated in this analysis with central value and 1 $\sigma$ uncertainty of $0.111 \pm 0.024$.

### 5.2.2.3 Double Chooz

The Double Chooz data was separated in energy bins, for the measurement of $\theta_{13}$. However, for the measurement of $\Delta\tilde{m}_{31}^2$ by baseline dependence, the energy dependence is not necessary, and the total number of events is used instead. The $\chi^2$ used for the Double Chooz data is similar to equation 5.4, but with only one bin for each data set. This Rate Only (RO) analysis gives $\sin^2 2\theta_{13} = 0.111 \pm 0.047$. If the data taken during the period that the reactors were stopped is used to constrain the backgrounds on the fit, the result becomes $\sin^2 2\theta_{13} = 0.108 \pm 0.044$, which is closed to the one got from the shape and rate analysis.

### 5.2.2.4   Correlation Evaluation of Systematic Uncertainties

In reactor neutrino experiments, the expected number of observed events is given by equation 4.2. For each experiment, $L$, $N_{\text{p}}$, $\varepsilon$, and $P_{\text{th}}$ terms are determined independently, thus they can be assumed to be uncorrelated. On the other hand, $\langle E_f \rangle$ and $\langle \sigma_f \rangle$ terms are taken from the same references and the uncertainties of these terms are correlated between the experiments. From the Bugey and Chooz experimental results, the total uncertainty on spectrum prediction is 2.7%, where a 2% correlation is expected between the experiments as treated in [43]. Fully correlated signal prediction uncertainties between experiments, which come from neutrino flux and detection efficiency, can be cancelled by overall normalization factors used in the analyses of the Daya Bay and RENO. It allows us only to take into account remaining uncertainties between detectors or periods for each experiment. Daya Bay and RENO treat the remaining uncertainties as uncorrelated in their publications.

### 5.2.2.5   Combined Analysis

As explained before, the main method of this work is to combine all the data of the current neutrino reactor experiments in a single $\chi^2$ function, and search for the minimum $\chi^2$ value. Thus, the calculation of $\Delta\chi^2$ distribution is performed to determine the confidence level regions. The $\chi^2$ function used for such analysis was chosen to use the data from tables 5.9 to 5.13 and the Double Chooz data presented in section 5.1. Therefore, the global $\chi^2$ is defined as,

$$\chi^2_{\text{G}} \equiv \chi^2_{\text{DB}} + \chi^2_{\text{DC}} + \chi^2_{\text{RE}}, \tag{5.27}$$

with the $\chi^2$ of each experiment defined in the beginning of this section. Thus, this function has 30 pull terms: 18 for Daya Bay (6 reactors, 6 detectors and 6 backgrounds), 10 for RENO (6 reactors, 2 detectors and 2 backgrounds) and 2 for Double Chooz (cosmogenic and FN backgrounds). It also contains the two overall normalization factors, one for Daya Bay and the other for RENO dataset.

For all combinations of $\Delta m^2$ and $\sin^2 2\theta$, the $\chi^2_{\text{G}}$ is minimized with respect to the pull terms. Figure 5.19 shows a map of the absolute $\chi^2$ and figure 5.20 shows the $\Delta\chi^2$ contour map near the $\chi^2_{\text{min}}$, obtained by such procedure. From the minimum point and the 1 $\sigma$ error region in the 1-D $\chi^2$ distribution,

$$\begin{aligned}
\chi^2_{\text{min}} &= 5.14 \,/\, 6 \text{ Degrees of Freedom,} \\
\Delta\tilde{m}^2_{31} &= 2.95^{+0.42}_{-0.61} \times 10^{-3} \text{ eV}^2, \\
\sin^2 2\theta_{13} &= 0.099^{+0.016}_{-0.012}
\end{aligned}$$

are obtained. This $\Delta\tilde{m}^2_{31}$ is consistent with $\Delta\tilde{m}^2_{32}$ measured by accelerator experiments [23, 105], confirming the standard three flavor neutrino oscillation within the error. The $\sin^2 2\theta_{13}$ obtained here is independent from $\Delta\tilde{m}^2_{32}$. The small $\chi^2_{\text{min}}/\text{DoF}$ means the data from the three reactor neutrino experiments are consistent with each other.

All the pull terms output were within 1 $\sigma$ from the input value, and the normalization factors obtained from the fit to the data, were both less than 1%.

In figure 5.21 the baseline dependence of the disappearance probability of each detector is shown, where the probability is calculated using the parameters output which give the best fit. In this figure, the horizontal axis is a weighted baseline $\langle L \rangle$ and the horizontal bar in each data point shows the standard deviation of the distribution of the baselines, since one detector sees several reactors, and is defined by

$$\sigma_L = \sqrt{\langle L \rangle^2 - \langle L^2 \rangle}, \tag{5.28}$$
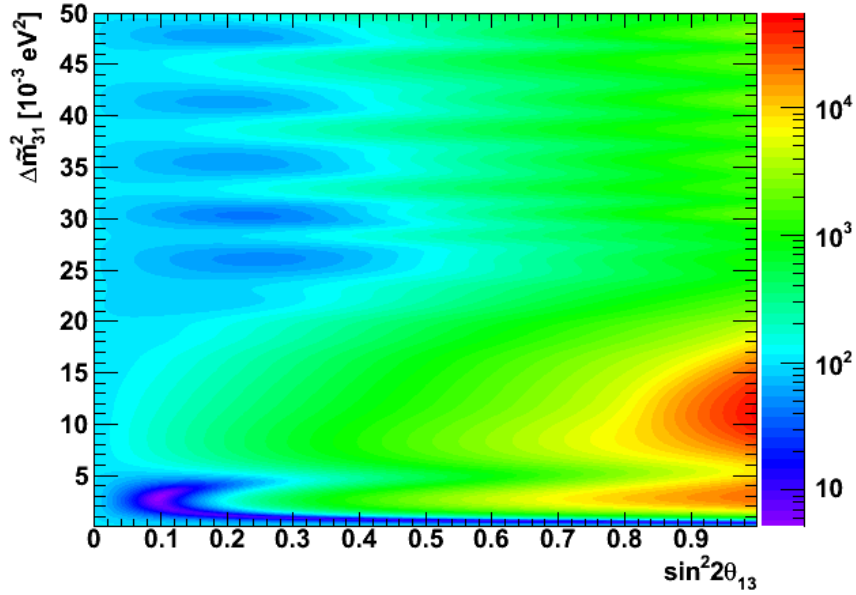
Figure 5.19: Absolute $\chi^2$ value calculated for each pair of $\Delta m^2_{31}$ and $\sin^2 2\theta_{13}$, and by the minimization of the pull terms. For higher values of $\Delta m^2_{31}$ (bigger than $10^{-2} \text{eV}^2$) some valleys are present, although they are about more than ten times less sensitive than the minimum $\chi^2$.
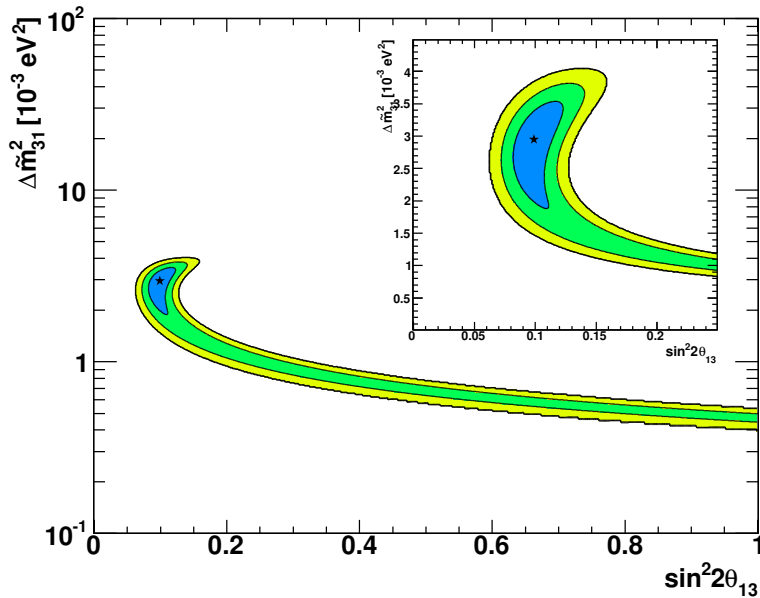


Figure 5.20: $\Delta\chi^2$ distribution around the $\chi^2_{\min}$. From the inner to the outer part, the lines correspond to 1 $\sigma$, 2 $\sigma$ and 3 $\sigma$ confidence level. The star shows the best fit point. There is no solution more significant than 3 $\sigma$ except for the $\chi^2_{\min}$ valley.

with

$$\langle L^n \rangle \equiv \sum_k P_k L_k^{n-2} / \sum_k P_k L_k^{-2}, \tag{5.29}$$

where $k$ is the reactor index and $L_k$ and $P_k$ are the baseline and thermal power of the reactor $k$. Moreover, from the figure, is possible to see that the Double Chooz has a large effect on this $\Delta \tilde{m}_{31}^2$ determination because it locates at a baseline where the slope of the oscillation is large. In the near future, when the near detector of the Double Chooz experiment starts operation, the accuracy of this $\Delta \tilde{m}_{31}^2$ measurement is expected to improve much.
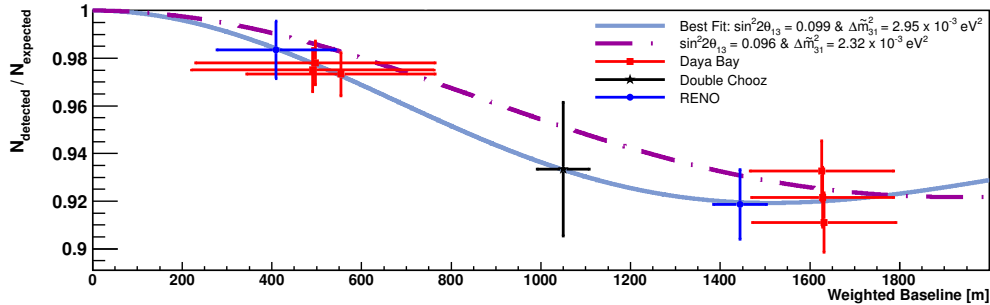


Figure 5.21:   Reactor $\bar{\nu}_e$ survival probabilities.   The solid line is the oscillation pattern obtained in this analysis and dot-dashed line uses MINOS $\Delta m_{32}^2$ and the $\sin^2 2\theta_{13}$ that returns the minimum $\chi^2$. The data points are below the $\Delta m_{32}^2$ because they are calculated using the parameters returned by the best fit solution. Vertical uncertainties were calculated from the detector systematics and horizontal uncertainties from equation 5.28.

This result is compatible to the measurement from the baseline dependence of the disappearance probabilities of the three reactor-$\theta_{13}$, a simpler but robust method, showed in the previous section. In addition, a similar $\Delta \chi^2$ distribution is presented in [106, figure 4]. However, the central value of $\Delta \tilde{m}_{31}^2$ could not be compared since only the distribution is presented, without further details of their method.

### 5.2.3   Spectral Analysis

So far, the reactor neutrino experiments have not presented yet a spectral analysis to retrieve the value of $\Delta \tilde{m}_{31}^2$. In figure 5.22, the comparison of the energy spectrum in the far and near detector, for Daya Bay and RENO [103, 104], is presented. When comparing these spectra with figure 5.5, some common structure are present, as the lack of events around 6 MeV for example, where an almost null oscillation probability is expected. A better understanding of the systematics and more statistics are needed in order to make a measurement of $\Delta \tilde{m}_{31}^2$ using the spectral information of each experiment. In the near future, when more data and an improved analysis will be available, such measurement will be viable.

(a) Daya Bay                                          (b) RENO
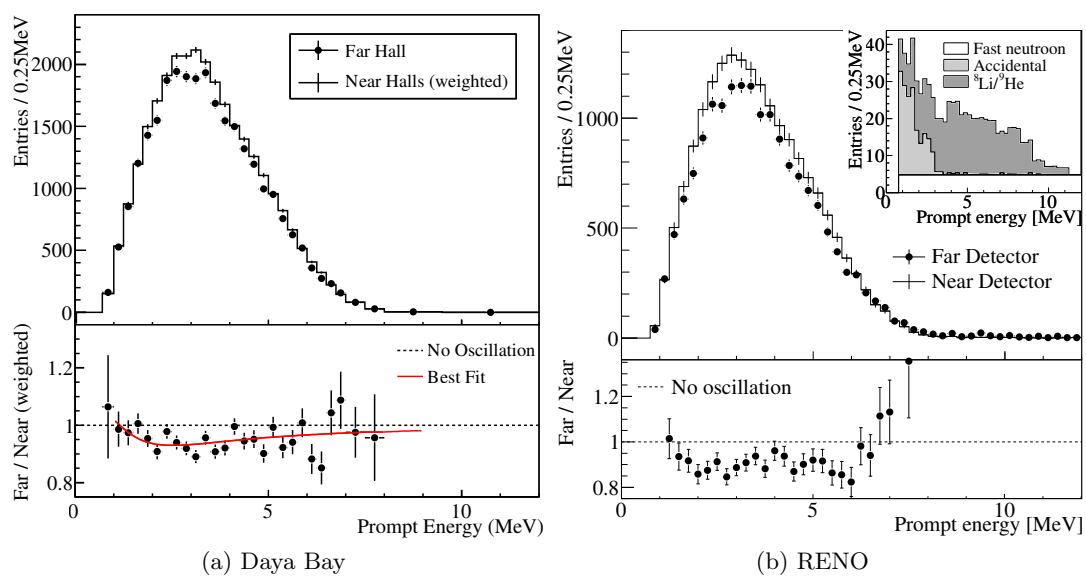
Figure 5.22: Daya Bay and RENO near and far detectors spectra and their ratio.

# Chapter 6

# Conclusions

The Double Chooz experiment started its data taking on April of 2011, measuring the electron antineutrino flux from the two Chooz B nuclear reactors, 1050 m far away. A rate and shape analysis of the selected IBD candidates energy spectrum was performed to search for distortions, which is an indication of oscillation. Using an analysis that searches for neutron capture on Gadolinium atoms, to identify IBD interactions, results on $\sin^2 2\theta_{13} = 0.100 \pm 0.039$. Complementary, using analysis that searches for neutron capture on Hydrogen atoms, which comprehend an independent data set, results on $\sin^2 2\theta_{13} = 0.096 \pm 0.049$. A combined analysis, using both data sets, improves the measurement of the mixing angle, resulting in $\sin^2 2\theta_{13} = 0.100 \pm 0.034$. The precision and accuracy of the measurement relies on the precise knowledge of the rates and spectral shapes of the backgrounds, which contaminate the event selection over the oscillation expected region. This result shows a relatively large value of the mixing angle, corroborated by the other two similar reactor neutrino experiments and accelerator based ones, indicating that this value was just below the upper limit set the Chooz experiment. In the near future, the near detector will further improve the Double Chooz result, entering in the precision era of the oscillation parameters measurement, which will be crucial for the future experiments that will measure the CP violation phase and determine the neutrino mass hierarchy.

Complementary, a global fit of the data from all the current reactor-$\theta_{13}$ experiments was performed to measure $\Delta \tilde{m}^2_{31}$ for the fist time. The combination of the data from Daya Bay, Double Chooz and RENO resulted in $\Delta \tilde{m}^2_{31} = 2.95^{+0.42}_{-0.61} \times 10^{-3}$ eV$^2$. This is consistent with $\Delta \tilde{m}^2_{32}$ and it confirms that the experiments are observing the standard three flavour neutrino oscillations within the error. The mixing angle obtained in this analysis is $\sin^2 2\theta_{13} = 0.099^{+0.016}_{-0.012}$, which is independent from the knowledge of $\Delta \tilde{m}^2_{32}$. The small $\chi^2_{\min}$/DoF value indicates that the data from the three reactor experiments are consistent with each other. This analysis uses independent information from the energy spectrum distortion and it is possible to improve the accuracy of $\Delta \tilde{m}^2_{31}$ combining with results from energy spectrum analysis. It will be important to perform this kind of analysis to improve $\Delta \tilde{m}^2_{31}$ accuracy and to check the consistency of the results from the reactor-$\theta_{13}$ experiments.

The authors contributions can be summarised on the following points:

- **Double Chooz $\theta_{13}$** : Help on the development of the combined analysis method, applied to DC $\theta_{13}^{\mathrm{Gd}}$ and $\theta_{13}^{\mathrm{H}}$ data. It will be used for the next available data set of DC, and consequently in the collaboration next publication;

- **Double Chooz Hardware**: Test of all the 390 Double Chooz near detector PMTs and spares, looking for damaged and glowing candidates. Validation of all the 46 near detector cables flanges and epoxy;

- **Double Chooz Software**: Creation of codes to perform IBD event selection and accidental background rate and prompt shape estimation. Light noise tests and stability over the data set.

- **$\Delta\tilde{m}^2_{31}$** : Weighted baseline method and reproduction of all reactor neutrino experiment analysis and global fit procedure;

# Appendix A

# Weighted Baseline Analysis

The weighted baseline analysis (section 5.2.1), for the determination of $\Delta\tilde{m}^2_{31}$ was presented during the XXV International Conference on Neutrino Physics and Astrophysics (Neutrino 2012), held in Kyoto on June, 2012 [107], and the analysis details is publicly available in [108]. This reference is reproduced in the following pages.

# Measurement of Effective $\Delta m_{31}^2$ using Baseline Differences of Daya Bay, RENO and Double Chooz Reactor Neutrino Experiments

T.J.C. Bezerra,* H. Furuta,† and F. Suekane‡

*Research Center for Neutrino Science*
*Tohoku University, Sendai, 980-8578, JAPAN*
(Dated: July 4, 2012. Version 2: November 30, 2012)

In 2011 and 2012, three reactor neutrino experiments, Double Chooz, Daya Bay and RENO showed positive signals of reactor neutrino disappearance and measured a mixing parameter $\sin^2 2\theta_{13}$ at average baselines 1.05, 1.65 and 1.44 km, respectively. It is possible to measure effective $\Delta m_{31}^2$ ($\Delta m^2$ defined in two flavor oscillation formula, hereafter referenced as $\Delta \tilde{m}_{31}^2$) from distortion of neutrino energy spectrum ($E$ dependence of the oscillation) in those experiments. However, since it requires a precise energy calibration, such measurements have not been reported yet. $\Delta \tilde{m}_{31}^2$ can also be measured from baseline ($L$) dependence of the neutrino oscillation. In this paper $\Delta \tilde{m}_{31}^2$ is measured from disappearance probabilities of the three reactor experiments which have different baselines, to be $2.99^{+1.13}_{-1.58}(^{+0.86}_{-0.88}) \times 10^{-3}$ eV$^2$, where the errors are two (one) dimensional uncertainties. This is consistent with $\Delta \tilde{m}_{32}^2$ measured by $\nu_\mu$ disappearance in accelerator experiments. Importance of $\Delta \tilde{m}_{31}^2$ measurement and future possibilities are also discussed.

## I. INTRODUCTION

Neutrino oscillation is, so far, the only firm phenomenon which is not accounted for by the standard model of elementary particles, which assume neutrinos as massless. The neutrino oscillation is, like other oscillations, such as $K^0 \Leftrightarrow \overline{K^0}$, $B^0 \Leftrightarrow \overline{B^0}$(CP violation), $d \Leftrightarrow s$ (Cabbibo angle), $(ud) \Leftrightarrow (du)$ (isospin), $B \Leftrightarrow W_3$ (Weinberg angle), $p(\uparrow)e(\downarrow) \Leftrightarrow p(\downarrow)e(\uparrow)$ in hydrogen atom (21 cm HI line) etc, assumed also to carry very important physics and we should be able to learn much about our world from it.

There are six parameters in standard three flavor neutrino oscillation [1]. Three mixing angles between flavor eigenstates and mass eigenstates: $\theta_{12}$, $\theta_{13}$, $\theta_{23}$, one CP violating imaginary phase: $\delta$ and 2 independent squared mass differences: $\Delta m_{jk}^2 \equiv m_j^2 - m_k^2$, where $m_i$ are neutrino masses ($m_1$, $m_2$, $m_3$) of the three mass eignestates ($\nu_1$, $\nu_2$, $\nu_3$) which correspond to the largest component of ($\nu_e, \nu_\mu, \nu_\tau$), respectively. Before 2011, $\sin^2 2\theta_{12}$, $\sin^2 2\theta_{23}$, $\Delta m_{21}^2$, $|\Delta m_{32}^2|$ were measured by various experiments and observations [1]. $\theta_{13}$ was known to be small, $\sin^2 2\theta_{13} < 0.15$, from Chooz reactor neutrino experiment [2]. In order to measure $\delta$, to determine mass hierarchy and to solve $\theta_{23}$ degeneracy, $\theta_{13}$ has to be relatively large. Thus finite value of $\theta_{13}$ had been eagerly sought for.

The years 2011 and 2012 will be regarded as an epoch making ones of neutrino experiments. T2K group showed 6 $\nu_\mu \rightarrow \nu_e$ appearance candidates over 1.5 expected backgrounds in June 2011 [3]. MINOS group showed also an indication of $\nu_\mu \rightarrow \nu_e$ appearance [4]. Double Chooz showed an indication of the reactor neutrino disappearance in November, 2011 [5]. Daya Bay and RENO showed more precise disappearances on March and April 2012, respectively [6, 7]. In June 2012, at neutrino conference held in Kyoto, Double Chooz [8], Daya Bay [9], T2K [10] and MINOS [11] updated their $\sin^2 2\theta_{13}$ measurements. All those results show relatively large $\theta_{13}$ and have opened up a brilliant path to future neutrino experiments.

Reactor neutrino oscillation probability is expressed as follow.

$$P_R(\bar{\nu}_e \rightarrow \bar{\nu}_e) \sim 1 - \sin^2 2\theta_{13} \sin^2 \frac{\Delta \tilde{m}_{31}^2}{4E_\nu} L, \qquad (1)$$

where, $E_\nu$ is neutrino energy ($\sim$ a few MeV) and $L$ is baseline ($1 \sim 2$ km). $\Delta \tilde{m}_{31}^2$ is an "effective" squared mass difference often mentioned as $\Delta m_{31}^2$ in two flavor analyses. In three flavor oscillations, it is an average of $\Delta m_{31}^2$ and $\Delta m_{32}^2$, as will be described in the next section. In principle both $\sin^2 2\theta_{13}$ and $\Delta \tilde{m}_{31}^2$, can be measured from the oscillation. However, all the reactor neutrino experiments use $\Delta \tilde{m}_{32}^2$, which was measured by $\nu_\mu$ disappearance by MINOS group [12], as $\Delta \tilde{m}_{31}^2$ to extract $\sin^2 2\theta_{13}$ since the difference between them is in an order of $|\Delta m_{21}^2/\Delta m_{32}^2| \sim 3\%$ which is smaller than current accuracy of the measurements.

It is important to measure $\Delta \tilde{m}_{31}^2$ independently from $\Delta \tilde{m}_{32}^2$ to check if the standard three flavor scheme is correct. If there is significant difference between $\Delta \tilde{m}_{32}^2$ and $\Delta \tilde{m}_{31}^2$, it indicates an existence of new physics. Moreover if they are measured with precision of 1% or better, mass hierarchy can be solved and $\cos \delta$ may be measured as described in the next section.

Experimentally, $\Delta \tilde{m}_{31}^2$ can be measured by analyzing either $E$ dependence of the oscillation or $L$ dependence of the oscillation. Both methods use independent information, namely energy distortion and normalization, so that combining both analyses, accuracy of the $\Delta \tilde{m}_{31}^2$ will improve. The former requires a precise energy calibration and no results have been reported yet. The latter

* thiago@awa.tohoku.ac.jp
† furuta@awa.tohoku.ac.jp
‡ suekane@awa.tohoku.ac.jp

2

analysis can be performed by combining currently available disappearance information at different baselines.

In this paper $\Delta\tilde{m}_{31}^2$ is measured using reported $\sin^2 2\theta_{13}$ and baseline of each reactor experiment. The contents of this paper is based on our poster presentation in the conference of neutrino 2012 [13]. In next section, neutrino oscillation formula is described stressing on relation between $\Delta\tilde{m}_{31}^2$ and $\Delta\tilde{m}_{32}^2$ and importance of $\Delta\tilde{m}_{31}^2$ measurement will be discussed. In section-III, how we treat reactor neutrino will be described. In section-IV, most recent Double Chooz, Daya Bay and RENO results [7–9] are combined and $\Delta\tilde{m}_{31}^2$ is extracted. In section-V, a new experiment is proposed to measure $\Delta\tilde{m}_{31}^2$ more precisely by using the reactor complementarity.

## II. NEUTRINO OSCILLATION FORMULA AND EFFECTIVE $\Delta m^2$

The mixing matrix between flavor eigenstats and mass eigenstats is [1],

$$U_{\alpha j} = \begin{pmatrix} c_{12}c_{13} & s_{12}c_{13} & s_{13}e^{-i\delta} \\ -s_{12}c_{23} - c_{12}s_{23}s_{13}e^{i\delta} & c_{12}c_{23} - s_{12}s_{23}s_{13}e^{i\delta} & s_{23}c_{13} \\ s_{12}s_{23} - c_{12}c_{23}s_{13}e^{i\delta} & -s_{23}c_{12} - s_{12}c_{23}s_{13}e^{i\delta} & c_{23}c_{13} \end{pmatrix}, \tag{2}$$

where $\alpha$ is an index of flavor ($\alpha = e, \mu, \tau$) and $j$ is an index of mass eigenstates ($j = 1, 2, 3$), $c_{jk} = \cos\theta_{jk}$, $s_{jk} = \sin\theta_{jk}$, and $t_{jk} = \tan\theta_{jk}$ will be used later. $\delta$ is so called CP violating imaginary phase. Currently these parameters are measured as follows [14]. $\theta_{12} \sim 34°$, $\theta_{23} \sim 39°$, $\theta_{13} \sim 9°$, $\Delta m_{21}^2 \sim 7.5 \times 10^{-5}\text{eV}^2$ and $|\Delta m_{32}^2| \sim 2.4 \times 10^{-3}\text{eV}^2$.

Neutrino oscillation probability going to the same flavor is expressed by following formula,

$$P(\nu_\alpha \to \nu_\alpha) = 1 - 4\sum_{j>k} |U_{\alpha j}|^2 |U_{\alpha k}|^2 \sin^2 \frac{\Delta_{jk}}{2}, \tag{3}$$

where $\Delta_{jk} \equiv \frac{\Delta m_{jk}^2 L}{2E}$. The second term in right hand side is called disappearance probability. This oscillation formula is valid for both neutrino and antineutrino cases.

Reactor neutrino experiments use $\bar{\nu}_e$ generated by $\beta$-decays of the fission elements in the reactor core. Energy of the neutrino is a few MeV. At around the first oscillation maximum of $\Delta_{32}$, survival probability of $\bar{\nu}_e$ is expressed as,

$$P(\overline{\nu}_e \to \overline{\nu}_e) =$$
$$1 - \sin^2 2\theta_{13} \left( c_{12}^2 \sin^2 \frac{\Delta_{31}}{2} + s_{12}^2 \sin^2 \frac{\Delta_{32}}{2} \right) + O(10^{-3}). \tag{4}$$

On the other hand, the survival probability of high energy $\nu_\mu$ which is produced by accelerator is,

$$P(\nu_\mu \to \nu_\mu) = 1 - \sin^2 2\theta_{23} \times$$
$$\begin{pmatrix} (s_{12}^2 + s_{13}t_{23}\sin 2\theta_{12}\cos\delta)\sin^2 \frac{\Delta_{31}}{2} \\ +(c_{12}^2 - s_{13}t_{23}\sin 2\theta_{12}\cos\delta)\sin^2 \frac{\Delta_{32}}{2} \end{pmatrix} + O(10^{-2}). \tag{5}$$

Usually oscillation data are analyzed by assuming two flavor oscillation formula,

$$P(\nu_\alpha \to \nu_\alpha) = 1 - \sin^2 2\theta \sin^2 \frac{\Delta\tilde{m}^2 L}{4E}, \tag{6}$$

and the measured mass square difference corresponds to a weighted mean of $|\Delta m_{32}^2|$ and $|\Delta m_{31}^2|$ [15],

$$\Delta\tilde{m}_{31}^2 = c_{12}^2 |\Delta m_{31}^2| + s_{12}^2 |\Delta m_{32}^2|,$$
$$\Delta\tilde{m}_{32}^2 = (s_{12}^2 + s_{13}t_{23}\sin 2\theta_{12}\cos\delta) |\Delta m_{31}^2|$$
$$+ (c_{12}^2 - s_{13}t_{23}\sin 2\theta_{12}\cos\delta) |\Delta m_{32}^2|. \tag{7}$$

They are called effective $\Delta m^2$. Note that $\Delta\tilde{m}^2$ is not a difference of the mass square and is positive definite. Since there is a relation

$$\Delta m_{31}^2 = \Delta m_{32}^2 + \Delta m_{21}^2, \tag{8}$$

in the standard three flavor scheme, the difference of $\Delta\tilde{m}_{31}^2$ and $\Delta\tilde{m}_{32}^2$ is expressed as follows.

$$\frac{2(\Delta\tilde{m}_{31}^2 - \Delta\tilde{m}_{32}^2)}{\Delta\tilde{m}_{31}^2 + \Delta\tilde{m}_{32}^2} \sim \pm (1 - s_{13}t_{23}\tan 2\theta_{12}\cos\delta)$$
$$\times \frac{2\cos 2\theta_{12}|\Delta m_{21}^2|}{|\Delta m_{31}^2| + |\Delta m_{32}^2|} \sim \pm 0.012 \times (1 \pm 0.3), \tag{9}$$

where the overall sign depends on mass hierarchy. If $\Delta\tilde{m}_{31}^2 > \Delta\tilde{m}_{32}^2$, it is normal hierarchy, and vise versa. In order to distinguish the mass hierarchy cases, it is necessary to distinguish the separation of 1.7~3.1% depending on $\delta$. $\Delta\tilde{m}_{32}^2$ has been measured with precision of $\sim 3.5\%$ [14]. So far there has been no reported measurement of $\Delta\tilde{m}_{31}^2$ and this paper is on the first measurement of it. If difference between $\Delta\tilde{m}_{31}^2$ and $\Delta\tilde{m}_{32}^2$ is larger than 1.6%, it can not be explained by the standard three flavor oscillation scheme. If both $\Delta\tilde{m}_{31}^2$ and $\Delta\tilde{m}_{32}^2$ are measured with accuracy 1% or better in the future, the mass hierarchy and $\cos\delta$ can be measured.

## III. REACTOR NEUTRINO OSCILLATION

In nuclear reactors uranium and plutonium perform fission reaction; after absorbing a thermal neutron they

break up into two large nuclei called fission products, and two or three neutrons which sustains the chain reaction of the fission. The fission products are generally neutron rich nuclei and unstable. They perform $\sim 6$ $\beta$-decays on average before becoming stable. In each $\beta$-decay, a $\bar{\nu}_e$ is produced. On the other hand, 200 MeV of energy is released per fission [16], which means $\sim 6 \times 10^{20} \bar{\nu}_e$ are produced every second in a typical power reactor with 3 GW thermal energy. At 1 km from such reactors, $\bar{\nu}_e$ flux amounts to $\sim 5 \times 10^9/\text{s}/\text{cm}^2$. The energy spectrum of the reactor neutrinos is a sum of the energy spectrum of neutrinos originated from the four fissile elements.

$$S_\nu(E_\nu) = \sum_{i=^{235}\text{U},^{238}\text{U},^{239}\text{Pu},^{241}\text{Pu}} \beta_i f_i(E_\nu), \qquad (10)$$

where $f_i(E_\nu)$ is reactor neutrino spectrum per fission from fissile element $i$ and $\beta_i$ is a fraction of fission rate of fissile element $i$. There is a relation $\sum_i \beta_i = 1$. For equilibrium light water reactors, $\beta_i$ are similar and we use the values in Bugey paper [16], namely $^{235}\text{U} : {}^{238}\text{U} : {}^{239}\text{Pu} : {}^{241}\text{Pu} = 0.538: 0.078: 0.328: 0.056$. In this study, $f_i(E)$ is approximated as an exponential of a polynomial function which is defined in [17],

$$f_i(E_\nu) \propto \exp(\sum_{j=1}^{6} \alpha_j E_\nu^{(j-1)}). \qquad (11)$$

In reactor neutrino experiments, usually organic liquid scintillator is used to detect $\bar{\nu}_e$. It is rich in free protons and reactor $\bar{\nu}_e$ performs inverse $\beta$-decay interaction with a proton.

$$\bar{\nu}_e + p \rightarrow e^+ + n \qquad (12)$$

This is an inverse process of neutron $\beta$-decay (IBD) with very small $q^2$ and the cross section is precisely calculated from the neutron lifetime [18]. In this analysis, information of absolute normalization is not necessary. The energy dependence of the IBD cross section is,

$$\sigma_{\text{IBD}}(E_\nu) \propto (E_\nu[\text{MeV}] - 1.29)\sqrt{E_\nu^2 - 2.59 E_\nu + 1.4}. \qquad (13)$$

The disappearance probability, $P_d$, can be related to the oscillation parameters such as [19],

$$P_d = \sin^2 2\theta \frac{\int S_\nu(E)\sigma_{\text{IBD}}(E)\sin^2\left(\frac{\Delta m^2 L}{4E}\right)dE}{\int S_\nu(E)\sigma_{\text{IBD}}(E)dE}$$
$$\equiv \sin^2 2\theta \Lambda(\Delta m^2 L). \qquad (14)$$

Reactor measurement of $\theta_{13}$ is a pure $\sin^2 2\theta_{13}$ measurement in contrast to accelerator based measurements which depend on unknown parameters. It means that by combining reactor results and accelerator results, information of such unknown parameters can be derived [20]. Under such motivations, several reactor-$\theta_{13}$ experiments were proposed in the past [21] and now Double Chooz,

Daya Bay and RENO experiments have published positive results of the reactor neutrino disappearance and measured $\sin^2 2\theta_{13}$. These experiments make use of the same concept to reduce systematic uncertainties significantly [22] over the previous experiments of Chooz [2] and PaloVerde [23]. That is, they construct far detector(s) at around oscillation maximum and measure the "oscillated" spectrum. On the other hand, near detector(s) with same structure as the far detector is constructed at around a few hundreds of meters from their reactors to measure the neutrino spectrum before the oscillation. By comparing the data taken by the near and far detectors, the only effect caused by the oscillation can be derived by canceling systematic uncertainties of reactor neutrino flux and detection efficiencies. The flux-weighted average baselines of the far detectors, $\langle L \rangle$, for the three reactor experiments are 1.05 km for Double Chooz, 1.44 km for RENO and 1.65 km for Daya Bay, respectively. The average baseline of RENO experiment was calculated using neutrino flux shown in [24] and distances between the far detector and each reactor. Published values are used for Daya Bay and Double Chooz.

## IV. COMBINATION OF THE RESULTS FROM THE THREE REACTOR EXPERIMENTS

From measured disappearance probability, an allowed line can be drawn in $\sin^2 2\theta - \Delta m^2$ parameter space using the relation (14). Since the baselines are different for the three reactor neutrino experiments, there are three different allowed lines as shown in fig.-1(a). The point of intersection indicates the solution of $\Delta \tilde{m}_{31}^2$ and $\sin^2 2\theta_{13}$. In real experiments, due to errors, the three lines do not cross at same point. When combining different reactor results, $\chi^2$ values are calculated by using following formula for each point of the parameter space.

$$\chi^2 = \sum_{k=\text{exp.}} \left( \frac{\sin^2 2\theta \Lambda(\Delta m^2 \langle L \rangle_k) - (P_d)_k}{\sigma_k} \right)^2, \qquad (15)$$

where $k$ is index of the three experiments and $\sigma_k$ is measurement error of experiment-$k$. Fig.-1(b) shows contour of the significance in case each experiment measures the disappearance with 0.5% accuracy. In this case, $\Delta \tilde{m}_{31}^2$ can be determined with precision of $\sim 23(9)\%$ with two (one) dimensional uncertainty. The large difference between the one dimensional error and the two dimensional error is because the shape of one $\sigma$ contour island has long tail as shown in fig.-1(b). Since there are two parameters to measure, at least three experiments are necessary to redundantly measure the parameters.

In the actual analysis, $P_d$ is not directly written in papers and it is calculated from measured $\sin^2 2\theta_{13}$ and flux-weighted mean distance $\langle L \rangle$. In their papers, $\sin^2 2\theta_{13}$ were derived by assuming the MINOS $\Delta \tilde{m}_{32}^2$ [12]. Relations between these parameters and the disappearance
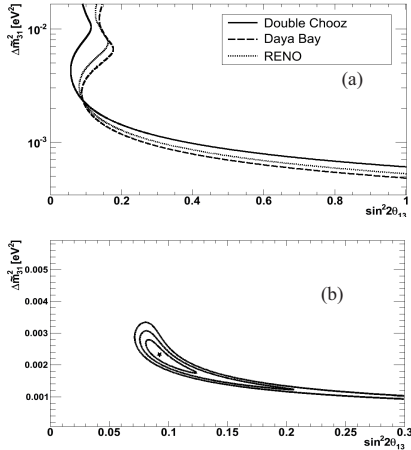
4





FIG. 1. Hypothetical sensitivity plots assuming true parameter values are $\Delta m^2 = 2.32 \times 10^{-3}$ eV$^2$ and $\sin^2 2\theta = 0.092$. (a) Allowed lines if disappearance probabilities are measured as expected. (b) Allowed regions after combining the three reactor experiments. The contour lines correspond to, from inner to outer, $1\sigma$, $2\sigma$ and $3\sigma$ significances. Disappearance error of 0.5 % is assumed for each experiment. $\Delta\tilde{m}_{31}^2$ is expected to be measured with $\sim 23(9)$ % accuracy corresponding to two (one) dimensional uncertainty.

probability, and allowed line are shown below.

$$P_\mathrm{d} = \sin^2 2\theta_{13}\Lambda(\Delta\tilde{m}_{32}^2\langle L\rangle_\mathrm{Far})$$
$$= \sin^2 2\theta\Lambda(\Delta m^2\langle L\rangle_\mathrm{Far}). \qquad (16)$$

The calculated disappearance probabilities are shown in table-I together with other parameters.

TABLE I. Parameters of the three reactor neutrino experiments.

| Item | Double Chooz | Daya Bay | RENO |
|---|---|---|---|
| $\langle L\rangle_\mathrm{Far}$[km] | 1.05 | 1.65 | 1.44 |
| $\sin^2 2\theta_{13}$ | $0.109 \pm 0.039$ | $0.089 \pm 0.011$ | $0.113 \pm 0.023$ |
| $P_\mathrm{d}@\langle L\rangle_\mathrm{Far}$ | $5.5 \pm 2.0\%$ | $7.0 \pm 0.9\%$ | $8.2 \pm 1.6\%$ |

The $\sin^2 2\theta_{13}$ were measured using both near and far detector at Daya Bay and RENO but only far detector was used in Double Chooz experiment. It is important to point out that although the reactor experiments assume $\Delta\tilde{m}_{32}^2$ to extract $\sin^2 2\theta_{13}$, this analysis is independent of the assumption for the first order. If the experiments used different $\Delta\tilde{m}^2$, they would obtain different $\sin^2 2\theta_{13}$ but the $P_\mathrm{d}$ calculated by the equation (16) would be the same. $\Delta\tilde{m}_{32}^2$ was used just as a reference point. Fig.-2 shows the combination of the three reactor experiments calculated this way. The most probable oscillation pa-
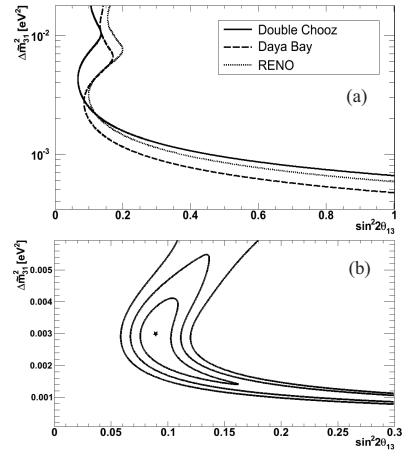
FIG. 2. Same as fig.-1 but disappearance probabilities and their errors are calculated from measured $\sin^2 2\theta_{13}$.

rameters and their errors are,

$$\Delta\tilde{m}_{31}^2 = 2.99^{+1.13}_{-1.58}(^{+0.86}_{-0.88}) \times 10^{-3}\mathrm{eV}^2$$
$$\sin^2 2\theta_{13} = 0.089^{+0.071}_{-0.013}(^{+0.014}_{-0.013}), \qquad (17)$$

where the errors are for two (one) dimensional uncertainty. This result is consistent with $\Delta\tilde{m}_{32}^2$ within one $\sigma$ and there is no deviation from 3 flavor oscillation within this accuracy. The most probable $\sin^2 2\theta_{13}$ value coincides with the Daya Bay result but this $\sin^2 2\theta_{13}$ has meaning that it was derived without assuming $\Delta\tilde{m}_{31}^2$. The minimum $\chi^2$ is 0.43 with one degree of freedom which means that the results of three reactor experiments are consistent with each other.

Baseline dependence of observed disappearance probability and various expectation lines are shown in fig.-3. This figure clearly shows the relation of the calculated disappearance probabilities and expected oscillation patterns. The meaning of disappearance probability is also described in its caption. In the near future, errors of the experiments are expected to improve much and the oscillation pattern will be determined much more precisely.

## V. FUTURE POSSIBILITIES

It is important to evaluate how precisely we can measure $\Delta\tilde{m}_{31}^2$ since it may resolve the mass hierarchy comparing with $\Delta\tilde{m}_{32}^2$ in the future. In order to make the most of the reactor complementarity, we studied a case to add a fourth experiment and calculated an optimum baseline to measure $\Delta\tilde{m}_{31}^2$ by combining with the current three experiments. Fig.-4 shows dependence of the two dimensional uncertainty on baseline of the fourth experiment. The accuracy improves rapidly when $L$ ex-
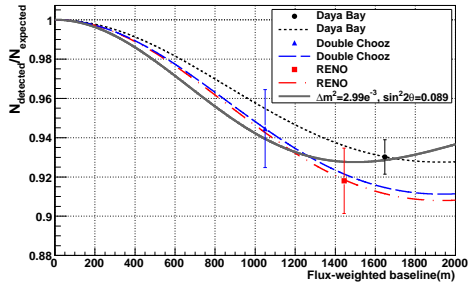
FIG. 3. Baseline dependence of $\bar{\nu}_e$ survival probabilities. Dashed and/or dotted lines are expected oscillation pattern calculated using $\sin^2 2\theta_{13}$ measured in each experiment and MINOS $\Delta \tilde{m}_{32}^2$. The calculated disappearance probabilities correspond to the values of the expected lines at their flux-averaged baselines. The solid line is expectation from the most probable $\Delta m_{31}^2$ and $\sin^2 2\theta_{13}$ measured by this analysis.



FIG. 4. Dependence of the two dimensional uncertainty on baseline of fourth experiment.



FIG. 5. Same as fig.-1 but a hypothetical fourth experiment with baseline 2.5 km is added. $\Delta \tilde{m}_{31}^2$ can be measured with precision $\sim 7\%$.

## VI. SUMMARY

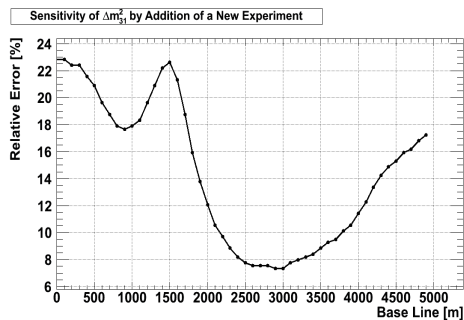In this paper, measurements of $\Delta \tilde{m}_{31}^2$ by using the baseline differences between currently running reactor neutrino experiments were studied and we obtained following results.

(1) About motivations, independent measurement of $\Delta \tilde{m}_{31}^2$ is important with following reasons. (i) The standard three flavor oscillation scheme can be tested. (ii) Consistency among results from reactor neutrino experiments can be checked. In order to perform the consistency check, at least three experiments are necessary. (iii) It may resolve mass hierarchy and give information of $\cos \delta$ in future experiments. (iv) The reactor complementarity method uses independent information from spectrum shape analysis and accuracy of $\Delta \tilde{m}_{31}^2$ will improve if they are combined.

(2) The current data from Daya Bay, RENO and Double Chooz were combined and $\Delta \tilde{m}_{31}^2 = 2.99^{+1.13}_{-1.58}(^{+0.86}_{-0.88})$ eV$^2$ was obtained, where the first (second) error was two (one) dimensional uncertainty. This is consistent with $\Delta \tilde{m}_{32}^2$ measured by the accelerator experiment. Minimum $\chi^2$ was small which shows that the results of the three experiments were consistent with each other.

(3) It was demonstrated that $\Delta \tilde{m}_{31}^2$ could be measured with precision $\sim 23(9)$ % by combining the three experiments if the error for their disappearance probabilities would reach 0.5%.

(4) A new detector with baseline 2.5 km will reduce both the one and two dimensional uncertainties of $\Delta \tilde{m}_{31}^2$ to $\sim 7\%$ by combining with the current three reactor

ceeds Daya Bay baselines of 1.6km and reaches to $\sim 7\%$ at 2.5 km. This is because that the tail of the island in the sensitivity contour plot vanishes thanks to the almost perpendicular intersection of the fourth allowed line. Fig.-5 shows sensitivities with the fourth experiment with baseline 2.5 km. Since the combined allowed region no more has tails, one and two dimensional errors become similar. This baseline is mere 1.5 times of Daya Bay far detector baselines and thus it is not unrealistic. After detailed energy calibrations are finished, the current reactor experiments will perform spectrum shape analysis to extract $\Delta \tilde{m}_{31}^2$. Since the shape analysis and the baseline analysis use independent information, the accuracy of the $\Delta \tilde{m}_{31}^2$ is expected to improve by combining them. However, in order to determine the mass hierarchy, one step more improvement of the accuracy will be needed for both $\Delta \tilde{m}_{31}^2$ and $\Delta \tilde{m}_{32}^2$.
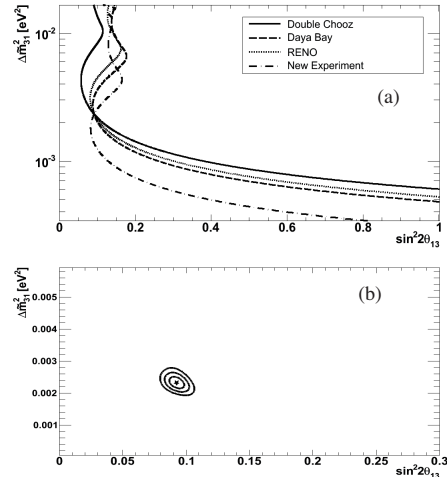
6

experiments.

[1]  K. Nakamura *et al.* (Particle Data Group), J. Phys. G **37**, 075021 (2010).

[2]  M. Apollonio *et al.* (Chooz Collaboration) Phys. Lett. B466(1999)415.

[3]  K. Abe *et al.* (T2K Collaboration), Phys. Rev. Lett.107 (2011) 041801.

[4]  P. Adamson et al. (MINOS Collaboration), Phys. Rev. Lett. 107, 181802 (2011).

[5]  Y. Abe *et al.* (Double Chooz Collaboration), Phys. Rev. Lett.108 (2012) 131801.

[6]  F.P. An *et al.* (Daya Bay Collaboration), Phys. Rev. Lett. 108 (2012) 171803.

[7]  J.K. Ahn *et al.* (RENO Collaboration), Phys. Rev. Lett. 108 (2012) 191802.

[8]  M. Ishitsuka, Invited talk on 'Double Chooz Results', http://neu2012.kek.jp/.

[9]  D. Dwyer, Invited talk on 'Daya Bay Results', http://neu2012.kek.jp/.

[10]  T. Nakaya, Invited talk on 'Results from T2K', http://neu2012.kek.jp/.

[11]  R. Nichol, Invited talk on 'Final MINOS Results', http://neu2012.kek.jp/.

[12]  P. Adamson *et al.* (MINOS Collaboration), Phys. Rev. Lett. 106: 181801, (2011).

[13]  T.J.C. Bezerra, H. Furuta and F. Suekane, Neutrino2012, Poster ID.250-1, 4.June.2012, http://neu2012.kek.jp/.

[14]  G.L. Fogli, Invited talk on 'Global Analysis of Neutrino Oscillations', http://neu2012.kek.jp/.

[15]  H. Nunokawa *et al.* Phys. Rev. D72 (2005), 013009.

[16]  Y. Declais *et al.* Phys. Lett. B 338 (1994), 383.

[17]  Th.A. Mueller *et al.* Phys.Rev. C83 (2011) 054615.

[18]  P. Vogel and J.F. Beacom, Phys. Rev. D 60, 053003(1999).

[19]  M. Aoki *et al.* (KASKA collaboration.) hep-ex/0607013, (2006).

[20]  H. Minakata *et al.* Phys. Rev. D 68, 033017 (2003) and Erratum Phys. Rev. D 70, 059901(E).

[21]  K. Anderson *et al.* (International Reactor $\theta_{13}$ Working Group), hep-ex/0402041, (2004).

[22]  Yu. Kozkov, L. Mikaelyan, V. Sinev, hep-ph/0109277, (2001).

[23]  F. Boehm *et al.* Phys. Rev. D64 (2001) 112001.

[24]  S-B. Kim, Invited talk on 'Results from RENO', http://neu2012.kek.jp/.

# Appendix B

# Reactor Neutrino Global Fit Analysis

The details of the reactor neutrino global fit analysis (section 5.2.2), for the determination of $\Delta \tilde{m}_{31}^2$ is publicly available in the Physics Letters B (PLB) journal [109]. This reference is reproduced in the following pages.

# A Global Fit Determination of Effective $\Delta m_{31}^2$ from Baseline Dependence of Reactor $\bar{\nu}_e$ Disappearance

T.J.C. Bezerra,[*] H. Furuta,[†] and F. Suekane[‡]

*Research Center for Neutrino Science, Tohoku University, Sendai, 980-8578, Japan*

T. Matsubara[§]

*Department of Physics, Tokyo Metropolitan University, Tokyo, 192-0397, Japan*
(Dated: July 5, 2013)

Recently, three reactor neutrino experiments, Daya Bay, Double Chooz and RENO have directly measured the neutrino mixing angle $\theta_{13}$. In this paper, another important oscillation parameter, effective $\Delta m_{31}^2$ ($= \Delta \tilde{m}_{31}^2$) is measured using baseline dependence of the reactor neutrino disappearances. A global fit is applied to publicly available data and $\Delta \tilde{m}_{31}^2 = 2.95^{+0.42}_{-0.61} \times 10^{-3} \text{ eV}^2$, $\sin^2 2\theta_{13} = 0.099^{+0.016}_{-0.012}$ are obtained by setting both parameters free. This result is complementary to $\Delta \tilde{m}_{31}^2$ to be measured by spectrum shape analysis. The measured $\Delta \tilde{m}_{31}^2$ is consistent with $\Delta \tilde{m}_{32}^2$ measured by $\nu_\mu$ disappearance in MINOS, T2K and atmospheric neutrino experiments within errors. The minimum $\chi^2$ is small, which means the results from the three reactor neutrino experiments are consistent with each other.

## I. INTRODUCTION

Neutrino oscillation is a phenomenon which is not accounted for by the Standard Model of elementary particles, which assumes neutrinos as massless. There are six parameters in standard three flavor neutrino oscillation [1]: three mixing angles between flavor eigenstates and mass eigenstates ($\theta_{12}$, $\theta_{13}$ and $\theta_{23}$), one CP violating imaginary phase ($\delta$), and two independent squared mass differences: $\Delta m_{jk}^2 \equiv m_j^2 - m_k^2$, where $m_i$ are neutrino masses ($m_1$, $m_2$, $m_3$) of the three mass eigenstates ($\nu_1$, $\nu_2$, $\nu_3$) which correspond to the largest component of ($\nu_e$, $\nu_\mu$, $\nu_\tau$), respectively. $\theta_{12}$ and $\Delta m_{21}^2$ have been measured by solar neutrino disappearance experiments ($\nu_e \to \nu_e$) and long baseline reactor neutrino disappearance experiments ($\bar{\nu}_e \to \bar{\nu}_e$). $\theta_{23}$ and $\Delta \tilde{m}_{32}^2$ have been measured by ($\nu_\mu \to \nu_\mu$) disappearance experiments at accelerators and atmospheric experiments. All these measurements are summarized in [1]. Here, $\Delta \tilde{m}^2$ is a weighted average of $\Delta m_{31}^2$ and $\Delta m_{32}^2$, called effective $\Delta m^2$ as described in detail later in this section. Recently, finite $\theta_{13}$ was finally measured by short baseline reactor neutrino experiments ($\bar{\nu}_e \to \bar{\nu}_e$) [2–4] and long baseline accelerator experiments ($\nu_\mu \to \nu_e$) [5, 6].

Another effective mass squared difference $\Delta \tilde{m}_{31}^2$ can be measured by energy spectrum distortion and baseline dependence of the reactor-$\theta_{13}$ experiments. This paper is to measure $\Delta \tilde{m}_{31}^2$ by baseline dependence of the reactor neutrino-$\theta_{13}$ experiments.

In reactor-$\theta_{13}$ experiments, usually the neutrino disappearance is analysed by a two flavor neutrino oscillation formula;

$$P(\bar{\nu}_e \to \bar{\nu}_e) = 1 - \sin^2 2\theta_{13} \sin^2 \frac{\Delta \tilde{m}_{31}^2}{4E_\nu} L, \qquad (1)$$

where $L$ is baseline which is $\sim 1$ km and $E_\nu$ is neutrino energy, which is around a few MeV. $\Delta \tilde{m}_{31}^2$ is a weighted average of the two mass square differences, $|\Delta m_{31}^2|$ and $|\Delta m_{32}^2|$ of the standard parametrization,

$$\Delta \tilde{m}_{31}^2 = c_{12}^2 \left| \Delta m_{31}^2 \right| + s_{12}^2 \left| \Delta m_{32}^2 \right|, \qquad (2)$$

with $c_{ij}$ and $s_{ij}$ representing $\cos \theta_{ij}$ and $\sin \theta_{ij}$, respectively [7]. In the analyses of reactor-$\theta_{13}$ experiments so far published, $\sin^2 2\theta_{13}$ is extracted assuming $\Delta \tilde{m}_{31}^2 = \Delta \tilde{m}_{32}^2$, which is measured by MINOS experiment [8]. $\Delta \tilde{m}_{32}^2$ can be expressed as,

$$\begin{aligned} \Delta \tilde{m}_{32}^2 = &(s_{12}^2 + s_{13} t_{23} \sin 2\theta_{12} \cos \delta) \left| \Delta m_{31}^2 \right| \\ &+ (c_{12}^2 - s_{13} t_{23} \sin 2\theta_{12} \cos \delta) \left| \Delta m_{32}^2 \right|, \end{aligned} \qquad (3)$$

where $t_{ij} = \tan \theta_{ij}$ [7]. Since there is a relation

$$\Delta m_{31}^2 = \Delta m_{32}^2 + \Delta m_{21}^2, \qquad (4)$$

in the standard three neutrino flavor scheme, the difference between $\Delta \tilde{m}_{31}^2$ and $\Delta \tilde{m}_{32}^2$ is expressed as follows,

$$\begin{aligned} &\frac{2(\Delta \tilde{m}_{31}^2 - \Delta \tilde{m}_{32}^2)}{\Delta \tilde{m}_{31}^2 + \Delta \tilde{m}_{32}^2} \sim \pm (1 - s_{13} t_{23} \tan 2\theta_{12} \cos \delta) \\ &\times \frac{2 \cos 2\theta_{12} |\Delta m_{21}^2|}{|\Delta m_{31}^2| + |\Delta m_{32}^2|} \sim \pm 0.012 \times (1 \pm 0.3), \end{aligned} \qquad (5)$$

where the overall sign depends on mass hierarchy, and the $\pm 0.3$ term comes from the ambiguity of $\cos \delta$. The difference is much smaller than the current precisions of measurements and can be treated practically equivalent. A precision better than 1% is necessary to distinguish

the mass hierarchy. However, if $\Delta\tilde{m}_{31}^2$ and $\Delta\tilde{m}_{32}^2$ are separately measured and if they turn out to be significantly different, it means the standard three flavour neutrino scheme is wrong. Thus it is important to measure $\Delta\tilde{m}_{31}^2$ independently from $\Delta\tilde{m}_{32}^2$ to test the standard three flavour neutrino oscillation.

The $E$ dependence and $L$ dependence analyses to extract $\Delta\tilde{m}_{31}^2$ use independent information, namely energy distortion and normalization and thus are complementary. Some of the authors demonstrated $\Delta\tilde{m}_{31}^2$ measurement using $L$ dependence of deficit value of each reactor-$\theta_{13}$ experiment in 2012 [9, 10]. In this paper the analysis is significantly improved by applying a detailed global fit making use of the publicly available information of the three reactor neutrino experiments.

In next section we re-analyze the published data of each experiment and compare with the results written in the papers in order to demonstrate our analysis produces identical result. Section-III discusses about possible correlations between the experiments. In section-IV, most recent Double Chooz, Daya Bay and RENO results [2, 4, 11] are combined and $\Delta\tilde{m}_{31}^2$ is extracted. Finally, a summary of this study is presented in section-V.

## II. REACTOR NEUTRINO DATA

Details of each experiment and their data are presented in this section and they are re-analysed by the authors in order to demonstrate that the analysis methods used in this work are consistent with the publications from the experimental groups. The $\chi^2$ used in this section will be used to form global $\chi^2$ function in section-IV.

### A. Daya Bay

The Daya Bay (DB) reactor neutrino experiment consists of three experimental halls (EH), containing one or more antineutrino detectors (AD). The AD array sees 6 reactors clustered into 3 pairs: Daya Bay (DB1, DB2), Ling Ao (L1, L2) and Ling Ao-II (L3, L4) power stations. Fig.-1 shows the relative locations of reactors and AD and table-I shows the distance between each combination of reactor and detector. All reactors are functionally identical pressurized water reactors with maximum thermal power of 2.9 GW [3].

In DB publication, the $\chi^2$ is defined as

$$
\begin{aligned}
\chi_{\mathrm{DB}}^2(\theta_{13}, \Delta m_{31}^2) = \\
\sum_d^6 \frac{\left[M_d + \eta_d - T_d\left(1 + a + \sum_r^6 \omega_r^d \alpha_r + \epsilon_d\right)\right]^2}{M_d + B_d} \\
+ \sum_r^6 \frac{\alpha_r^2}{\sigma_r^2} + \sum_d^6 \left(\frac{\epsilon_d^2}{\sigma_d^2} + \frac{\eta_d^2}{(\sigma_d^b)^2}\right),
\end{aligned} \quad (6)
$$
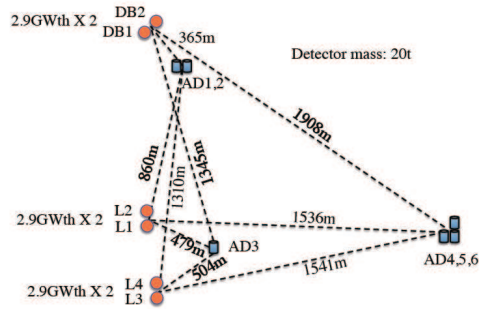


FIG. 1: Relative locations of detectors and reactors of Daya Bay Experiment. Scale is approximate.

where $M_d$ are the measured neutrino candidate events of the $d$-th AD with background subtracted, $B_d$ is the corresponding background, $T_d$ is the prediction from neutrino flux, Monte Carlo simulation (MC) and neutrino oscillation. $\omega_r^d$ is the fraction of neutrino event contribution of the $r$-th reactor to the $d$-th AD determined by baselines and reactor fluxes. The uncorrelated reactor uncertainty is $\sigma_r$. $\sigma_d$ is the uncorrelated detection uncertainty, and $\sigma_d^b$ is the background uncertainty, with the corresponding pull-terms $(\alpha_r, \epsilon_d, \eta_d)$. An absolute normalization factor $a$ is determined from the fit to the data.

The values of $\omega_r^d$ are not shown in Daya Bay publications and was estimated using

$$
\omega_r^d = \frac{p_r/L_{rd}^2}{\sum_r (p_r/L_{rd}^2)} \quad \text{with} \quad p_r = \frac{w_r}{\sum_r w_r}, \quad (7)
$$

where $w_r$ is the thermal power of each reactor and $L_{rd}$ is the baseline of $r$-th reactor to $d$-th detector. In this analysis, the value of $p_r$ is considered $1/6$ since all reactors have same nominal thermal power. The calculated $\omega_r^d$ is shown in table-II. All the others terms are shown in table-III.

By using equation-(6) and the data from tables-II and -III, we were able to reproduce Daya Bay's result, where $T_d$ was multiplied by the value of the deficit probability $(P_{dr}^{\mathrm{def}})$, defined as:

$$
P_{dr}^{\mathrm{def}} = 1 - \sin^2 2\theta \frac{\int_{1.8\mathrm{MeV}}^{8.0\mathrm{MeV}} \sin^2(1.27\frac{\Delta m^2 L_{dr}}{E})n_\nu(E)dE}{\int n_\nu(E)dE},
$$
$$(8)$$

with $\Delta m^2$ being measured in eV$^2$, $L_{dr}$ in meters and $E$ in MeV. $n_\nu(E)$ is the expected energy spectrum of the observed neutrinos which is calculated by $n_\nu(E) = S(E)\sigma_{\mathrm{IBD}}(E)$. $S(E)$ is the energy spectrum of the reactor neutrinos, which is a sum of the energy spectrum of neutrinos from the four fissile elements:

$$
S(E_\nu) = \sum_{i=^{235}\mathrm{U},^{238}\mathrm{U},^{239}\mathrm{Pu},^{241}\mathrm{Pu}} \beta_i S_i(E_\nu), \quad (9)
$$

where $S_i(E_\nu)$ is reactor neutrino spectrum per fission from fissile element $i$ and $\beta_i$ is a fraction of fission rate of fissile element $i$. For equilibrium light water reactors, $\beta_i$ are similar and we use the values of Bugey paper [12], namely $^{235}U$ : $^{238}U$ : $^{239}Pu$ : $^{241}Pu = 0.538 : 0.078 : 0.328 : 0.056$. In this study, $S_i(E)$ is approximated as an exponential of a polynomial function which is defined in [13],

$$S_i(E_\nu) \propto \exp\left[\sum_{j=1}^{6} \alpha_j E_\nu^{(j-1)}\right]. \qquad (10)$$

$\sigma_{IBD}$ is the cross section of the inverse process of neutron $\beta$-decay (IBD), that can be precisely calculated from the neutron lifetime [14]. The energy dependence of the IBD cross section is,

$$\sigma_{IBD}(E_\nu) \propto (E_\nu[\text{MeV}] - 1.29)\sqrt{E_\nu^2 - 2.59E_\nu + 1.4}. \qquad (11)$$

$\sin^2 2\theta_{13}$ is extracted by fixing $\Delta\tilde{m}_{31}^2$ as the MINOS $\Delta\tilde{m}_{32}^2 = 2.32 \times 10^{-3}$ eV$^2$ [8]. The $\chi^2$ distributions of the Daya Bay paper and our calculation are compared in fig.-2. The Daya Bay central value and uncertainty is $\sin^2 2\theta_{13DB} = 0.089 \pm 0.011$ while our analysis showed $\sin^2 2\theta_{13} = 0.090^{+0.011}_{-0.010}$, in good agreement with the published value. We also verified how different values for the fission rates coefficients of equation-(10) and different assumptions for equation-(7), affect the final result. Dependence on the burn-up values is less than 0.001, as it was determined by replacing the burn-up assumption with that of the Chooz reactors at the beginning and end of the reactor cycle. Extreme assumptions on equation-(7) (one or two reactors off for the whole data period, for example) had an effect of less than 0.002 on the central value, with no change on the sensitivity. Moreover, the good agreement between the $\chi^2$ distributions, shows that the assumptions are reasonable.
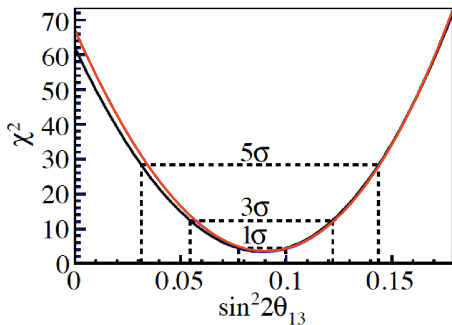


FIG. 2: $\chi^2$ distribution with respect to $\sin^2 2\theta_{13}$ by fixing $\Delta m^2$ as $\Delta\tilde{m}_{32}^2$ for Daya Bay data. The black curve is the $\chi^2$ distribution shown in their paper [11] with central value and $1\sigma$ uncertainty of $0.089 \pm 0.011$, while the red curve shows the $\chi^2$ distribution calculated in this analysis with central value and $1\sigma$ uncertainty of $0.090^{+0.011}_{-0.010}$.

## B. RENO

The Reactor Experiment for Neutrino Oscillation (RENO) is located in South Korea and has two identical detectors, one near (ND) and one far (FD) from an array of six commercial nuclear reactors, as shown in fig.-3.
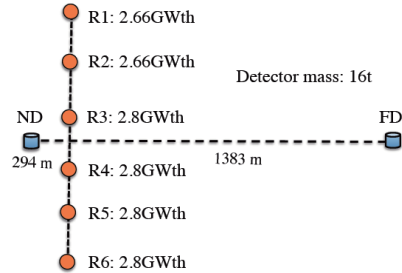


FIG. 3: Relative locations of detectors and reactors of RENO. Scale is approximate.

Together with the distances of each detector reactor pair, the contribution of each reactor flux to each detector for the period of their first analysis is available [15] and are summarized in table-IV.

The RENO $\chi^2$ is defined as:

$$\chi_{RE}^2(\theta_{13}, \Delta m_{31}^2) =$$
$$\sum_{d}^{2} \frac{\left[N_{obs}^d + b_d - (1 + n + \xi_d)\sum_{r}^{6}(1 + f_r)N_{exp}^{d,r}\right]^2}{N_{obs}^d}$$
$$+ \sum_{d}^{2}\left(\frac{\xi_d^2}{(\sigma_d^\xi)^2} + \frac{b_d^2}{(\sigma_d^b)^2}\right) + \sum_{r}^{2}\frac{f_r^2}{\sigma_r^2}, \qquad (12)$$

where $N_{obs}^d$ is the number of observed IBD candidates in each detector after background subtraction and $N_{exp}^{d,r}$ is the number of expected neutrino events, including detection efficiency, neutrino oscillations and contribution from the $r-$th reactor to each detector determined from baseline distances and reactor fluxes. A global normalization $n$ is taken free and determined from the fit to the data. The uncorrelated reactor uncertainty is $\sigma_r$, $\sigma_d^\xi$ is the uncorrelated detection uncertainty, and $\sigma_d^b$ is the background uncertainty, and the corresponding pull parameters are ($f_r$, $\xi_d$, $b_d$). The values of these variables are shown in the table-V.

The expected number of events for both detectors are not present in the RENO paper, but the ratio between data and expectation is shown. This ratio and the quantities of table-IV were used to calculate the expectation value ($N_{exp}^{d,r}$).

Using the data in the table-V, equation-(8) and the MINOS $\Delta\tilde{m}_{32}^2$, we obtained $\sin^2 2\theta_{13} = 0.111 \pm 0.024$ which is in good agreement with their published value

4

of $\sin^2 2\theta_{13\mathrm{RE}} = 0.113 \pm 0.023$. The $\chi^2$ distributions are also very similar as shown in fig.-4.
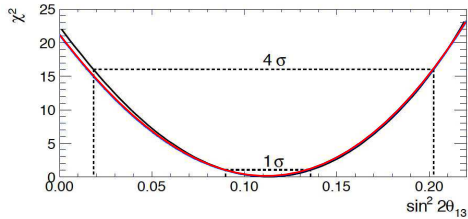


FIG. 4: $\chi^2$ distribution with respect to $\sin^2 2\theta_{13}$ by fixing $\Delta m^2$ as $\Delta \bar{m}_{32}^2$ for RENO data. The black curve shows the $\chi^2$ distribution shown in their paper [4] with central value and $1\,\sigma$ uncertainty of $0.113 \pm 0.023$, while the red curve shows the $\chi^2$ distribution calculated in this analysis with central value and $1\,\sigma$ uncertainty of $0.111 \pm 0.024$.

### C. Double Chooz

The Double Chooz (DC) experiment uses the two Chooz B reactors with thermal power of $4.25\ \mathrm{GW_{th}}$ each. Currently, the experiment is using only the far detector, since its near detector is not complete yet. The Bugey-4 measurement [12] is used as a reference of the absolute neutrino flux in the analysis, and the relative location of the far detector and reactors are shown in fig.-5, where the distances from the detector to each reactor are 998.1 and 1114.6 meters [16].
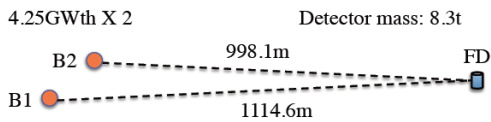


FIG. 5: Relative locations of detector and reactors of Double Chooz experiment. Scale is approximate.

The Double Chooz collaboration published a rate plus shape analysis result [2]. An effect of the shape analysis in this case is an evaluation of main backgrounds of $^9\mathrm{Li}$ and fast-neutron from the energy spectrum beyond the reactor neutrino energy range. Since information of detailed energy spectrum, which is necessary to reproduce the analysis, are not publicly available, we do not consider here the shape analysis but restrict only to the rate analysis. After the second publication on the $\sin^2 2\theta_{13}$ measurement, the Double Chooz group published a result of the direct measurement of backgrounds by making use of 7.53 days reactor-OFF period [17]. We used these data in addition to the background evaluation inputs written in [2] to improve the background estimation instead of the

energy spectrum analysis. The relative neutrino-flux uncertainty for reactor-OFF period is much larger than reactor-ON period. The dominant uncertainty comes from long-life isotopes whose abundance are not well known. It has negligible contribution in reactor-ON period [17]. Therefore, we regard the error correlation on neutrino flux between the reactor ON and OFF periods to be uncorrelated. We performed a similar $\chi^2$ analysis as Daya Bay and RENO cases, assuming that the detector and background related uncertainties of [17] and [2] are fully correlated.

$$
\begin{aligned}
\chi^2_{\mathrm{DC}}(\theta_{13}, \Delta m_{31}^2) = & \\
& \sum_{i=1}^{2} \frac{\left[ N_i^{\mathrm{obs}} - (N_i^{\mathrm{exp}}(1 + \alpha_i + \epsilon) + B_i(1 + b)) \right]^2}{N_i^{\mathrm{exp}} + B_i} \\
& + \sum_i^{2} \left( \frac{\alpha_i}{\sigma_r^i} \right)^2 + \frac{\epsilon^2}{\sigma_d^2} + \frac{b^2}{\sigma_b^2},
\end{aligned}
\tag{13}
$$

where $N^{\mathrm{obs}}$ is the number of the observed neutrino event candidates. The subscript "$i$" represents reactor-ON and OFF period. $N^{\mathrm{exp}}$ is the number of expected neutrino events, including detection efficiency and oscillation effects, and $B$ is the total expected number of background events. The $\sigma_r$, $\sigma_d$, and $\sigma_b$ are the reactor, detection and background uncertainties, respectively. The corresponding pull parameters are $(\alpha, \epsilon, b)$. Using the parameters shown in table-VI, we obtained $\sin^2 2\theta_{13} = 0.131 \pm 0.048$ which is consistent with the result of the DC publication, $\sin^2 2\theta_{13} = 0.109 \pm 0.039$, although the background evaluation methods are different using different data sets. We also did a rate only analysis of the Double Chooz data, which result agreed with the published one.

### III. CORRELATION EVALUATION OF SYSTEMATIC UNCERTAINTIES

In reactor neutrino experiments, the expected number of observed events ($N_{\mathrm{exp}}$) is defined by:

$$
N_{\mathrm{exp}} = \frac{1}{4\pi L^2} N_{\mathrm{p}} \varepsilon \frac{P_{\mathrm{th}}}{\langle E_f \rangle} \langle \sigma_f \rangle,
\tag{14}
$$

where $L$ is the reactor-detector baseline, $N_{\mathrm{p}}$ is the number of targets in the detector, $\varepsilon$ is the detector efficiency, $P_{\mathrm{th}}$ is the reactor thermal power, $\langle E_f \rangle$ is the mean energy released per fission, and $\langle \sigma_f \rangle$ is the cross-section per fission defined as:

$$
\langle \sigma_f \rangle = \sum_i \beta_i \int S_i(E) \sigma_{\mathrm{IBD}}(E) dE.
\tag{15}
$$

For each experiment, $L$, $N_{\mathrm{p}}$, $\varepsilon$, and $P_{\mathrm{th}}$ terms are determined independently. Therefore they can be assumed to be uncorrelated. On the other hand, $\langle E_f \rangle$ and $\langle \sigma_f \rangle$ terms are taken from the same references and the uncertainties

of these terms are correlated between the experiments. From the Bugey and Chooz experimental results, the total uncertainty on spectrum prediction is 2.7%, where a 2% correlation is expected between the experiments as treated in [18]. Fully correlated signal prediction uncertainties between experiments, which come from neutrino flux and detection efficiency, can be cancelled by overall normalization factors used in the analyses of the Daya Bay and RENO. It allows us only to take into account remaining uncertainties between detectors or periods for each experiment. Daya Bay and RENO treat the remaining uncertainties as uncorrelated in their publications.

## IV.  COMBINED ANALYSIS

As explained before, the main method of this work is to combine all the data of the current neutrino reactor experiments in a single $\chi^2$ function. Then we look for the minimum $\chi^2$ value, calculate the $\Delta\chi^2$ distribution, and determine the confidence level regions. The $\chi^2$ function used for such analysis was chosen so as to use the data from tables-I to -VI as well as the correlation as described in section-III. The definition of our global $\chi^2$ is,

$$\chi^2_{\mathrm{G}} \equiv \chi^2_{\mathrm{DB}} + \chi^2_{\mathrm{DC}} + \chi^2_{\mathrm{RE}}, \qquad (16)$$

with the $\chi^2$ of each experiment defined as in section-II. Therefore, this function has 32 pull terms: 18 for Daya Bay (6 reactors, 6 detectors and 6 backgrounds), 10 for RENO (6 reactors, 2 detectors and 2 backgrounds) and 4 for Double Chooz (2 reactors, 1 detector and 1 background).    It also contains the two overall normalization factors, one for Daya Bay and the other for RENO data set.

For all combinations of $\Delta m^2$ and $\sin^2 2\theta$, the $\chi^2_{\mathrm{G}}$ is minimized with respect to the pull terms. Fig.-6 shows a map of the absolute $\chi^2$ and fig.-7 shows the $\Delta\chi^2$ contour map near the $\chi^2_{\min}$, obtained by such procedure. From the minimum point and the 1 $\sigma$ error region in the 1-D $\chi^2$ distribution,

$$\chi^2_{\min} = 5.14 / 6 \text{ Degrees of Freedom,}$$
$$\Delta\tilde{m}^2_{31} = 2.95^{+0.42}_{-0.61} \times 10^{-3} \text{ eV}^2,$$
$$\sin^2 2\theta_{13} = 0.099^{+0.016}_{-0.012}$$

are obtained.    This $\Delta\tilde{m}^2_{31}$ is consistent with $\Delta\tilde{m}^2_{32}$ measured by accelerator experiments [8, 19], confirming the standard three flavor neutrino oscillation within the error. The $\sin^2 2\theta_{13}$ obtained here is independent from $\Delta\tilde{m}^2_{32}$. The small $\chi^2_{\min}$/DoF means the data from the three reactor neutrino experiments are consistent with each other.

All the pull terms output were within 1 $\sigma$ from the input value, and the normalization factors obtained from the fit to the data, were both less than 1%.

In fig.-8 the baseline dependence of the disappearance probability of each detector is shown, where the
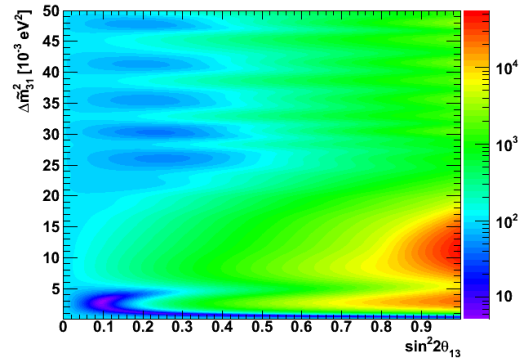


FIG. 6: Absolute $\chi^2$ value calculated for each pair of $\Delta\tilde{m}^2_{31}$ and $\sin^2 2\theta_{13}$, and by the minimization of the pull terms. For higher values of $\Delta\tilde{m}^2_{31}$ (bigger than $10^{-2}$eV$^2$) some valleys are present, although they are about more than ten times less sensitive than the minimum $\chi^2$.
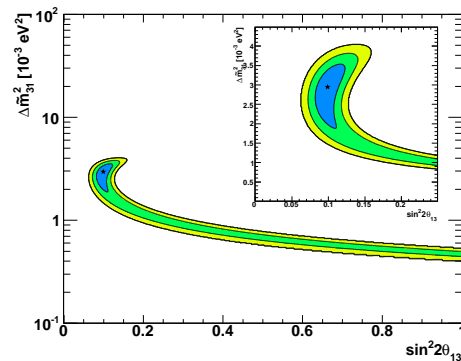


FIG. 7: $\Delta\chi^2$ distribution around the $\chi^2_{\min}$. From the inner to the outer part, the lines correspond to 1 $\sigma$, 2 $\sigma$ and 3 $\sigma$ confidence level. The star shows the best fit point. There is no solution more significant than 3 $\sigma$ except for the $\chi^2_{\min}$ valley.

probability is calculated using the parameters output which give the best fit. The Double Chooz has a large effect on this $\Delta\tilde{m}^2_{31}$ determination because it locates at a baseline where the slope of the oscillation is large. In the near future, when the near detector of the Double Chooz experiment starts operation, the accuracy of this $\Delta\tilde{m}^2_{31}$ measurement is expected to improve much.

FIG. 8: Reactor $\bar{\nu}_e$ survival probabilities. The solid line is the oscillation pattern obtained in this analysis and dot-dashed line uses MINOS $\Delta\tilde{m}_{32}^2$ and the $\sin^2 2\theta_{13}$ that returns the minimum $\chi^2$. The data points are below the $\Delta\tilde{m}_{32}^2$ because they are calculated using the parameters returned by the best fit solution. Generally, a detector sees several reactors. The horizontal axis is a weighted baseline $\langle L \rangle$ and the horizontal bar in each data point shows the standard deviation of the distribution of the baselines, which is defined by $\sigma_L = \sqrt{\langle L \rangle^2 - \langle L^2 \rangle}$, where $\langle L^n \rangle \equiv \sum_k P_k L_k^{n-2} / \sum_k P_k L_k^{-2}$. $k$ is the reactor index and $L_k$ and $P_k$ are the baseline and thermal power of the reactor $k$.
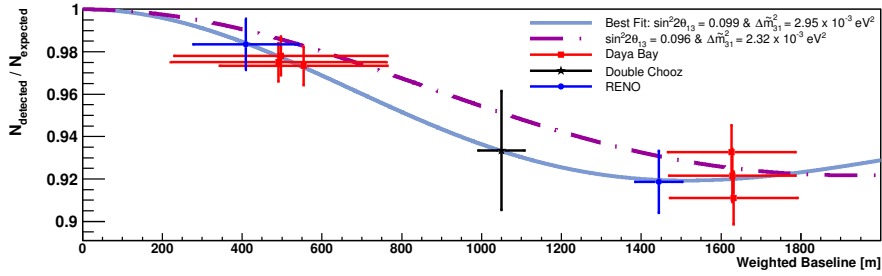
Complementary to this study, we demonstrated a similar, but simpler and robust measurement of the effective $\Delta\tilde{m}_{31}^2$ from the baseline dependence of the disappearance probabilities of the three reactor-$\theta_{13}$ experiments [9, 10]. The result obtained on that work of $\Delta\tilde{m}_{31}^2 = 2.99_{-1.58}^{+1.13} \times 10^{-3}$ eV$^2$, is compatible with the value obtained in this paper. In addition, a similar $\Delta\chi^2$ distribution is presented in [20, fig.-4]. However, the central value of $\Delta\tilde{m}_{31}^2$ could not be compared since only the distribution is presented.

## V.  SUMMARY

In this work, a global fit of the data from all the current reactor-$\theta_{13}$ experiments was performed to measure $\Delta\tilde{m}_{31}^2$. The combination of the data from Daya Bay, RENO and Double Chooz resulted in $\Delta\tilde{m}_{31}^2 = 2.95_{-0.61}^{+0.42} \times 10^{-3}$ eV$^2$. This is consistent with $\Delta\tilde{m}_{32}^2$ and it confirms that the experiments are observing standard three flavor neutrino oscillations within the error. The mixing angle obtained this analysis is $\sin^2 2\theta_{13} = 0.099_{-0.012}^{+0.016}$. The small $\chi_{\min}^2$/DoF value indicates that the data from the three reactor experiments are consistent with each other. This analysis uses independent information from the energy spectrum distortion and it is possible to improve the accuracy of $\Delta\tilde{m}_{31}^2$ combining with results from energy spectrum analysis. It will be important to perform this kind of analysis to improve $\Delta\tilde{m}_{31}^2$ accuracy and to check the consistency of the results from the reactor-$\theta_{13}$ experiments.

# Tables

TABLE I: Daya Bay: Baselines, in meters, between each detector and core [11, tab.-2].

|  | DB1 | DB2 | L1 | L2 | L3 | L4 |
|---|---|---|---|---|---|---|
| AD1 | 362 | 372 | 903 | 817 | 1354 | 1265 |
| AD2 | 358 | 368 | 903 | 817 | 1354 | 1266 |
| AD3 | 1332 | 1358 | 468 | 490 | 558 | 499 |
| AD4 | 1920 | 1894 | 1533 | 1534 | 1551 | 1525 |
| AD5 | 1918 | 1892 | 1535 | 1535 | 1555 | 1528 |
| AD6 | 1925 | 1900 | 1539 | 1539 | 1556 | 1530 |

TABLE II: Daya Bay: Contribution to each detector from reactor, $\omega_r^d$, calculated using equation-(7).

|  | DB1 | DB2 | L1 | L2 | L3 | L4 |
|---|---|---|---|---|---|---|
| AD1 | 0.4069 | 0.3854 | 0.0654 | 0.0799 | 0.0291 | 0.0333 |
| AD2 | 0.4089 | 0.3870 | 0.0643 | 0.0785 | 0.0286 | 0.0327 |
| AD3 | 0.0330 | 0.0318 | 0.2676 | 0.2441 | 0.1882 | 0.2354 |
| AD4 | 0.1208 | 0.1241 | 0.1894 | 0.1892 | 0.1851 | 0.1914 |
| AD5 | 0.1201 | 0.1248 | 0.1895 | 0.1895 | 0.1847 | 0.1913 |
| AD6 | 0.1209 | 0.1241 | 0.1892 | 0.1892 | 0.1851 | 0.1914 |

TABLE III: Daya Bay: Fitting parameters. Differently from [11], here the efficiency and backgrounds (BKG) are combined in a single quantity for each detector. The total BKG is subtracted from the IBD candidates giving $M_d$.

|  | AD1 | AD2 | AD3 | AD4 | AD5 | AD6 |
|---|---|---|---|---|---|---|
| $\nu$ candidate | 69121 | 69714 | 66473 | 9788 | 9669 | 9452 |
| $T_{d0}$ | 68613 | 69595 | 66402 | 9922.9 | 9940.2 | 9837.7 |
| Total BKG [day$^{-1}$] | $13.68 \pm 1.54$ | $13.55 \pm 1.54$ | $10.38 \pm 1.17$ | $3.56 \pm 0.24$ | $3.55 \pm 0.24$ | $3.44 \pm 0.24$ |
| Live Time [days] | 127.5470 | 127.5470 | 127.3763 | 126.2646 | 126.2646 | 126.2646 |
| Efficiency | 0.8015 | 0.7986 | 0.8364 | 0.9555 | 0.9552 | 0.9547 |
| $M_d$ | 67723.59 | 68334.17 | 65363.96 | 9358.7 | 9240.98 | 9037.24 |
| $\sigma_b$ | 157.43 | 156.86 | 124.65 | 28.95 | 28.94 | 28.93 |
| $\sigma_d$ | 0.002 | 0.002 | 0.002 | 0.002 | 0.002 | 0.002 |
| $\sigma_r$ | 0.008 | 0.008 | 0.008 | 0.008 | 0.008 | 0.008 |

TABLE IV: RENO: Baselines and neutrino flux contributions [15, page-7].

|  | R1 | R2 | R3 | R4 | R5 | R6 |
|---|---|---|---|---|---|---|
| FD baseline [m] | 1556.5 | 1456.2 | 1395.9 | 1381.3 | 1413.8 | 1490.1 |
| FD contribution | 0.1373 | 0.1574 | 0.1809 | 0.1856 | 0.1780 | 0.1608 |
| ND baseline [m] | 667.9 | 451.8 | 304.8 | 336.1 | 513.9 | 739.1 |
| ND contribution | 0.0678 | 0.1493 | 0.3419 | 0.2701 | 0.1150 | 0.0558 |

TABLE V: RENO: Fitting parameters. Differently from [4], here the BKGs are summed into a single quantity. The total BKG is subtracted from the IBD candidates giving $N_{\text{obs}}$. $N_{\text{exp}}^d$ is calculated as described in section II B.

|  | ND | FD |
|---|---|---|
| IBD candidates | 154088 | 17102 |
| $N_{\text{exp}}^d$ | 151723.54 | 17565.72 |
| Total BKG [day$^{-1}$] | $21.75 \pm 5.93$ | $4.24 \pm 0.75$ |
| Live Time [days] | 192.42 | 222.06 |
| Efficiency | 0.647 | 0.745 |
| $N_{\text{obs}}$ | 149902.86 | 16160.46 |
| $\sigma_d$ | 0.002 | 0.002 |
| $\sigma_r$ | 0.009 | 0.009 |
| $\sigma_b$ | 1141.05 | 166.54 |

8

TABLE VI: Double Chooz: Fitting parameters [2, 17]. The detector uncertainty is the combination of detector response and efficiency uncertainties, and the BKGs are combined in a single quantity for each data set.

|  | Reactor-On | Reactor-Off |
| --- | --- | --- |
| IBD candidates | 8249 | 8 |
| IBD prediction | 8439.6 | 1.42 |
| Total BKG [$\text{day}^{-1}$] | $2.18 \pm 0.58$ | $2.00 \pm 0.58$ |
| Live Time [days] | 227.93 | 6.84 |
| $\sigma_d$ | 0.010 | 0.010 |
| $\sigma_r$ | 0.017 | 0.40 |

[1] K. Nakamura *et al.* (Particle Data Group), J. Phys. G **37**: 075021 (2010).

[2] Y. Abe *et al.* (Double Chooz Collaboration), Phys. Rev. D 86: 052008 (2012).

[3] F.P. An *et al.* (Daya Bay Collaboration), Phys. Rev. Lett. 108: 171803 (2012).

[4] J.K. Ahn *et al.* (RENO Collaboration), Phys. Rev. Lett. 108: 191802 (2012).

[5] P. Adamson *et al.* (MINOS Collaboration), Phys. Rev. D 82: 051102 (2011).

[6] K. Abe *et al.* (T2K Collaboration), Phys. Rev. Lett. 107: 041801 (2011).

[7] H. Nunokawa *et al.* Phys. Rev. D 72: 013009 (2005).

[8] P. Adamson *et al.* (MINOS Collaboration), Phys. Rev. Lett. 106: 181801, (2011).

[9] T.J.C. Bezerra, H. Furuta and F. Suekane, arXiv 1206.6017[Hep-ex], 26/June/2012.

[10] T.J.C. Bezerra, H. Furuta and F. Suekane, Neutrino2012, Poster ID.250-1, 4.June.2012, http://neu2012.kek.jp/.

[11] F.P. An *et al.* (Daya Bay Collaboration), Chinese Phys. C 37: 011001 (2013).

[12] Y. Declais *et al.* Phys. Lett. B 338 (1994).

[13] Th.A. Mueller *et al.* Phys. Rev. C83: 054615 (2011).

[14] P. Vogel and J.F. Beacom, Phys. Rev. D 60: 053003 (1999).

[15] S-B. Kim, Invited talk on 'Results from RENO', http://neu2012.kek.jp/.

[16] M. Apollonio *et al.* (Chooz Collaboration), Phys. Lett. B 466: 415 (1999).

[17] Y. Abe *et al.* (Double Chooz Collaboration), Phys. Rev. D 87: 011102 (2013).

[18] G. Mention *et al.* Phys. Rev. D 83: 073006 (2011).

[19] K. Abe *et al.* (T2K Collaboration), Phys. Rev. D 85: 031103 (2012).

[20] M.C. Gonzalez-Garcia *et al.*, J. High Energy Phys. 12: 1-24 (2012).

# Bibliography

[1] G. Aad *et al.* (ATLAS Collaboration). Observation of a new particle in the search for the standard model higgs boson with the ATLAS detector at the LHC. *Physics Letters B*, 716(1):1 – 29, 2012. 5

[2] B. Pontecorvo. Mesonium and anti-mesonium. *Sov.Phys.JETP*, 6:429, 1957. 5

[3] Z. Maki, M. Nakagawa, and S. Sakata. Remarks on the unified model of elementary particles. *Progress of Theoretical Physics*, 28(5):870–880, 1962. 5

[4] S. P. Mikheev and A. Yu. Smirnov. Resonance Amplification of Oscillations in Matter and Spectroscopy of Solar Neutrinos. *Sov.J.Nucl.Phys.*, 42:913–917, 1985. 7

[5] L. Wolfenstein. Neutrino Oscillations in Matter. *Phys.Rev.*, D17:2369–2374, 1978. 7

[6] A. De Rújula, M. B. Gavela, and P. Hernández. Atmospheric neutrino anomaly without maximal mixing? *Phys. Rev. D*, 63:033001, Jan 2001. 7

[7] B. Richter. Conventional beams or neutrino factories: The Next generation of accelerator based neutrino experiments. arXiv:hep-ph/0008222, Aug 2000. 7

[8] H. Nunokawa, S. Parke, and R. Z. Funchal. What fraction of Boron-8 solar neutrinos arrive at the Earth as a $\nu_2$ mass eigenstate? *Phys. Rev. D*, 74:013006, Jul 2006. 8

[9] J. N. Bahcall, A. M. Serenelli, and S. Basu. New solar opacities, abundances, helioseismology, and neutrino fluxes. *The Astrophysical Journal Letters*, 621(1):L85, 2005. 10, 14

[10] R. Davis, D. S. Harmer, and K. C. Hoffman. Search for neutrinos from the Sun. *Phys. Rev. Lett.*, 20:1205–1209, May 1968. 9

[11] W. Hampel *et al.* (GALLEX Collaboration). GALLEX solar neutrino observations: results for GALLEX IV. *Physics Letters B*, 447(1–2):127 – 133, 1999. 9

[12] M. Altmann *et al.* (GNO Collaboration). GNO solar neutrino observations: results for GNO I. *Physics Letters B*, 490(1–2):16 – 26, 2000. 9

[13] J. N. Abdurashitov *et al.* (SAGE Collaboration). Results from SAGE (The Russian-American gallium solar neutrino experiment). *Physics Letters B*, 328(1–2):234 – 248, 1994. 9

[14] Y. Fukuda *et al.* (Super-Kamiokande Collaboration). Measurements of the solar neutrino flux from Super-Kamiokande's first 300 days. *Phys. Rev. Lett.*, 81:1158–1162, Aug 1998. 10

[15] B. Aharmim *et al.* (SNO Collaboration). Determination of the $\nu_e$ and total $^8$B solar neutrino fluxes using the Sudbury Neutrino Observatory phase I data set. *Phys. Rev. C*, 75:045502, Apr 2007. 10

[16] S. Abe *et al.* (KamLAND Collaboration). Precision measurement of neutrino oscillation parameters with KamLAND. *Phys. Rev. Lett.*, 100:221803, Jun 2008. 11, 12

[17] A. Gando *et al.* (KamLAND collaboration.). Reactor on-off antineutrino measurement with KamLAND. arXiv:1303.4667 [hep-ex], Mar 2013. 12, 19

[18] J. Beringer *et al.* (Particle Data Group). Review of particle physics. *Phys. Rev. D*, 86:010001, Jul 2012. 14, 21

[19] Y. Ashie *et al.* (Super-Kamiokande Collaboration). Evidence for an oscillatory signature in atmospheric neutrino oscillations. *Phys. Rev. Lett.*, 93:101801, Sep 2004. 14

[20] M. H. Ahn *et al.* (K2K Collaboration). Measurement of neutrino oscillation by the k2k experiment. *Phys. Rev. D*, 74:072003, Oct 2006. 15

[21] P. Adamson *et al.* (MINOS Collaboration). Search for the disappearance of muon antineutrinos in the NuMI neutrino beam. *Phys. Rev. D*, 84:071103, Oct 2011. 15

[22] P. Adamson *et al.* (MINOS Collaboration). Improved search for muon-neutrino to electron-neutrino oscillations in MINOS. *Phys. Rev. Lett.*, 107:181802, Oct 2011. 15

[23] P. Adamson *et al.* (MINOS Collaboration). Measurement of the neutrino mass splitting and flavor mixing by MINOS. *Phys. Rev. Lett.*, 106:181801, May 2011. 16, 124, 145, 150, 153

[24] U. Kose *et al.* (OPERA Collaboration). Study of neutrino oscillations in the OPERA experiment. arXiv:1305.2513 [hep-ex], May 2013. 15

[25] M. Apollonio *et al.* (CHOOZ Collaboration). Search for neutrino oscillations on a long baseline at the Chooz nuclear power station. *Eur.Phys.J.*, C27:331–374, 2003. 16

[26] K. Abe *et al.* (T2K Collaboration). Indication of electron neutrino appearance from an accelerator-produced off-axis muon neutrino beam. *Phys. Rev. Lett.*, 107:041801, Jul 2011. 17

[27] K. Abe *et al.* (T2K Collaboration). Evidence of electron neutrino appearance in a muon neutrino beam. arXiv:1304.0841 [hep-ex], Apr 2013. 17

[28] F. P. An *et al.* (Daya Bay Collaboration). Observation of electron-antineutrino disappearance at Daya Bay. *Phys. Rev. Lett.*, 108:171803, Apr 2012. 18, 149

[29] Y. Abe *et al.* (Double Chooz Collaboration). Indication of reactor $\bar{\nu}_e$ disappearance in the Double Chooz experiment. *Phys. Rev. Lett.*, 108:131801, Mar 2012. 19, 62

[30] Y. Abe *et al.* (Double Chooz Collaboration). Reactor $\bar{\nu}_e$ disappearance in the Double Chooz experiment. *Phys. Rev. D*, 86:052008, Sep 2012. 19, 62, 63

[31] H. Nunokawa, S. Parke, and R. Z. Funchal. Another possible way to determine the neutrino mass hierarchy. *Phys. Rev. D*, 72:013009, Jul 2005. 20

[32] G. L. Fogli. Invited talk on 'Global analysis of neutrino oscillations'. In *The XXV International Conference on Neutrino Physics and Astrophysics (Neutrino 2012)*, Jun 2012. Kyoto, Japan - http://neu2012.kek.jp/. 20

[33] K. Nakamura *et al.* (Particle Data Group). Review of particle physics. *Journal of Physics G: Nuclear and Particle Physics*, 37(7A):075021, 2010. 21, 59, 128

[34] C. Arnaboldi *et al.* (CUORE Collaboration). Results from a search for the 0$\nu\beta\beta$-decay of $^{130}$Te. *Phys. Rev. C*, 78:035502, Sep 2008. 22

[35] I. Abt *et al.* (GERDA Collaboration). A New Ge-76 double beta decay experiment at LNGS: Letter of intent. arXiv:hep-ex/0404039, Apr 2004. 22

[36] M. Danilov *et al.* (EXO Collaboration). Detection of very small neutrino masses in double-beta decay using laser tagging. *Physics Letters B*, 480(1–2):12 – 18, 2000. 22

[37] F. Piquemal. The SuperNEMO project. *Physics of Atomic Nuclei*, 69(12):2096–2100, 2006. 22

[38] A. Aguilar *et al.* (LSND Collaboration). Evidence for neutrino oscillations from the observation of $\overline{\nu}_e$ appearance in a $\overline{\nu}_\mu$ beam. *Phys. Rev. D*, 64:112007, Nov 2001. 22

[39] A. A. Aguilar-Arevalo *et al.* (MiniBooNE Collaboration). Unexplained excess of electronlike events from a 1 GeV neutrino beam. *Phys. Rev. Lett.*, 102:101802, Mar 2009. 22

[40] A. A. Aguilar-Arevalo *et al.* (MiniBooNE Collaboration). Event excess in the MiniBooNE search for $\overline{\nu}_\mu \rightarrow \overline{\nu}_e$ oscillations. *Phys. Rev. Lett.*, 105:181801, Oct 2010. 22

[41] W Hampel *et al.* (GALLEX Collaboration). Final results of the $^{51}$Cr neutrino source experiments in GALLEX. *Physics Letters B*, 420(1–2):114 – 126, 1998. 22

[42] J. N. Abdurashitov *et al.* (SAGE Collaboration). Measurement of the response of a ga solar neutrino experiment to neutrinos from a $^{37}$Ar source. *Phys. Rev. C*, 73:045805, Apr 2006. 22

[43] G. Mention, M. Fechner, Th. Lasserre, Th. A. Mueller, D. Lhuillier, M. Cribier, and A. Letourneau. Reactor antineutrino anomaly. *Phys. Rev. D*, 83:073006, Apr 2011. 23, 153

[44] K. N. Abazajian *et al.* Light Sterile Neutrinos: A White Paper. arXiv:1204.5379 [hep-ph], Apr 2012. 23

[45] Carlo Bemporad, Giorgio Gratta, and Petr Vogel. Reactor-based neutrino oscillation experiments. *Rev. Mod. Phys.*, 74:297–328, Mar 2002. 28

[46] Th. A. Mueller, D. Lhuillier, M. Fallot, A. Letourneau, S. Cormon, M. Fechner, L. Giot, T. Lasserre, J. Martino, G. Mention, A. Porta, and F. Yermia. Improved predictions of reactor antineutrino spectra. *Phys. Rev. C*, 83:054615, May 2011. 28, 29, 145

[47] P. Huber. Determination of antineutrino spectra from nuclear reactors. *Phys. Rev. C*, 84:024617, Aug 2011. Erratum: Phys. Rev. C, 85:029901, Feb 2012. 28, 29

[48] K. Schreckenbach, G. Colvin, W. Gelletly, and F. Von Feilitzsch. Determination of the antineutrino spectrum from $^{235}$U thermal neutron fission products up to 9.5 MeV. *Physics Letters B*, 160(4–5):325 – 330, 1985. 28

[49] A. A. Hahn, K. Schreckenbach, W. Gelletly, F. von Feilitzsch, G. Colvin, and B. Krusche. Antineutrino spectra from $^{241}$Pu and $^{239}$Pu thermal neutron fission products. *Physics Letters B*, 218(3):365 – 368, 1989. 28

[50] D. Franco, G. Consolati, and D. Trezzi. Positronium signature in organic liquid scintillators for neutrino experiments. *Phys. Rev. C*, 83:015504, Jan 2011. 30

[51] P. Vogel. Analysis of the antineutrino capture on protons. *Phys. Rev. D*, 29:1918–1922, May 1984. 30

[52] L. Mikaelyan. Future reactor neutrino oscillation experiments at Krasnoyarsk. *Nuclear Physics B - Proceedings Supplements*, 91(1–3):120 – 124, Jan 2001. Neutrino 2000. 31

[53] H. Minakata, H. Sugiyama, O. Yasuda, K. Inoue, and F. Suekane. Reactor measurement of $\theta_{13}$ and its complementarity to long-baseline experiments. *Phys. Rev. D*, 68:033017, Aug 2003. 31

[54] V. P. Martemyanov, L. A. Mikaelyan, V. V. Sinev, V. I. Kopeikin, and Yu. V. Kozlov. The Kr2Det project: Search for mass-3 state contribution $|U_{e3}|^2$ to the electron neutrino using a one-reactor-two-detector oscillation experiment at the krasnoyarsk underground site. *Physics of Atomic Nuclei*, 66(10):1934–1939, Oct 2003. 31

[55] C. Aberle *et al.* Large scale Gd-beta-diketonate based organic liquid scintillator production for antineutrino detection. *Journal of Instrumentation*, 7(06):P06008, 2012. 34, 35, 36, 40

[56] C. Aberle, C. Buck, F. X. Hartmann, and S. Schönert. Light yield and energy transfer in a new Gd-loaded liquid scintillator. *Chemical Physics Letters*, 516(4–6):257 – 262, 2011. 36

[57] T. Matsubara *et al.* Evaluation of 400 low background 10-in. photo-multiplier tubes for the Double Chooz experiment. *Nuclear Instruments and Methods in Physics Research Section A: Accelerators, Spectrometers, Detectors and Associated Equipment*, 661(1):16 – 25, 2012. 39, 40

[58] Hamamatsu Photonics K.K. http://www.hamamatsu.com/. 40

[59] K. Zbiri. Note on Drexel tests of the IMB R1408 PMTs used in the inner veto of both far and near detectors of the Double Chooz experiment. arXiv:1104.4045, Apr 2011. 40

[60] CAEN. http://www.caentechnologies.com/. 50, 54

[61] F. Sato, J. Maeda, T. Sumiyoshi, and K. Tsukagoshi. High voltage system for the Double Chooz experiment. *Physics Procedia*, 37(0):1164 – 1170, 2012. Proceedings of the 2nd International Conference on Technology and Instrumentation in Particle Physics (TIPP 2011). 51

[62] MySQL. http://www.mysql.com/. 52

[63] B. Reinhold. *Development of a Level-1 Trigger and Timing System for the Double Chooz Neutrino Experiment.* PhD thesis, RWTH Aachen, 2009. 53

[64] F. Ardellier *et al.* Double Chooz: A search for the neutrino mixing angle $\theta_{13}$. arXiv:0606025[Hep-ex], Oct 2006. 55

[65] R. Brun and F. Rademakers. ROOT - An object oriented data analysis framework. *Nuclear Instruments and Methods in Physics Research Section A: Accelerators, Spectrometers, Detectors and Associated Equipment*, 389(1–2):81 – 86, 1997. New Computing Techniques in Physics Research V. 56, 131

[66] T. Konno. *Measurement of reactor anti-neutrino disappearance using the Double Chooz detector.* PhD thesis, Tokyo Institute of Technology, 2013. 56, 57, 58

[67] Debian/GNU Linux. http://www.debian.org/. 56

[68] Ada. http://www.adaic.org/. 56

[69] A. Lucotte *et al.* A front-end read out chip for the OPERA scintillator tracker. *Nuclear Instruments and Methods in Physics Research Section A: Accelerators, Spectrometers, Detectors and Associated Equipment*, 521(2–3):378 – 392, 2004. 57

[70] CC-IN2P3. http://cc.in2p3.org/. 57

[71] A. Remoto. *Correlated background and impact on the measurement of $\theta_{13}$ with the Double Chooz detector.* PhD thesis, Nates University, 2012. 57

[72] iRODS. http://www.irods.org/. 57

[73] High Performance Sotrage System - HPSS. http://www.hpss-collaboration.org/. 57

[74] Java SE Specifications. http://docs.oracle.com/javase/specs/. 58

[75] G. Marleau, R. Roy and A. Hébert. DRAGON: A collision probability transport code for cell and supercell calculations. http://www.polymtl.ca/nucleaire/DRAGON/en/. 61, 65

[76] Méplan *et al.* MURE : MCNP Utility for Reactor Evolution - Description of the methods, first applications and results. In *Proceedings of the ENC 2005 (CD-Rom)*, pages 1–7, Versailles, France, 2005. European Nuclear Society. PACS LPSC05142. 61, 65

[77] G. A. Horton-Smith. Generic liquid-scintillator Geant4 simulation, 2005. http://neutrino.phys.ksu.edu/~GLG4sim/. 62

[78] Y. Abe *et al.* (Double Chooz Collaboration). First measurement of $\theta_{13}$ from delayed neutron capture on hydrogen in the Double Chooz experiment. *Physics Letters B*, 723(1–3):66 – 70, 2013. 62, 63

[79] Y. Abe *et al.* (Double Chooz Collaboration). Direct measurement of backgrounds using reactor-off data in Double Chooz. *Phys. Rev. D*, 87:011102, Jan 2013. 62, 125

[80] Y. Abe *et al.* (Double Chooz Collaboration). First test of lorentz violation with a reactor-based antineutrino experiment. *Phys. Rev. D*, 86:112009, Dec 2012. 62

[81] V. I. Kopeikin, L. A. Mikaelyan, and V. V. Sinev. Reactor as a source of antineutrinos: Thermal fission energy. *Physics of Atomic Nuclei*, 67(10):1892–1899, Oct 2004. 65

[82] A. Onillon and C. Jones. Reactor and antineutrino spectrum calculation for the Double Chooz first phase results. In *The XXV International Conference on Neutrino Physics and Astrophysics (Neutrino 2012)*, Jun 2012. Poster ID.146-2 - http://neu2012.kek.jp/. 66

[83] C. L. Jones *et al.* Reactor simulation for antineutrino experiments using DRAGON and MURE. *Phys. Rev. D*, 86:012001, Jul 2012. 66

[84] Y. Nakahara, K. Suyama, and T. Suzaki. Technical development on burn-up credit for spent LWR fuel. Technical Report JAERI-Tech 2000-071, Japan Atomic Energy Research Institute (JAERI), 2000. ORNL/TR-2001/01 English Translation, Oak Ridge National Laboratory, January 2002. 66

[85] Y. Declais *et al.* Study of reactor antineutrino interaction with proton at Bugey nuclear power plant. *Physics Letters B*, 338(2 - 3):383 – 389, 1994. 68, 145

[86] S. Agostinelli *et al.* Geant4 - A simulation toolkit. *Nuclear Instruments and Methods in Physics Research Section A: Accelerators, Spectrometers, Detectors and Associated Equipment*, 506(3):250 – 303, 2003. 72

[87] Stephen M. Seltzer and Martin J. Berger. Procedure for calculating the radiation stopping power for electrons. *The International Journal of Applied Radiation and Isotopes*, 33(11):1219 – 1226, 1982. 73

[88] V. McLane *et al.* ENDF/B-VI summary documentation. Technical Report BNL-NCS-17541, Nuclear Data Service of International Atomic Energy Agency, 1996. $4^{\text{th}}$ edition, suppl. I. 73

[89] J. B. Birks. Scintillations from organic crystals: Specific fluorescence and relative response to different radiations. *Proceedings of the Physical Society. Section A*, 64(10):874, 1951. 74

[90] J. Haser. Spill in/out technical note. Double Chooz private document DocDB 4127-v3, Nov 2012. 101

[91] K. Terao *et al.* Neutrino selection using neutron caputre on hydrogen. Double Chooz private document DocDB 3667-v2, Feb 2012. 102

[92] K. Terao *et al.* Spill in/out and global normalisation studies for n-H analysis. Double Chooz private document DocDB 4156-v13, Oct 2012. 104

[93] S. Abe *et al.* (KamLAND Collaboration). Production of radioactive isotopes through cosmic muon spallation in KamLAND. *Phys. Rev. C*, 81:025807, Feb 2010. 117

[94] D. R. Tilley *et al.* Energy levels of light nuclei. *Nuclear Physics A*, 745(3–4):155 – 362, 2004. 118

[95] V. A. Kudryavtsev. Muon simulation codes MUSIC and MUSUN for underground physics. *Computer Physics Communications*, 180(3):339 – 346, 2009. 119

[96] C. N. Maesano. $^9Li$ *Production from Stopped Muons in the Double Chooz Detector*. PhD thesis, University of California - Davis, 2012. 119

[97] K. Nakajima. Report of Cluster Events and $^{214}$Bi-Po Increase. Double Chooz private document DocDB 4104-v2, Jun 2012. 121

[98] P. Novella. Gd-H combined reactor rate modulation (RRM) analysis. Double Chooz private document DocDB 4920-v6, Jun 2013. 124, 125

[99] G. L. Fogli, E. Lisi, A. Marrone, D. Montanino, and A. Palazzo. Getting the most from the statistical analysis of solar neutrino oscillations. *Phys. Rev. D*, 66:053010, Sep 2002. 129

[100] F. James. *MINUIT - Function Minimization and error analysis. Reference manual.* CERN Program Library Long Writeup D506. http://wwwasdoc.web.cern.ch/wwwasdoc/minuit/minmain.html. 131

[101] M. Aoki *et al.* (KASKA collaboration.). Letter of intent for KASKA: High accuracy neutrino oscillation measurements with anti-$\nu_e$ from Kashiwazaki-Kariwa nuclear power station. arXiv:hep-ex/0607013, Jul 2011. 144

[102] S-B. Kim. Invited talk on 'Results from RENO'. In *The XXV International Conference on Neutrino Physics and Astrophysics (Neutrino 2012)*, Jun 2012. Kyoto, Japan - http://neu2012.kek.jp/. 145, 151

[103] F. P. An *et al.* (Daya Bay Collaboration). Improved measurement of electron antineutrino disappearance at Daya Bay. *Chinese Physics C*, 37(1):011001, 2013. 149, 150, 151, 155

[104] J. K. Ahn *et al.* (RENO Collaboration). Observation of reactor electron antineutrinos disappearance in the RENO experiment. *Phys. Rev. Lett.*, 108:191802, May 2012. 152, 155

[105] K. Abe *et al.* (T2K Collaboration). First muon-neutrino disappearance study with an off-axis beam. *Phys. Rev. D*, 85:031103, Feb 2012. 153

[106] M. C. Gonzalez-Garcia, M. Maltoni, J. Salvado, and T. Schwetz. Global fit to three neutrino mixing: critical look at present precision. *Journal of High Energy Physics*, 2012(12):1–24, 2012. 155

[107] T. J. C. Bezerra, H. Furuta, and F. Suekane. $\Delta m^2_{31}$ measurement using reactor complementary study. In *The XXV International Conference on Neutrino Physics and Astrophysics (Neutrino 2012)*, Jun 2012. Poster ID.250-1 - http://neu2012.kek.jp/. 159

[108] T. J. C. Bezerra, H. Furuta, and F. Suekane. Measurement of effective $\Delta m^2_{31}$ using baseline differences of Daya Bay, RENO and Double Chooz reactor neutrino experiments. arXiv:1206.6017[hep-ex], Jun 2012. 159

[109] T. J. C. Bezerra, H. Furuta, F. Suekane, and T. Matsubara. A global fit determination of effective from baseline dependence of reactor disappearance. *Physics Letters B*, 725(4-5):271 – 276, 2013. 167